

Static Aeroelastic Optimization of Composite Wings with Variable Stiffness Laminates



Johannes Karl Stefan Dillinger

Static Aeroelastic Optimization of Composite Wings with Variable Stiffness Laminates

Static Aeroelastic Optimization of Composite Wings with Variable Stiffness Laminates

PROEFSCHRIFT

ter verkrijging van de graad van doctor
aan de Technische Universiteit Delft,
op gezag van de Rector Magnificus Prof. ir. K.C.A.M. Luyben,
voorzitter van het College voor Promoties,
in het openbaar te verdedigen op woensdag 4 juni 2014 om 10.00 uur
door

Johannes Karl Stefan DILLINGER

ingenieur luchtvaart en ruimtevaart
geboren te Bernkastel-Kues, Duitsland.

Dit proefschrift is goedgekeurd door de promotor:

Prof. dr. Z. Gürdal

Copromotor: Dr. M.M. Abdalla

Samenstelling promotiecommissie:

| | |
|--------------------------------|---|
| Rector Magnificus | voorzitter |
| Prof. dr. Z. Gürdal | Technische Universiteit Delft / Skoltech, Rusland, promotor |
| Dr. M.M. Abdalla | Technische Universiteit Delft, copromotor |
| Prof. dr. ir. W. Krüger | DLR - Institut für Aeroelastik, Duitsland |
| Prof. dr. ir. U. Ringertz | KTH - Kungliga Tekniska Högskolan, Zweden |
| Prof. dr. ir. L. Tichy | DLR - Institut für Aeroelastik, Duitsland |
| Dr. ir. B. Tomschke | Airbus (retired), Duitsland |
| Prof. dr. ir. L. Veldhuis | Technische Universiteit Delft |
| Emeritus Prof. dr. A. Rothwell | Technische Universiteit Delft, reservelid |

This research work was supported by DLR-Institute of Aeroelasticity, Delft University of Technology and the Clean Sky JTI project, part of the European Union Seventh Framework Program.

Clean Sky JTI Project partners:



ISBN: 978-94-6203-589-8

Copyright © 2014 by J.K.S. Dillinger

All rights reserved. No part of the material protected by this copyright notice may be reproduced or utilized in any form or by any means, electronic or mechanical, including photocopying, recording or by any information storage and retrieval system, without the prior permission of the author.

Printed by Wöhrmann Print Service, Zutphen, The Netherlands
Typeset by the author with the L^AT_EX Documentation System

Wat dann weilen?

*Dedicated to my parents,
Melanie, and the little one ...*

The application of composite material in load carrying structural components of an aircraft is rapidly gaining momentum. While part of the reason for this can certainly be attributed to an increasing confidence of designers in the new material as a result of growing experience, two other crucial points can be made. One, the continuous enhancements in the area of automated production technologies, which are an absolute necessity for ensuring consistent quality in a series production. Two, the progress in the development of computational methods to analyze and optimize composite structures in order to fully exploit their possible advantages over homogeneous materials. Nevertheless, it is still by virtue of challenges in their production as well as computational complexity, that full-fledged variable stiffness designs have not yet found their way in industrial large scale applications. Considering the complex path from the stiffness of a single laminate to the aeroelastic performance of an entire aircraft wing, it becomes clear that variable stiffness optimization is a non-trivial, laborious task. Not only does it require a large amount of design variables in order to achieve an adequate resolution, in addition the diverseness of responses impedes the problem definition.

The research presented in this thesis aims at an advancement of the computational treatment, i.e. the development of a variable stiffness composite optimization framework, allowing for the consideration of static aeroelastic responses in the structural design of aircraft wings. Considering the different ways of optimizing composite structures, the strategy pursued in this thesis relates to a separation of the problem in three consecutive parts, the advantage being that each step can be handled with the most suitable optimization tools. The first part comprises an optimization based on laminate stiffnesses and is the main subject of this dissertation. It will be discussed in more detail below. The second part involves a stacking sequence optimization on the basis of the optimal stiffnesses derived in the first part. Part three deals with the optimal conversion of stacking sequences to fiber paths suitable for the chosen production technology. Parts two and three do not depend significantly on the physics of the problem. However, since it closely relates to the continuous optimization in part one, the stacking sequence optimization will also shortly be addressed. Part three is not dealt with in this thesis.

The composite optimization framework consists of a successive convex subproblem iteration procedure, in which a gradient based optimizer consecutively solves a local approximation problem. Each response to be considered in the optimization, either as objective or as constraint, is approximated as a linear and/or reciprocal

function of the laminate membrane and bending stiffness matrices \mathbf{A} and \mathbf{D} . Together with the laminate thicknesses h , they constitute the design variables in the optimization process. The distribution of design fields – each of which comprises its own set of \mathbf{A} , \mathbf{D} , h variables – within a structural entity like a wing skin, determines the variable stiffness resolution. Inside the optimization algorithm, stiffness matrices are parametrized by means of lamination parameters, resulting in a reduction in the amount of design variables on the one hand, and the constitution of a continuous, well-posed optimization problem on the other. The response sensitivities with respect to the design variables form an essential input in the assembly of response approximations. In this research, the finite element (FE) software NASTRAN is applied in order to generate sensitivities. Three major reasons account for this choice: one, the ability of specifying various types of responses, two, the time efficient implementation, and three, its prevalence in the aircraft industry. A NASTRAN FE model, suitable for the derivation of the required responses, is generated in a parametric model generation process. Aside from the structural FE representation, the model comprises a doublet lattice description for the computation of aeroelastic loads, and a mass model to incorporate non-structural masses like leading and trailing edge or fuel.

Structural responses considered in the stiffness optimization are strength, buckling and mass. For strength, a failure criterion in lamination parameter space is adopted. Buckling is covered by a simply supported flat plate buckling model. Aside from the regular structural responses, the aeroelastic responses aileron effectiveness, divergence, and twist are also directly considered in the optimization process. While response values and sensitivities are an immediate result of NASTRAN, their approximations with respect to the design variables originate from a sensitivity convexification process, ensuring the approximation to incorporate as much reciprocal share as possible.

The stiffness optimization fully relying upon the applied aeroelastic loads, a correction strategy by means of a higher order computational fluid dynamics (CFD) method is developed to enhance the doublet lattice aeroelastic loads.

Eventually, the functionality of the stiffness optimization framework is verified by three applications, comprising different levels of complexity. Mostly wing skin weight serves as objective to be minimized, but also the maximization of aileron effectiveness for a prescribed weight is demonstrated. The possible advantages of unbalanced over balanced laminates are studied, as well as the influence of different sets of aeroelastic constraints on the achievable minimum wing skin weight. Finally, the modifications implied by an aero load correction are analyzed.

De toepassing van composieten materialen in dragende constructies van vliegtuigen wordt steeds belangrijker. Dit is deels te verklaren door een toegenomen vertrouwen van ontwerpers in dit nieuwe materiaal ten gevolge van groeiende expertise. Er zijn nog twee andere belangrijke redenen. Ten eerste de continue verbeteringen in de automatisatie van productietechnologieën die van cruciaal belang zijn om de kwaliteit van serieproductie te garanderen. Ten tweede de vooruitgang in de ontwikkeling van rekenmethoden om composieten constructies te analyseren en te optimaliseren om hun voordelen ten opzichte van homogene materialen ten volle te kunnen benutten. Desalniettemin komt het door de uitdagingen wat betreft productie en complexiteit van rekenmethodes dat volledige variabele stijfheidsontwerpen hun weg nog niet gevonden hebben naar industriële toepassing op grote schaal. De optimalisatie van de variabele stijfheid is niet triviaal omdat de weg van de stijfheid van een enkel laminaat naar de aeroelastische prestaties van een volledig vliegtuig lang en lastig is. Dit komt door zowel het grote aantal ontwerpvariabelen om voldoende resolutie te verkrijgen, alsook door de variatie in analysesresultaten.

Het onderzoek dat gepresenteerd wordt in deze thesis draagt bij aan een vooruitgang in de manier van rekenen aan dit soort problemen. Dit wil zeggen dat er een raamwerk ontwikkeld is waarbinnen de variabele stijfheid van composieten van vliegtuigvleugels geoptimaliseerd kan worden, in acht nemende de statische aeroelasticiteit. De strategie die ontwikkeld is in deze thesis bestaat uit het opdelen van het probleem in drie delen omdat er verschillende manieren zijn om composieten constructies te optimaliseren. Het voordeel hiervan is dat elk deel aangepakt kan worden met de meest geschikte manier van optimaliseren. Deel één is de optimalisatie van de laminaatstijfheden en zal het leeuwendeel van de dissertatie beslaan. Dit zal later in meer detail uitgelegd worden. Deel twee is de optimalisatie van de laagjesvolgorde die gebaseerd is op de optimale stijfheid van deel één. Deel drie is de optimale omzetting van van de laagjesvolgorde naar vezelpaden die geschikt zijn voor de geselecteerde productietechnologie. Delen twee en drie zijn niet dermate afhankelijk van de fysica van de probleemstelling. Echter zal de optimalisatie van de laagjesvolgorde kort behandeld worden omdat het nauw verwant is met de continue optimalisatie van deel één. Deel drie wordt niet behandeld in deze thesis.

Het composietenoptimalisatieraamwerk bestaat uit een reeks van opeenvolgende iteratieprocedures voor convexe deelproblemen waarbij een optimalisatietechniek gebaseerd op afgeleiden een reeks van lokale benaderingen oplost. Elk analysesresultaat wordt meegenomen in de optimalisatie, zowel als doel of als randvoorwaarde. Het

analyseresultaat wordt benaderd als een lineaire en/of inverse functie van de axiale en buigstijfheidsmatrixen \mathbf{A} en \mathbf{D} van het laminaat. Dit zijn de ontwerpvariabelen van het optimalisatieproces samen met de laminaatdikte h . De resolutie van de variabele stijfheid wordt bepaald door de verdeling van de ontwerpvlakken. Deze ontwerpvlakken zijn delen van de vleugel huid met een constante waarde voor \mathbf{A} , \mathbf{D} en h . De stijfheidsmatrixen worden intern in de optimalisatieprocedure geparameteriseerd door laminaatparameters. Dit resulteert in een vermindering van het aantal ontwerpvariabelen enerzijds, terwijl er op die manier een goed gesteld continu optimalisatieprobleem geformuleerd wordt. De gevoeligheid van de analyseresultaten met veranderende ontwerpvariabelen is essentieel voor het opstellen van de benaderingen. De gevoeligheden zijn gegenereerd door NASTRAN in dit onderzoek. Er zijn drie hoofdredenen voor deze keuze: ten eerste de mogelijkheid om verschillende types van analyseresultaten te specificeren; ten tweede, rekenefficiëntie; ten derde, aanwezigheid van de software in de luchtvaartindustrie. Het eindige elementenmodel in NASTRAN, dat geschikt is voor analyse, wordt gegenereerd door een parametrisch modelleringsproces. Naast het structurele eindige elementenmodel is er een aerodynamisch rastermodel om de aeroelastische belastingen te berekenen en er is tenslotte nog een massamodel om niet structurele massa's, zoals de vleugelvoorraad, vleugelachterrand en brandstof, in rekening te brengen.

De analyseresultaten voor de stijfheidsoptimalisatie zijn sterkte, stijfheid en massa. Een bezwijkingscriterium is geïmplementeerd in de laminaatparameterruimte om de sterkte te optimaliseren. Het knikgedrag wordt meegenomen door te kijken naar een opgelegde vlakke plaat. Behalve de standaard structurele analyseresultaten worden er ook aeroelastische analyseresultaten meegenomen, zoals rolroereffectiviteit, divergentie en vleugelrotatie. De analyseresultaten en hun gevoeligheden worden rechtstreeks berekend door NASTRAN maar hun benaderingen zijn een resultaat van een convexificatie van de gevoeligheden. Dit zorgt ervoor dat de benadering zo veel mogelijk een iners karakter heeft.

De stijfheidsoptimalisatie hangt volledig af van de aeroelastische belastingen. Deze belastingen worden gecorrigeerd door een hogere orde numerieke vloeistofdynamica-methode om de lagere orde belastingen te verbeteren.

Uiteindelijk is de functionaliteit van het stijfheidsoptimalisatieraamwerk geverifieerd door middel van drie toepassingen van verschillende complexiteit. Meestal is het gewicht van de huid geminimaliseerd, maar ook de rolroereffectiviteit is gemaximaliseerd voor een gegeven gewicht. De mogelijke voordelen van ongebalanceerde laminaten ten opzichte van gebalanceerde laminaten zijn bestudeerd, alsook de invloed van de verschillende types aeroelastische randvoorwaarden op het minimale huidgewicht. Tenslotte zijn de implicaties van de belastingscorrecties geanalyseerd.

“After a time, you may find that having is not so pleasing a thing, after all, as wanting. It is not logical, but it is often true.”

Lieutenant Commander Spock

I have to admit that this part of the thesis is among the most difficult, and at the same time also most relieving parts to write. Hopefully not because all the other stuff was too easy or boring; that is something you will have to decide for yourself: but honestly, because it is difficult to find words of thanks for all the support I have received in the past years. Reflecting on the people to thank I realized, that confining myself to no more than fifteen pages of preface text would have required an optimization in itself. It is somewhat ironic that the process developed in this work was unable to support the search for an optimum. . . I then realized that it is not about optimizing, but only about showing my great thankfulness to all of you that helped, supported, guided, and trusted me.

First of all, I wish to thank my promoter Prof. Zafer Gürdal and co-promoter Dr. Mostafa Abdalla, not only did they support me during my Master Thesis for an unexpectedly long period, they even took me back when I knocked at their door after a short industrial interlude. With only minimum physical attendance in Delft, they were able to guide me along the path that I am trying to describe in this thesis. It is yet absolutely unbelievable to me, how Mostafa can keep such a huge amount of knowledge in his head, able to share it at any time, and in a way that also I could understand – part of it. I wish to thank Prof. Lorenz Tichy and Prof. Wolf Krüger. They provided me with all the freedom to form my research work at DLR into this dissertation, and I am extremely grateful for that. I would like to thank Prof. Leo Veldhuis, Prof. Ulf Ringertz and Dr. Bernd Tomschke for their willingness to participate in the doctoral committee. I hope that the contents of the thesis compensate for the time and effort required to read and judge it. I also would like to thank Prof. Wolf Röger from FH Aachen, who supervised me during my Diploma Thesis and established the initial contact with TU Delft.

I am grateful to have found two great office mates. I wish to thank Yves for all his software support, the bicycle training, and for always being a good friend, and I wish to thank Roeland for his constant technical support, the valuable exchange of ideas, and for his friendship. I wish to thank Sam and Attila, for their great support on the optimizer, and all the input and ideas they shared with me. I also wish to thank Yasser, Marius and Etana for their important contributions to my work

during their internships at DLR in Göttingen. I wish to thank Jan for his problem solving capabilities concerning cluster, software and administration. I wish to thank Laura for all her help with everything relating to the administrative part of my Delft experience. I still owe her a *Bitburger Pils*. I would like to thank Miranda for her great commitment to proofreading my papers and this thesis. I consider it an honor Prof. Wolfgang Kloß was also willing to proofread parts of the thesis.

I wish to thank Diliانا, Jan, 2xJens, Markus, Olli, Reik and René for helping me with all kind of FEM, CFD and texting related stuff. I could contact them at any time day and night. I wish to thank Thomas for his exhaustless support during the generation of finite element models, this research would have lasted twice as long without his contributions. A special thanks goes to David for his valuable SUMO software and the support for it. I wish to thank Daniela and Mrs. Metz for all their administrative help, and Urte for her constant support for a Linux noob like me. She always found a solution. Moreover I wish to thank all the race and mountain bike people at the Institute, who dragged me out of the office regularly, for keeping me in touch with the three-dimensional world and muscle pain. Special thanks go to Holger and Olli, who taught me all about bicycles, yet, I still just share a fraction of their knowledge. And I wish to thank all my other colleagues at the Institute, where I have found many good friends. It truly is a great team.

I owe my deepest gratitude to Loek, Gerhard and Dick. Being part of the Concordia team was the greatest opportunity of all. It was a most interesting, exciting and fascinating experience. A very special thank goes to Stefan. Sharing most of our collegiate times, the weekly trips from Mosel to Aachen or Delft an back would not have been possible without him. Moreover, he always provided me with a place to lay my head during my visits in Delft, something which cannot be taken for granted. I wish to thank *cee* buddies Jaro and Eva for taking over when it really got tight in terms of finishing the thesis. I don't want to sound pathetic, but I would like to thank my friends at the Mosel, who all contributed in one way or the other to this work.

Ok, here we are. Undoubtedly, I owe the deepest gratitude to my parents. They provide me with the greatest possible support for all the weird turns I take in my life, and give me a safe home and unlimited love. I am truly thankful for this. The same holds for Melanie. I have no words to express my thanks for her encouragement and love. To you I dedicate this thesis. I would also like to say a big thank you to my sister Renée and all her family for their support and believe.

Noting that *Lieutenant Commander Spock* will speak the words at the beginning of this Preface in the year 2267, I would like to close with some words spoken by an ancient philosopher from my home town Bernkastel-Kues. Some 800 years before *Spock*, *Nikolaus von Kues* said basically the exact same thing, so there is no need to translate it:

“In jedem Wunsch schlummert die Enttäuschung seiner Erfüllung.”

Nikolaus von Kues

It is not for the sake of not wanting to finish my thesis that I choose these words; I am truly happy to have achieved this, and will also be happy tomorrow. It is the great support from all the nice people that I am going to miss. Thank you very much!

Eulen Uhu!
Johannes

| | |
|---|------------|
| Summary | i |
| Samenvatting | iii |
| Preface | v |
| Contents | vii |
| List of Symbols | xi |
| 1 Introduction | 1 |
| 1.1 Composite Technology | 4 |
| 1.1.1 Classical Lamination Theory | 6 |
| 1.1.2 Lamination Parameters | 10 |
| 1.1.3 Membrane Stiffness Visualization | 12 |
| 1.2 Composite Optimization | 14 |
| 1.2.1 Lamination Parameter Optimization | 15 |
| 1.3 Composites and Aircraft Wings | 15 |
| 1.3.1 Wing Structural Layout | 16 |
| 1.3.2 Aeroelastic Optimization | 17 |
| 1.4 Objectives and Thesis Layout | 19 |
| I Optimization Methodology | 21 |
| 2 Basic Concept | 23 |
| 2.1 Optimization Framework | 24 |
| 2.1.1 Finite Element Model | 25 |
| 2.1.2 Optimization Model | 26 |
| 2.1.3 Sensitivity Analysis | 26 |
| 2.1.4 Approximation Setup | 26 |

| | | |
|----------|---|-----------|
| 2.1.5 | Optimization | 27 |
| 2.2 | Static Aeroelastic Responses | 27 |
| 2.2.1 | Aileron Effectiveness | 27 |
| 2.2.2 | Divergence | 29 |
| 2.2.3 | Wing Twist | 31 |
| 2.3 | Stacking Sequence Optimization | 32 |
| 2.3.1 | Stacking Sequence Table | 33 |
| 2.3.2 | Genetic Algorithm | 35 |
| 2.3.3 | Successive Approximations and Shepard's Interpolation | 38 |
| 2.3.4 | Response Approximations | 40 |
| 2.3.5 | Objective Function | 41 |
| 2.4 | Summary | 41 |
| 3 | Parametric Wing Model Generation | 43 |
| 3.1 | Geometry Model | 44 |
| 3.2 | Finite Element Model | 45 |
| 3.3 | Mass Model | 46 |
| 3.3.1 | Interface Model | 47 |
| 3.3.2 | Fuel Model | 47 |
| 3.4 | Double Lattice Model | 48 |
| 3.4.1 | Control Surfaces | 49 |
| 3.4.2 | Camber and Twist Correction | 49 |
| 3.4.3 | Coupling | 49 |
| 3.5 | Summary | 51 |
| 4 | Optimization Model Setup | 53 |
| 4.1 | Design Fields | 53 |
| 4.1.1 | Subdivision of Structural Entities | 54 |
| 4.2 | Design Variable Definition | 56 |
| 4.3 | Response Definition | 57 |
| 4.4 | Finite Element Sensitivity Analysis | 59 |
| 4.5 | Output Definition | 60 |
| 4.5.1 | Sensitivities and Responses | 60 |
| 4.5.2 | Aerodynamics | 61 |
| 4.5.3 | Displacements | 62 |
| 4.5.4 | Correcting Alters | 62 |
| 4.6 | Summary | 62 |
| 5 | Response Approximation Formulation | 63 |
| 5.1 | Approximation Methods in Structural Optimization | 63 |
| 5.2 | General Approximation Form | 64 |
| 5.3 | Sensitivity Processing | 67 |
| 5.4 | Sensitivity Convexification | 67 |
| 5.5 | Sensitivity Convexification Sample | 70 |

| | | |
|-----------|---|-----------|
| 5.6 | Structural Responses | 72 |
| 5.6.1 | Strength | 73 |
| 5.6.2 | Buckling | 74 |
| 5.6.3 | Mass | 76 |
| 5.7 | Aeroelastic Responses | 76 |
| 5.7.1 | Aileron Effectiveness | 76 |
| 5.7.2 | Twist | 77 |
| 5.7.3 | Divergence | 78 |
| 5.8 | Summary | 78 |
| 6 | Aero Load Correction | 79 |
| 6.1 | Doublet Lattice | 80 |
| 6.2 | Correction Methods | 81 |
| 6.2.1 | Doublet Lattice Correction | 81 |
| 6.2.2 | CFD Correction | 85 |
| 6.3 | Process Methodology | 87 |
| 6.4 | CFD Correction Module | 90 |
| 6.4.1 | Mesh Generation | 91 |
| 6.4.2 | Mesh Deformation and Force Coupling | 92 |
| 6.4.3 | CFD Tools | 93 |
| 6.5 | Summary | 95 |
| II | Design Studies | 97 |
| 7 | Aeroelastic Optimization of a Swept Back Wing | 99 |
| 7.1 | Model Description | 100 |
| 7.2 | Flight Envelope and Load Cases | 101 |
| 7.3 | Finite Element Model | 103 |
| 7.4 | Optimization Model | 106 |
| 7.4.1 | Design Variables and Responses | 106 |
| 7.4.2 | Approximations | 107 |
| 7.5 | Starting Design | 107 |
| 7.6 | Sensitivity Check | 110 |
| 7.7 | Numerical Results: Mass Minimization | 116 |
| 7.7.1 | Balanced Laminates | 116 |
| 7.7.2 | Unbalanced Laminates | 119 |
| 7.8 | Numerical Results: Aileron Effectiveness Maximization | 124 |
| 7.8.1 | Balanced Laminates | 124 |
| 7.8.2 | Unbalanced Laminates | 126 |
| 7.9 | Summary | 129 |

| | | |
|------------|---|------------|
| 8 | Aeroelastic Optimization of a Forward Swept Wing | 131 |
| 8.1 | Model Description | 132 |
| 8.2 | Flight Envelope and Load Cases | 133 |
| 8.3 | Finite Element Model | 135 |
| 8.4 | Optimization Model | 140 |
| 8.5 | Starting Design | 141 |
| 8.6 | Numerical Results: Aileron Effectiveness Constraint | 143 |
| 8.7 | Numerical Results: Divergence Pressure Constraint | 148 |
| 8.8 | Numerical Results: Twist Constraint | 153 |
| 8.9 | Some Remarks on Stringers | 156 |
| 8.10 | Summary | 158 |
| 9 | Aeroelastic Optimization With Aero Correction | 159 |
| 9.1 | Finite Element and Optimization Model | 160 |
| 9.2 | CFD Model | 162 |
| 9.3 | Aeroelastic Trim Application | 164 |
| 9.4 | Numerical Results: Mass Minimization | 175 |
| 9.4.1 | Optimization Results | 177 |
| 9.4.2 | Aeroelastic Results | 179 |
| 9.4.3 | Aerodynamic Results | 184 |
| 9.5 | Numerical Results: Mass Minimization Including Shear Webs | 190 |
| 9.6 | Numerical Results: Stacking Sequence Optimization | 194 |
| 9.7 | Summary | 199 |
| III | Summary | 203 |
| 10 | Conclusions and Recommendations | 205 |
| 10.1 | Conclusions | 205 |
| 10.1.1 | Stiffness Optimization Process | 206 |
| 10.1.2 | Wing Design with Aeroelastic Constraints | 207 |
| 10.2 | Recommendations | 210 |
| A | Finite Element Analysis Alter | 211 |
| | Bibliography | 215 |
| | Curriculum Vitae | 225 |
| | List of Publications | 227 |

Abbreviations:

| | |
|------|---|
| ACM | Aircraft mass |
| AIC | Aerodynamic influence coefficients |
| CAS | Calibrated airspeed |
| CFD | Computational fluid dynamics |
| CFL | <i>Courant-Friedrichs-Lewy</i> number |
| CLT | Classical Lamination Theory |
| CWT | Center wing tank |
| DLM | Doublet lattice method/model |
| DOF | Degree of freedom |
| DV | Design variable |
| EASA | European aviation safety agency |
| FC | Fuel case |
| FEM | Finite element method/model |
| FRP | Fiber reinforced plastic |
| GA | Genetic algorithm |
| ID | Identification number |
| LC | Load case |
| LRA | Load reference axis |
| MC | Mass case |
| MDO | Multidisciplinary design optimization |
| NACA | National advisory committee for aeronautics |
| NSM | Non-structural mass |
| OWE | Operational weight empty |
| RBF | Radial basis function |
| RPK | Revenue passenger kilometer |
| SC | Sub case |
| SST | Stacking sequence table |

Greek Symbols:

| | |
|--------------------------|---|
| α | Linear response sensitivity with respect to thickness, also angle of attack |
| α_0 | Zero lift angle of attack |
| δ | Aileron deflection |
| δ_{ij} | <i>Kronecker</i> delta |
| ϵ | Increment in finite difference scheme |
| η_{ail} | Aileron effectiveness |
| Γ_i | Material invariant matrices |
| γ_s | Strain allowable in shear |
| γ_{xy} | In-plane shear strain |
| κ_x, κ_y | Out-of-plane bending curvature |
| κ_{xy} | Out-of-plane twisting curvature |
| λ | <i>Lagrange</i> multiplier, inequality constraint |
| μ | <i>Lagrange</i> multiplier, equality constraint |
| ν_{12}, ν_{21} | <i>Poisson's</i> ratio in 1-2 plane |
| ω | Roll velocity |
| ϕ | <i>Lobatto</i> bubble function |
| ρ | Air density |
| ρ_f | Fiber density |
| σ^u, σ^l | In-plane normal stress, upper and lower laminate end |
| σ_x, σ_y | In-plane normal stress |
| τ_{xy} | In-plane shear stress |
| θ | Twist of a 2D section, also fiber angle |
| ϵ_c | Strain allowable in compression |
| ϵ_t | Strain allowable in tension |
| ϵ_x, ϵ_y | In-plane normal strain |
| Ξ | Bending-torsion coupling index |

Roman Symbols:

| | |
|------------------|--|
| b | Wing span |
| c_{ref} | Reference chord |
| \bar{c} | Average chord |
| C_0 | Constant in approximation formulation |
| C_D, C_d | Overall and sectional drag coefficient |
| C_{l_α} | Lift curve slope |
| C_{l_δ} | Roll coefficient due to aileron deflection |
| C_{l_p} | Roll coefficient due to rolling (roll damping) |
| C_L, C_l | Overall and sectional lift coefficient |
| C_M, C_m | Overall and sectional moment coefficient |
| \tilde{d}, d^+ | Eigenvalues for sensitivity convexification, initial and optimized |
| E_1 | Modulus of elasticity in fiber direction (1) |
| E_2 | Modulus of elasticity orthogonal to fiber direction (2) |
| E_f | Modulus of elasticity of fiber |

| | |
|--------------------|---|
| f | Arbitrary function |
| \tilde{f}_i^g | Global multi-point approximation according to <i>Shepard</i> |
| \tilde{f}_i^l | Local approximation applied in <i>Shepard's</i> method |
| G_{12} | Shear modulus in 1-2 plane |
| h | Laminate/shell thickness |
| H | Flight altitude |
| K_θ | Torsional stiffness |
| m | Mass |
| M | <i>Mach</i> number |
| M_0 | Airfoil moment about quarter chord |
| M_D | Design dive <i>Mach</i> number |
| M_x, M_y, M_{xy} | Moment resultants |
| n_z | Load factor |
| N_{min}, N_{max} | Minimum and maximum number of plies in a stacking sequence |
| N_x, N_y, N_{xy} | Stress resultants |
| p | Roll rate |
| q | Dynamic pressure |
| Q_{ij} | Components of the reduced stiffness matrix in the orthotropic coordinate system |
| r | Strain/buckling failure index |
| R_{far} | Farfield radius of CFD mesh |
| s | Wing semispan |
| S_{ref} | Wing reference area |
| U_i | Material invariants |
| V_∞ | Free stream velocity |
| V_D | Design dive speed |
| V_{iA} | Membrane stiffness matrix lamination parameter |
| V_{iB} | Coupling stiffness matrix lamination parameter |
| V_{iD} | Bending stiffness matrix lamination parameter |
| w | <i>Shepard</i> weight |

Vectors and Matrices:

| | |
|--|---|
| Φ | Reciprocal response sensitivity with respect to an inverse stiffness matrix |
| Ψ | Linear response sensitivity with respect to a stiffness matrix |
| λ | Adjoint vector |
| $\mathbf{A}, \hat{\mathbf{A}}$ | Membrane stiffness matrix, regular and thickness normalized |
| $\mathbf{B}, \hat{\mathbf{B}}$ | Coupling stiffness matrix, regular and thickness normalized |
| $\mathbf{D}, \hat{\mathbf{D}}$ | Bending stiffness matrix, regular and thickness normalized |
| $\tilde{\mathbf{D}}, \mathbf{D}^+$ | Diagonal matrix of eigenvalues for sensitivity convexification, initial and optimized |
| \mathbf{D}_{ja} | Differentiation matrix, relating downwash to displacements in DLM |
| \mathbf{f} | Load vector |
| $\mathbf{f}_{DLM}, \mathbf{f}_\tau, \mathbf{f}_{ie}$ | DLM, TAU and inertial/external load vector |

| | |
|--------------------------------|---|
| \mathbf{g} | Sensitivity of failure index with respect to element strain |
| \mathbf{H} | Aero-Structure coupling matrix |
| \mathbf{K}_g | Geometric stiffness matrix |
| \mathbf{K} | Stiffness matrix |
| \mathbf{K}^A | Aerodynamic stiffness matrix |
| \mathbf{M} | Mass matrix |
| \mathbf{p}_j | DLM box pressure vector |
| $\mathbf{Q}, \bar{\mathbf{Q}}$ | Reduced stiffness matrix in orthotropic and rotated coordinate system |
| \mathbf{R} | Rotation matrix |
| \mathbf{s} | Sensitivity of failure index with respect to stress resultant |
| $\mathbf{S}_{a,j}$ | DLM integration matrix |
| \mathbf{T} | Transformation matrix |
| \mathbf{u} | Displacement and rotation vector |
| $\mathbf{w}_j, \mathbf{w}_j^g$ | Downwash and geometric downwash |

Other:

| | |
|---------------|--|
| : | Matrix contraction, multiplication of two matrices and subsequent summation of diagonal elements |
| \mathcal{L} | <i>Lagrange</i> function |
| \mathcal{U} | Panel strain energy |
| \mathcal{V} | Potential energy of in-plane loads |
| \sim | Indicator for an approximation |

Subscript:

| | |
|-----|--|
| 0 | Function evaluation point for approximation generation |
| a | Aerodynamic indicator |
| i | Response counter, also matrix/vector element |
| j | Material counter, also matrix/vector element |
| k | Layer number |
| s | Structure indicator, also stacking symmetry |

Superscripts:

| | |
|-------|---|
| * | Indicator for scaled and shifted response approximation |
| b | Bending indicator |
| k,n | Counter for TAU correction and structural iterations |
| m | Membrane indicator |
| P | Power parameter in <i>Shepard's</i> method |

CHAPTER 1

Introduction

“He has the deed half done who has made a beginning.”

Horace

The main goal of the research presented in this thesis is the increase in performance of aircraft wings, by either minimizing or maximizing objective functions like weight or aileron effectiveness, while constraining indispensable boundary conditions for the design to remain within feasible regions.

Seen in this context, this research is *just another example* in the long-standing history of the human race to either invent new, or optimize existing systems. The type of systems we seek to invent or optimize, and the reasons we want to do so span a large range, including for instance optimization of our everyday lives by improving or inventing mechanical systems, like washing machines or escalators, or, as in the present case, improving the efficiency of an existing mechanical system so that it performs in the best possible manner in its field of application. The goals of such research are manifold, and often include the objectives to make something cheaper, faster or lighter.

When narrowing down the field of vision to the area of transportation and aircraft in particular, history shows that we have sought to build efficient systems since the beginning, and today with all the environmental and economic pressures faced by airliners and aircraft designers, there is an ever increasing need for better aircraft. In the early years of manned flight designers focused on taking off, staying in the air, being able to steer the aircraft and landing safely. Then it was realized that aircraft could provide an efficient means for transport, and they could be used for military purposes. Aircraft needed to be designed that could carry armament and a pilot, and be faster and more maneuverable than other sides aircraft. This led early aircraft designers to be faced with an enormous optimization task. Keeping in mind that the design space was not yet completely discovered by existing aircraft types, the planes featured a large variations in terms of their aerodynamic and structural layout.

Important milestones in the early convergence to a conventional monoplane-fuselage-tail configuration, which was capable of carrying a significant amount of

payload, took place in the 1920s and 30s with wooden structures being replaced by metal alloys for the load carrying structures and increasingly aerodynamic designs to reduce drag or increase lift performance and maneuverability. The limitations on speed and payload capacity was primarily due to limited power available from regular piston engines, and was overcome with the advent of the jet engine in civil transport aircraft in the late 1940s. Along with a considerable increase in cruise velocity and the accompanying necessity for swept wings, the impression may arise that with the introduction of *Boeing 707* and *Douglas DC-8* at the end of the 1950s the optimization process either fully converged or got stuck in a local optimum. That is, for a layman it might be difficult to discover differences between passenger aircraft developed in the past 50 years.

It is needless to say that despite the perpetuation of the basic concept with a swept back wing, tailplanes, and a payload carrying fuselage the optimization did of course not stagnate but, quite the contrary, gained momentum. Several reasons for this can be identified, the most important of which, economic feasibility, is more than ever a key issue in modern aircraft design. Given that the upper limit on meaningful cruise *Mach* numbers, beyond which wave drag penalty starts to form a natural transonic velocity boundary, could be reached with the adoption of jet engines, very soon economical aspects became the driving force in the optimization of the overall system.

Since economic feasibility inherently incorporates multiple disciplines, the field of multidisciplinary design optimization (MDO) started to develop, for example Haftka [Haf77] and Jr, Schmit [Jr 81], by incorporating new disciplines in the structural optimization process which aimed at a mass minimization of the load carrying components. Several overviews and surveys on the field of multidisciplinary design optimization can be found in literature, for example Sobieszczanski-Sobieski [Sob90], [Sob97], Balling et al. [Bal96], Wit et al. [Wit10] and Martins et al. [Mar13], aside from practical applications in the aircraft industry as shown for example by Schuhmacher et al. [Sch02]. A strong and most certainly indispensable contribution was provided by means of fast evolving computer science and the corresponding optimization algorithms, which rapidly broadened not only the design space, but also the possibilities for simultaneous treatment of disciplines featuring a large variety of design variable types. The finite element software NASTRAN is a typical example of a computational tool whose development emerged in the late 1960s, and which has been around ever since.

Having appointed economic feasibility to be the main objective in aircraft design nowadays, this statement can be substantiated by two very important facts. One, according to *Boeing's* "[Current Market Outlook 2013-2032](#)" fuel accounted for 13% of the operating costs in 2002 and already 34% in 2012 for mid-sized aircraft, the considerable growth being attributed to increasing fuel costs. Accordingly, the necessity for more efficient aircraft is directly related to the the prospect of considerable cost savings on the one hand, but also to comply with the *European Union's* emission trading system [Leg12], officially introduced in 2012 but postponed to take effect in 2013. The most promising means of fuel saving can be attributed to engine performance, aerodynamic efficiency and aircraft weight. Two, both large aircraft manufacturers *Boeing* and also *Airbus* in its "[Global Market Forecast 2012-2031](#)" project an annual growth of $\approx 5.0\%$ in revenue passenger kilometers (RPK), Figure 1.1. The amount of

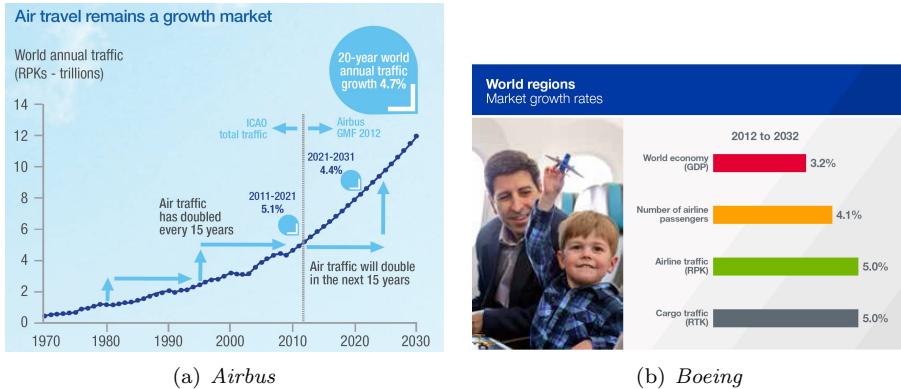


Figure 1.1: Revenue passenger kilometer forecast (source: annual forecast reports)

new aircraft required within the next 20 years to extend and renew airliner fleets for coping with the growing passenger demand, is projected to 28,200 units according to *Airbus*, and 35,300 units according to *Boeing*'s forecast. These numbers illustrate the vast potential to save fuel, but also the inevitable need to enhance economic feasibility of new aircraft in order to minimize the ecological impact and guarantee affordability. Among others, the need for evermore ecological aircraft is also reflected in the “[ACARE Vision 2020](#)”, and the successor “[ACARE Flightpath 2050](#)” programs, the latter one aiming at a reduction of CO_2 by 75% and NO_x by 90%, possible through the development of new technologies by the year 2050.

As mentioned above, the aircraft mass plays a decisive role for two reasons. Decreasing the mass does either result in an overall reduction in take-off weight or allows for increased payload. In both cases, overall efficiency can considerably increase. To this end, the adoption of fiber reinforced plastics (FRP) represented one of the most important milestones in the latest aviation history, leading to an essential incision with respect to existing construction and optimization techniques that were traditionally tailored to homogeneous materials, towards an entirely new design and optimization philosophy. A prominent advantage of composites over metal-based materials is found in the excellent stiffness to mass and strength to mass ratios that go along with the considerably lower material density. No less important are the orthotropic stiffness properties of a single composite layer, which in combination with other layers allows for a selective application and adjustment of stiffness to best respond to loading conditions on the one hand, and the evocation of in- and out-of-plane force and displacement couplings on the other hand. These characteristics form the basis for a concerted manipulation of the displacement behavior of the wing, also known as aeroelastic tailoring, and thus the foundation for effectively influencing static aeroelastic responses by means of stiffness variations. In this context, stiffness variation denotes the local adaptation of stiffness characteristics by means of customized directional stiffness distributions and thicknesses.

The first large-scale applications of FRP in aircraft wing design date back to the 1960s, when sailplane designers discovered the benefits of their orthotropic characteristics and low mass, as described for example in Thomas et al. [Tho99] and Simons [Sim02]. While the development of composite modeling and optimization methods essentially started in the 1970s, for example Schmit Jr et al. [Sch73], [Sch77], it might

seem odd that aircraft manufacturers like *Airbus* and *Boeing* with the *A350* and *B787* have just lately introduced aircraft types featuring entire components like wing and fuselage made of composites.

Several reasons account for the seemingly late adoption of FRP in the load carrying structure of large passenger aircraft. Aside from the cost factor due to the initially limited amount of fiber manufacturers, an even more profound reason can be attributed to the complex fabrication process. Section 1.1 will therefore provide a brief insight into general composite material and manufacturing aspects, along with an introduction to basic analytical methods in the derivation of stiffness properties. An outline on the research work in the field of composite optimization with a special focus on lamination parameter based optimizations is given in section 1.2. Concentrating in this research on the stiffness optimization of aircraft wings, section 1.3 presents an overview on the structural layout of modern aircraft wings and discusses the research development in the field of stiffness optimization with aeroelastic constraints. Eventually, section 1.4 summarizes the dissertations objective and depicts its layout.

1.1 Composite Technology

The general principle of fiber reinforced plastic consists of the synergetic effect when combining the excellent mechanical properties of thin, application tailored filaments with a supporting matrix material. Filaments are usually gathered to continuous tows, so-called rovings, unidirectional tapes, or be interweaved to a fabric that can directly be adopted in a two-dimensional coverage. Typical fiber materials used in the aircraft industry are glass, carbon and aramid. Carbon fiber in particular allows for an adaptation of the mechanical properties within a wide range of elastic moduli and failure strains. Table 1.1 lists some basic fiber properties.

Table 1.1: *Fiber properties*

| name | type | E_f, GPa | $\varepsilon_{max}, \%$ | $\rho_f, kg/m^3$ |
|----------------|----------|------------|-------------------------|------------------|
| Silenka E-Glas | glas | 74 | 3.5 | 2550 |
| Kevlar | aramid | 130 | 2.8 | 1450 |
| Toray T300 | carbon | 220 | 1.5 | 1760 |
| Toray M40J | carbon | 377 | 1.2 | 1810 |
| Toray M60J | carbon | 588 | 0.7 | 1940 |
| Dialead K63712 | coal tar | 640 | 0.4 | 2120 |

To unfold their full potential, fibers need to be embedded in a matrix material to fix the intended position and shape, keeping in mind that without a support the compressive strength is zero. In principle, two matrix types exist. Thermosets like epoxy consist of two components, resin and hardener, that usually are liquid at room temperature and cure once combined in the appropriate mixture ratio. Depending on the particular matrix system, the available processing time after mixing determines how long the resin can be used to impregnate the fibers. A variety of techniques exist to facilitate and automate the impregnation process, such as resin infusion or resin transfer molding, where resin can either be pushed or sucked through the dry

fiber layup. The curing process for thermosets is irreversible, while the other type of matrix material, so-called thermoplastics, are solid at ambient temperature and start to liquefy once heated above a resin-specific temperature. To efficiently facilitate the process of placing dry fibers and subsequent impregnation with thermoset resin, the use of pre-impregnated fibers, also known as prepregs, allows for a reduction of the involved steps. The resin contained in prepregs is activated and cured by heating up the part, mostly in combination with the application of pressure in an autoclave process.

Apart from fiber and resin, a mold that constitutes the shape of the part to be built is required. Unless applying a hand layup process, where fiber layers are consecutively placed in the mold and impregnated one after the other, the laminate consisting of multiple plies according to the so-called stacking sequence needs to be arranged in dry state inside the mold, before initiating one of the impregnation processes addressed above. This shows, that in principle composite parts develop on site, hence, other than with homogeneous materials, the resulting structural properties are strongly coupled to the production process. Accordingly, in order to enable the manufacturing of large components not only in a finite amount of time, but also in a well reproducible manner, the invention of automated fiber placement machines was a logical and also inevitable step towards reliable serial production. Figure 1.2 gives an impression of the working principle. Numerous research activities concentrate on advancements of

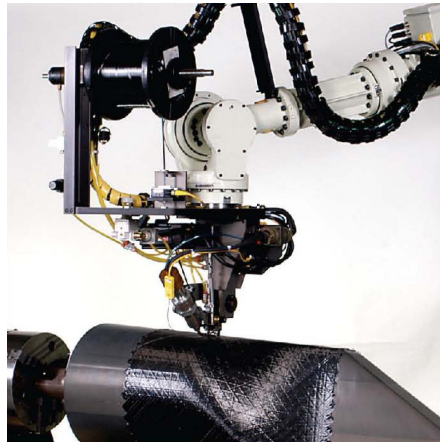


Figure 1.2: *Automated fiber placement (source: automated dynamics)*

placement techniques on the one hand, and optimization tools directly considering constraints imposed by fiber placement on the other hand, for example Van Campen [Van11].

Before being actually able to produce a composite part, an analytical and/or optimization procedure most likely has been involved in the derivation of the fiber paths to be followed in the automated placement, or in the stacking sequences to be produced in a hand layup technique. However, some approach to identify the stiffness properties inherent to the stacking sequences most likely was involved. The analytical treatment of composite material in terms of mechanical properties such as stiffness, stress and strain distributions, failure types and so forth has been an

important research topic for decades. A standard work that covers many composite related topics is provided for example by Schürmann [Sch07], while the work by Gürdal et al. [Gur99] focuses on the optimization related topics in composites.

The following sections exemplify two possibilities in parameterizing the stiffness properties of a laminate, which will later on serve as design variables in the optimization process. While both methods are based on the classical lamination theory, the first one derives laminate stiffnesses on the basis of single layers comprising thickness and fiber angles, section 1.1.1. The specification of stiffnesses by means of lamination parameter as described in section 1.1.2 makes use of so-called material invariants and allows for a continuous stiffness matrix parametrization. Section 1.1.3 eventually introduces a stiffness visualization methodology.

1.1.1 Classical Lamination Theory

The stress-strain relation in the principal direction of a single composite layer as depicted in Figure 1.3 can be written as:

$$\begin{Bmatrix} \sigma_1 \\ \sigma_2 \\ \tau_{12} \end{Bmatrix} = \begin{bmatrix} Q_{11} & Q_{12} & 0 \\ Q_{12} & Q_{22} & 0 \\ 0 & 0 & Q_{66} \end{bmatrix} \begin{Bmatrix} \varepsilon_1 \\ \varepsilon_2 \\ \gamma_{12} \end{Bmatrix}, \quad (1.1)$$

$$\boldsymbol{\sigma} = \mathbf{Q}\boldsymbol{\varepsilon}, \quad (1.2)$$

where “1” denotes the fiber direction and “2” the direction orthogonal to the fiber direction. The relation results from the general 3D stress-strain relation with the

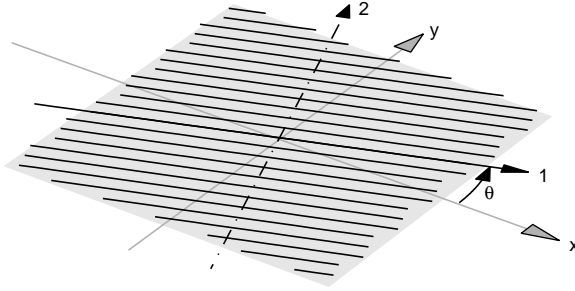


Figure 1.3: *Coordinate systems and fiber angle in a single layer*

plain stress assumption $\sigma_3 = \tau_{31} = \tau_{23} = 0$. The matrix elements in \mathbf{Q} , denoted as reduced stiffnesses, can be written as:

$$Q_{11} = \frac{E_1}{1 - \nu_{12}\nu_{21}}, \quad (1.3)$$

$$Q_{22} = \frac{E_2}{1 - \nu_{12}\nu_{21}}, \quad (1.4)$$

$$Q_{12} = \frac{\nu_{12}E_2}{1 - \nu_{12}\nu_{21}} = \frac{\nu_{21}E_1}{1 - \nu_{12}\nu_{21}}, \quad (1.5)$$

$$Q_{66} = G_{12}. \quad (1.6)$$

The transformation from the 1-2-coordinate system to a x-y-coordinate system that is rotated by an angle θ with respect to the 1-2-coordinate system, is accomplished by a transformation matrix \mathbf{T} , equation (1.7), that transforms stresses and strains according to equation (1.8); the coordinate systems and fiber angle definition are shown in Figure 1.3:

$$\mathbf{T} = \begin{bmatrix} \cos^2\theta & \sin^2\theta & 2\cos\theta\sin\theta \\ \sin^2\theta & \cos^2\theta & -2\cos\theta\sin\theta \\ -\cos\theta\sin\theta & \cos\theta\sin\theta & \cos^2\theta - \sin^2\theta \end{bmatrix}, \quad (1.7)$$

$$\begin{Bmatrix} \sigma_1 \\ \sigma_2 \\ \tau_{12} \end{Bmatrix} = \mathbf{T} \begin{Bmatrix} \sigma_x \\ \sigma_y \\ \tau_{xy} \end{Bmatrix}, \quad \begin{Bmatrix} \varepsilon_1 \\ \varepsilon_2 \\ \varepsilon_{12} \end{Bmatrix} = \mathbf{T} \begin{Bmatrix} \varepsilon_x \\ \varepsilon_y \\ \varepsilon_{xy} \end{Bmatrix}. \quad (1.8)$$

Attention has to be paid to the difference in engineering shear strain γ_{12} in equation (1.1) and tensorial shear strain ε_{12} in the strain transformation, equation (1.8), where engineering shear strain is equal to twice the tensorial shear strain:

$$\mathbf{R} = \begin{bmatrix} 1 & 0 & 0 \\ 0 & 1 & 0 \\ 0 & 0 & 2 \end{bmatrix}, \quad (1.9)$$

$$\begin{Bmatrix} \varepsilon_1 \\ \varepsilon_2 \\ \gamma_{12} \end{Bmatrix} = \mathbf{R} \begin{Bmatrix} \varepsilon_1 \\ \varepsilon_2 \\ \varepsilon_{12} \end{Bmatrix}, \quad \begin{Bmatrix} \varepsilon_x \\ \varepsilon_y \\ \gamma_{xy} \end{Bmatrix} = \mathbf{R} \begin{Bmatrix} \varepsilon_x \\ \varepsilon_y \\ \varepsilon_{xy} \end{Bmatrix}. \quad (1.10)$$

Combining equations (1.1), (1.8) and (1.10) leads to an equation expressing the stress strain relationship in the rotated x-y-coordinate system:

$$\begin{Bmatrix} \sigma_x \\ \sigma_y \\ \tau_{xy} \end{Bmatrix} = \mathbf{T}^{-1} \mathbf{Q} \mathbf{R} \mathbf{T} \mathbf{R}^{-1} \begin{Bmatrix} \varepsilon_x \\ \varepsilon_y \\ \gamma_{xy} \end{Bmatrix}, \quad (1.11)$$

where the stiffness matrix of the rotated layer is written as:

$$\bar{\mathbf{Q}} = \mathbf{T}^{-1} \mathbf{Q} \mathbf{R} \mathbf{T} \mathbf{R}^{-1}. \quad (1.12)$$

The stiffness derivation of a laminate consisting of multiple layers is based on an important assumption in the classical lamination theory. Each layer subject to the rotated stress-strain relationship is assumed to bond perfectly with its neighboring layers with an infinitely thin adhesive film. The layers are assumed to undergo the same shear deformation for in-plane loading and a linearly varying shear deformation in thickness direction for bending loads. A laminate of k layers, not necessarily symmetric about the mid-plane and comprising varying layer thicknesses is shown in Figure 1.4. The strain deformation expressed as function of the thickness coordinate z then becomes:

$$\begin{Bmatrix} \varepsilon_x \\ \varepsilon_y \\ \gamma_{xy} \end{Bmatrix} = \begin{Bmatrix} \varepsilon_x^0 \\ \varepsilon_y^0 \\ \gamma_{xy}^0 \end{Bmatrix} + z \begin{Bmatrix} \kappa_x \\ \kappa_y \\ \kappa_{xy} \end{Bmatrix}, \quad (1.13)$$

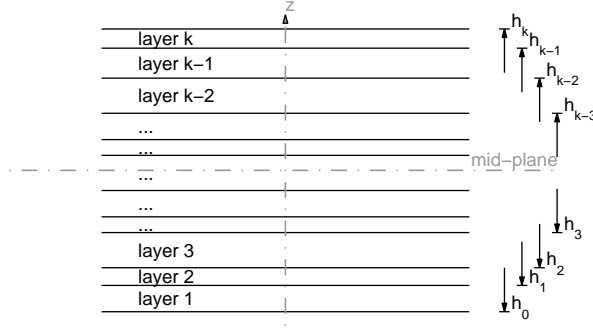


Figure 1.4: Laminate cross section, made up of single layers

where superscript “0” denotes the shear deformation of the mid-plane, κ is the radius of curvature, and z is the coordinate in thickness direction. Combining equations (1.11), (1.12), and (1.13) results in a position dependent stress-strain relationship of a layer within a laminate:

$$\begin{Bmatrix} \sigma_x \\ \sigma_y \\ \tau_{xy} \end{Bmatrix}_{(k)} = \bar{\mathbf{Q}}_{(k)} \begin{Bmatrix} \varepsilon_x^0 \\ \varepsilon_y^0 \\ \gamma_{xy}^0 \end{Bmatrix} + z \bar{\mathbf{Q}}_{(k)} \begin{Bmatrix} \kappa_x \\ \kappa_y \\ \kappa_{xy} \end{Bmatrix}. \quad (1.14)$$

Integrating the stresses over the thickness leads to overall stress resultants, equation (1.15). Accordingly, considering the distance z with respect to the mid-plane, the stresses generate moment resultants, equation (1.16). Since the stress distribution throughout a laminate is not continuous, the integration has to be split up in an integration over each layer and subsequent summation:

$$\begin{Bmatrix} N_x \\ N_y \\ N_{xy} \end{Bmatrix} = \sum_{k=1}^n \int_{h_{k-1}}^{h_k} \begin{Bmatrix} \sigma_x \\ \sigma_y \\ \tau_{xy} \end{Bmatrix} dz, \quad (1.15)$$

$$\begin{Bmatrix} M_x \\ M_y \\ M_{xy} \end{Bmatrix} = \sum_{k=1}^n \int_{h_{k-1}}^{h_k} z \begin{Bmatrix} \sigma_x \\ \sigma_y \\ \tau_{xy} \end{Bmatrix} dz. \quad (1.16)$$

Finally, inserting equation (1.14) in equation (1.15) and (1.16), considering the independence of $\bar{\mathbf{Q}}$, ε and κ with respect to z , and performing the simple integrations leads to:

$$\begin{Bmatrix} N_x \\ N_y \\ N_{xy} \end{Bmatrix} = \sum_{k=1}^n \left\{ \bar{\mathbf{Q}}_{(k)} \begin{Bmatrix} \varepsilon_x^0 \\ \varepsilon_y^0 \\ \gamma_{xy}^0 \end{Bmatrix} (h_k - h_{k-1}) + \bar{\mathbf{Q}}_{(k)} \begin{Bmatrix} \kappa_x \\ \kappa_y \\ \kappa_{xy} \end{Bmatrix} \frac{1}{2} (h_k^2 - h_{k-1}^2) \right\}, \quad (1.17)$$

$$\begin{Bmatrix} M_x \\ M_y \\ M_{xy} \end{Bmatrix} = \sum_{k=1}^n \left\{ \bar{\mathbf{Q}}_{(k)} \begin{Bmatrix} \varepsilon_x^0 \\ \varepsilon_y^0 \\ \gamma_{xy}^0 \end{Bmatrix} \frac{1}{2} (h_k^2 - h_{k-1}^2) + \bar{\mathbf{Q}}_{(k)} \begin{Bmatrix} \kappa_x \\ \kappa_y \\ \kappa_{xy} \end{Bmatrix} \frac{1}{3} (h_k^3 - h_{k-1}^3) \right\}, \quad (1.18)$$

and rewritten:

$$\begin{Bmatrix} N_x \\ N_y \\ N_{xy} \end{Bmatrix} = \mathbf{A} \begin{Bmatrix} \varepsilon_x^0 \\ \varepsilon_y^0 \\ \gamma_{xy}^0 \end{Bmatrix} + \mathbf{B} \begin{Bmatrix} \kappa_x \\ \kappa_y \\ \kappa_{xy} \end{Bmatrix}, \quad (1.19)$$

$$\begin{Bmatrix} M_x \\ M_y \\ M_{xy} \end{Bmatrix} = \mathbf{B} \begin{Bmatrix} \varepsilon_x^0 \\ \varepsilon_y^0 \\ \gamma_{xy}^0 \end{Bmatrix} + \mathbf{D} \begin{Bmatrix} \kappa_x \\ \kappa_y \\ \kappa_{xy} \end{Bmatrix}, \quad (1.20)$$

where:

$$\mathbf{A} = \sum_{k=1}^n \bar{\mathbf{Q}}_{(k)} (h_k - h_{k-1}), \quad (1.21)$$

$$\mathbf{B} = \frac{1}{2} \sum_{k=1}^n \bar{\mathbf{Q}}_{(k)} (h_k^2 - h_{k-1}^2), \quad (1.22)$$

$$\mathbf{D} = \frac{1}{3} \sum_{k=1}^n \bar{\mathbf{Q}}_{(k)} (h_k^3 - h_{k-1}^3), \quad (1.23)$$

denote the laminate membrane, coupling, and bending stiffness matrices, respectively. The coupling matrix \mathbf{B} establishes a connection between in-plane and out-of-plane deformations and loadings; it vanishes for symmetric laminates. Rewriting equation (1.19) and (1.20) in matrix notation results in:

$$\begin{Bmatrix} N_x \\ N_y \\ N_{xy} \\ \bar{M}_x \\ M_y \\ \bar{M}_{xy} \end{Bmatrix} = \begin{bmatrix} A_{11} & A_{12} & A_{13} & B_{11} & B_{12} & B_{13} \\ & A_{22} & A_{23} & & B_{22} & B_{23} \\ -sym. & & A_{33} & sym. & & B_{33} \\ B_{11} & B_{12} & B_{13} & D_{11} & D_{12} & D_{13} \\ & B_{22} & B_{23} & & D_{22} & D_{23} \\ sym. & & B_{33} & sym. & & D_{33} \end{bmatrix} \begin{Bmatrix} \varepsilon_x^0 \\ \varepsilon_y^0 \\ \gamma_{xy}^0 \\ \kappa_x \\ \kappa_y \\ \kappa_{xy} \end{Bmatrix}. \quad (1.24)$$

Equation (1.24) best explains the possible coupling mechanisms that can arise as a consequence of non-zero elements in the membrane stiffness matrix \mathbf{A} and the bending stiffness matrix \mathbf{D} . Postulating symmetrical stacking sequences only, the coupling matrix \mathbf{B} vanishes and will not be considered. The in-plane coupling of deformations ε_x^0 and ε_y^0 via matrix element A_{12} reflects the elongation-contraction effect described by the *Poisson's* ratio. Since A_{12} will never be zero, the coupling will always exist. More interesting however are stiffness elements A_{13} and A_{23} , which couple the in-plane extension and shear deformations. When non-zero, a laminate loaded in tension will simultaneously experience a shear deformation. Later on it will be demonstrated that extension-shear coupling constitutes one of the fundamental instruments in aeroelastic tailoring. The magnitudes of A_{13} and A_{23} are directly related to the laminate stacking sequence. A designated rank is devoted to balanced laminates, which feature a ply with negative angle $-\theta$ for each ply with positive θ . Along with the restriction to symmetric laminates, extension-shear coupling terms in the \mathbf{A} matrix will be zero. Unbalanced laminates however do feature non-zero coupling elements, indicating their superior suitability for aeroelastic tailoring.

Similar considerations can be employed for the bending stiffness coupling terms D_{13} and D_{23} . These terms cause twisting of a laminate that is purely loaded in bending, and are therefore denoted as bending-twist coupling terms. The latter should not be confused with what is commonly denoted as bending-twist coupling of a wing. This effect in turn is caused to a large extent by the previously described extension-shear coupling of the mostly membrane-loaded wing skins.

More details on coupling effects in combination with aeroelastic tailoring will be provided in the chapters dedicated to the application of the developed stiffness optimization process.

1.1.2 Lamination Parameters

The derivation of stiffness matrices with classical lamination theory demonstrated the direct link of stiffness properties with the stacking sequence in terms of layer thicknesses and fiber angles. Another possibility is to express the laminate stiffness matrices not as function of the stacking, but as function of lamination parameters exists and will be discussed below.

Lamination parameter were first introduced by Tsai et al. [Tsa68], [Tsa80], and represent an integrated form of the layer angles over the laminate thickness as shown in equation (1.25):

$$\begin{aligned} (V_{1A}, V_{2A}, V_{3A}, V_{4A}) &= \frac{1}{h} \int_{-h/2}^{h/2} (\cos 2\theta, \sin 2\theta, \cos 4\theta, \sin 4\theta) dz, \\ (V_{1B}, V_{2B}, V_{3B}, V_{4B}) &= \frac{4}{h^2} \int_{-h/2}^{h/2} z (\cos 2\theta, \sin 2\theta, \cos 4\theta, \sin 4\theta) dz, \\ (V_{1D}, V_{2D}, V_{3D}, V_{4D}) &= \frac{12}{h^3} \int_{-h/2}^{h/2} z^2 (\cos 2\theta, \sin 2\theta, \cos 4\theta, \sin 4\theta) dz. \end{aligned} \quad (1.25)$$

In combination with the material invariant matrices Γ_i , lamination parameters constitute a set of twelve continuous variables that along with a laminate thickness h suffice to compute the material stiffness matrices according to equation (1.26):

$$\begin{aligned} \mathbf{A} &= h(\Gamma_0 + \Gamma_1 V_{1A} + \Gamma_2 V_{2A} + \Gamma_3 V_{3A} + \Gamma_4 V_{4A}), \\ \mathbf{B} &= \frac{h^2}{4}(\Gamma_1 V_{1B} + \Gamma_2 V_{2B} + \Gamma_3 V_{3B} + \Gamma_4 V_{4B}), \\ \mathbf{D} &= \frac{h^3}{12}(\Gamma_0 + \Gamma_1 V_{1D} + \Gamma_2 V_{2D} + \Gamma_3 V_{3D} + \Gamma_4 V_{4D}). \end{aligned} \quad (1.26)$$

Equation (1.26) also suggests a thickness normalized version of the stiffness matrices, denoted with a hat symbol:

$$\hat{\mathbf{A}} = \mathbf{A} \frac{1}{h}, \quad \hat{\mathbf{B}} = \mathbf{B} \frac{4}{h^2}, \quad \hat{\mathbf{D}} = \mathbf{D} \frac{12}{h^3}. \quad (1.27)$$

Lamination parameters in principle are allowed to vary independently, however, only within feasible regions that in turn will result in feasible stacking sequences. This implies that the boundaries within which a parameter can be varied depend on the magnitude of all other parameters. The application of lamination parameters has

been hampered by the lack of definition of the the feasible region for simultaneously optimizing in-plane and bending behavior. Recently, many attempts have been made to remedy this, such as Setoodeh et al. [Set06a] who give approximate feasible regions for any combination of lamination parameters.

The material invariant matrices $\mathbf{\Gamma}_i$ result from the material invariants U_i . As their name implies, they only depend on material properties and not on the fiber angle. They can be derived from elements of the reduced stiffness matrix, equation (1.1):

$$\begin{aligned} U_1 &= (3Q_{11} + 3Q_{22} + 2Q_{12} + 4Q_{66})/8, \\ U_2 &= (Q_{11} - Q_{22})/2, \\ U_3 &= (Q_{11} + Q_{22} - 2Q_{12} - 4Q_{66})/8, \\ U_4 &= (Q_{11} + Q_{22} + 6Q_{12} - 4Q_{66})/8, \\ U_5 &= (Q_{11} + Q_{22} - 2Q_{12} + 4Q_{66})/8. \end{aligned} \quad (1.28)$$

The material invariants U_i can also be applied in derivation of the directional stiffness matrix of a single layer. The generation of a transformation matrix \mathbf{T} and the according matrix multiplications shown in equation (1.12) are not required:

$$\begin{aligned} \bar{Q}_{11} &= U_1 + U_2 \cos 2\theta_{(k)} + U_3 \cos 4\theta_{(k)}, \\ \bar{Q}_{22} &= U_1 - U_2 \cos 2\theta_{(k)} + U_3 \cos 4\theta_{(k)}, \\ \bar{Q}_{12} &= U_4 - U_3 \cos 4\theta_{(k)}, \\ \bar{Q}_{66} &= U_5 - U_3 \cos 4\theta_{(k)}, \\ \bar{Q}_{16} &= (U_2 \sin 2\theta_{(k)} + 2U_3 \sin 4\theta_{(k)})/2, \\ \bar{Q}_{26} &= (U_2 \sin 2\theta_{(k)} - 2U_3 \sin 4\theta_{(k)})/2. \end{aligned} \quad (1.29)$$

From the invariants, equation (1.28), follow the material invariant matrices $\mathbf{\Gamma}_i$, equation (1.30), that are applied in the derivation of the laminate stiffness matrices according to equation (1.26). Again, it should be stressed that $\mathbf{\Gamma}_i$ do only depend on material properties.

$$\begin{aligned} \mathbf{\Gamma}_0 &= \begin{bmatrix} U_1 & U_4 & 0 \\ U_4 & U_1 & 0 \\ 0 & 0 & U_5 \end{bmatrix}, \quad \mathbf{\Gamma}_1 = \begin{bmatrix} U_2 & 0 & 0 \\ 0 & -U_2 & 0 \\ 0 & 0 & 0 \end{bmatrix}, \quad \mathbf{\Gamma}_2 = \begin{bmatrix} 0 & 0 & U_2/2 \\ 0 & 0 & U_2/2 \\ U_2/2 & U_2/2 & 0 \end{bmatrix}, \\ \mathbf{\Gamma}_3 &= \begin{bmatrix} U_3 & -U_3 & 0 \\ -U_3 & U_3 & 0 \\ 0 & 0 & -U_3 \end{bmatrix}, \quad \mathbf{\Gamma}_4 = \begin{bmatrix} 0 & 0 & U_3 \\ 0 & 0 & -U_3 \\ U_3 & -U_3 & 0 \end{bmatrix}. \end{aligned} \quad (1.30)$$

While a physical interpretation of the influence of each lamination parameters on the membrane stiffness matrix is provided by IJsselmuiden [IJs11], an examination of equations (1.26) and (1.30) already provides some hints. With a full set of twelve lamination parameters, the description of an arbitrary stacking sequence is possible. Imposing a restriction to symmetric laminates, the coupling matrix \mathbf{B} vanishes along with $V_{i\mathbf{B}} = 0$. The eight remaining lamination parameters for \mathbf{A} and \mathbf{D} in general specify a symmetric and unbalanced laminate, with fully populated stiffness matrices. Noting that only invariants $\mathbf{\Gamma}_2$ and $\mathbf{\Gamma}_4$ exhibit non-zero elements in the coupling terms (1, 3) and (2, 3), the description of a balanced laminate is to hand when setting

lamination parameters V_{2A} , V_{4A} , V_{2D} , V_{4D} equal to zero. Accordingly, symmetric and balanced laminates can be described with four lamination parameters only.

The description of laminate stiffness properties with lamination parameters offers two distinct advantages over a representation with layer thicknesses and angles. One, the number of variables describing the stiffness properties is fixed to a maximum of twelve lamination parameters and one thickness, further reducing with the above mentioned restrictions on the laminate. The stacking sequence description on the other hand requires the definition of $2n$ variables, where n is the number of layers within the laminate. With stacking sequences in industrial applications featuring tens or even hundreds of layers within a laminate, the amount of variables required for a stiffness description greatly exceeds the one required with lamination parameter. Two, while stiffness matrices in the lamination parameter description are a linear function of continuous lamination parameter variables, the stiffness matrices when parametrized with layer thicknesses and angles are related in a highly non-linear manner to the defining variables. Considering the implementation of stiffness matrices in an optimization, both above mentioned arguments impose an inordinately more difficult optimization problem. For one thing, by virtue of the larger number of design variables, and for another thing due to the irregular design space as a result of the non-linear stiffness dependency.

Nevertheless, a drawback when using lamination parameters is the requirement of an additional subsequent step that converts stiffness matrices into realistic stacking sequences. Many researchers have and are still investigating this topic, for example IJsselmuiden et al. [IJs09], Bloomfield et al. [Blo09], Van Campen et al. [Van12], Liu et al. [Liu13]. While the research in this dissertation is focused on a continuous stiffness matrix optimization, an insight into the subsequent stacking sequence derivation based on the optimized stiffness matrices according to the process developed by Irisarri et al. [Iri13] will be provided in section 2.3.

1.1.3 Membrane Stiffness Visualization

To later on visualize the in-plane stiffness distribution of a given \mathbf{A} matrix, the thickness normalized engineering modulus of elasticity $\hat{E}_{11}(\theta)$, $\theta = 0^\circ$ to 360° , can be calculated from:

$$\hat{E}_{11}(\theta) = \frac{1}{\hat{A}_{11}^{-1}(\theta)}, \quad (1.31)$$

where:

$$\hat{\mathbf{A}}^{-1}(\theta) = \mathbf{T}^T \hat{\mathbf{A}}^{-1} \mathbf{T}. \quad (1.32)$$

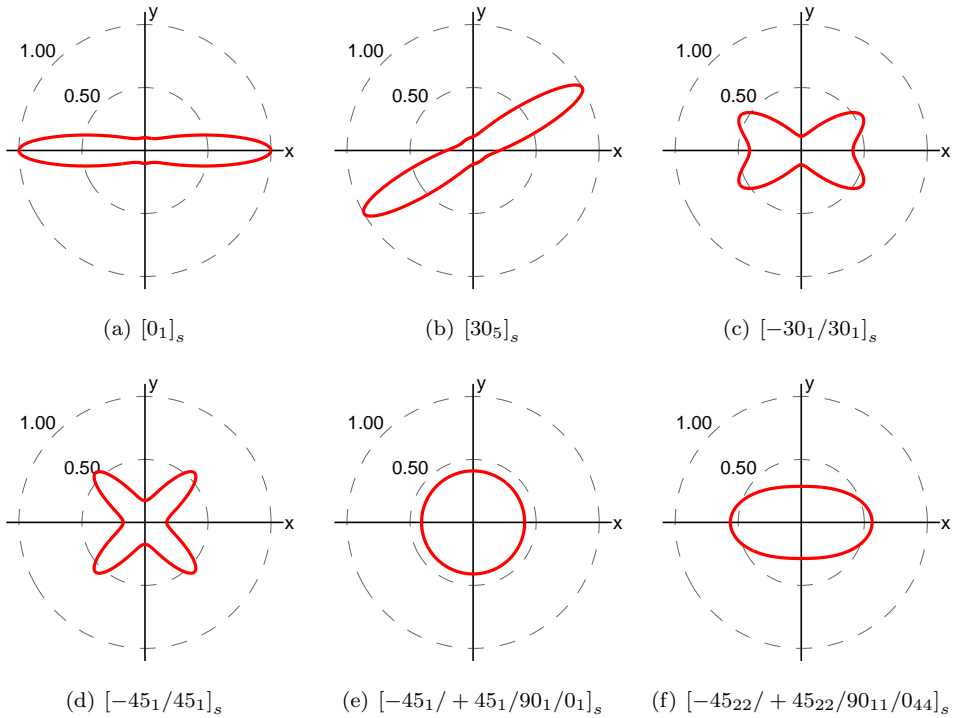
The transformation matrix \mathbf{T} corresponds to the one used in the stress-strain relationship derivation, equation (1.7).

Characteristic polar stiffness distributions as calculated with equation (1.31) are shown in Figure 1.5, where the x-axis constitutes the 0° direction. The material properties of a single ply are listed in table 1.2. They correspond to the properties applied in the structural components considered for optimization throughout all design studies depicted in part II of this work. The stiffness distributions are all normalized by the largest value occurring for a single fiber direction as shown in Figure 1.5(a), featuring only a single, but mirrored 0° ply and accordingly a maximum normalized stiffness of 1.0 in the x-direction. The laminate is defined by the notation $[0_1]_s$, where

Table 1.2: *Single ply material properties*

| E_{11} | E_{22} | G_{12} | ν_{12} | ρ |
|------------|-----------|-----------|------------|------------------------|
| 83.0e9 GPa | 8.5e9 GPa | 4.2e9 GPa | 0.35 | 1452 kg/m ³ |

the subindex number denotes the contribution to the overall thickness, which again results from the summation of thicknesses of all contributing ply angles. Subindex $_s$ indicates a symmetric stack, for which all plies are mirrored. Since the normalized stiffness matrix $\hat{\mathbf{A}}$ does not depend on the overall thickness, it is only the relative thickness of each contributing ply that influences the stiffness distribution. This is demonstrated by the $[30_5]_s$ distribution shown in Figure 1.5(b), which despite the increased thickness exhibits an identical shape and magnitude as the distribution in Figure 1.5(a), only rotated by 30° . Adding an equivalent thickness ply with -30° to

**Figure 1.5:** $\hat{E}_{11}(\theta)$ stiffness distributions for characteristic laminates

the 30° direction leads to the distribution shown in Figure 1.5(c). Compared to the single ply direction, the maximum stiffness reduces to approximately 56%. Nearly the same maximum stiffness is obtained with a $[-45_1/45_1]_s$ stacking, Figure 1.5(d), however, with a much more pronounced directional stiffness alignment. The special case of a quasi-isotropic laminate with equivalent stiffness in all directions is shown in Figure 1.5(e). The stiffness distribution belonging to a stacking sequence that is used as optimization starting point for the design studies in part II is shown in Figure 1.5(f). As a result of the dominant 0° ply, the stiffness extends mainly in x-direction.

1.2 Composite Optimization

With the emergence of fiber reinforced plastics and the identification of their potential benefits when applied in aircraft structures, the development of modeling and optimization methods began, which in the past decades has entailed a considerable amount of research work. The books by Gürdal et al. [Gur99] and Haftka et al. [Haf92] yield detailed insight into composite optimization in particular and structural optimization in general.

An elaborate review on the various optimization strategies developed for variable stiffness designs is presented in Ghiasi et al. [Ghi10]. The report provides a valuable overview on methods which basically are all directed towards finding optimum composite stiffness or stacking sequence distributions. Denoting a stiffness distribution as variable is motivated by, by definition, a gradual or patchwise adaptation of stiffness within a structural component, [IJs11]. A stiffness variation for this is to hand, when varying at least one of the two parameters fiber angle or thickness within a part. Variable stiffness represents a crucial contribution to the search for a weight optimal design for an efficient application of composites in a load carrying component of an aircraft. Constant stiffness designs in contrast features constant stiffness throughout the entire component. Ghiasi et al. [Ghi09] provide a review of optimization strategies for these kind of laminates.

The composite optimization strategy to be adopted for variable stiffness applications depends strongly on the selected stiffness parametrization. Two parametrization methods were presented in section 1.1, consisting of an explicit definition of the stiffness using a stacking sequence, hence layer thicknesses and fiber angles, section 1.1.1, or through an implicit description of stiffness using lamination parameters, section 1.1.2. With the research presented in this thesis being based on the continuous optimization of laminate stiffnesses, the focus of section 1.2.1 will be on a review of the research performed on lamination parameter optimization. Composite optimization based on discrete stacking sequences will be discussed in conjunction with its application in wing design, section 1.3.2.

A third method to express stiffnesses, which can be ranked among the explicit parameterizations, involves a fiber path description using mathematical functions and will only be briefly addressed for sake of completeness. This method was first applied by Olmedo et al. [Olm93] for the maximization of buckling loads of a plate. To this end the fiber angle was varied linearly along one of the spatial dimensions, finally resulting in a considerable increase in buckling load of 80% over the corresponding straight fiber design. Blom et al. [Blo08] demonstrate the optimization of conical shells for maximum fundamental frequency by means of various fiber path definitions. A more recent application, addressing a minimization of tow-placed ply overlaps, while describing fiber paths using a streamline analogy, is presented in Blom et al. [Blo10].

Another detailed survey of composite optimization procedures in general is provided in [Ken13], while the main purpose of the paper is a proposed new laminate parametrization technique, in which each structural segment is composed of a fixed number of layers featuring fiber angles limited to a fixed set of angles. They introduce adjacency constraints to avoid large jumps in fiber angles within a layer and demonstrate the new parametrization using plate and stiffened plate compliance minimizations and buckling optimizations.

1.2.1 Lamination Parameter Optimization

One of the first applications of lamination parameters in structural optimization was done by Miki et al. [Mik93]. Considering symmetric and balanced laminates, they present optimizations for maximized in-plane and bending stiffness, buckling strength and natural frequency of a laminated plate.

Fukunaga et al. [Fuk94] in their paper demonstrate a fundamental frequency maximization for a plate featuring an unbalanced laminate. They show that the frequency reduces with the consideration of bending-twist coupling. Similar research, but with buckling load as the objective to be maximized, is discussed in Fukunaga et al. [Fuk95]. Different trends of bending-twist coupling can be disclosed, depending on the buckling failure mode. Compliance maximization on a lamination parameter basis for various clamping conditions and load cases is discussed in Hammer et al. [Ham97]. Liu et al. [Liu04] compare genetic optimization with a continuous, lamination parameter based optimization for a buckling load maximization within a defined range of possible stacking sequences and find a good agreement between methods, except for thin, low aspect ratio laminates.

The considerable leap in performance when adopting variable, instead of constant stiffness laminates in a lamination parameter based optimization is demonstrated in Setoodeh et al. [Set06b], by minimizing compliance of a variable stiffness composite plate, moreover they show, that designs based on lamination parameters are superior to the results obtained using a fiber angle parametrization. A similar investigation with the objective of maximizing the fundamental frequency of a composite plate is provided in Abdalla et al. [Abd07b]. An improved convergence behavior could be obtained by introducing a reciprocal approximation of the objective function. The variable stiffness designs are shown to clearly outperform constant stiffness designs. IJsselmuiden et al. [IJs10] have demonstrated a lamination parameter based, variable stiffness buckling load maximization for a composite plate using a mixed, linear and reciprocal approximation of the objective function.

A missing link for the adaptability of lamination parameter based optimizations to strength related problems is filled in by IJsselmuiden et al. [IJs08]. They present the development of a strength failure criterion in lamination parameter space and demonstrate its functionality using a strength maximization on a plate under combined axial and shear loading. Khani et al. [Kha11] demonstrate the functionality of the strength failure criterion along with a hybrid approximation of the strength failure index using a variable stiffness panel with a central hole. They draw the conclusion that stiffness as a surrogate for strength design in the presence of large stress gradients is not to be recommended. Bloomfield et al. [Blo09] develop a two-level optimization, comprising a lamination parameter based continuous optimization first, followed by a modified particle swarm optimization in the search for an optimal stacking sequence. The functionality is demonstrated using the minimized mass of a constant stiffness composite plate, subjected to various loading cases.

1.3 Composites and Aircraft Wings

Having established the theory of composite modeling in section 1.1 and presented a review of composite optimization with a focus on lamination parameters in section

1.2, this section completes the required groundwork by discussing the application of composite in aircraft wings. First, some fundamental principles on aircraft wing structures in general are presented, section 1.3.1, followed by an outline on the research performed in the field of composite optimization in aircraft wings with and without a consideration of aeroelastic responses, section 1.3.2.

1.3.1 Wing Structural Layout

In an evolutionary process, starting at the very beginning of manned flight, and influenced by prevailing materials of their time, wood to metal to composites, as well as production technology the, nowadays widely accepted, load carrying wing box design was developed. In this section, rather than a historical review, the status quo in modern aircraft structural layout will be highlighted, and some general terminology will be defined.

The developments in structural layout for 24 commercial transport jets is presented in Sensmeier et al. [Sen04], who investigated the aircraft families of three major transport aircraft manufacturers. They depict the temporal evolution of the front and rear spar position, as well as the rib spacing. Niu [Niu88] in his book gives a very elaborate insight into constructional details with respect to aircraft structures in general, and a valuable overview on the global structural layout of, among others, modern transport aircraft wings. Focusing less on the constructional aspects, and more on the mathematical and engineering methods used to calculate structure-related quantities like stresses, strains and displacements, the work of Megson [Meg99] provides the link between the wing structural layout and simplified methods used to determine their structural properties.

Independent of the addressed resources, the schematized structure depicted in Figure 1.6 can be considered to be the general layout of a modern transport aircraft wing, usually denoted a wing box. The box is covered top and bottom by stringer

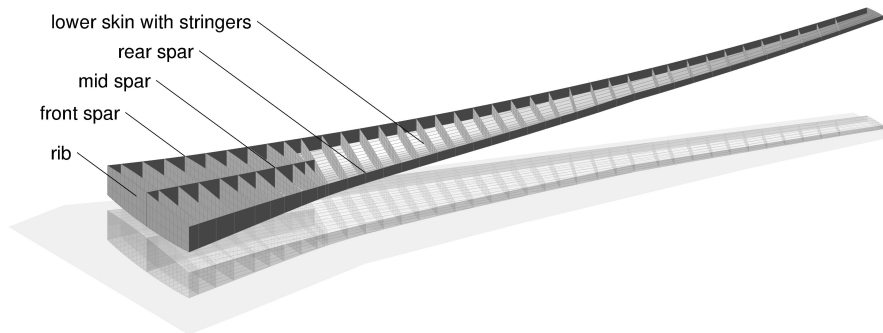


Figure 1.6: *Structural layout of an aircraft wing, top skin removed*

stiffened wing skins. Stringers are responsible mainly for reducing the buckling field size, but simultaneously, along with the wing skins, contribute to the bending stiffness of the wing. In front and rear, the wing box is terminated by spars. Depending mostly on the manufacturers design philosophy, a mid spar in the inner wing may or may not exist [Sen04]. Playing a key role in the support of shear forces, the spars shell structure is also denoted as shear web. Both terminologies, spar and shear web, are

used in this work. Eventually, ribs are introduced to preserve the cross-sectional shape, which is necessary for aerodynamic and structural reasons. While ribs are usually oriented perpendicular to one of the spars, no general rule exists so that an alignment with the flow, as shown in the inner wing of the structure in Figure 1.6, is not unusual. The reasons for designing the load carrying wing structure as a box are basically twofold. One, a box allows for storing fuel in the wing, which due to the amount of fuel required for a flight is an inevitable premise for passenger aircraft. Two, the space in front and aft of the wing box is allocated to various kinds of systems, the most prominent of which are the high lift systems in leading and trailing edge, roll control surfaces and the landing gear.

1.3.2 Aeroelastic Optimization

Optimization based on stacking sequence

The optimization of composite materials used to form the load carrying structure of a wing is a research topic that has been discussed for decades, see for example Starnes Jr et al. [Sta79], where the authors apply an approximation based optimization to minimize the weight of a wing structure subjected to different combinations of buckling, strength, displacement and twist constraints. While fiber angles of a balanced and symmetric stacking sequence are prescribed, the layer thicknesses serves as design variables. Although not optimizing, but analyzing the effect of bending-twist coupling on the aeroelastic behavior of composites plates with various symmetric, unbalanced stacking sequences, Hollowell et al. [Hol84] demonstrate the considerable effects induced by the coupling terms in the bending stiffness matrix. Green [Gre87] investigates the influence of non-symmetric laminates on the aeroelastic behavior of high aspect ratio wings by applying an integrating matrix method to derive divergence and flutter speeds of various stacking sequences. The differences between a sequential and an integrated design on the performance of a sailplane are investigated in Grossman et al. [Gro86]. Design variables comprise skins, spar cap and web thicknesses, and they depict the advantages of simultaneously designing aerodynamics and structure.

A valuable survey on aeroelastic tailoring effects as a result of the directional stiffness in orthotropic composites is provided in Shirk et al. [Shi86]. They investigate possible influences of rotated fiber angles on minimum weight, twist, normal modes, flutter and aerodynamic performance for various configurations, reaching from fighter aircraft to forward swept configurations. A general overview on optimization technologies reaching from optimizations on panel level to the aeroelastic optimization of composites in aircraft wings is provided in Vanderplaats et al. [Van89].

Ringertz [Rin94] performs a mass optimization for a cantilevered beam subjected to aeroelastic loads derived from doublet lattice. The thicknesses of the unbalanced wing skin laminates serve as design variables, with the wing being subjected to divergence and flutter constraints. Subsequently, the design is analyzed for imperfection sensitivity. Eastep et al. [Eas99] investigate the influence of layup orientation in a straight fiber design on the optimized mass of a low aspect ration wing, constrained by strength, roll-reversal and flutter velocity. Using the thicknesses of a symmetric and balanced layup as design variables, they come to the conclusion that tilting the entire stack in 5° steps does not have a significant influence on the optimized mass.

In a more recent work, Leon et al. [Leo12] maximize the flutter eigenfrequency of a composite plate wing with ply angles as design variables, considering symmetric and non-symmetric stackings. A related research, but for a tow steered composite plate featuring symmetric layups is described in Stodieck et al. [Sto13]. They investigate the effect of varying tow angles on eigenmodes, elastic axis, as well as divergence and flutter speed.

Guo et al. [Guo12] present a two-stage procedure, where in a first step layer thicknesses and angles serve as the design variables in minimizing mass, subject to strength and damage tolerance constraints. The second stage focuses on a reduction of the wings response to a gust, measured by its transverse tip deflection. Applied to the skins of a transport aircraft wing, optimization results indicate considerable potential for weight saving. Dillinger et al. [Dil13b] demonstrate the application of membrane coupling induced by unbalanced laminates to aeroelastically tailor the twist distribution of a high aspect ratio sailplane wing.

Optimization based on lamination parameter

Aeroelastic tailoring studies based on lamination parameters have been attempted previously, though not to the same extent as the previously depicted optimizations comprising discrete stacking sequences.

Kameyama et al. [Kam07] using a composite plate wing demonstrated the influence of lamination parameters on the flutter and divergence characteristics. They consider a parametrization of the bending stiffness matrix only, while implying symmetric laminates. All calculations are performed for forward, backward and an unswept wings. In addition to the analyses Kameyama et al. perform a genetic algorithm based mass optimization with constraints on flutter and divergence speed.

Herencia et al. [Her07] demonstrate a two-step optimization scheme to minimize mass of an aeroelastically loaded wing. In a first step, lamination parameters describing symmetric but potentially unbalanced laminates in the skins and spars, are used in a gradient based mass optimization comprising strength, buckling and practical design and ply contiguity constraints. Moreover, lift and induced drag are considered as aeroelastic responses. The second step comprises a genetic algorithm based stacking sequence optimization, where the sum of square difference between the actual and the optimum obtained in the first step serves as objective. The results disclose a considerable influence of aeroelastic tailoring on the optimized weight.

Minimization of compliance of a variable stiffness slender wing that is represented as a beam is demonstrated in Abdalla et al. [Abd07a]. The cross-sectional properties of the beam are parametrized using lamination parameters that define the membrane stiffnesses of the box cross section. Results show that variable stiffness layups can significantly outperform structures comprising constant stiffness. Unbalanced laminates in particular, comprising bending-torsion coupling, lead to the best performance in terms of compliance.

Thuwis et al. [Thu10] demonstrate the possibility of reducing the induced drag of a Formula One wing using passive twist adaption resulting from an aeroelastic tailoring optimization based on lamination parameters. Exploiting the effect of bending-torsion coupling, the applied aerodynamic analysis code *VSAERO* indicates there is considerable potential to lower drag in straight passages, while maintaining the required downforce in turns.

Another two-level optimization strategy has recently been proposed by [Liu13]. Allowing for symmetric and unbalanced laminates, a lamination parameter based weight minimization is performed before applying genetic algorithms for the derivation of stacking sequences. The objective function in the second optimization step comprises a minimization of the square distance of lamination parameters. The research relates to a preceding two-level optimization, [Liu00], where in the first step, instead of lamination parameters, the thickness of fixed angle plies is optimized.

1.4 Objectives and Thesis Layout

The principal objective of the research reported here was to develop a variable stiffness composite laminate optimization process that incorporated the possibility of considering static aeroelastic responses in the structural design of aircraft wings. A special focus was laid on the direct inclusion of deflection dependent aerodynamic loading in the structural optimization loop. Taking the membrane and bending stiffness matrices of the shell-type structural entities serving as design variables, a lamination parameter based optimization strategy developed by IJsselmuiden [IJ11] was employed, necessitating a methodology for generating the appropriate responses and sensitivities using a finite element solver. The gradient based optimizer was based on linear and reciprocal response approximations in the design variables, appropriate formulations for the aeroelastic responses aileron effectiveness, divergence and twist in terms of the stiffness matrices also needed to be generated. Eventually, with regard to aeroelastic optimizations in the transonic regime, a correction method for the presumed to be inaccurate aeroelastic loads resulting from the doublet lattice method, using computational fluid dynamics, was targeted.

The path followed to achieve the above mentioned objectives is, to a certain extent, reflected in the layout of this dissertation. The thesis is divided in three parts, comprising optimization methodology, design studies and a summary. A general overview on the developed optimization framework is presented in chapter 2. Each step involved is briefly introduced and linked to the appropriate chapters that provide a deeper insight in the respective topic. As the static aeroelastic constraints constitute an important ingredient in the optimization, they are discussed in more detail in this chapter, and to envision the continuative step that follows the stiffness optimization presented in the dissertation, the general idea of a stacking sequence derivation is discussed.

The parametric wing model concept as it was applied to generate the required analysis models is described in chapter 3. The model setup incorporates details of the geometric representation of the wing, the finite element model deduced from it, and descriptions of mass modeling and the generation of an appropriate aerodynamic model allowing for the derivation of aeroelastic loads.

A detailed description of the optimization model, which serves the derivation of responses and sensitivities using the finite element solver are presented in chapter 4. The concept of design fields, comprising equal stiffness properties, is introduced. The solver specific procedures used to define the design variables and responses are explained, along with the routines developed to export the data required for, amongst other things, setting up the response approximations. The derivation of the latter is presented in chapter 5. First, the general form of an approximation in terms of

stiffness matrices is discussed, followed by a description of the methodology that was developed to maximize the reciprocal portion of a response approximation. Finally, individual descriptions of the structural and aeroelastic approximations employed in this research are presented.

The theoretical part of this work is concluded in chapter 6 with a depiction of the aero load correction process. Starting with a description of the governing matrices involved in the doublet lattice method, two correction strategies, comprising either a direct manipulation of the doublet lattice method or a correction using computational fluid dynamics are introduced. The correction module developed for the latter strategy is also discussed.

The functionality of the optimization methodology developed in the first part of this thesis is demonstrated by means of design studies in the second part of the thesis. The optimization of a simplified model of a swept back wing is presented in chapter 7. First, the required analysis models comprising geometry, load cases, finite element model and optimization model are presented along with a detailed description of the starting design. Sensitivities generated using the finite element solver are compared to the results of a finite difference approach to ensure their correctness. Optimization results for a mass minimization of the wing skins and an aileron effectiveness maximization are presented. Both cases involve a comparison between balanced and unbalanced laminate optimizations.

A detailed study into the effects of aeroelastic constraints on the wing skin mass is discussed in Chapter 8. Starting with a description of the analysis models, load cases and the starting design, the influence of aileron effectiveness, divergence pressure and twist constraints are highlighted in three separate investigations. Both, balanced and unbalanced laminates are considered.

Concluding the design studies, the aeroelastic optimization of a forward swept wing with corrected aerodynamic forces is presented in chapter 9. First, a trim application without structural optimization is discussed, to demonstrate the convergence behavior of the correction forces. The results of a wing skin mass minimization with balanced and unbalanced laminates are then presented, highlighting in particular the differences between optimizations with and without aero correction. Moreover, the consequences of adding spars to the optimization model are discussed, followed by a demonstration of a stacking sequence optimization for the forward swept wing.

Finally, conclusions drawn from the present, and recommendations for further research are provided in chapter 10.

Part I

Optimization Methodology

CHAPTER 2

Basic Concept

“Although personally I am quite content with existing explosives, I feel we must not stand in the path of improvement.”

Winston Churchill

At present it is an enormously difficult and complex task to perform an entire composite optimization process for a large scale product design such as an aircraft wing or fuselage in a single shot, comprising responses ranging from material related strain and buckling constraints over aeroelastic constraints, down to manufacturing constraints and constraints relating to a specific layup technique. In this regard it seems sensible to split up the process into steps to circumvent the problems of inconsistent design variables and constraints. Then in each step the problems specific to that set, and the variables and constraints of the set, can be dealt with using problem tailored optimization algorithms.

In the strategy followed in this thesis, the composite optimization is split into three steps. These steps are, one, a stiffness-based optimization with continuous variables and the applicability of gradient based optimization strategies. Two, a stacking sequence optimization, featuring the optimized stiffnesses of step one as the objective, and three, a fiber path optimization. Steps two and three incorporate constraints with regard to producibility and manufacturing, which evolve from the chosen manufacturing technique, e.g. fiber placement. In this thesis the focus is on the first step in the optimization chain, aiming at the development of a variable stiffness optimization process with static aeroelastic responses. The second step, comprising a stacking sequence optimization, will be addressed briefly, step three in the chain will not be discussed further in this thesis. All the steps highlighted above form part of the composite optimization strategy pursued at Delft University of Technology. For those missing, further information on steps two and three are covered in detail in, for example, IJsselmuiden et al. [IJ09], Van Campen [Van11], Nagy [Nag11], Van Campen et al. [Van12].

Before looking at each module contributing to the variable stiffness optimization of composite structures in more detail, an overview of the developed methodology is

presented in this chapter. The major steps in setting up and performing the optimization along with the tools used to do so are described in section 2.1. The consideration of static aeroelastic responses is a core issue, and therefore requires a proper characterization, this is done in section 2.2.

Optimized stiffness matrices constitute the final outcome of the process presented here, a subsequent optimization step is required that transforms membrane and bending stiffnesses into feasible, discrete stacking sequences. Thus, the concept of stacking sequence tables, forming an efficient basis for stacking sequence optimizations based on the continuous stiffness output, is introduced in section 2.3.

2.1 Optimization Framework

Designating the optimization developed in this thesis a *framework* indicates that several well understood components are designed to interact such as to result in a process, capable of performing a desired task. The task to hand consists of designing a composite stiffness optimization for shell-like components used in the structural layout of an aircraft wing. In addition it should be possible for the framework to be used to determine optimum stiffness in non-wing and non-aircraft related structures, keeping in mind however that an important aspect is the allowance for static aeroelastic responses.

The framework for the optimization of aircraft wings with aeroelastic constraints consists of several components and steps, each of which will be described briefly in the following sections, and in more detail in the corresponding chapters thereafter. An overview of the process is depicted in Figure 2.1. It corresponds to a successive convex subproblem iteration procedure, in which a gradient based optimizer consecutively solves a local approximation problem.

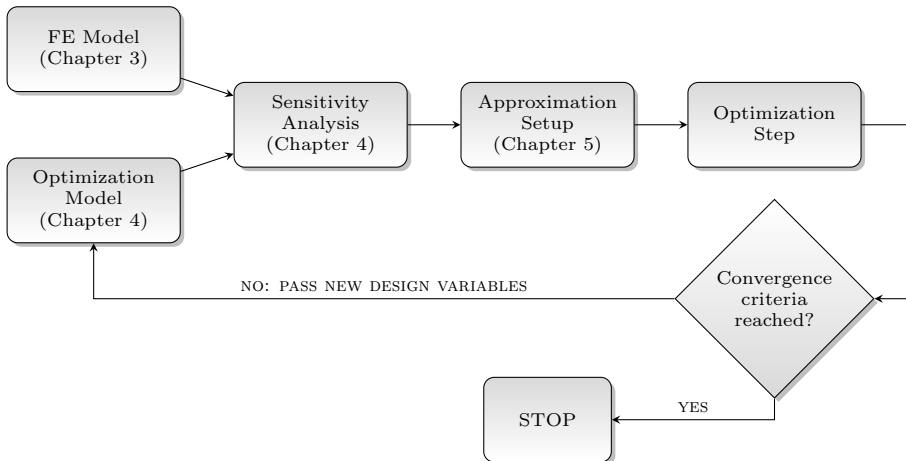


Figure 2.1: Schematic overview of the optimization framework

The process is geared towards the optimization of the load carrying, shell-like structural components in a wing, the properties of which can be represented as membrane \mathbf{A} and bending stiffness matrices \mathbf{D} . Along with the shell thickness, they

represent the design variables used in the optimization process. When only symmetric laminates are considered, the coupling stiffness matrices \mathbf{B} are equal to $\mathbf{0}$ and therefore not part of the design variables.

The process basis is formed from a finite element model of the wing structure that serves as an analysis model for the desired responses f , and as the evaluation of sensitivities $\frac{\partial f}{\partial \mathbf{x}}$ of the responses with respect to the design variables \mathbf{x} . To this end, an optimization model is defined, specifying the design variables and responses in the terminology of the applied finite element code. The responses and sensitivities serve as input for the derivation of an analogous analysis model that describes the behavior of each response in the surrounding of the analyzed design. For this purpose, each response is approximated as function of potentially each design variable, while satisfying the essential properties of convexity, separability and conservativeness. The approximation model replaces the actual analysis model in the search of the optimizer for a minimum of the objective function, greatly accelerating the function evaluations required during the optimization. The optimization step results in a new set of design variables that represent the global optimum of the convex approximation subproblem. If the convergence criterion is met, basically an upper bound on the change in the objective function for subsequent feasible iterations, the optimization is stopped. Otherwise the process continues with the derivation of new responses and sensitivities.

In order to broaden the understanding of the contribution of each, a short description of the tasks within the optimization process is provided in the following sections.

2.1.1 Finite Element Model

A finite element model (FE model) that allows for the calculation of the required responses and the derivation of their sensitivities with respect to the design variables forms the starting point of the optimization. The FE model takes a central position in the optimization process, which is built solely on the responses and sensitivities produced by the finite element model. The NASTRAN finite element analysis software [Moo04] takes over the function of the structural solver.

The wing skins, shear webs and ribs are represented by shell elements; stiffening structural entities like stringers in the wing skins, shear webs and ribs are represented by beam elements. Elements in the wing skins are grouped in the spanwise and chordwise direction, with the elements in a group sharing the same membrane and bending stiffness matrix and thickness. The models topology and element resolution remain unchanged throughout the optimization, only the properties that define the shell stiffnesses will change, based on the modifications proposed by the optimizer. All masses that are not covered by the load carrying structural entities can be taken into account by point masses, including for example the nose and trailing edge sections, high-lift devices, local installations, actuators, fuel, and so on. The wing is clamped at the root section, integrating with a rigid element all nodes belonging to the root rib into a single node. No structural representation of fuselage and tailplanes is considered in the present work, their contribution to the overall mass is represented in a point mass attached to the clamping node.

A more detailed insight into the FE model generation is presented in chapter 3.

2.1.2 Optimization Model

The optimization model is part of the finite element model. It defines the design variables and the responses that are to be used in the optimization. Since the optimizer is tailored for the optimization of composite stiffness matrices, the only design variables specified in the optimization model are elements of the normalized \mathbf{A} and \mathbf{D} matrices, see section 1.1.1, and the associated thicknesses h . The response definition, effecting the generation of various analysis model outputs, is also a part of the optimization model. Depending on the optimization objective and the constraints to be met, different kinds of responses are requested. The standard responses, apart from the aeroelastic ones, are mass, element stresses and displacements. Further details of the optimization model and its implementation in NASTRAN will be given in chapter 4.

2.1.3 Sensitivity Analysis

Once all the required input components for the FE analysis are prepared, NASTRAN can be invoked, resulting in the generation of response vectors and sensitivity matrices. Details of the NASTRAN statements needed to export those are given in section 4.5.

Each aircraft mass case to be included in the optimization and consisting of variable mass contributions like fuel and passenger mass, requires its own NASTRAN run, along with a proper definition of the aeroelastic load cases to be analyzed. These load cases can be divided into symmetric static maneuvers, antisymmetric static rolling maneuvers and divergence. NASTRAN computes the trimmed aeroelastic solution and generates the requested responses and sensitivities, which can be defined separately for each load case. The same holds for static load cases that do not require aerodynamic, but static nodal or distributed forces.

2.1.4 Approximation Setup

The most general form of a response approximation as function of the design variables $\mathbf{A}_j, \mathbf{D}_j, h_j$ is shown in equation (2.1). The sensitivities generated with NASTRAN are converted to linear, Ψ_j , and reciprocal, Φ_j , sensitivities with respect to the stiffness matrices, where superscripts m and b denote sensitivities with respect to membrane and bending stiffness, respectively. α_j is the sensitivity with respect to the thickness design variable:

$$\tilde{f} = \sum_{j=1}^N \left(\hat{\Psi}_j^m \Big|_0 : \hat{\mathbf{A}}_j + \hat{\Psi}_j^b \Big|_0 : \hat{\mathbf{D}}_j + \Phi_j^m \Big|_0 : \mathbf{A}_j^{-1} + \Phi_j^b \Big|_0 : \mathbf{D}_j^{-1} + \alpha_j \Big|_0 h_j \right) + C_0 . \quad (2.1)$$

Three important properties characterize the approximation: convexity, separability, and conservativeness. They will be discussed in more detail in section 5.2.

Knowledge concerning the physical background of the response for which an approximation has to be generated for, is required to make a reasonable choice of the linear and reciprocal contributions to the overall approximation. Details on the general approximation form, and a discussion on the composition of the structural and aeroelastic approximations are presented in chapter 5.

2.1.5 Optimization

Having prepared the response approximations in terms of linear and reciprocal sensitivity matrices for the membrane and bending stiffness matrices, and the sensitivities with respect to the thicknesses, they are passed along with the responses to the optimizer. The minimization of the objective leads to a new set of design variables that correspond to the optimum solution of the approximation model. The details of the internal optimization procedure are well described in IJsselmuiden [IJs11]. As depicted in Figure 2.1, the new set of design variables is passed to the optimization model to generate new responses and sensitivities for the next approximation model and optimization step.

Aside from optimizer specific variables like maximum iteration number and response damping, an important parameter to be set is the design type, defining either an optimization with the restriction to balanced, or an optimization with unbalanced laminates. In both cases, thickness can either be included in the optimization, or not; the first being essential for optimizations including a mass response.

2.2 Static Aeroelastic Responses

With the focus of this work being on a structural optimization including static aeroelastic responses, the responses considered in the optimization along with a definition and their impact on aircraft design are described in this section.

2.2.1 Aileron Effectiveness

The control of an aircraft is an important measure in the assessment of its performance. Such assessments bundle in the handling qualities experienced by a pilot, determining on how accurately and fast an aircraft can be navigated. The most common means used to alter an unaccelerated steady flight motion is to apply aerodynamic forces that result in rotational responses about one or more aircraft axes, denoted as roll, pitch and yawing motions about the x, y, and z axes. Movable trailing edge control surfaces provide an efficient way of altering the aerodynamic moments of an aircraft, while keeping the structural complexity low compared to, for example, a control surface on the leading edge of a wing. As a result of their distance to the aircraft center of gravity, pitch and yaw motion are usually controlled by the elevator and rudder control surfaces on the horizontal and vertical tail. Aircraft rolling about the x-axis is induced using control surfaces on the wing, typically designed as trailing edge devices, i.e. ailerons, or as spoilers on the upper wing surface. The rolling moment initiating the rotational motion is generated by an antisymmetric deflection of the ailerons, leading to an antisymmetric force distribution on the right and left wing.

As a result of the control surface deflection not only the lift force is altered, but also an additional airfoil moment arises. Both loadings can have a noticeable influence on the elastic behavior of the wing, depending on its bending and torsional rigidity. The additional loading in a section when deflecting the aileron is depicted in Figure 2.2. The additional airfoil camber caused by the deflection leads to an additional lift force. Since most of the additional lift is produced in the vicinity of the flap, hence aft of the elastic axis, the section will twist nose-down. In response to the reduction of

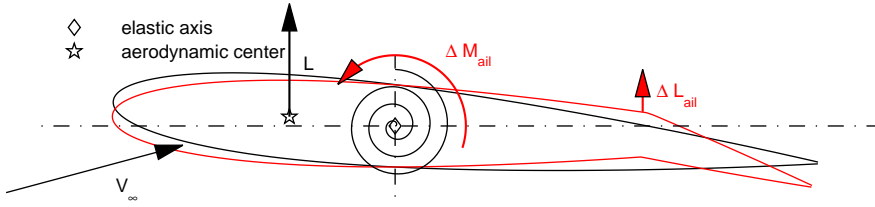


Figure 2.2: *Aileron deflection and additional loading (red)*

the local angle of attack, the local lift decreases accordingly and this reduces the effect intended by the aileron deflection. The amount of angle of attack change depends on the torsional stiffness of the wing, represented by a torsional spring in Figure 2.2.

For the following explanation it is essential to distinguish between aerodynamic twist and structural twist, Figure 2.3. Aerodynamic twist, in the following denoted as twist, relates to the rotation about an unswept axis, parallel to the global y-axis. Structural twist on the other hand, in the following denoted as torsion, specifies the rotation in a wing-related coordinate system, basically aligning with the elastic axis of the wing. Switching from 2D to the elastic behavior of the entire wing, a

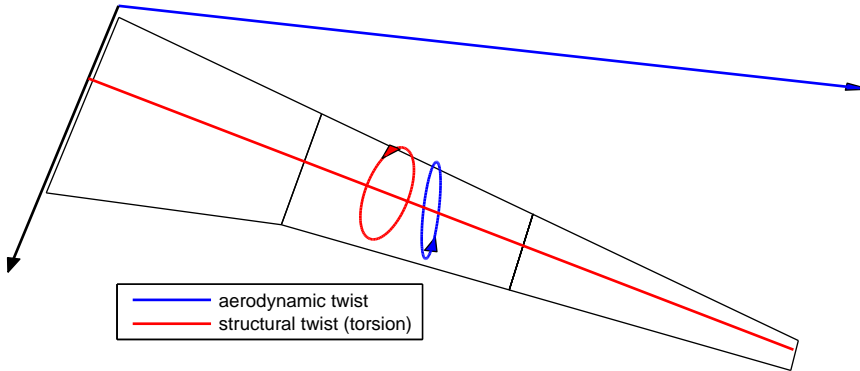


Figure 2.3: *Aerodynamic and structural twist*

mechanism exists, which has an essential influence on the resulting forces due to an aileron deflection. As an answer to the additional lift the wing will bend up and, depending on the global sweep direction of the elastic axis, the geometric coupling of bending and twist will lead to a change in twist; a decrease from the wing root towards the aileron for the swept back wing, and an increase for the swept forward wing. While the twist decrease in the backward swept wing diminishes the overall lift and therefore reduces the effect of a downward aileron deflection, the increase in lift in the case of a forward swept wing supports the aileron deflection by increasing the lift. It should be mentioned that bending-torsion coupling, enabled for example by unbalanced laminates, can essentially affect the twisting behavior, but will be excluded in the current considerations.

Overall, the increase in lift for a downward deflected aileron is crucially affected by the elastic properties of the wing structure. For a sweptback, torsionally weak wing the lift decrease due to angle of attack reduction can surpass the additional component of the camber increase and hence result in an opposite directed lift force. This state is called aileron reversal, since the aircraft will roll in the direction opposite to that intended. Depending on the type of aircraft, certification regulations require an aircraft will not suffer from aileron reversal within a specified velocity and altitude range. For passenger type aircraft, the CS-25 regulation [EAS12] asks for reversal free aileron action within an aeroelastic stability envelope boundary that results from the regular flight envelope boundary velocity V_D/M_D multiplied by 1.15. In the high speed regime, aileron effectiveness degradation tends to be an active constraint, yielding a lower bound on the torsional flexibility of a swept back wing.

Multiple ways of assessing the aircraft reaction on an aileron deflection exist, among which are aileron efficiency and aileron effectiveness. Aileron efficiency expresses the ratio of roll rate for the elastic and the, virtually, rigid wing, see Wright et al. [Wri08]. With increasing bending and torsional stiffness the aileron efficiency approaches a value of one, while an ineffective aileron has zero efficiency, and a negative efficiency when aileron reversal occurs.

Aileron effectiveness is computed as the negative ratio of roll coefficient due to aileron deflection and the roll coefficient due to rolling (roll damping), both for the elastic wing:

$$\eta_{ail} = -\frac{C_{l_\delta}}{C_{l_p}}. \quad (2.2)$$

Equation (2.2) can be derived from a consideration of the moment equilibrium for a steady roll maneuver. The sum of rolling moment due to aileron deflection, M_δ , and the rolling moment due to rolling, known as roll damping, M_p , has to vanish in a steady roll motion:

$$\begin{aligned} M_\delta + M_p &= 0, \\ C_{l_\delta} \delta (qS_{ref}s) + C_{l_p} p \frac{s}{V_\infty} (qS_{ref}s) &= 0, \\ -\frac{C_{l_\delta}}{C_{l_p}} \delta &= \frac{ps}{V_\infty}, \end{aligned} \quad (2.3)$$

where p is the roll rate, δ the aileron deflection, and $s = b/2$ the wing semispan.

The expression on the right side of equation (2.3) corresponds to the arc tangent of the helix angle, outlined in Figure 2.4, being the angle between flight path velocity V_∞ and the wing tip velocity, rotating with a circumferential velocity ps . The aileron effectiveness is equal to the arc tangent of the helix angle for unit aileron deflection $\delta = 1.0$.

Due to the vividness of the helix angle and the ability to derive a roll rate p simply by multiplying η_{ail} with $\delta \frac{V_\infty}{s}$, aileron effectiveness will be the response considered as the objective or constraint in this work.

2.2.2 Divergence

Divergence is a static aeroelastic instability phenomenon that can have a large influence on wing design. The aeroelastic flight envelope mentioned in the previous section

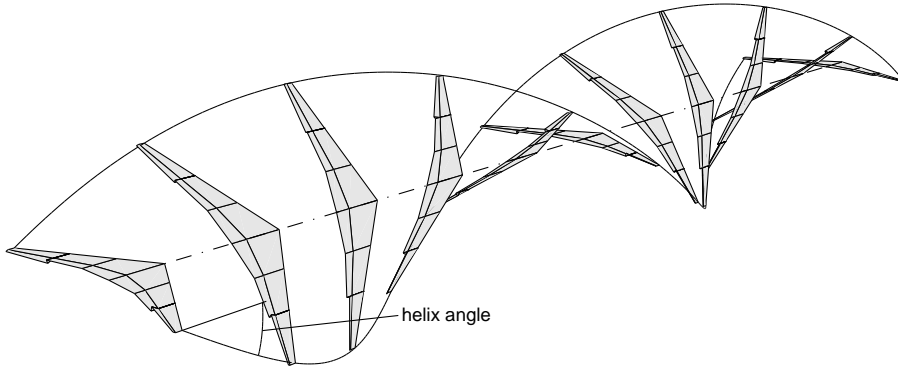


Figure 2.4: *Helix angle definition*

2.2.1 for aileron reversal also applies to divergence, demanding a divergence free aircraft within the aeroelastic stability envelope. As is the case for aileron effectiveness, divergence is a result of the finite wing stiffness and can be illustrated using a 2D section, Figure 2.5.

With the aerodynamic center lying typically in the quarter chord, an increase in lift force results in an additional, elastic angle of attack θ , which in turn leads to a further increase in lift force and therefore to an increase in elastic angle of attack. Depending on the distances of the aerodynamic center to the elastic axis, x_{ac} , and on the torsional stiffness K_θ of the section, either a static equilibrium is obtained, or the elastic angle of attack θ increases further and further until the structural limit is reached and the section fails. This is referred to as divergence. The overall lift force

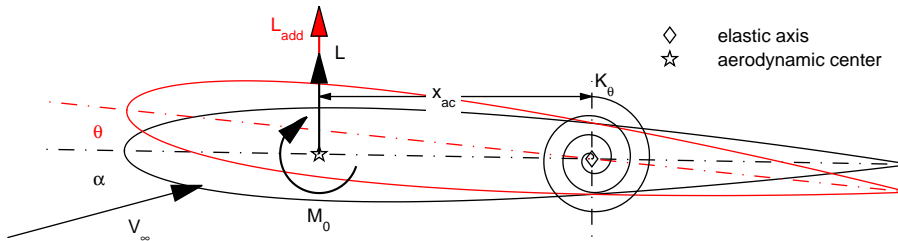


Figure 2.5: *Static rotation of a 2D section*

can be expressed in terms of the lift curve slope C_{l_α} , dynamic pressure $q = \frac{\rho}{2} V_\infty^2$, reference chord c_{ref} and the overall angle of attack $\alpha + \theta$ as:

$$L + L_{add} = qc_{ref}C_{l_\alpha}(\alpha + \theta). \quad (2.4)$$

Summing up the moments about the elastic axis yields:

$$qc_{ref}C_{l_\alpha}(\alpha + \theta)x_{ac} + M_0 - K_\theta\theta = 0, \quad (2.5)$$

and after solving for θ :

$$\theta = \frac{M_0 + qc_{ref}C_{l_\alpha}\alpha x_{ac}}{K_\theta - qc_{ref}C_{l_\alpha}x_{ac}}, \quad (2.6)$$

where an aerodynamic center upstream of the elastic axis corresponds to a positive x_{ac} . The airfoil moment about the quarter chord M_0 can be treated as a constant in the linear, incompressible aerodynamic regime. Divergence exists when the denominator in equation (2.6) becomes zero. Solving for divergence dynamic pressure yields:

$$q_{div} = \frac{K_\theta}{c_{ref}C_{l_\alpha}x_{ac}}. \quad (2.7)$$

Equation (2.7) states that divergence pressure is influenced mainly by the torsional stiffness K_θ and the distance between the elastic axis and the aerodynamic center, x_{ac} . Shifting the elastic axis towards the aerodynamic center reduces x_{ac} and therefore helps to increase the divergence pressure. Divergence cannot occur when the elastic axis lies on, or in front of the aerodynamic center, indicated by a negative x_{ac} . In the latter case, an additional lift force L_{add} results in a decrease in the elastic angle of attack θ and thus a decrease in lift. However, structural restrictions usually limit the possibility of modifying the position of the elastic axis.

While the above considerations are carried out for a two-dimensional section, the results can be transferred to an unswept wing, for which no geometric coupling of bending and torsion is present; ignoring for the time being the coupling mechanisms arising from unbalanced laminates. Swept back wings usually do not suffer from divergence problems since geometric coupling of bending and twist, resulting in a aerodynamic twist reduction, prevails the twist increase by the mechanisms described for the 2D section. The opposite holds for a forward swept wing, for which geometric bending-twist coupling adds to the sectional effect and aggravates the divergence tendency by lowering the critical divergence pressure.

2.2.3 Wing Twist

The elastic wing twist distribution as function of span is an important aeroelastic parameter for multiple reasons. Resulting from an aerodynamic shape optimization, an optimum flight shape arises, which produces the least possible drag for the targeted flight regime. Passenger type aircraft typically spend most of their flight time in a steady cruise, demanding maximum aerodynamic efficiency for economic transport in this condition. Since aerodynamic loads and mass forces can have a strong influence on wing twist in cruise condition, the wing shape without any of the mentioned loadings will most likely have to feature a different twist distribution. The unloaded shape is referred to as the jig-shape, Figure 2.6, and corresponds to the built wing shape.

Contrary to divergence and control surface reversal, elastic wing twist is not constrained by aircraft regulations. Nevertheless, by virtue of the above mentioned reasons, it is an important characteristic that needs to be considered in the structural design process for a new aircraft.

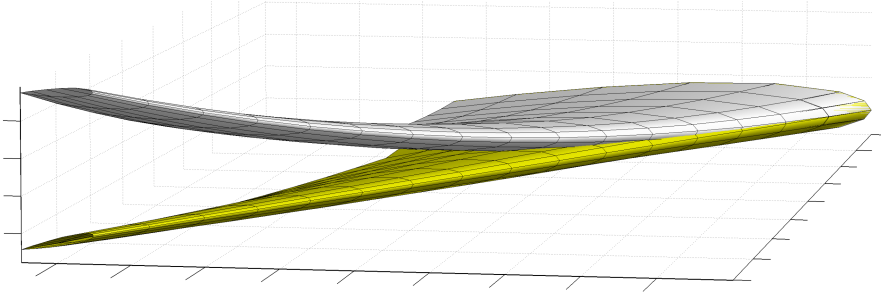


Figure 2.6: *Wing in jig (yellow) and deformed (white) shape*

2.3 Stacking Sequence Optimization

The optimization process presented in this section is based on the work of Irisarri et al. [Iri13] and Meddaikar [Med13] and is concerned with the stacking sequence design of blended composite structures. It constitutes the next step subsequent to the continuous optimization process depicted in section 2.1, which in turn provides the required stiffness matrix input and/or sensitivities. In the following a survey on the functionality of the stacking sequence table optimization will be presented, noting though that its development was not achieved in the context of this thesis, however, an interface was established to exchange the required information between the continuous and the discrete optimization.

To better understand the concept of describing a stacking sequence by means of a stacking sequence table (SST), the idea of guide-based blending is discussed first. In a variable stiffness design, usually a finite number of panels exist that comprise constant stiffness and thus constant stacking sequence. The process of dropping or adding plies among adjacent panels is denoted blending. Different types of blending exist, a selection of which is depicted in Figure 2.7. For inner and outer blending, as

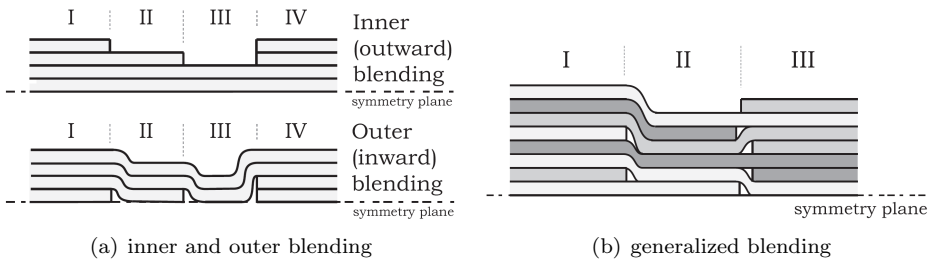


Figure 2.7: *Laminate blending (source: [Van11])*

shown in Figure 2.7(a), ply dropping is only allowed in a sequential order from outside to inside or vice versa, for example Adams et al. [Ada04]. Another type of blending as suggested in Van Campen [Van11] is depicted in Figure 2.7(b). Continuing all layers from the thinner to the thicker stacking, panel II to I in Figure 2.7(b), is denoted as generalized blending, while dropping the constraint to continue all plies from the

thinner to the thicker stack leads to relaxed generalized blending, panel II to III in Figure 2.7(b).

Both types of blending can be combined with the guide approach. A guide denotes a stack of single plies, capable of covering at least the thickest panel under consideration. The blending depicted in Figure 2.7(a) can efficiently be described using a guide and the information of how many plies are dropped from the guide in each panel. Thus, the stacking sequence is fully described by defining the fiber angles in the guide along with the information on how many plies are dropped per panel.

2.3.1 Stacking Sequence Table

In order to relax the constraints imposed by dropping only outer plies, a generalized blending approach, see above, is required. An intuitive way of combining the guide philosophy with the idea of generalized blending is provided by stacking sequence tables, as proposed in Irisarri et al. [Iri13]. Starting with the stack featuring the smallest thickness, plies are added successively until reaching the maximum number of plies. An SST of a symmetric laminate with ply numbers reaching from 10 to

Table 2.1: *Stacking sequence table with minimum of 10 and maximum of 18 plies*

| N_{min} | | | | | | | | N_{max} | |
|-----------|----------|----------|-----|----------|-----|-----------|------------|-----------|--|
| 10 | 12 | 14 | 16 | 18 | 18 | 18 | 18 | 18 | |
| -45 | -45 | -45 | -45 | -45 | -45 | -45 | -45 | -45 | |
| 0 | 0 | 0 | 0 | 0 | 0 | 0 | 0 | 0 | |
| | 0 | 0 | 0 | 0 | 0 | 0 | 0 | 0 | |
| | | | | | | | -45 | -45 | |
| | | 0 | 0 | 0 | 0 | 0 | 0 | 0 | |
| 45 | 45 | 45 | 45 | 45 | 45 | 45 | 45 | 45 | |
| 90 | 90 | 90 | 90 | 90 | 90 | 90 | 90 | 90 | |
| | | | | | | 45 | 45 | 45 | |
| 90 | 90 | 90 | 90 | 90 | 90 | 90 | 90 | 90 | |
| 90 | 90 | 90 | 90 | 90 | 90 | 90 | 90 | 90 | |
| | | | | | | | 45 | 45 | |
| 90 | 90 | 90 | 90 | 90 | 90 | 90 | 90 | 90 | |
| 45 | 45 | 45 | 45 | 45 | 45 | 45 | 45 | 45 | |
| | | | | 0 | 0 | 0 | 0 | 0 | |
| | | | | | | | -45 | -45 | |
| | 0 | 0 | 0 | 0 | 0 | 0 | 0 | 0 | |
| 0 | 0 | 0 | 0 | 0 | 0 | 0 | 0 | 0 | |
| -45 | -45 | -45 | -45 | -45 | -45 | -45 | -45 | -45 | |

18 is exemplified in table 2.1. In order to maintain symmetry when adding a ply, an equivalent ply must be introduced in its symmetric position. Accordingly, each second column in the SST depicted in table 2.1 corresponds to a symmetric layout. If moreover the laminate is to be balanced, after completing the symmetry of a ply with angle θ , two additional columns in the SST are used to add a symmetric layer of angle $-\theta$. Eventually, appointing a stacking sequence from the SST to each structural panel results in a fully blended structure with the only restriction in generalized blending, so that all layers in a thinner stack are also part of the thicker stacks. The advantages of applying SST can be summarized as follows:

- implementation of ply-dropping guidelines
- definition of stacking sequence guidelines
- explicit specification of ply dropping sequence among adjacent panels
- efficient implementation with genetic algorithms (GA)

All listed items support the requirement of including industrial design guidelines in the stacking sequences, but also in blending. An elaborate compilation of design guidelines is provided in Irisarri et al. [Iri13], only the most important of which are highlighted in the following:

- **local guidelines:**

1. *symmetry*: stacking sequence symmetric about mid-plane
2. *contiguity*: maximum allowed number of consecutive plies featuring the same fiber angle
3. *disorientation*: maximum allowed change in fiber angle of consecutive plies
4. *covering*: no dropping of outermost layers
5. *maximum taper slope*: minimum stagger distance for dropped plies
6. *ply-drop alternation*: successive ply drops should be alternating in terms of distance to mid-plane

- **global guidelines:**

1. *continuity*: plies in the thinnest stack continue on in all other thicker stacks
2. Δn -rule: maximum allowed number of ply drops between two panels

It is in the context of the genetic algorithm applied for stacking sequence optimization, that the above mentioned design guidelines will need to be incorporated.

The blending between two panels according to the SST in table 2.1, featuring 14 and 10 plies, is demonstrated in Figure 2.8. The resulting taper section length depends on the stagger distance that is required per ply drop, which in turn is simply a function of ply thickness. It should be noted however, that stagger distance and

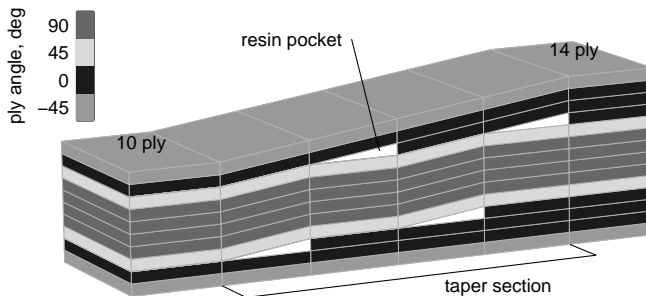


Figure 2.8: Ply dropping between panels of 14 and 10 plies

taper section, despite being a result of the SST, are usually not considered in the global finite element analysis model. Nevertheless, they reflect the requirements imposed by manufacturing considerations.

2.3.2 Genetic Algorithm

Genetic algorithms (GA) are inspired by the biological evolutionary process and boil down to the fact that within a group of individuals typically only the fittest succeed in transferring their presumably superior genotype to subsequent generations. Accordingly, characteristics that allowed an individual to survive and reproduce are carried on, while weak characteristics die out. The principle of evolution, when transferred to structural optimization problems, can be used to determine the optimal combination of design variables that lead to the maximum fitness. While in a biological sense the fitness is reflected for instance in the ability to run fast or think quick (noting that the latter most likely won't help when being chased by a lion, in which case velocity will win; unless being smart enough to operate the nearby *A350*), fitness in terms of structural optimization simply corresponds to the objective function that is to be maximized or minimized.

GA can be considered as the most popular tool applied in composite optimization, when dealing with discrete variables like fiber angles and ply numbers. A detailed survey on their application in the context of composite panel optimization was provided by Venkataraman et al. [Ven99]. Moreover, section 1.3.2 provided some examples of GA applications in composite wing design related research. The terminology involved in GA is mostly adopted from the biological counterpart, an overview on which is provided for example by Mitchell [Mit99]. Once having decided how to encode the involved design variables, they can be grouped together and form a chromosome. The set of all chromosomes involved in the optimization is called a genotype. In this context, encoding designates the way of expressing the design variables in a format that is suitable for the GA. Most GA initially worked with a binary encoding of the design variables, owing to the discrete nature, however, also a continuous encoding can be applied. Given the fact that an individual design is fully described by one genotype, a GA is initiated with the construction of an initial population of individual genotypes. The population size depends on the amount of design variables involved in the optimization. Each genotype is analyzed and sorted according to its fitness. The best designs are selected for crossover and mutation, to form the new generation of genotypes. For crossover, randomly selected parts of the chromosomes of the two crossing genotypes are exchanged. Mutation denotes random alterations of chromosome parts in a single genotype, in order to maintain diversity (the chances are almost impossible, but it might be that also the lion, if living close to a source of heavy radiation, is capable of flying the *A350*). The new generation is assembled from new genotypes, but also from the fittest designs of the previous generation. Thus, it is guaranteed that the overall fitness cannot decrease in advancing generations. Differences of the SST-tailored GA with respect to the general description will be, when applicable, discussed below.

Encoding

A most prominent advantage inherent to stacking sequence tables is the compact and therefore efficient form of its encoding for a GA optimization using only two chromosomes SST_{lam} and SST_{ins} . SST_{lam} defines the stacking sequence of the thickest laminate, listing its fiber angles. SST_{ins} specifies the sequence by which plies enter the SST, that are not part of the thinnest laminate. Accordingly, a "0" in SST_{ins}

indicates a ply that is already part of the thinnest laminate and therefore will be present in all other stacking sequences. The chromosomes listed in table 2.2 fully

Table 2.2: *SST genotype, consisting of three chromosomes*

| | | | | | | | | | | | | | | | | | | | | |
|-------------|---|-----|----|----|-----|---|----|----|----|----|----|----|----|----|---|-----|---|---|-----|---|
| SST_{lam} | [| -45 | 0 | 0 | -45 | 0 | 45 | 90 | 45 | 90 | 90 | 45 | 90 | 45 | 0 | -45 | 0 | 0 | -45 |] |
| SST_{ins} | [| 0 | 0 | 1 | 7 | 3 | 0 | 0 | 5 | 0 | 0 | 6 | 0 | 0 | 4 | 8 | 2 | 0 | 0 |] |
| N_{str} | [| 18 | 16 | 17 | 11 |] | | | | | | | | | | | | | | |

define the SST shown in table 2.1. A third chromosome N_{str} in table 2.2 defines the column of the SST that is to be attributed to the, in this case, four panels to be blended. In combination, the three chromosomes make up a genotype. As a result of the symmetry requirement, the genotype can be simplified to the one listed in table 2.3. A great advantage of the presented encoding strategy is the complete decoupling

Table 2.3: *SST genotype, exploiting symmetry*

| | | | | | | | | | | | |
|-------------|---|-----|----|----|-----|---|----|----|----|----|---|
| SST_{lam} | [| -45 | 0 | 0 | -45 | 0 | 45 | 90 | 45 | 90 |] |
| SST_{ins} | [| 0 | 0 | 1 | 7 | 3 | 0 | 0 | 5 | 0 |] |
| N_{str} | [| 18 | 16 | 17 | 11 |] | | | | | |

of stacking sequence and thickness distribution in the panels to be blended. Considerably less design restrictions are thus imposed compared to, for instance, inner/outer blending.

Initialization

The above table fulfills all design guidelines depicted in section 2.3.1. To make sure that this also holds for the genotypes in the initial population of the GA, a specific initialization process has to be followed, described in the following and schematized for the first step in table 2.4. Initialization starts with the generation of a stack with N_{min} plies, which has to fulfill the design guidelines, for instance a maximum change in fiber angle of $\pm 45^\circ$ in adjacent plies. Then a random position within the stack is chosen, along with a set of all feasible ply angles that are in agreement with the guidelines. From the set an angle is picked randomly and added to the SST. To restore symmetry, in the next step the same ply is added on the corresponding symmetry position, thus generating another column in the SST. If balance also has to be preserved, another two-step-cycle is required, if the added layer does not feature 0° or 90° . In the sample shown in table 2.4 a 0° ply was added, in which case no further restoring is required. Irisarri et al. [Iri13] denotes these restoring steps a *symmetry and balance-cycle* (*SB-cycle*). Designing with unbalanced laminates will therefore only require *SB-cycles* of length two. The *SB-cycles* process is continued until it reaches the maximum amount of plies N_{max} , in which case SST_{lam} and SST_{ins} are fully defined. The third chromosome N_{str} results from randomly picking as many numbers between N_{min} and N_{max} as there are panels to be blended. The only guideline to be considered is the Δn -rule which ensures that only a limited amount of plies can be dropped among adjacent panels.

From table 2.3 it can be seen that the stacking sequences pointed at by N_{str} are not necessarily symmetric or balanced. Thus, before evaluating the fitness of the genotype,

Table 2.4: *SST initialization, $N_{min} = 10$, symmetry restoring step*

| | | | | | |
|-----|--------------|--------------|---------------|-----|-----|
| 10 | 11 | 12 | | 10 | 12 |
| | -45 | -45 | | -45 | -45 |
| -45 | 0 | 0 | | 0 | 0 |
| 0 | +1: 0 | 0 | | 0 | 0 |
| 45 | 45 | 45 | | 45 | 45 |
| 90 | 90 | 90 | | 90 | 90 |
| 90 | 90 | 90 | \Rightarrow | 90 | 90 |
| 90 | 90 | 90 | | 90 | 90 |
| 90 | 90 | 90 | | 90 | 90 |
| 45 | 45 | 45 | | 45 | 45 |
| 0 | 0 | +1: 0 | | 0 | 0 |
| -45 | -45 | 0 | | 0 | 0 |
| | | -45 | | -45 | -45 |

a chromosome repair is performed, which modifies the infeasible pointers in N_{str} to the nearest feasible neighbor, however, the original genotype remains unchanged, ensuring that the GA will not be influenced by the repair.

Reproduction

In principle, crossover and mutation are available for both the SST and the thickness definition N_{str} . They are explained to a great extent in the work of [Iri13] and [Med13] and will therefore only be described briefly here.

Mutation of the chromosome SST_{lam} comprises the change of a plies $\pm\theta$ (balanced) or ply θ (unbalanced) within the stacking sequence by randomly selecting from the admissible set of ply angles at that position. Mutation of the chromosome SST_{ins} basically corresponds to a random exchange of two *SB-cycles*. Since the order of plies is not influenced, but only their appearance within the SST, the only guideline to be considered is ply drop alternation. The only guideline to be considered in the mutation of N_{str} , where single parts are replaced by randomly generating numbers between N_{min} and N_{max} , is the Δn -rule.

A crossover operation for the SST consists of the selection of plies with the same length, hence equal numbers in SST_{ins} , from two different genotypes, and a subsequent exchange of these sublaminates. Since the operation is prone to the generation of defects, mostly a violation of the disorientation guideline, a subsequent repair according to the technique described for population initialization is applied. Crossover for N_{str} comprises again the random selection of two groups of equal length from two genotypes and a subsequent exchange. In this case, the SST is checked for accordance with the Δn -rule before performing the crossover.

The selection of genotypes that are to be part of the reproduction pool for the next generation deviates from the regular *survival of the fittest* methodology, instead, the following scheme will apply:

1. divide population into feasible and unfeasible designs
2. sort feasible designs according to fitness, and unfeasible designs according to constraint violation
3. again merge the sorted feasible and unfeasible designs to a single population

4. select the first n_{best} genotypes for reproduction – might involve infeasible designs
5. binary tournament selection out of n_{best} genotypes: randomly select two and place in new pool n_{repro} according to
 - (a) both feasible: genotype with better fitness placed in n_{repro}
 - (b) one feasible: feasible genotype placed in n_{repro}
 - (c) no feasible: genotype with lowest failure margin placed in n_{repro}

Out of n_{repro} as many crossover operations, obtained by randomly selecting two contributor, are performed as are required to generate a fully populated generation. Eventually, a mutation according to a specified percentage is performed, finalizing the new generation.

2.3.3 Successive Approximations and Shepard's Interpolation

A direct link between the stacking sequence optimization discussed here and the continuous optimization as outlined in section 2.1 is given by the applicability of the local response approximations. The reason for this is explained in the following.

When performing a stacking sequence optimization for a wing as optimized previously using a continuous optimization, a single genotype describes a fully-blended stacking and thus stiffness distribution. Accordingly, to evaluate the fitness of a genotype along with the corresponding constraints, a finite element analysis will be required. Keeping in mind though, that in a regular GA the population size times the amount of generations that are required to achieve convergence can easily amount to tens of thousands of function evaluations, it falls into place that a direct FE calculation for each fitness test is not an option, however, as a consequence of stiffness dependent aeroelastic forces and load redistribution, reanalyzing the structure is inevitable. Therefore, it seems obvious to use the same approximation methodology as applied in the continuous optimization for the GA optimization.

The general principle of the successive approximation method is shown in Figure 2.9. The stacking sequence optimization initiates with the generation of an initial population and the provision for responses and sensitivities with respect to the previously evaluated optimal design point, resulting from the continuous optimization. The derivation of stiffness matrices from the SST is denoted phenotype decoding. The stiffness matrices, corresponding to the design variables of the continuous optimization, are applied in the derivation of the relevant responses including the objective. The required response approximations will be discussed hereafter. Having evaluated objective and constraints for all genotypes, reproduction according to the description given in section 2.3.2 is performed, resulting in the next generation of genotypes. With this generation the GA loop continues with the next phenotype decoding, and so forth. Once an initially defined maximum amount of generations is reached, the GA is stopped to enter the outer loop for the derivation of new responses and sensitivities in the optimal design point resulting from the GA optimization. The GA is restarted with the last genotype generation and new response approximations.

Meddaikar [Med13] in his work presents a method of reusing previously generated approximation points to improve the current approximation. It is denoted a modified *Shepard's* method and will be discussed briefly in the following. The method was suggested in Irisarri et al. [Iri11]. The original method introduced by Shepard [She68]

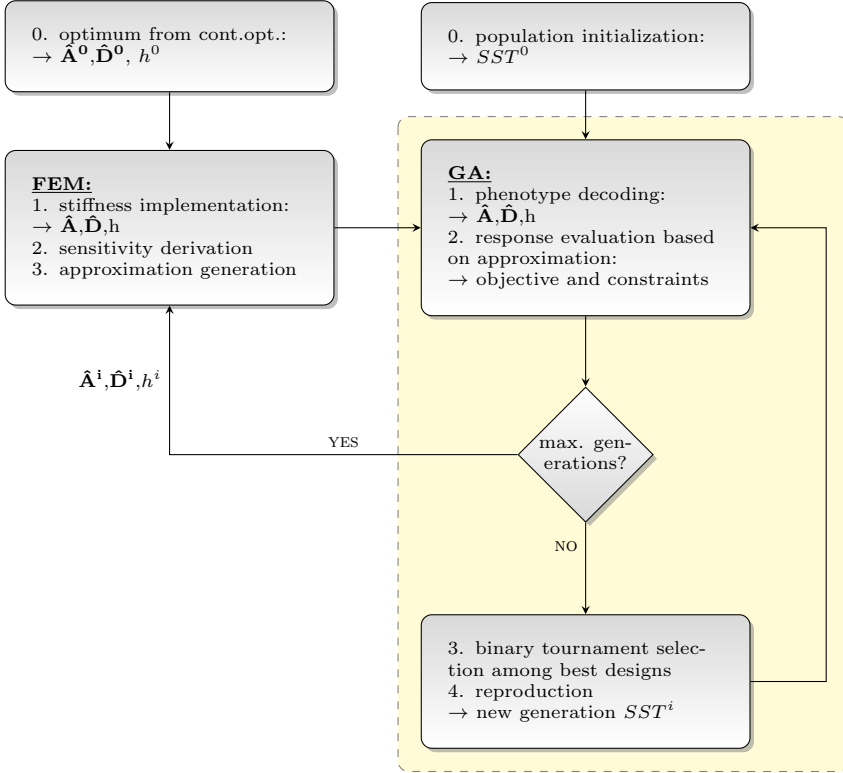


Figure 2.9: Schematic overview of a GA stacking sequence optimization in combination with successive approximations

is denoted an inverse distance weighting interpolation. It considers the influence of known data points with respect to the point to be interpolated using their inverse distance. Accordingly, the greater the distance of an unknown point from the known data points, the less influence it has on the interpolation. For function value u this can be expressed as:

$$u(\mathbf{x}) = \sum_{i=1}^N \frac{w_i(\mathbf{x})u_i}{\sum_{i=1}^N w_i(\mathbf{x})}, \quad (2.8)$$

with:

$$w_i(\mathbf{x}) = \frac{1}{d(\mathbf{x}, x_i)^P}, \quad (2.9)$$

where x_i denote the N known data points, and w_i its corresponding weight, based on the distance measure d . P is a power parameter which can be used to modify the distance influence. A first application of *Shepard's* method in composite optimizations were shown by Gantovnik et al. [Gan03]. The modified *Shepard's* method as suggested in Irisarri et al. [Iri11] and implemented in Meddaikar [Med13] aims at reusing previous

function approximations in the construction of a multi-point approximation:

$$\tilde{f}_i^g(x) = \sum_{i=1}^n \frac{w_i(x) \tilde{f}_i^l}{\sum_{i=1}^n w_i(x)}, \quad (2.10)$$

with:

$$w_i(x) = \frac{1}{\|x - x^{(i)}\|_2^2}. \quad (2.11)$$

Here n describes the total amount of previous approximations \tilde{f}^i that the global approximation \tilde{f}^i will be constructed from. $w_i(x)$ is the *Euclidian* distance between the actual function evaluation point and the reference point of the i^{th} approximation. The approximations being expressed in laminate stiffness space rather than a spatial distance expressible by a length, requires the definition of a laminate stiffness distance. Irisarri et al. [Iri11] in their paper suggest a distance measure fulfilling the following requirements:

1. positive inverse weight outside the origin, $1/w_i(x) > 0$
2. zero inverse weight at the origin, $1/w_i(x) = 0$
3. differentiable at the origin

which according to Komargodski et al. [Kom06] are required for the interpolation to be of *Hermit*-type and thus be exact in value and derivative at the latest approximation derivation point. According to Irisarri et al. [Iri11], the non-homogeneous distance between two pairs of membrane and bending stiffness matrices can be expressed as:

$$d_{AD}(\mathbf{AD}_1, \mathbf{AD}_2) = \frac{1}{6}(\mathbf{A}_1^{-1} : \mathbf{A}_2 + \mathbf{A}_1 : \mathbf{A}_2^{-1} - 6) + \frac{1}{54}(\mathbf{D}_1^{-1} : \mathbf{D}_2 + \mathbf{D}_1 : \mathbf{D}_2^{-1} - 6). \quad (2.12)$$

They also suggest a homogeneous laminate distance definition, which is skipped here.

2.3.4 Response Approximations

Other than the usual direct approximation of strain and buckling, as for instance seen in [Abd07b], [IJs09], [IJs10], [Dil13c], mostly in combination with a continuous stiffness based optimization, a different method is implemented by Meddaikar [Med13]. Rather than approximating strain and buckling, an approximation of load is considered instead:

$$\tilde{N}_i = \sum_j \Psi_{i,j}^m : \mathbf{A}_j + \Psi_{i,j}^b : \mathbf{D}_j + C_0. \quad (2.13)$$

This enables the application of more sophisticated, ply based strain and buckling failure methods, as compared to the continuous optimization, where inherently no stacking sequence information is available. For the sake of convenience, the strain and buckling failure analyses as applied in the continuous optimizations and described in section 5.6 are implemented, however, based on load approximations.

2.3.5 Objective Function

A variety of possibilities exist for choosing an appropriate objective function. Given that the continuous optimization results in sets of membrane and bending stiffnesses, a meaningful objective can be to match the stiffnesses resulting from laminate blending with the optimal continuous results. The clear advantage of this approach can be seen in the possible dispensability of response approximations and thus finite element analyses are not required for pure stiffness matching. The objective therefore represents the fastest option to obtain stacking sequences. Stiffness matching can also be combined with a constrained optimization, in the sense that designs are not only judged on the basis of fitness, but also feasibility of the design. Meddaikar [Med13] however, notes that the nearest discrete result is not necessarily the best discrete design. Hence, many other possible objectives in combination with and without response approximation consideration can be devised, these are, without claim to completeness, listed in table 2.5.

Table 2.5: *Stacking sequence objectives*

| | objective | approx. required | description |
|---|----------------------|------------------|---|
| 1 | A, D matching | – | matching of membrane and bending stiffness elements in each design field |
| 2 | A, D matching | ✓ | same as 1, approximations are used for response evaluation and feasibility judgment |
| 3 | V_i, W_i matching | – | matching of lamination parameters in each design field |
| 4 | V_i, W_i matching | ✓ | same as 3, approximations are used for response evaluation and feasibility judgment |
| 5 | direct optimization | ✓ | in GA directly optimize for the objective specified in continuous optimization; from the latter only the initial approximation point is adopted |

The application of the stacking sequence optimization as depicted here will be demonstrated, along with the problem specific selection of the objective function, in section 9.6.

2.4 Summary

An overview on the major steps in the optimization process, the types of static aeroelastic responses considered in this work, and an overview on stacking sequence optimization was given. Where applicable, the reader will find more information on each subtask of the optimization in the appropriate chapters referred to above.

CHAPTER 3

Parametric Wing Model Generation

“I hear and I forget. I see and I remember. I do and I understand.”

Confucius

Clearly, the finite element model assumes an important part of the optimization process. It computes the responses and sensitivities that are transformed into response approximation, which in turn serve as the only input to the optimizer. The finite element software NASTRAN [Moo04] was chosen as solver due to its wide acceptance and propagation in the aircraft industry. The most prominent reason to do this is its capability to compute the required sensitivities efficiently for a large variety of predefined design variables and responses, in combination with coupled, aero-structural analysis, e.g. trim analysis. Details of the optimization model will be presented in chapter 4. The generation of a finite element model with shell and beam elements, based on a parametric approach, is described in the following sections.

The advantage of parametric modeling can be seen in the fast generation and adoption of the FE model, without having to consider elaborate redesign every time the influence of a major layout parameter, like planform shape, sweep angle, number of spars or ribs, is to be examined. To be suitable within an automated design process, the generation of the parametric model must be able to provide adequate resolution in span and chord direction of a wing box, including stringer and spar caps, represented as beams, to exploit the advantages of a shell over a beam model. Such a parametric process, called MODGEN, has been developed at the *DLR-Institute of Aeroelasticity*, see Klimmek [Kli09; Kli12].

The parametric process MODGEN is a *Fortran* program that is available for *Linux* and *Windows* platforms, using a standardized text input file. The input file contains entries similar to the Bulk Data Section of NASTRAN. To some extent some entries are even identical to NASTRAN. At first, a geometry model of the wing geometry and the structural entities of the wing is generated, section 3.1, which serves as a basis for the discretization in finite elements, depending on the specified element types and densities, section 3.2. The methodology and procedures of accounting for non-structural masses are described in section 3.3, while details on the, likewise, parametrically

generated doublet lattice model, which is responsible for the computation of the aerodynamic forces, are provided in section 3.4. Details are presented on control surface modeling, a camber correction method, and the splining method used to transform forces from the aerodynamic model to the structural model and displacements from the structural model to the aerodynamic model.

The concept of separate geometry and finite element models supports the parametric concept. A change in the geometry automatically transfers to the finite element model, which inherits its shape from the geometry model and does not have to be adapted manually. This approach allows for fast model generation based on a geometry model of the structural parts of the wing box. Therefore, the slight geometrical modifications of the structural concept result in comparable structural finite element models.

3.1 Geometry Model

The general build-up of a modern civil aircraft wing structure was laid out in section 1.3.1. This section deals with the creation of geometric representations of all the load carrying structural entities of a modern civil aircraft wing, these form the basis for the generation of the finite element representation illustrated in the following section. A geometric representation in the platform independent *iges* format, [US 96], corresponds to a mathematical description, thus allowing for the calculation of, for example, point coordinates on a surface, or the intersection of surfaces and/or lines. Curves and surfaces are defined as *iges* entity type 126, B-spline curve, and 128, B-spline surface, a widely used entity type for parametric curves and surfaces, e.g. by CATIA and PATRAN.

In preliminary aircraft design, but also in later, more detailed design stages, the person in charge of the structural design faces the task of adopting the outer aerodynamic shape for the creation of the internal structure. The first step in the parametric wing model generation is therefore the definition of the aerodynamic shape, which can be achieved by one of the following two methods:

- definition of the wing planform via trapezoid segments, made up of point coordinates for leading and trailing edge position and 2D airfoil coordinates spanned in-between
- geometry file in *iges* format, defining the outer wing contour

If the first method is chosen, MODGEN constructs a geometric representation of the outer wing contour in the form of *iges* surfaces.

Subsequent structural entities will be modeled inside the outer aerodynamic shape. The wing box is bound by a front and a rear spar, which are defined in the parametric process via absolute or relative positions with respect to the leading or trailing edge. These spars can span multiple spanwise wing segments, or be modeled with kinks at arbitrary positions. The spar definition contains information to set up planes, which intersect with the wing segment and lead to a B-spline surface, representing the spar web. The wing outer surface in-between front and rear spar is called a skin. More spars can be modeled, each one leading to a chordwise division of the skins. Spar cap geometric entities in the form of line elements are generated automatically along with the spar definition.

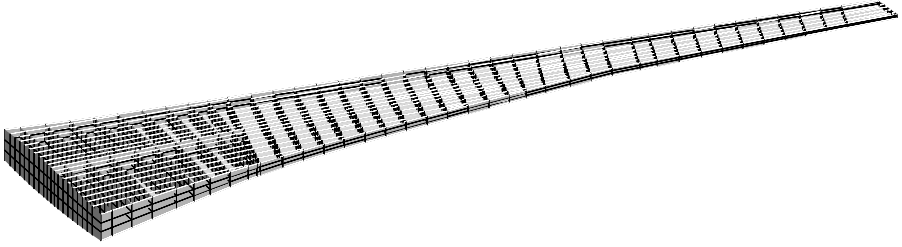


Figure 3.1: MODGEN geometry model with removed top skin

Ribs are modeled in a similar manner. The definition of their position and angle suffices to constitute planes which intersect with the wing skins and spars, resulting in bound surfaces. Depending on the number of spars, a rib is further divided into subribs in chord direction in-between consecutive spars; likewise the subdivision of spars into subspars by the rib planes. Ribs also further divide the wing skins into smaller subsegments.

Stringers are generated based on the definition of stringer direction and a stringer pitch. Again, the planes that can be constructed from these data intersect with the wing skins to construct the stringers geometric definition as line elements. These lines are used later on to guarantee a consistent finite element mesh. A geometry model with removed top skin, as it is generated in MODGEN, is shown in Figure 3.1.

This concludes the first part of the parametric definition, which sets up the geometric representation of all major load carrying structural entities. MODGEN offers the possibility to export the geometry model as a whole or in parts to *iges* format, to inspect the geometrical model in terms of an error-free setup.

3.2 Finite Element Model

Based on the geometry model, the finite element model is generated in the next step. It is up to the user to decide which *iges* surfaces are to be meshed, since not necessarily every surface or line entity in the geometry model has to be used for the finite element model. Wing skin elements, for example, that are bound by spars and ribs are referred to as SUBSEGR in MODGEN terminology, each of which featuring a unique identifier. The identifier is used for the specification of the element type, the element properties and the element distribution in the two spatial dimensions of the corresponding surface; the denotation of the corresponding MODGEN card is BDFOUT. Elements are by default distributed equidistantly, but also allow user-defined spacings. The fact that properties are assigned when specifying the paneling clarifies that all elements on the current *iges* surface will, per default, have the same properties, and hence stiffness and thickness attributes.

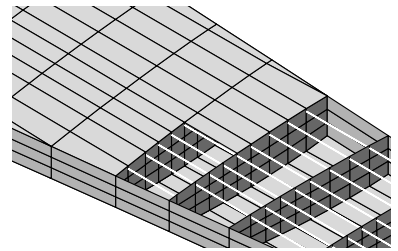


Figure 3.2: Finite element model

The same procedure applies to ribs and spar webs. The user has to ensure a

matching number of elements at the intersection of subsurfaces, while MODGEN takes care of equivalencing element nodes that lie within a specified distance from each other. If stringers are present, the chordwise panel distribution is prescribed by the stringer pitch. The elements employed for the discretization of the shell-like surfaces are NASTRAN CQUAD4 and CTRIA3, where the latter elements are applied solely in the vicinity of stringers that, due to different sweep angles, end at a spar, to accomplish the transition; see Figure 3.2

A similar treatment also applies to the stringer and spar cap meshing with one-dimensional NASTRAN CBEAM elements. These require the input of longitudinal, bending and torsional stiffnesses, together with the material to be used and an offset in case of a defined cross section. Stiffeners in spar webs and ribs are modeled likewise, but restricted in position, automatically matching the shell element boundaries of the underlying surface entity.

The derivation of the membrane \mathbf{A} and bending stiffness matrix \mathbf{D} for a stack of single layers was described in section 1.1.1. NASTRAN shell elements allow for two different ways to define composite stiffness properties. One possibility is the specification of a stacking sequence with PCOMP shell element property cards. Each layer is defined with thickness, angle, and the orthotropic material properties. The material properties are defined on MAT8 cards, reflecting the materials *Youngs* modulus in fiber direction and perpendicular to it, *Poisson* ratios, shear moduli, density and stress/strain allowables. The other possibility comprises the definition of the thickness normalized stiffness matrices $\hat{\mathbf{A}}$ and $\hat{\mathbf{D}}$ with MAT2 cards ($\hat{\mathbf{B}} = \mathbf{0}$ due to symmetry). The cards are referred to on property cards PSHELL, which among others defines the shell thickness. Both methods described here can be realized in MODGEN, while only the combination PSHELL/MAT2 with its direct declaration of stiffness matrices is suitable and essential for the specification and derivation of the necessary design variables and sensitivities in this work.

3.3 Mass Model

There are basically two important reasons why an accurate mass model is indispensable for the optimization task. One, the load carrying structure that is to be discretized with the finite element model has to have mass properties for computing a weight response and sensitivities; it is the material density that relates shell weight to shell thickness. This requires material density information, which can be specified on the corresponding NASTRAN cards, for example, MAT2 for the wing skins. Two, an accurate static aeroelastic analysis requires an accurate mass distribution because of its influence on the overall load and displacement distribution. For a steady aeroelastic trim condition the wing is loaded with aerodynamic forces, and the inertial forces induced by the distributed masses of the wing structure and clustered masses like engines, actuators, or fuel. Only the sum of both loads needs to be supported by the wing structure, thus, the releasing contribution of mass should be considered in the optimization.

In the following two sections the consideration of additional masses and their attachment via interface models, as well as the generation of a fuel mass model are discussed.

3.3.1 Interface Model

The interface model is simply an extension to the finite element model that provides for additional grid points and their rigid or multi point, weighted connection to existing grid points of the finite element model. A rigid connection simply links specified degrees of freedom of the new grid point to the existing ones, while a weighted connection leads to an averaged displacement of the new grid point, according to the displacements of the grid points it connects to. The corresponding NASTRAN elements are called RBE2 and RBE3. The points to link to in the finite element model are selected on the corresponding MODGEN cards. MODGEN follows the designers intuition of introducing loads only at rib planes and offers a variety of possible combinations for grid point selection in one or more rib planes.

While the rigid RBE2 connection is mainly used for clamping the model at the root rib, and the attachment of small, rather local point masses to single points in the finite element model, the weighted connection with RBE3 elements serves as a junction for larger masses, the influence of which is not limited to a single point. The latter connection type can be employed for modeling the structural parts that do not contribute to the wings main stiffness and that are not part of the finite element representation. This includes masses in front and aft of the load carrying wing box, integrating the structure of the high lift devices, of flaps, or engine, pylon and landing gear, to name only a few. At this point, it is rather a lack of trustworthy data than the capacity to consider it in the finite element model that limits the application.

3.3.2 Fuel Model

Integration of the large portions of the overall fuel in integral tanks in a wing box is a well approved practice, and it is essential for several reasons. One, the sheer amount of fuel required for a passenger plane necessitates storage in the wing. Two, the load releasing inertial effect that counteracts the lift force significantly reduces wing bending, and hence structural weight, as a result of stress reduction. Three, decentral storage of fuel in separable integral tanks increases system reliability in the case of damage to one or more of the integrated tanks. Reason number two is the driving force behind integrating a fuel mass model in the finite element model.

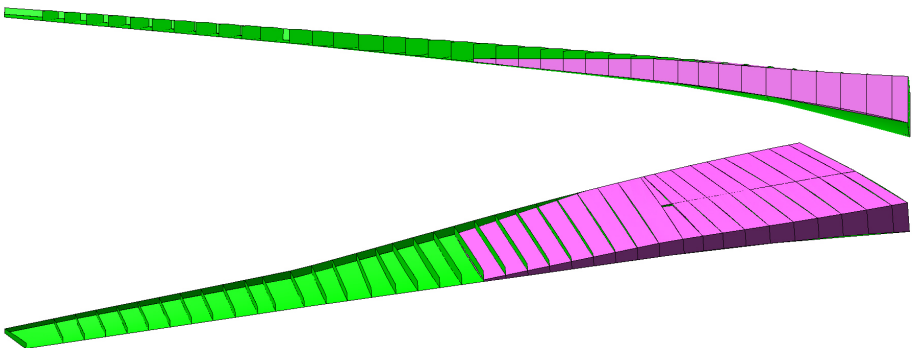


Figure 3.3: *Fuel modeling with CHEXA elements*

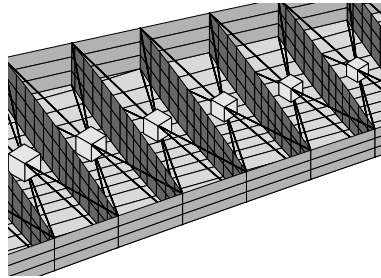


Figure 3.4: *Fuel model*

The parametric process MODGEN provides routines to generate such a fuel mass model. For this purpose, a fuel tank is automatically divided in subparts specified by the rib-bays, each one reaching from rib to rib and bound in chordwise direction by the spars. Depending on user-specified filling level and inclination, volume elements that exactly match the fuel volume are generated, Figure 3.3, and automatically analyzed in separate NASTRAN runs, to determine their volume, respectively center of gravity, and along with fuel density their complete mass and inertia matrix. Finally, not the volume elements will be part of the finite element model, but rather point mass elements of NASTRAN type CONM2 will be used, which obtain their mass properties from the previous fuel model analysis. The masses are attached to the finite element model with the multi point connection (RBE3) as described in section 3.3.1. The mass elements and their attachment via RBE3 elements is depicted in Figure 3.4.

Again, it is rather a lack of accurate data than a lack in modeling ability that limits the application of detailed fuel burn scenarios in most cases. Therefore, meaningful assumptions for the spanwise division of the wing fuel tanks in three or four major tanks, along with fuel burn sequences need to be conceived for aircraft, where no related data are accessible or simply does not exist at present.

3.4 Double Lattice Model

It was mentioned in the beginning of this chapter that one reason for picking NASTRAN is its provision for aerodynamic tools that along with the finite element model allow for coupled aeroelastic calculations. Depending on the *Mach* number, different aerodynamic methods can be applied. The doublet lattice subsonic lifting surface theory (DLM), see Rodden et al. [Rod04], was chosen as the most suitable for the present investigations. It belongs to the potential theory methods, where singularities like sources, vortices or doublets are superimposed with the undisturbed free-stream. The singularity distribution results from the kinematic boundary condition for the deformed surface.

The wing planform is discretized with flat trapezoidal panels that are partitioned into boxes, each of which comprises a control point for a flow tangency reference and a point, at which the pressure will be calculated. This finally leads to an aerodynamic influence coefficient matrix (AIC) that relates the pressure in each box to the local downwash angle of each box. MODGEN features input cards to generate the input for a NASTRAN doublet lattice model. Following the parametrization approach in MOD-

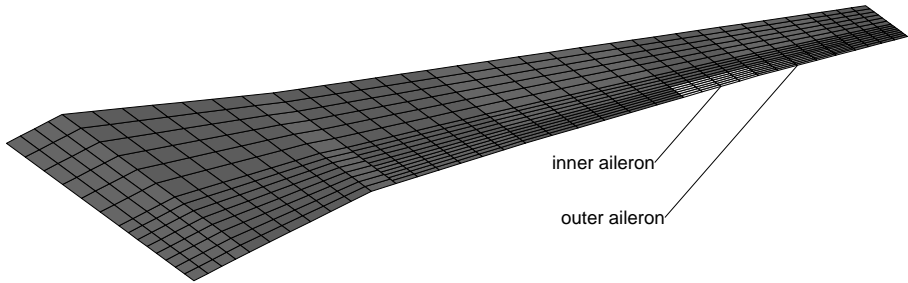


Figure 3.5: *Doublet lattice model*

GEN, the required input links to the geometry model and thus will adapt accordingly. A typical doublet lattice model that reproduces the wing planform with several panels is shown in Figure 3.5.

More insight into the derivation of doublet lattice forces and the propagation onto the structural model will be provided in section 6.1 in conjunction with aero load corrections.

3.4.1 Control Surfaces

Control surfaces in DLM are modeled just as another flat trapezoidal panel connecting to the panel representing the fixed wing, with the addition of a coordinate system, the y-axis of which defines the hinge line for deflections, i.e. rotation axis. The declaration of a control surface is done with a `AESURF` card in NASTRAN. Dedicated parametrization routines in MODGEN allow for linking the flap definition to geometric entities like spars and fractions of segments, note, Figure 3.5 includes doublet lattice panels representing an inner and outer aileron.

3.4.2 Camber and Twist Correction

Per default, the doublet lattice model corresponds to the aerodynamic representation of a flat, untwisted plate. NASTRAN offers a correction of the downwash angle of each box with the help of a matrix called `W2GJ`. This allows for an adaption of the downwash angles as it comes into existence for a cambered airfoil or a twisted wing. In the first case, the angle correction corresponds to the chordwise local angle of the camber line, while in the second case the correction varies only in spanwise direction according to local twisting. Since airfoil and twist information are essential for the correction, the matrices can only be generated if the outer aerodynamic shape for the geometry model is generated with a manual planform definition along with 2D airfoil coordinates.

More details on correcting the box angles by camber and twist, and its influence on aerodynamic loading will be provided in section 6.2.1.

3.4.3 Coupling

Bending and mainly twisting of a wing in flight will change the aerodynamic loading as a result of altered local angles of attack along the span. For this reason, the struc-

tural and aerodynamic models describing the wing will have to experience equivalent deformations, if the aerodynamic loading is to predict the real, aeroelastic influence of the elastic structure. Coupling then denotes the linking of deformations of the structural and aerodynamic grid points. In NASTRAN the deformation interpolation is denoted *splining*, and basically two types of splines are available, beam splines and surface splines. Due to the surface-like extension of the shell FE model, as opposed to a beam model, the latter spline type is adopted; details on which can be found in Harder et al. [Har72]. The splining matrix that results from these considerations can be used to transfer deformations from the structural to the aerodynamic mesh, and in a transposed version to transform the aerodynamic forces to the structural points. Details will be provided in section 6.1.

The parametric process MODGEN automatically generates the required NASTRAN input, while assuming that the structural nodes used for coupling will consist of all rib grid points that intersect with the upper skin of the wing box. These nodes are gathered on a NASTRAN SET1 card. As many SPLINE1 cards will be generated as there are panels in the doublet lattice model, linking each to the entire set of structural interpolation nodes. Investigations have shown that a less dense and more

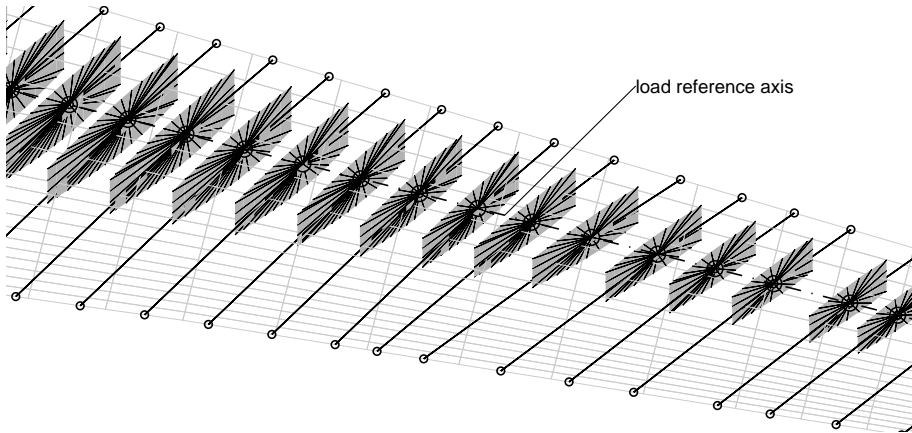


Figure 3.6: *Load reference axis coupling*

distributed spline node allocation can be favorable in terms of the “smoothness” of the loads that are interpolated to the structure nodes. For this reason, the MODGEN capability of modeling a load reference axis (LRA) was adapted. The LRA basically consists of a virtual axis in spanwise direction that is marked by grid points in each rib plane. The grid points are attached with RBE3 multi point connections to the corresponding circumferential rib nodes. Each rib comprises two RBE2 rigid elements, one extending to the leading edge of the underlying planform and one to the trailing edge. This guarantees a full coverage of the aerodynamic surface with points belonging to the structural model. The principle is shown in Figure 3.6.

The set of structural nodes that are used for coupling consists of the nodes on the load reference axis and the nodes on the RBE2 rigid body elements. Aerodynamic loads transferred to the points on the RBE2 will be distributed by the corresponding RBE3 element over the entire rib.

3.5 Summary

The generation of a NASTRAN aeroelastic finite element model by means of the parametrized preprocessor MODGEN was described in detail. More background on individual adaptations of the process for the modeled test cases will be given in the associated chapters.

The parametric process MODGEN allows for the generation of a NASTRAN input deck containing the basic design variable and response definitions to perform optimizations with the algorithms provided by NASTRAN, however, the development of a new optimization strategy with a problem tailored stiffness optimization necessitates the specification of a problem tailored optimization model, the development and disposition of which will be described in the following chapter.

“Make everything as simple as possible, but not simpler.”

Albert Einstein

Seen in the context that the number of design variables in a stiffness optimization can be in the range of thousands and the number of responses in the range of tens of thousands, obtaining the sensitivities of all responses with respect to all design variables is a non-trivial task. With the dimensions of the sensitivity matrix being equal to the product of number of responses and design variables, the sensitivity matrix might easily comprise several million entries. It is therefore unquestionable that an efficient method to compute the required sensitivities in a limited amount of time is indispensable. NASTRAN is well suited to adopt to this task, which is why in this chapter solver specific input definitions are addressed.

The concept of design fields comprising identical structural properties is introduced in section 4.1. Details on the terminology required to define design variables and responses are presented in section 4.2 and 4.3, then how NASTRAN computes sensitivities is briefly discussed in section 4.4. Given the large amount of responses and sensitivities to be generated, bookkeeping and exporting those to files is an important issue, and discussed in section 4.5.

4.1 Design Fields

The concept of a design field comprises a grouping of shell elements within the finite element structure that will share the same stiffness properties, defined by normalized stiffness matrices of a symmetric layup $\hat{\mathbf{A}}$ and $\hat{\mathbf{D}}$ and a thickness \hat{h} . Design fields can be generated for all structural entities that are represented by shell elements, hence wing skins, shear webs and ribs. In most cases it will be meaningful to not overlap a design field between structural entities, while within a structural entity, like the upper wing skin, at first no limitation exist on how to group the elements.

While it is possible to choose freely the element resolution in each entity of the finite element model via an appropriate MODGEN parametrization, certain limitations

are entailed by the responses that are to be extracted from the model. The imposed buckling constraint requires a buckling field to be represented by a single shell element, details on which will be presented in section 5.6.2. Since a buckling field in the wing skins is usually bound by two ribs in spanwise and two stringers in chordwise direction, the element resolution is prescribed accordingly.

The question of how to group shell elements into design fields is influenced by multiple factors. Within a design field consisting of several elements that all comprise the same thickness and stiffness properties, there will usually be only a limited amount of elements with active sizing constraints, while the remaining elements are not fully loaded. Sizing constraints in this respect refer to strain and buckling failure and will be discussed in more detail in section 5.6. Elements not being fully loaded is a result of gradually changing loads throughout the entire wing and eventually implies that they could have been thinner and therefore lighter in case they would not adopt the stiffness of the sizing elements within the design field. Thus, augmenting the stiffness resolution by increasing the amount of fields in spanwise and chordwise direction leads to a finer gradation of the stiffness parameters and an increased design space. A high design field resolution in particular helps in the case of local force transmissions like engine and landing gear attachment along with the corresponding load cases that are considered in the optimization.

A prominent downside of increasing the design field number and therefore design variable number and design space is the computational power required to solve for the minimum within the approximated analysis model. Moreover, the real, non-convex design space will most likely feature more local minima. Eventually, the production technology and in particular the layup process might stipulate a minimum and maximum field size comprising constant properties, in which case it will be most reasonable to stay within these preset bounds.

A possible design field distribution with 34 fields per wing skin is exemplified in Figure 4.1.



Figure 4.1: *Design fields*

4.1.1 Subdivision of Structural Entities

In order to divide the structural entities selected for the optimization into design fields, a multi-step methodology was developed in which in the first step the shell

element topology is evaluated. The goal is to generate a map of all elements belonging to an entity, e.g. the upper wing skin, that clarifies the relative position of each element with respect to all neighboring elements. Despite the fact that in this work only finite element models emanating from MODGEN were adopted, this step allows for a straightforward consideration of NASTRAN finite element models that are not necessarily generated with MODGEN. Moreover, the element topology in MODGEN might vary likewise, meaning that no strict element ordering can be assumed.

To construct the element map, elements belonging to the entity must be detected, along with the corresponding NASTRAN specific element definition. The mapping algorithm relies on the fact that all elements in the entity under consideration possess equally directed element normals. The connection table that defines the corner points of an element is employed to detect elements connecting to its three or four edges. Independent of the element numbering the reordering results in a map displaying the relative position of each element. Such a map is shown in Figure 4.2, where each black square represents a three- or four-sided element. The map belongs to the upper skin depicted in Figure 4.1. Once the map is generated, elements can easily be grouped

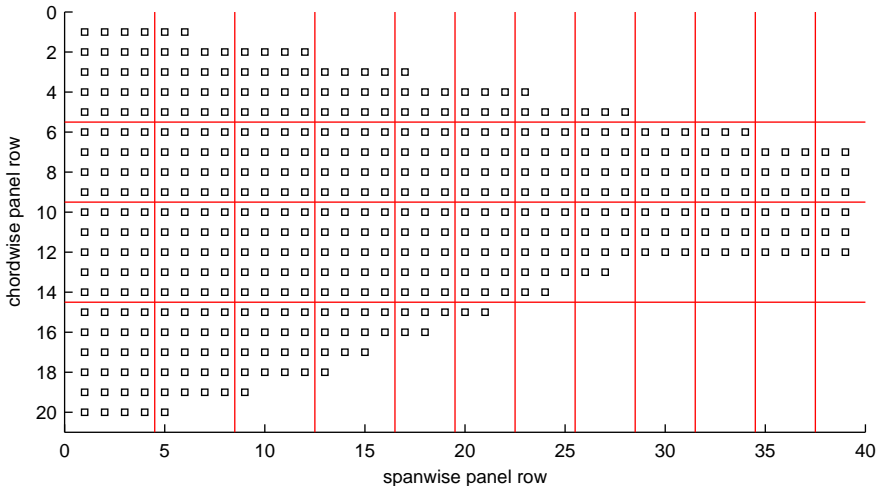


Figure 4.2: *Design field map*

into fields by defining desired spanwise and chordwise partitions, indicated by the red lines in Figure 4.2. It was mentioned in section 4.1 that the chordwise element distribution is prescribed by the stringer pitch, while in spanwise direction elements are limited by ribs. With a constant stringer pitch and an equidistant rib distribution, choosing a constant amount of elements in chordwise and spanwise direction for each field results in nearly equal design field areas. The sample in Figure 4.2 for instance features four spanwise elements in the wing root area and three elements in the outer wing to capture a higher resolution in the aeroelastically important outer wing. As a result of the chosen partitioning concept, design fields at chordwise boundaries might arise that only consist of very few elements. It is therefore possible to join such fields to adjacent ones. In Figure 4.2 for example the design field including elements [20, 15] and [21, 15], numbers in brackets indicating spanwise and chordwise panel row respectively, will be joined to the chordwise neighbor.

Each design study presented in part II will feature its own optimization model with the corresponding reasoning for the chosen design field distribution.

4.2 Design Variable Definition

Property cards are employed in NASTRAN to specify the structural characteristics of a finite element. Shell elements obtain their properties usually from a PSHELL card, which specifies the shell thickness and points to cards that specify the material properties. In the case of orthotropic fiber composite, the thickness normalized membrane, coupling and bending stiffness matrices $\hat{\mathbf{A}}$, $\hat{\mathbf{B}}$, $\hat{\mathbf{D}}$, see section 1.1.2, are specified via MAT2 material cards. For symmetric laminates the coupling matrix might be omitted.

As described in section 3.2, the smallest entity of elements featuring the same stiffness properties in MODGEN are elements belonging to one *iges* surface. This means that, for example, all skin elements bound by two ribs and two spars (*iges* surface denoted as SUBSEGR), will feature equivalent stiffness properties. Grouping shell elements in design fields however implies a need to allocate the same properties for all of them, which is why for each field a new unique set of stiffness matrices is induced.

By default, MODGEN generates a single NASTRAN PSHELL card for every shell element. Therefore, the property cards of elements belonging to a design field have to be rewritten to point to the correct, newly appointed set of stiffness matrices. Other than a unique set of stiffness matrices for each design field, each element retains its own PSHELL card and therefore a distinct shell thickness definition. A common design field thickness is accomplished by appointing one common design variable for all shell thicknesses in a design field; details on which are given below.

The specification of a design variable (DV) in NASTRAN is arranged on two cards. The DESVAR card is used to create the variable and set an initial value and a label, while the second card, DVPREL1 or DVMREL1, links the design variable to a field on the property or material card that is to be modified. The two types are shown in Figure 4.3. In order to link the thickness of shell elements belonging to a common

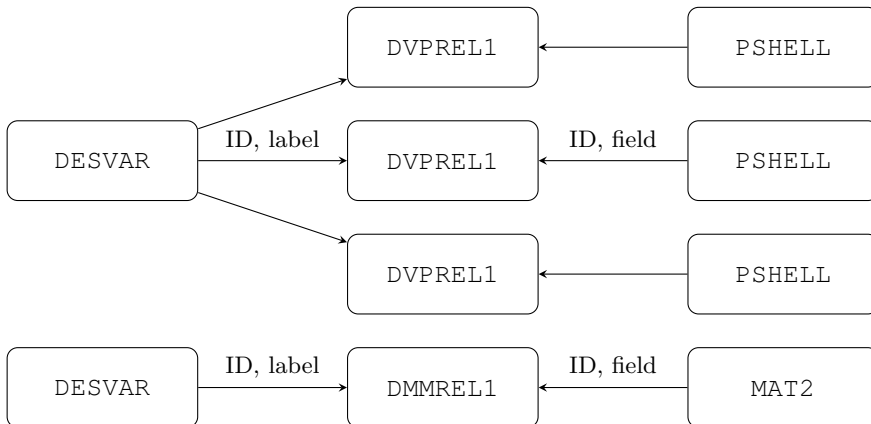


Figure 4.3: Design variable definition in NASTRAN

design field to a single design variable, the corresponding DVPREL1 cards have to address the same DESVAR card, which then simultaneously alters the thickness of all those elements. The unique label on the design variable definition card is composed of the letter T or M , for thickness or material DV respectively, followed by the design variable ID.

With the stiffness properties of a design field being entirely covered by the specification of $\hat{\mathbf{A}}$, $\hat{\mathbf{D}}$, h and a single stiffness matrix being defined by six entries, in total thirteen design variables are required per design field in NASTRAN.

4.3 Response Definition

The consideration of structural responses and sensitivities derived from the finite element model is a key feature, making NASTRAN the appropriate tool for generating the essential input to the stiffness optimization process. Two possibilities exist to specify responses in NASTRAN. The definition of structural responses is accomplished with the specification of DRESP1 cards, while DRESP2 cards are appropriate for the functional combination of structural responses into new ones.

Stress

In section 5.6 there will be a discussion of how strain and buckling responses are derived, knowledge of the element stress responses is sufficient for this purpose. Hence, the first type of response that is asked for with the DRESP1 card is stress. Each shell element that is part of a design field is considered for six different types of stress responses, requiring six DRESP1 cards, each with the response type identifier STRESS.

Table 4.1: *Stress responses per element with DRESP1*

| type | distance | item code |
|-------------|----------|-----------|
| σ_x | z1 | 3 |
| σ_y | z1 | 4 |
| τ_{xy} | z1 | 5 |
| σ_x | z2 | 11 |
| σ_y | z2 | 12 |
| τ_{xy} | z2 | 13 |

As listed in table 4.1, three stresses at the top (z1) and three stresses at the bottom (z2), seen in shell thickness direction, are asked for, along with the NASTRAN specific item code that is required on the DRESP1 card. The identification of the property card to be considered for stress output is achieved by the specification of property card type and ID. It is important to note that NASTRAN per default outputs stresses in the element coordinate system. Only when specifying the parameter “PARAM OMID yes”, will the stress output be provided in the material coordinate system. This is important for the failure and buckling index analysis, discussed in sections 5.6.1 and 5.6.2. Each response is associated with a unique ID and a label, composed of the ID preceded by the letter S .

Weight

The weight response is activated with a DRESP1 card exhibiting the response type identifier `WEIGHT`, a unique ID and a label.

Twist

Aeroelastic responses that can be specified with a DRESP1 card are twist and divergence. Twist simply belongs to the displacement responses that are evoked with the `DISP` keyword, along with the specification of a grid node for which the deformation is to be recovered and the degree of freedom to be monitored. The central grid points belonging to the load reference axis, see section 3.4.3, are a meaningful choice for the points to be monitored. Their displacement is a weighted average of the displacements of all circumferential grid points in the corresponding rib. An important choice has to be made when deciding about the twist to be monitored. NASTRAN allows for the specification of a displacement coordinate system, independently for each grid point, that is also devoted for the response output. As stated in Weisshaar [Wei98], the twist around the global unswept y -axis, rather than the twist around the elastic axis of a swept wing, is responsible for the lift distribution and therefore for the induced drag of the wing. Accordingly, the global coordinate system was chosen as the displacement coordinate system for the nodes belonging to the load reference axis. The twist response is set to be the rotation about the y -axis, see Figure 4.4.

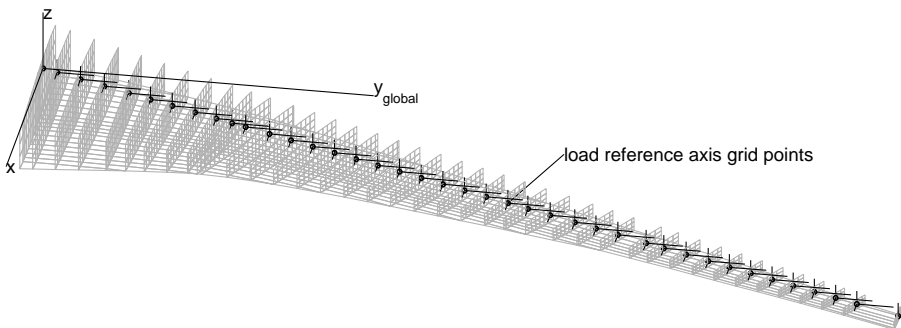


Figure 4.4: *Twist response definition*

Divergence

A divergence response is triggered with the `DIVERG` keyword on the DRESP1 card. It requires the specification of a divergence analysis with the `DIVERG` card, which in turn necessitates an eigenvalue analysis with an `EIGC` card. The eigenvalue analysis requires the specification of number of roots to be calculated, while the divergence analysis only asks for the *Mach* numbers at which the divergence analysis is to be performed. Unfortunately, the divergence analysis in combination with the derivation of responses and sensitivities does not allow for the specification of several, but only one *Mach* number per NASTRAN run. This is a know issue which will hopefully be fixed in a future NASTRAN release.

Aileron Effectiveness

Aileron effectiveness is the only response that is generated with the help of a DRESP2 card, hence a combination of responses originating from two DRESP1 outputs. The computation of aileron effectiveness was laid out in section 2.2.1. The equation is repeated here for ease of reading:

$$\eta_{ail} = -\frac{C_{l_\delta}}{C_{l_p}}. \quad (4.1)$$

NASTRAN can compute responses for C_{l_δ} and C_{l_p} with the keyword STABDER on the DRESP1 card, where for the roll coefficient due to aileron deflection, C_{l_δ} , the corresponding DRESP1 card is linked to the ID of the aileron, defined with an AESURF card. For the computation of the roll coefficient due to rolling, C_{l_p} , the corresponding DRESP1 links to the roll degree of freedom of the entire model, defined with an AESTAT card. Having prepared the two necessary responses with DRESP1, they can be combined on a DRESP2 card by pointing to DEQATN, which simply defines the functional relation according to equation (4.1). Finally, with the help of the DRESP2 entry the response and sensitivity for a quantity that is not directly accessible with a DRESP1 card, like aileron effectiveness, can be obtained, greatly improving the flexibility of the finite element software.

4.4 Finite Element Sensitivity Analysis

Aside from the analysis and the optimization model, the specification of appropriate load cases is indispensable for performing the response and sensitivity derivation with NASTRAN. This section will briefly exemplify the way NASTRAN computes its sensitivities. Details on particular sizing load cases in the optimization will be provided in the appropriate examples in part II of this work.

The design optimization solution sequences is accessed with the executive control statement SOL 200. To attain a halt after the generation of responses and sensitivities, NASTRAN offers a card DSAPRT that controls the design sensitivity output sequence. Setting the parameter END=SENS stops the calculation at the desired point.

Different ways to obtain sensitivities exist, among which, depending on the type of response, NASTRAN applies a direct sensitivity method or an adjoint method, [Moo04]. Both methods start by defining the response as function of the displacement solution \mathbf{u} and the design variable vector \mathbf{x} . The partial differentiation of the response with respect to a design variable x becomes:

$$f = f(\mathbf{u}, \mathbf{x}), \quad (4.2)$$

$$\frac{\partial f}{\partial x} = \frac{\partial f}{\partial \mathbf{u}} \frac{\partial \mathbf{u}}{\partial x}. \quad (4.3)$$

Deriving the static equilibrium equation $\mathbf{K}\mathbf{u} = \mathbf{f}$, e.g. Zienkiewicz et al. [Zie00] – \mathbf{f} denoting the load vector – with respect to a design variable x leads to:

$$\mathbf{K} \frac{\partial \mathbf{u}}{\partial x} = \frac{\partial \mathbf{f}}{\partial x} - \frac{\partial \mathbf{K}}{\partial x} \mathbf{u}, \quad (4.4)$$

where the right hand side is denoted as pseudo load vector \mathbf{f}_{pl} . Solving equation (4.4) for $\frac{\partial \mathbf{u}}{\partial x}$ and replacing in equation (4.3) leads to the adjoint equation for the calculation of the sensitivity with respect to x :

$$\boldsymbol{\lambda}^T = \frac{\partial f}{\partial \mathbf{u}} \mathbf{K}^{-1}, \quad (4.5)$$

$$\frac{\partial f}{\partial x} = \boldsymbol{\lambda}^T \mathbf{f}_{\text{pl}}. \quad (4.6)$$

The direct sensitivity method applies a forward finite difference step to derive the response sensitivity:

$$\frac{\partial f}{\partial x} \approx \frac{f(\mathbf{u} + \Delta \mathbf{u}, \mathbf{x} + \Delta x) - f(\mathbf{u}, \mathbf{x})}{\Delta x}. \quad (4.7)$$

The differential displacement vector $\Delta \mathbf{u}$ is evaluated from the pseudo load equation (4.4), in which the derivative of load vector \mathbf{f} and stiffness matrix \mathbf{K} with respect to the design variable x are calculated with forward (default) or central finite differencing.

4.5 Output Definition

A standard method for accessing NASTRAN results is the consolidation of the standard *f06* output file, where user defined vectors and matrices generated during a NASTRAN run are saved to in ASCII format. However, when facing large models, a large number of design variables or responses, or the combination of both, the output file size grows substantially and importing into another software becomes increasingly tedious and inefficient. Furthermore, not all data can be exported to the standard output. For this reason, NASTRAN provides the possibility to interfere with its internal solution sequence by means of so-called “alters”. The NASTRAN programming language is called DMAP (linguistic family: klingon), Raymond [Ray04], and so are DMAP alters. This language allows for inserting additional commands which amongst others can evoke the export of a matrix during the execution of a NASTRAN solution module. It is up to the user to find the right SUBDMAP module and the right position within the module where to insert the additional DMAP statements that perform the desired action.

Several alters were generated, which will be described in more detail in the following sections. The alters have in common that they export the corresponding vectors, matrices and tables to external files. They will be provided in NASTRAN-specific output formats `op4` and `op2`, where `op4` applies mainly for vectors and matrices, and `op2` in case of tables. Specifications of the output format can be found in [Ray04].

4.5.1 Sensitivities and Responses

For an optimization model consisting of n design variables and m responses, the sensitivity matrix comprises $n * m$ elements. With characteristic quantities of 80 design fields and 10,000 responses this amounts to $80 * 13 * 10,000 = 10.4\text{e}6$ entries. No doubt, an efficient method for importing the responses and sensitivities can help to speed up the process of generating the required optimizer input.

This is accomplished by exporting the design sensitivity matrix `DSCM2` and the response vectors `R1VALRG` and `R2VALRG`, as evoked with the `DRESP1` and `DRESP2` cards. The alter commands required in the NASTRAN file management section and the executive control section are listed in appendix A.1. The module to which the required code modifications are added is called `EXITOPT`. Both, matrix and vectors are exported in binary `op4` format, the reason being a substantial reduction in file size for large sensitivity matrices and a considerable reduction of the time required to import in subsequent routines.

Along with the sensitivity matrix `DSCM2`, the alter exports a table called `DSCMCOL`, which provides a list that correlates each response to the corresponding column in the sensitivity matrix. This information is of utmost importance when it comes to optimizations with different response types and multiple load cases. The table is written in binary `op2` format and a detailed description of its content is given in [Moo04]. Basically, `DRESP1` responses are sorted first by load case, inside a load case by response type (weight, stress, twist and so on) and inside response type by the response identification number (ID). `DRESP2` responses are added to the end and sorted by response ID.

4.5.2 Aerodynamics

This alter is threefold, performing the export of the trim variables, the DLM box displacements and forces, and the export of the aerodynamic forces at the splining points. The reason for gathering the above into one alter is simply the fact that all corresponding matrices are generated in the module `AESTATRS`, which is why the required export commands can be combined into one compile statement. The alter is listed in appendix A.2.

DLM Forces at Grid Points

The extraction of aerodynamic loads calculated with the NASTRAN doublet lattice method in a static aeroelastic analysis is an essential premise to perform a correction of low-fidelity DLM with higher order CFD, as will be described in chapter 6. Moreover, visualizing the aerodynamic forces at the splining points greatly facilitates the quality assessment of the selected splining method and splining points.

The alter generates and exports three different load sets for each static aeroelastic analysis performed in a NASTRAN run. The first set `PRG` corresponds to the aerodynamic loads generated by DLM and splined to the structure coupling points for a virtually rigid structure, hence without the influence of flexibility on the aerodynamic loads. The second set `PRGPERG` corresponds to the first set plus the altered loads as they arise from the wing flexibility. This set correlates to the real aerodynamic loads as they are experienced by the flexible structure. The third set, `AIPG`, combines all loads acting on the grid points, flexible aerodynamic loads plus inertial loads. Despite that for the first two sets only the grid points belonging to the coupling points will have non-zero loads, the alter exports matrices in dimensions corresponding to all grid points.

DLM Forces at Box Centers

Other than the previous load sets, the matrices exported with this part of the alter refer to the pure aerodynamic forces and displacements of the doublet lattice model, rather than forces splined to the structure. It will provide values for each aerodynamic box. The vector UKTOTAL contains values of the z-displacement and local angle of incidence change for each DLM box, which are the sole degrees of freedom. The vector FFAJ comprises the absolute pressure difference. Results are provided for each static aeroelastic analysis during the NASTRAN run.

Trim Variables

The trim variable vector contains all free and fixed aerodynamic degrees of freedom, like angle of attack, z-axis acceleration, roll acceleration and aileron deflections, and is called UX in the corresponding module. It is provided for each static aeroelastic analysis performed in a NASTRAN run. Again, the data that are essential in association with the CFD correction process, are described in chapter 6.

4.5.3 Displacements

This alter, listed in appendix A.3, exports the deformation vectors for all grid points and all trim load cases. It serves for result visualization, but more importantly, again as an input to the CFD correction process. The corresponding module is called SEDRCVR and the vector UG.

4.5.4 Correcting Alters

During development of the optimization process, going along with an increase in functionality by broadening for example the response type range or the allowance for multiple but dissimilar load case types, some NASTRAN errors arose, which could partly be solved with two additional correcting alters. The first alter, listed in appendix A.4.1, corrects an error in the DSCM2 sensitivity matrix sequence. It is crucial for the correlation of the DSCMCOL table, which is supposed to provide the column order within DSCM2, and the DSCM2 itself. The second alter, listed in appendix A.4.2, is required when mixing different boundary conditions in multiple load cases.

No solution could be found for example for the response and sensitivity calculation of several divergence *Mach* numbers within a single NASTRAN run. For this reason, the application is limited to a single divergence response per NASTRAN run; considering more than one *Mach* number will require a separate NASTRAN execution for each of them.

4.6 Summary

This concludes the description of the optimization model, consisting mainly of the definition of design fields, specification of design variables and responses, and the preparation of suitable data export routines. Once the responses and sensitivities are prepared, the assembly of the approximation model can be arranged, as discussed in chapter 5.

CHAPTER 5

Response Approximation Formulation

“That’s the secret to life... replace one worry with another.”

Charles M. Schulz

The application of a gradient based optimization method for the stiffness optimization is motivated by the fact that evaluating responses using subsequent analysis runs is very time consuming, and also does not yield an indication of how to alter the design variables in the search for an optimum of the objective function that meets all constraints. For this reason, replacing the analysis model with one that approximates the behavior of the real responses as function of the design variables can significantly reduce computational costs.

The design variables for the stiffness optimization consist of the thickness normalized membrane and bending stiffness matrices, $\hat{\mathbf{A}}$ and $\hat{\mathbf{D}}$, along with the laminate thickness h . Having derived, see chapter 4, the information on how much each response changes as a function of those design variables, there is sufficient information to construct a linear approximation model about the design point. After a brief introduction to approximation techniques in section 5.1, an improved approximation formulation, tailored for the application in a stiffness optimization is described in section 5.2.

The sensitivity matrix supplied by NASTRAN requires reordering and initializing steps to transform it into a suitable configuration for the approximation derivation; these steps are explained in section 5.3. The beneficial contribution of reciprocal parts in an approximation, introduced in section 5.2, is limited by the requirement of its convexity. A method to maximize the reciprocal contribution to an approximation is presented in section 5.4, and the setup of the structural and aeroelastic approximations used in this research are described in sections 5.6 and 5.7, respectively.

5.1 Approximation Methods in Structural Optimization

A structural optimization problem can generally be described as a search for the global minimum of an objective function $f_0(\mathbf{x})$ while complying with the constraints

$f_i(\mathbf{x})$. In equation (5.1) $n = 1 \dots i$ denotes the number of responses, and $m = 1 \dots j$ the number of design variables with a lower x_j^L and an upper limit x_j^U :

$$\begin{aligned} \min f_0(\mathbf{x}) , \\ f_i(\mathbf{x}) \leq f_i|_{max} , \\ x_j^L \leq x_j \leq x_j^U . \end{aligned} \quad (5.1)$$

Since the functional relation of objective and constraints with respect to the design variables \mathbf{x} is typically not known explicitly, numerical schemes are applied in the search for the optimal solution to equation (5.1).

Among those schemes, approximation methods are widely used in structural optimization problems. They can be grouped into problem and function approximation problems, where the latter deal with an approximation of the responses involved in the optimization problem, [IJs11]. The approximation type used in this research corresponds to locally applicable function approximations. Local in this respect identifies the validity of the approximation in the vicinity of the current design point, in contrast to globally applicable function approximations, such as response surface methods. The local function approximation generates an optimization subproblem of the form:

$$\begin{aligned} \min \tilde{f}_0(\mathbf{x}) , \\ \tilde{f}_i(\mathbf{x}) \leq f_i|_{max} , \\ x_j^L \leq x_j \leq x_j^U , \end{aligned} \quad (5.2)$$

where the tilde-superscript denotes an approximation. Solving the optimization problem (5.2) results in new design variables and hence a new design point. According to equation (5.3) the optimization is stopped when the change of the objective function f_0 in subsequent, feasible iterations (l) drops below a specified threshold δ_{stop} :

$$\left| \frac{\tilde{f}_0|_{(l+1)} - \tilde{f}_0|_{(l)}}{\tilde{f}_0|_{(l)}} \right| \leq \delta_{stop} . \quad (5.3)$$

If the convergence criterion is not met, an approximation model is generated at the new design point. The process is repeated till convergence of the objective function is reached. General information on the application of approximations in optimization can be found in Haftka et al. [Haf92].

5.2 General Approximation Form

The most common type of a local approximation is a *Taylor* series expansion of the response function about the approximation point \mathbf{x}_0 . Due to the computational costs for the evaluation of higher order terms, the series is usually expanded only up to the linear part, resulting in an error of order Δx^2 :

$$\tilde{f} = f(\mathbf{x}_0) + \sum_{j=1}^N \frac{\partial f}{\partial x_j} \Big|_0 (x_j - x_{0j}) + O(\Delta x^2) . \quad (5.4)$$

Two modifications to the *Taylor* expansion in equation (5.4) are implemented to obtain the general approximation form, introduced in section 2.1.4. One modification is to adapt the design variables employed in this work, namely stiffness matrices $\hat{\mathbf{A}}$ and $\hat{\mathbf{D}}$, as well as the thickness h . The second modification is to use, aside from the regular linear approximation, reciprocal contributions in terms of the stiffness matrices. The equation is repeated here for the sake of continuity:

$$\tilde{f} = \sum_{j=1}^N \left(\hat{\Psi}_j^m \Big|_0 : \hat{\mathbf{A}}_j + \hat{\Psi}_j^b \Big|_0 : \hat{\mathbf{D}}_j + \Phi_j^m \Big|_0 : \mathbf{A}_j^{-1} + \Phi_j^b \Big|_0 : \mathbf{D}_j^{-1} + \alpha_j \Big|_0 h_j \right) + C_0 . \quad (5.5)$$

Equation (5.5), a detailed derivation of which is described in [IJs11], constitutes the most general approximation form. The linear and reciprocal sensitivities with respect to membrane and bending stiffness are abbreviated as follows:

$$\Psi^m = \frac{\partial f}{\partial \mathbf{A}} , \quad (5.6)$$

$$\Psi^b = \frac{\partial f}{\partial \mathbf{D}} , \quad (5.7)$$

$$\Phi^m = \frac{\partial f}{\partial \mathbf{A}^{-1}} , \quad (5.8)$$

$$\Phi^b = \frac{\partial f}{\partial \mathbf{D}^{-1}} , \quad (5.9)$$

$$\alpha = \frac{\partial f}{\partial h} . \quad (5.10)$$

To increase approximation accuracy, a combination of linear and reciprocal expansion with respect to the stiffness matrices is applied, however, an approximation will not necessarily have contributions from all parts at once, but only the ones that presumably yield the most accurate reflection of the real response.

In equation (5.5) N is the number of design fields featuring independent structural properties, and C_0 is a constant, depending on the design point. When preparing approximations for the optimization routine, C_0 does not have to be considered since the optimizer can compute it based on the response value at the design point. The “:” matrix operation, known as matrix contraction, corresponds to a regular matrix multiplication and subsequent summation of the diagonal elements; albeit the equation is set up with thickness normalized laminate sensitivities in the linear approximations, sensitivity matrices (Ψ , Φ) are supplied to the optimizer in terms of the regular stiffness matrices.

The most prominent characteristics of the general approximation in equation (5.5) are convexity, separability and conservativeness, each of which will be discussed below.

Convexity of the approximation must be ensured by the choice of sensitivities contributing to it. Convexity is essential for the existence of a global optimum in the approximated model. While linear contributions are convex per definition, convexity of the reciprocal part is not necessarily the case. One possible way of dealing with non-convex approximations will be discussed in section 5.4.

Separability of the design variables is inherent in the formulation of the approximation, meaning that the response function is constructed only from linear combinations

of linear and reciprocal design variables. Separability allows for an independent consideration of each design variable set j in equation (5.5) and thus an efficient, parallel processing objective minimization.

Conservativeness ensures that the approximated response is always larger than the real response at the new design optimum of the approximation model. Conservativeness is taken care of within the optimization algorithm.

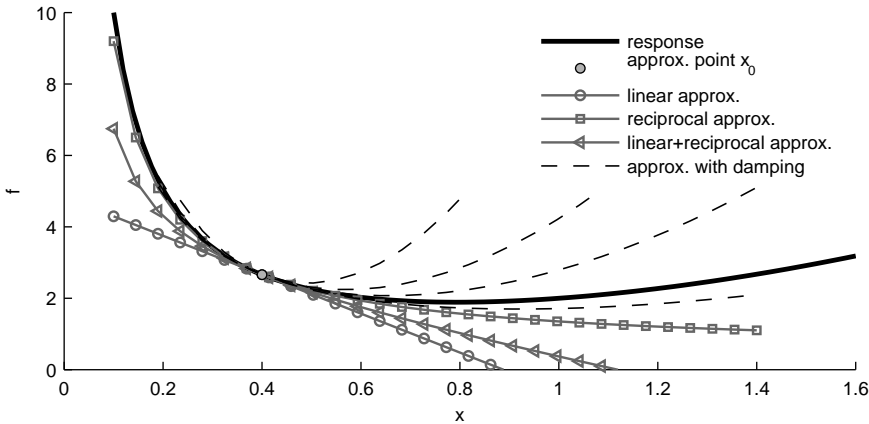


Figure 5.1: *Function approximation*

The approximation characteristics can be illustrated by means of a one-dimensional function as shown in Figure 5.1, where x is a (design) variable and f is a (response) function of x . The linear, reciprocal, and linear+reciprocal approximations are shown and compared to the real function value f . All three approximations are either convex or indetermined, but not concave. This will guarantee the existence of a minimum. The approximations not being conservative is indicated by the fact that the function values are always smaller than the real one. Therefore, a damping term is added to increase conservativeness; indicated by the dashed lines in Figure 5.1. The more damping that is added, the closer the approximation minimum shifts towards the approximation point and more iteration steps are necessary to reach the optimum. The optimizer applied in this work is able to adapt the degree of conservativeness throughout the iterations for each response by varying the amount of damping. While the damping term is not considered in equation (5.5), the reader is referred to [IJs11] for further details.

Since a reciprocal approximation is not necessarily convex, but since convexity is a necessity for the existence of a global optimum within the approximation model, reciprocal terms can not be applied in general. Depending on the type of response to be approximated, physical insight is required when setting up the approximation. If convexity of the reciprocal term can not be guaranteed, a convexification process as described in section 5.4 can be applied. In the following section 5.3 details of some necessary NASTRAN sensitivity preprocessing steps required for the approximation setup will be given.

5.3 Sensitivity Processing

The stiffness modeling with thickness normalized stiffness matrices $\hat{\mathbf{A}}$ and $\hat{\mathbf{D}}$ by means of MAT2 cards was discussed in section 3.2, the specification of each element of $\hat{\mathbf{A}}$ and $\hat{\mathbf{D}}$, and h as design variables was shown in section 4.2. Requiring six design variables for the definition of a stiffness matrix and one for the thickness results in thirteen DV per design field. Hence, the number of rows in the exported NASTRAN DSCM2 design sensitivity matrix amounts to thirteen times the number of considered design fields. The number of columns in the sensitivity matrix corresponds to the number of responses requested with DRESP1 and DRESP2 cards, compare section 4.3.

The first step when generating response approximations consists of grouping the sensitivities into matrices corresponding to the layout of the stiffness matrices. This is done for every response f in the sensitivity matrix, according to equation (5.11):

$$\frac{\partial f}{\partial \hat{\mathbf{A}}} = \begin{bmatrix} \frac{\partial f}{\partial \hat{A}_{11}} & \frac{\partial f}{\partial \hat{A}_{12}} & \frac{\partial f}{\partial \hat{A}_{13}} \\ \frac{\partial f}{\partial \hat{A}_{21}} & \frac{\partial f}{\partial \hat{A}_{22}} & \frac{\partial f}{\partial \hat{A}_{23}} \\ \frac{\partial f}{\partial \hat{A}_{31}} & \frac{\partial f}{\partial \hat{A}_{32}} & \frac{\partial f}{\partial \hat{A}_{33}} \end{bmatrix}, \quad \frac{\partial f}{\partial \hat{\mathbf{D}}} = \begin{bmatrix} \frac{\partial f}{\partial \hat{D}_{11}} & \frac{\partial f}{\partial \hat{D}_{12}} & \frac{\partial f}{\partial \hat{D}_{13}} \\ \frac{\partial f}{\partial \hat{D}_{21}} & \frac{\partial f}{\partial \hat{D}_{22}} & \frac{\partial f}{\partial \hat{D}_{23}} \\ \frac{\partial f}{\partial \hat{D}_{31}} & \frac{\partial f}{\partial \hat{D}_{32}} & \frac{\partial f}{\partial \hat{D}_{33}} \end{bmatrix}. \quad (5.11)$$

The design variables in NASTRAN are thickness normalized stiffness matrix elements and need to be transformed from normalized to absolute stiffnesses before generating approximations, $(\hat{\mathbf{A}}, \hat{\mathbf{D}}, \hat{h}) \rightarrow (\mathbf{A}, \mathbf{D}, h)$, where $\hat{h} = h$. For a response f , NASTRAN sensitivities based on $(\hat{\mathbf{A}}, \hat{\mathbf{D}}, \hat{h})$ have to be rewritten according to the dependencies given in equations (1.27):

$$\frac{\partial f}{\partial \mathbf{A}} = \frac{\partial f}{\partial \hat{\mathbf{A}}} \frac{1}{\hat{h}}, \quad (5.12)$$

$$\frac{\partial f}{\partial \mathbf{D}} = \frac{\partial f}{\partial \hat{\mathbf{D}}} \hat{h}^3, \quad (5.13)$$

$$\frac{\partial f}{\partial \mathbf{h}} = \frac{\partial f}{\partial \hat{\mathbf{A}}} \left(-\frac{1}{\hat{h}^2}\right) : \mathbf{A} + \frac{\partial f}{\partial \hat{\mathbf{D}}} \left(-\frac{36}{\hat{h}^4}\right) : \mathbf{D} + \frac{\partial f}{\partial \hat{h}}. \quad (5.14)$$

The general response approximation embeds linear and reciprocal sensitivities, see section 5.2, and accordingly requires the following conversion:

$$\frac{\partial f}{\partial \mathbf{A}^{-1}} = \Phi^m = -\mathbf{A}^T \Psi^m \mathbf{A}, \quad (5.15)$$

$$\frac{\partial f}{\partial \mathbf{D}^{-1}} = \Phi^b = -\mathbf{D}^T \Psi^b \mathbf{D}. \quad (5.16)$$

5.4 Sensitivity Convexification

Due to missing knowledge with respect to approximation convexity, physical insight into the response to approximate does not always allow for a selective application of a reciprocal approximation. For these particular responses, the necessity for the approximation to be convex to exhibit a global minimum on optimization level can either be dealt with by omitting the reciprocal approximation contribution in case of uncertainty, or by trying to convexify the reciprocal part. A method how to do so will be presented below.

The derivation of the convexification process is demonstrated here for the membrane stiffness sensitivity, while the method can also be used to convexify the bending stiffness contribution in the approximation. The reciprocal membrane stiffness contribution, equation (5.15), to the approximation is:

$$f = \Phi^m : \mathbf{A}^{-1} . \quad (5.17)$$

The first variation with respect to the membrane stiffness:

$$\delta f = -\text{trace} \left(\Phi^m \mathbf{A}^{-1} \delta \mathbf{A} \mathbf{A}^{-1} \right) , \quad (5.18)$$

can be rewritten to:

$$\delta f = -\text{trace} \left(\tilde{\Phi}^m \delta \tilde{\mathbf{A}} \right) , \quad (5.19)$$

where:

$$\tilde{\Phi}^m = \mathbf{A}^{-1/2} \Phi^m \mathbf{A}^{-1/2} , \quad (5.20)$$

$$\delta \tilde{\mathbf{A}} = \mathbf{A}^{-1/2} \delta \mathbf{A} \mathbf{A}^{-1/2} . \quad (5.21)$$

Accordingly, the second variation with respect to \mathbf{A} becomes:

$$\delta^2 f = 2 \text{trace} \left(\delta \tilde{\mathbf{A}} \tilde{\Phi}^m \delta \tilde{\mathbf{A}} \right) . \quad (5.22)$$

Rewriting equation (5.22) using (5.15) and (5.20) along with the *Cholesky* decomposition of \mathbf{A} :

$$\mathbf{A} = \mathbf{L}\mathbf{L}^T , \quad (5.23)$$

yields:

$$\delta^2 f = 2 \text{trace} \left(\delta \tilde{\mathbf{A}} (-\mathbf{L}^T \Psi^m \mathbf{L}) \delta \tilde{\mathbf{A}} \right) , \quad (5.24)$$

so that $\tilde{\Phi}^m$ inside the trace can also be expressed as:

$$\tilde{\Phi}^m = -\mathbf{L}^T \Psi^m \mathbf{L} . \quad (5.25)$$

In order for the second variation always to be ≥ 0 , constituting convexity of f with respect to \mathbf{A}^{-1} , $\tilde{\Phi}^m$ must be at least positive semidefinite.

Definiteness can be checked by investigating the eigenvalues of $\tilde{\Phi}^m$. Writing the eigenvalues in a diagonal matrix $\tilde{\mathbf{D}}$ and the corresponding eigenvectors in a matrix \mathbf{T} , allows for a representation of $\tilde{\Phi}^m$ as:

$$\tilde{\Phi}^m = \mathbf{T} \tilde{\mathbf{D}} \mathbf{T}^T . \quad (5.26)$$

$\tilde{\Phi}^m$ is at least positive semidefinite if its eigenvalues are greater or equal to zero. Hence, convexification aims at increasing negative eigenvalues to be at least ≥ 0 , while maintaining the modal basis \mathbf{T} :

$$\Phi^{+m} = \mathbf{T} \mathbf{D}^+ \mathbf{T}^T . \quad (5.27)$$

The task can be expressed as a minimization problem, where the difference between initial and modified eigenvalues is minimized, while constraining the modified eigenvalues to be ≥ 0 and the trace of initial and modified Φ to be the same, corresponding to the sum of the eigenvalues:

$$\begin{aligned} \min \|d^+ - \tilde{d}\|_2 &= \frac{1}{2} \left[(d_1^+ - \tilde{d}_1)^2 + (d_2^+ - \tilde{d}_2)^2 + (d_3^+ - \tilde{d}_3)^2 \right], \\ d_1^+ &\geq 0, \\ d_2^+ &\geq 0, \\ d_3^+ &\geq 0, \\ d_1^+ + d_2^+ + d_3^+ &= \tilde{d}_1 + \tilde{d}_2 + \tilde{d}_3. \end{aligned} \quad (5.28)$$

Introducing the substitutions:

$$x_1 = \tilde{d}_1 - d_1^+, \quad x_2 = \tilde{d}_2 - d_2^+, \quad x_3 = \tilde{d}_3 - d_3^+, \quad (5.29)$$

the problem simplifies to:

$$\begin{aligned} \min & \frac{1}{2} (x_1^2 + x_2^2 + x_3^2), \\ & x_1 \leq \tilde{d}_1, \\ & x_2 \leq \tilde{d}_2, \\ & x_3 \leq \tilde{d}_3, \\ & x_1 + x_2 + x_3 = 0. \end{aligned} \quad (5.30)$$

The *Lagrange* equation:

$$\begin{aligned} \mathcal{L} = \frac{1}{2} (x_1^2 + x_2^2 + x_3^2) + \lambda_1 (x_1 - \tilde{d}_1) + \lambda_2 (x_2 - \tilde{d}_2) + \lambda_3 (x_3 - \tilde{d}_3) \\ + \mu (x_1 + x_2 + x_3), \end{aligned} \quad (5.31)$$

leads to minima of the objective function for the three different cases with one, two, or three active constraints.

Case 1: $\lambda_1 \neq 0$, $\lambda_2 = \lambda_3 = 0$

This is the case, if $\tilde{d}_1 < 0$, while the other eigenvalues are at least zero or positive. The active *Lagrange* multiplier becomes $\lambda_1 = -3/2\tilde{d}_1$, while the modified eigenvalues can be computed to:

$$\begin{aligned} d_1^+ &= 0, \\ d_2^+ &= \tilde{d}_2 + \frac{1}{2}\tilde{d}_1, \\ d_3^+ &= \tilde{d}_3 + \frac{1}{2}\tilde{d}_1. \end{aligned} \quad (5.32)$$

All three new eigenvalues are ≥ 0 and thus fulfill the inequality constraints. The sum of all eigenvalues corresponds to the sum of the initial eigenvalues, as is required by the equality constraint.

Case 2: $\lambda_1, \lambda_2 \neq 0, \lambda_3 = 0$

When the first two eigenvalues \tilde{d}_1 and \tilde{d}_2 are negative, the present case applies. The *Lagrange* multiplier become $\lambda_1 = -2\tilde{d}_1 - \tilde{d}_2$ and $\lambda_2 = -\tilde{d}_1 - 2\tilde{d}_2$, and the modified eigenvalues are:

$$\begin{aligned} d_1^+ &= 0, \\ d_2^+ &= 0, \\ d_3^+ &= \tilde{d}_1 + \tilde{d}_2 + \tilde{d}_3. \end{aligned} \quad (5.33)$$

Case 3: $\lambda_1, \lambda_2, \lambda_3 \neq 0$

All three eigenvalues of $\tilde{\Phi}^m$ are negative. Accordingly, no convex part exists and only a linear approximation can be applied.

With the optimized eigenvalues d_1^+ to d_3^+ :

$$\mathbf{D}^+ = \begin{bmatrix} d_1^+ & 0 & 0 \\ 0 & d_2^+ & 0 \\ 0 & 0 & d_3^+ \end{bmatrix}, \quad (5.34)$$

the convexified Φ^{+m} can be calculated using equation (5.27).

The remaining sensitivity contribution follows from the difference of initial and optimized positive eigenvalues. The difference of initial, equation (5.26), and optimized positive eigenvalues, equation (5.27), results in the non-convex contribution Φ^{-m} :

$$\mathbf{D}^- = \tilde{\mathbf{D}} - \mathbf{D}^+, \quad (5.35)$$

$$\Phi^{-m} = \mathbf{T}\mathbf{D}^-\mathbf{T}^T. \quad (5.36)$$

The derivation of the final convexified reciprocal sensitivity $\Phi^m|_{conv}$ from Φ^{+m} and the linear sensitivity $\Psi^m|_{conv}$ from Φ^{-m} based on equation (5.23) and (5.25) yields:

$$\Phi^m|_{conv} = \mathbf{L}\Phi^{+m}\mathbf{L}^T, \quad (5.37)$$

$$\Psi^m|_{conv} = -(\mathbf{L}^T)^{-1}\Phi^{-m}\mathbf{L}^{-1}. \quad (5.38)$$

In case no convex part can be separated, the convexified linear sensitivity from equation (5.38) will be identical to the initial linear sensitivity $\Psi^m|_{conv} = \Psi^m$ that formed the basis for the convexification; $\Phi^m|_{conv}$ will then be zero.

5.5 Sensitivity Convexification Sample

The influence of response convexification can plausibly be demonstrated using a twist approximation as applied in the stiffness optimization of a wind-tunnel model. The finite element model is shown in Figure 5.2. In the optimization, the twist at the wing tip had to be constrained in both directions, $\Delta\vartheta_{min}|_{tip} \leq \Delta\vartheta|_{tip} \leq \Delta\vartheta_{max}|_{tip}$. The last spanwise point of the load reference axis was chosen as the monitoring point and the twist sensitivities Ψ with respect to all design field stiffnesses were computed

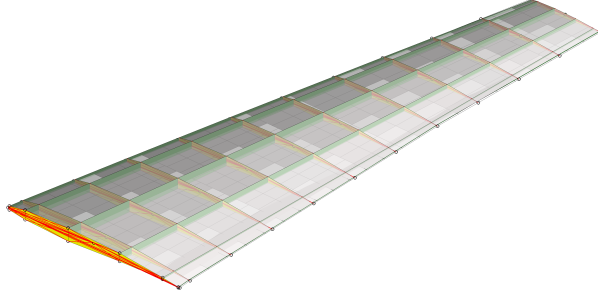


Figure 5.2: *FEM of a wind-tunnel model*

with NASTRAN. Since the optimizer can only handle upper limit constraints, the lower limit constraint $\Delta\vartheta|_{tip} \geq \Delta\vartheta_{min}|_{tip}$ had to be reversed by multiplying it with -1 in order to turn it into an upper limit constraint:

$$-\Delta\vartheta|_{tip} \leq -\Delta\vartheta_{min}|_{tip}, \quad (5.39)$$

$$\Delta\vartheta|_{tip} \leq \Delta\vartheta_{max}|_{tip}. \quad (5.40)$$

The most general form of the twist approximation is anticipated in equation (5.41) and will recur in section 5.7.2:

$$\tilde{\vartheta} = \sum_j \Psi_j^m : \mathbf{A}_j + \Psi_j^b : \mathbf{D}_j + \Phi_j^m : \mathbf{A}_j^{-1} + \Phi_j^b : \mathbf{D}_j^{-1} + \alpha_j h_j. \quad (5.41)$$

The convexification of Φ as resulting from equation (5.15) and (5.16) using the process described in section 5.4, has to take into account the different signs required for the approximation of lower and upper twist constraints, equation (5.39) and (5.40). This is important, since using the same convexified sensitivities of the upper limit also for the lower limit would result in a concave approximations due to the change in sign.

The considerable difference in the convexified approximation behavior of the upper and lower limit twist response is illustrated in Figure 5.3. To investigate the approximation behavior, the membrane stiffness in all design fields was altered by:

$$\mathbf{A}_{new} = \mathbf{A} + p \begin{bmatrix} A_{11} & 0 & 0 \\ 0 & -A_{11} & 0 \\ 0 & 0 & 0 \end{bmatrix}, \quad (5.42)$$

where p was varied between 0.65 ... 1.35, emulating a change in lamination parameter $V_{1\mathbf{A}}$ and thus a variation in stiffness in the material axis direction. According to equation (1.26) and (1.30) on page 11 a variation in $V_{1\mathbf{A}}$ leads to a similar change in matrix elements (1, 1) and (2, 2), only opposite in sign. The development of the real twist response, set to zero for the initial stiffness, along with the approximations in the design point of initial stiffness with $p = 1.0$ are depicted in Figure 5.3. Despite approximating the same response, the convexified upper limit response approximation contains, almost exclusively, linear contributions, while the convexified lower limit response approximation is dominated by reciprocal parts. It should be mentioned that,

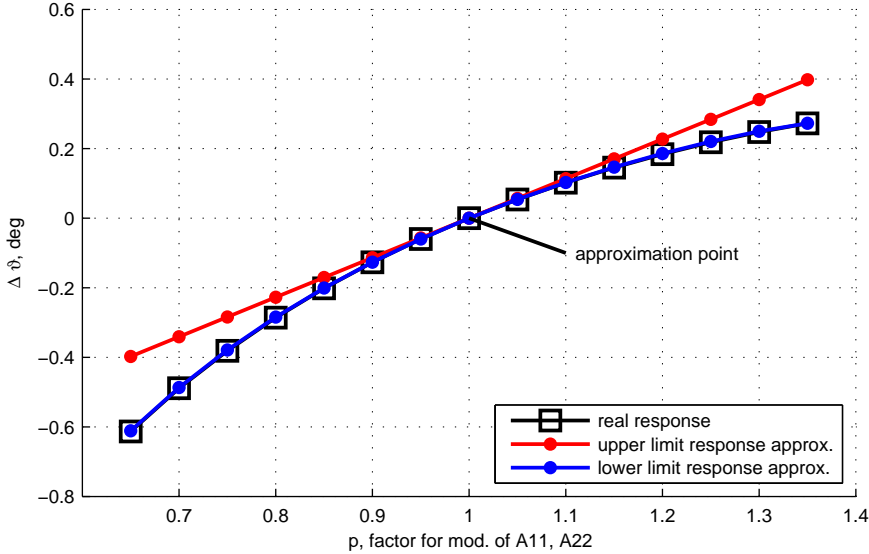


Figure 5.3: *Real response and convexified response approximations*

in spite of the linear appearance of the upper limit approximation, few design fields also add reciprocal contributions, while the lower limit approximation also contains few linear portions. Finally, this result in general also exemplifies the possible benefit of reciprocal approximations. The lower limit approximation almost exactly follows the behavior of the real response for the entire range of investigated stiffnesses.

5.6 Structural Responses

The approximations of the classical structural responses that are essential in a regular structural sizing optimization of a wing are described in the following sections. The approximations consist of a strength and buckling failure response, sections 5.6.1 and 5.6.2, and the approximation for mass of the structural components that are part of the optimization model, section 5.6.3. Strain and buckling are investigated for each shell element that is part of the optimization model and each sizing load case, while mass is a global property of the finite element model and therefore requires only a single response approximation.

Before elaborating the details of the structural response approximations, an approximation mutually used by the strength and buckling response needs to be discussed. The approximations of the stress resultants N_x , N_y , N_{xy} do not appear as independent responses in the optimization and are therefore derived below.

As explained in section 4.3, NASTRAN allows for the definition of stress responses at the upper and lower end of a laminate per shell element, σ^u and σ^l . The membrane stress resultants in element i therefore become:

$$N_i = \frac{1}{2} \hat{h}_i (\sigma_i^u + \sigma_i^l), \quad (5.43)$$

noting that, to simplify readability, equation (5.43) and following equations given in this section apply to all three stress components x , y and xy separately.

Since NASTRAN generates sensitivities with respect to thickness normalized stiffness matrices and thickness $\hat{\mathbf{A}}$, $\hat{\mathbf{D}}$, \hat{h} ($\partial\sigma/\partial\hat{\mathbf{A}}$, $\partial\sigma/\partial\hat{\mathbf{D}}$, $\partial\sigma/\partial\hat{h}$), equation (5.43) can be derived with respect to these to obtain the stress resultant sensitivities:

$$\frac{\partial N_i}{\partial \hat{\mathbf{A}}_j} = \frac{1}{2} \hat{h}_i \left(\frac{\partial \sigma_i^u}{\partial \hat{\mathbf{A}}_j} + \frac{\partial \sigma_i^l}{\partial \hat{\mathbf{A}}_j} \right), \quad (5.44)$$

$$\frac{\partial N_i}{\partial \hat{\mathbf{D}}_j} = \frac{1}{2} \hat{h}_i \left(\frac{\partial \sigma_i^u}{\partial \hat{\mathbf{D}}_j} + \frac{\partial \sigma_i^l}{\partial \hat{\mathbf{D}}_j} \right), \quad (5.45)$$

$$\frac{\partial N_i}{\partial \hat{h}_j} = \frac{1}{2} \hat{h}_i \left(\frac{\partial \sigma_i^u}{\partial \hat{h}_j} + \frac{\partial \sigma_i^l}{\partial \hat{h}_j} \right) + \frac{1}{2} (\sigma_i^u + \sigma_i^l) \delta_{ij}. \quad (5.46)$$

where j denotes the independent stiffness properties of each design field.

In order to take account for the change in stress resultant in element i as a result of a stiffness change in design field j , an approximation of the stress resultant change is introduced:

$$\Delta N_i = \sum_j \frac{\partial N_i}{\partial \mathbf{A}_j} : \mathbf{A}_j + \frac{\partial N_i}{\partial \mathbf{D}_j} : \mathbf{D}_j + \frac{\partial N_i}{\partial h_j} h_j. \quad (5.47)$$

The sensitivities shown in equations (5.47) are derived from equation (5.44) to (5.46), taking into account the general transformations depicted in equations (5.12) to (5.14).

Varying stress resultants in element i as a result of stiffness changes in design field j are mainly evoked by two mechanisms, one, load redistribution resulting from a statically indeterminate system, and two, indirectly via a change in the applied loads. In the context of this research, the influence of varying aeroelastic loads as a result of stiffness changes and consequently in the aerodynamic shape, are an important contribution to the assessment of meaningful sensitivities with NASTRAN.

5.6.1 Strength

The absence of a well-defined laminate stacking sequence does not allow for the application of classical strength failure criteria like fiber, shear or interlaminar failure, nor for use of theories describing the failure mechanics, like *Tsai-Wu* and *Puck*. For that reason, a new failure criterion, tailored for the application in stiffness optimizations was developed by IJsselmuiden et al. [IJs08], [IJs11]. It is based on the *Tsai-Wu* first-ply failure criterion as described for example in Daniel et al. [Dan94]. The approach consists of the construction of a convex failure envelope that accounts for the possible existence of all fiber angles; the analytic expressions defining the inner contour of the envelope that describes the allowable maximum strain vector are derived. The envelope description only depends on the strain allowables of the material to be used in the optimization and therefore, other than that, do not require knowledge about the stiffness matrices to be investigated. Since the failure envelope accounts for the occurrence of all possible fiber angles in the laminate, it describes a conservative boundary.

The stress strain relationship in a laminate with membrane stiffness \mathbf{A} and stress resultant \mathbf{N} is given by:

$$\boldsymbol{\varepsilon} = \begin{Bmatrix} \varepsilon_x \\ \varepsilon_y \\ \gamma_{xy} \end{Bmatrix} = \mathbf{A}^{-1}\mathbf{N}, \quad (5.48)$$

and as such is used in the computation of a failure index r that expresses the fraction of the actual strain vector relative to the vector extended onto the failure envelope. Failure indices $r \leq 1$ therefore denote the structurally feasible region, while $r > 1$ indicates strain failure. The derivation is illustrated in more detail in Khani et al. [Kha11]. The failure index can be expressed as:

$$r = \mathbf{N}^T \mathbf{A}^{-1} \mathbf{g}, \quad (5.49)$$

where \mathbf{g} describes the gradient of the failure index with respect to the strain vector $\mathbf{g} = \partial r / \partial \boldsymbol{\varepsilon}$.

Equation (5.49) indicates that a reciprocal approximation with respect to the membrane stiffness of the panel under consideration is preferable, along with a linear approximation in the stress resultant, $r_i(\mathbf{A}_i^{-1}, \mathbf{N}_i)$. The approximation then becomes:

$$\tilde{r}_i = \frac{\partial r_i}{\partial \mathbf{A}_i^{-1}} : \mathbf{A}_i^{-1} + \frac{\partial r_i}{\partial \mathbf{N}_i} \Delta \mathbf{N}_i. \quad (5.50)$$

The first term represents local stiffness changes, while the change in stress resultant in element i , $\Delta \mathbf{N}_i$, is approximated according to equation (5.47) and therefore adds a globally dependent term to the overall approximation.

Khani et al. [Kha11] state that $\Phi_i^m = \partial r_i / \partial \mathbf{A}_i^{-1}$ is not positive definite in general. A linear local approximation is added, replacing the non-definite part in Φ_i^m , so that the approximation finally can be written as:

$$\tilde{r}_i = \Phi_i^m : \mathbf{A}_i^{-1} + \Psi_i^m : \mathbf{A}_i + \mathbf{s}_i^t \Delta \mathbf{N}_i, \quad (5.51)$$

where $\mathbf{s}_i = \partial r_i / \partial \mathbf{N}_i$. Response and local sensitivities of r_i with respect to \mathbf{A}_i^{-1} , \mathbf{A}_i and \mathbf{N}_i (Φ_i^m , Ψ_i^m , \mathbf{s}_i , respectively), are generated based on the failure envelope and as function of \mathbf{A}_i and \mathbf{N}_i .

It should be noted that the terms strain and strength response/failure/constraint are used interchangeably throughout the thesis.

5.6.2 Buckling

The buckling analysis and the derivation for the approximation formulation is performed on the basis of an idealized buckling model. Each wing panel, between two stiffeners and two ribs, is idealized as a simply supported flat plate under constant in-plane loading. This way, a detailed finite element representation of the buckling fields for a FE based buckling analysis is not required, which considerably shortens calculation time and simplifies the FE model generation.

Each panel is represented by a quadrilateral element. First, the geometry is projected onto the element material coordinate system and the local z component is neglected to obtain a flat geometry. The flat panel is mapped to a standard square

$-1 \leq \xi \leq 1, -1 \leq \eta \leq 1$ using a bilinear transformation. The bending displacement $w(x, y)$ is represented in terms of hierarchical shape functions $w = \sum_i a_i \phi_i(\xi, \eta)$ [Bab89]. The hierarchical shape functions are formed by multiplying one-dimensional *Lobatto* (bubble) functions. In this way, the assumed shape functions satisfy simple supported kinematic conditions.

Setting up the buckling approximation is quite similar to the approximation for strain failure. Again, a failure index r is approximated describing the ratio between actual load and the lowest critical buckling load, see IJsselmuiden et al. [IJs10]. Instead of inverse membrane stiffness, the inverse bending stiffness is adopted in the approximation, along with a variation of the in-plane loading, affected by load redistribution for altered stiffnesses throughout the structure:

$$\tilde{r}_i = \frac{\partial r_i}{\partial \mathbf{D}_i^{-1}} : \mathbf{D}_i^{-1} + \frac{\partial r_i}{\partial \mathbf{N}_i} \Delta \mathbf{N}_i, \quad (5.52)$$

$$\tilde{r}_i = \mathbf{\Phi}_i^b : \mathbf{D}_i^{-1} + \mathbf{s}_i^t \Delta \mathbf{N}_i. \quad (5.53)$$

$\Delta \mathbf{N}_i$ is identical to the $\Delta \mathbf{N}_i$ in the failure index approximation and was defined in equation (5.47).

The response and sensitivities of r_i with respect to \mathbf{D}_i^{-1} and \mathbf{N}_i ($\mathbf{\Phi}_i^b$ and \mathbf{s}_i respectively), are obtained as follows.

The strain energy of the panel is written as:

$$2\mathcal{U} = \mathbf{a}^t \cdot \mathbf{K} \cdot \mathbf{a}, \quad (5.54)$$

while the potential energy of the in-plane loads is written as:

$$2\mathcal{V} = \mathbf{a}^t \cdot \mathbf{K}_g \cdot \mathbf{a}. \quad (5.55)$$

The stiffness matrix \mathbf{K} is expressed as:

$$\mathbf{K} = D_{11} \mathbf{K}^{11} + D_{12} \mathbf{K}^{12} + D_{16} \mathbf{K}^{16} + D_{22} \mathbf{K}^{22} + D_{26} \mathbf{K}^{26} + D_{66} \mathbf{K}^{66}. \quad (5.56)$$

The constant matrices \mathbf{K}^{lm} are obtained by integrating the second derivatives of the shape functions. For instance:

$$K_{pq}^{11} = \int_{\Omega} \phi_{p,xx} \phi_{q,xx} d\Omega, \quad (5.57)$$

where Ω is the area of the panel. Partial derivatives are evaluated using the chain rule and the integration is performed using Gauss quadrature.

The geometric matrix \mathbf{K}_g is expressed as:

$$\mathbf{K}_g = -N_x \mathbf{K}^{xx} - N_y \mathbf{K}^{yy} - N_{xy} \mathbf{K}^{xy}, \quad (5.58)$$

where the constant matrices \mathbf{K}^{xx} , \mathbf{K}^{yy} and \mathbf{K}^{xy} are given by:

$$\begin{aligned} K_{pq}^{xx} &= \int_{\Omega} \phi_{p,x} \phi_{q,x} d\Omega, & K_{pq}^{yy} &= \int_{\Omega} \phi_{p,y} \phi_{q,y} d\Omega, \\ K_{pq}^{xy} &= \int_{\Omega} \phi_{p,x} \phi_{q,y} + \phi_{p,y} \phi_{q,x} d\Omega. \end{aligned} \quad (5.59)$$

The inverse buckling factors r are obtained by solving the eigenvalue problem:

$$(\mathbf{K}_g - r\mathbf{K}) \cdot \mathbf{a} = \mathbf{0} . \quad (5.60)$$

The buckling modes are normalized to have a unit stiffness $\mathbf{a}_i^t \cdot \mathbf{K} \cdot \mathbf{a}_i = 1$. The sensitivity of the inverse buckling factor with respect to the panel bending stiffness is obtained using the standard eigenvalue sensitivity formulas in the form:

$$\frac{\partial r_i}{\partial D_{lm}} = -r_i \mathbf{a}_i^t \cdot \mathbf{K}^{lm} \cdot \mathbf{a}_i . \quad (5.61)$$

Similarly, the derivative of the inverse buckling factors with respect to the applied loads are obtained from:

$$\mathbf{s}_i^\bullet = \frac{\partial r_i}{\partial \mathbf{N}_\bullet} = \mathbf{a}_i^t \cdot \mathbf{K}^\bullet \cdot \mathbf{a}_i . \quad (5.62)$$

5.6.3 Mass

Since the structural mass only depends on the laminate thickness and not on its stiffness matrices, the approximation reduces to equation (5.63), where $\alpha_j = \frac{\partial m_i}{\partial h_j}$:

$$\tilde{m} = \sum_j \alpha_j h_j . \quad (5.63)$$

No further processing of the corresponding NASTRAN sensitivity is required prior to incorporating in the approximation.

In addition, mass sensitivities α can be used to calculate element weighing factors according to the ratio of element area to total area, as required by the optimizer. The element area being equal to $S_i = \alpha_i / \rho_i$, the weighing factor becomes $w_i = \alpha_i / \sum \alpha_i$, assuming the density to be the same for all elements.

5.7 Aeroelastic Responses

The structural responses strength and buckling, as described in the previous sections, relate to a specific condition and therefore approximation in each element. Direct physical coherence between the response and the design variables can be found, allowing response approximations to be constructed based on this knowledge. Aeroelastic responses, however, describe a global behavior, and for this reason it is not possible to construct explicit, functional relationships between the response and the design variables. For that reason, the convexification process as describe in section 5.4 is applied on the reciprocal sensitivities of membrane stiffness \mathbf{A} and bending stiffness \mathbf{D} . The corresponding approximations of aeroelastic responses will be described in the following sections.

5.7.1 Aileron Effectiveness

A detailed explanation on the derivation of aileron effectiveness was given in section 2.2.1. Since it is not know a priori if the reciprocal approximation is convex, as

discussed above, a convexified approximation is adopted:

$$\tilde{\eta}_{ail} = \sum_j \Psi_j^m : \mathbf{A}_j + \Psi_j^b : \mathbf{D}_j + \Phi_j^m : \mathbf{A}_j^{-1} + \Phi_j^b : \mathbf{D}_j^{-1} + \alpha_j h_j . \quad (5.64)$$

To set a lower bound or maximize aileron effectiveness, and to avoid sign switching during optimization, equation (5.64) is multiplied by -1 (scale) and a constant η_0 is added (shift). A reasonable value for η_0 is the rigid wing aileron effectiveness, but an estimate of this is sufficient to maintain the response sign. The modified approximation is shown in equation (5.65) and the lower bound constraint on aileron effectiveness in equation (5.66):

$$\tilde{\eta}_{ail}^* = -\tilde{\eta}_{ail} + \eta_0 , \quad (5.65)$$

$$\tilde{\eta}_{ail}^* \leq -\eta_{ail\min} + \eta_0 . \quad (5.66)$$

It should be noted that η_0 will not be required in the definition of the approximation itself, since following the discussion in section 5.2, the constant term will be computed internally in the optimizer. Nevertheless, the design point response that will be passed to the optimizer will contain both scaling and shifting as defined in equation (5.65).

5.7.2 Twist

While the importance of twist in an aeroelastic optimization was pointed out in section 2.2.3, the approximation for twist is treated in a similar manner to aileron effectiveness. Not being able to guarantee convexity of the reciprocal approximation, the reciprocal sensitivities are convexified:

$$\tilde{\vartheta} = \sum_j \Psi_j^m : \mathbf{A}_j + \Psi_j^b : \mathbf{D}_j + \Phi_j^m : \mathbf{A}_j^{-1} + \Phi_j^b : \mathbf{D}_j^{-1} + \alpha_j h_j . \quad (5.67)$$

To be able to set an upper and lower limit on twist, or to minimize or maximize twist when defining it as an objective, two variants are applied. A scaled and shifted approximation and a constraint for defining a lower limit or maximizing twist are given in equations (5.68) and (5.69):

$$\tilde{\vartheta}_{ail}^* = -\tilde{\vartheta}_{ail} + \vartheta_0 , \quad (5.68)$$

$$\tilde{\vartheta}_{ail}^* \leq -\vartheta_{ail\min} + \vartheta_0 . \quad (5.69)$$

A scaled and shifted approximation and a constraint for defining an upper limit or minimizing twist are given in equations (5.70) and (5.71):

$$\tilde{\vartheta}_{ail}^* = \tilde{\vartheta}_{ail} + \vartheta_0 , \quad (5.70)$$

$$\tilde{\vartheta}_{ail}^* \leq \vartheta_{ail\max} + \vartheta_0 . \quad (5.71)$$

In both cases, the responses are shifted by ϑ_0 in order to ensure that the response $\tilde{\vartheta}_{ail}^*$ passed to the optimizer will always be ≥ 0 .

The direct implication of defining lower and upper limit constraints as shown in equation (5.68) and (5.70) and a subsequent convexification of the sensitivities is demonstrated in section 5.5.

5.7.3 Divergence

Again, the same convexity uncertainty as stated for aileron effectiveness and twist holds also for the approximation of divergence pressure q_{div} , hence a convexified approximation is adopted, equation (5.72):

$$\tilde{q}_{div} = \sum_j \Psi_j^m : \mathbf{A}_j + \Psi_j^b : \mathbf{D}_j + \Phi_j^m : \mathbf{A}_j^{-1} + \Phi_j^b : \mathbf{D}_j^{-1} + \alpha_j h_j . \quad (5.72)$$

A description of divergence as an aeroelastic phenomenon was presented in section 2.2.2. Clearly, the most important application of the response will be a lower limit constraint, and therefore the approximation and the constraint are scaled, equations (5.73) and (5.74). With the divergence pressure being in the order of several tens of thousands, the response is not just scaled by -1 , but by $-1/q_{div0}$ instead, where a meaningful choice for q_{div0} can be the lower limit constraint value. In this case, for an active constraint the unshifted response will be equal to -1 . Hence, a useful choice for the shift is $q_{norm} = 2$:

$$\tilde{q}_{div}^* = -\frac{1}{q_{div0}} \tilde{q}_{div} + q_{norm} , \quad (5.73)$$

$$\tilde{q}_{div}^* \leq -\frac{1}{q_{div0}} q_{divmin} + q_{norm} . \quad (5.74)$$

5.8 Summary

In this chapter the derivation of response approximations in terms of the design variables were presented. The results constitute a key contribution to the stiffness optimization process. The general setup of a response approximation was discussed, followed by a description of the practical treatment of the sensitivities provided by NASTRAN. The convexification of reciprocal sensitivities was investigated, followed by a detailed description of the structural and aeroelastic approximations employed in this research work. The developed responses are summarized in table 5.1.

Table 5.1: *Response approximations*

| | | | |
|-----------------------|----------------------|-----|---|
| strength | \tilde{r}_i | $=$ | $\Phi_i^m : \mathbf{A}_i^{-1} + \Psi_i^m : \mathbf{A}_i + s_i^t \Delta N_i$ |
| buckling | \tilde{r}_i | $=$ | $\Phi_i^b : \mathbf{D}_i^{-1} + s_i^t \Delta N_i$ |
| mass | \tilde{m} | $=$ | $\sum_j \alpha_j h_j$ |
| aileron effectiveness | $\tilde{\eta}_{ail}$ | $=$ | $\sum_j \Psi_j^m : \mathbf{A}_j + \Psi_j^b : \mathbf{D}_j + \Phi_j^m : \mathbf{A}_j^{-1} + \Phi_j^b : \mathbf{D}_j^{-1} + \alpha_j h_j$ |
| twist | $\tilde{\vartheta}$ | $=$ | $\sum_j \Psi_j^m : \mathbf{A}_j + \Psi_j^b : \mathbf{D}_j + \Phi_j^m : \mathbf{A}_j^{-1} + \Phi_j^b : \mathbf{D}_j^{-1} + \alpha_j h_j$ |
| divergence | \tilde{q}_{div} | $=$ | $\sum_j \Psi_j^m : \mathbf{A}_j + \Psi_j^b : \mathbf{D}_j + \Phi_j^m : \mathbf{A}_j^{-1} + \Phi_j^b : \mathbf{D}_j^{-1} + \alpha_j h_j$ |

Before demonstrating the functionality of the stiffness optimization process using various applications, the following chapter will discuss the development of an aero load correction process to improve the aeroelastic loads prediction.

CHAPTER 6

Aero Load Correction

“Correction does much, but encouragement does more.”

Johann Wolfgang von Goethe

Despite *Goethe’s* veritable view on supporting encouragement rather than correction, aerodynamic forces calculated using the doublet lattice method have limitations, beyond which one has either to accept their deviation with respect to the absolute values, or one has to start thinking about correcting them; regrettably, encouragement will not help in this situation. Understandably, *Goethe* little cared about the doublet lattice method.

The doublet lattice method (DLM) was introduced in section 3.4 in association with the model generation process. DLM is the built-in method of choice for computing steady and unsteady aerodynamic loads in NASTRAN, [Rod04], the theory of which is established in Albano et al. [Alb69], Giesing et al. [Gie71], and Rodden et al. [Rod72]. A corresponding steady flow version of the doublet lattice method, closely relating to it, is the vortex lattice method described in, for example, Bertin et al. [Ber98]. The flat, two-dimensional aerodynamic panel mesh is coupled to structural reference grids and therefore undergoes the same structural deformations, resulting in deformation dependent aeroelastic loads, see section 3.4.3. Some more insight into the derivation of aeroelastic forces with DLM will be provided in section 6.1.

In the case of steady aerodynamic flows, as applied in this research work, the reason to perform a correction are the potential differences in wing surface pressures between DLM and presumably more correct higher order aerodynamic methods. The latter types of methods allow for the consideration of flow phenomena that cannot be reproduced with DLM. Among the flow phenomena that must be dealt with the most important are:

1. airfoil camber and thickness as opposed to the standard flat plate results obtained from DLM
2. compressibility effects including local recompression shocks

3. strongly non-linear aerodynamic forces resulting from viscous flow phenomena like separation.

The correction methods applied and developed during the research reported here and their limitations for ameliorating the above mentioned shortcomings are introduced in section 6.2. The implementation of the correction methods in the optimization framework is described in section 6.3, while in section 6.4 details of the routines developed are presented.

6.1 Doublet Lattice

In general, an aerodynamic method is aimed at computing the surface pressures \mathbf{p}_j in each of the boxes that make up the aerodynamic model, as a function of the free stream conditions. With panel methods like DLM, a relation between the surface pressure and the local angle of attack of each box with respect to the free stream vector can be generated. This angle is usually denoted as non-dimensional downwash \mathbf{w}_j , and the matrix establishing the relation between pressure \mathbf{p}_j and downwash is called aerodynamic influence coefficient matrix \mathbf{AIC} , [Rod04]. It is a direct outcome of the doublet lattice method:

$$\mathbf{w}_j = \frac{1}{q} \mathbf{AIC}_{jj} \mathbf{p}_j . \quad (6.1)$$

The downwash \mathbf{w}_j is composed of two parts, one, the purely geometric downwash vector \mathbf{w}_j^g and two, a part that results from the displacement of the aerodynamic mesh. For steady flow conditions, the spatial displacement of the aerodynamic mesh \mathbf{u}_a is used to compute the displacement related downwash via another matrix supplied by the doublet lattice method, \mathbf{D}_{ja} , so that in total the downwash becomes:

$$\mathbf{w}_j = \mathbf{D}_{ja} \mathbf{u}_a + \mathbf{w}_j^g . \quad (6.2)$$

Along with an integration matrix \mathbf{S}_{aj} that relates box pressures \mathbf{p}_j to box forces \mathbf{f}_a :

$$\mathbf{f}_a = \mathbf{S}_{aj} \mathbf{p}_j , \quad (6.3)$$

the combining of equations (6.1) to (6.3) leads to a relation between box forces \mathbf{f}_a and box displacements \mathbf{u}_a :

$$\mathbf{f}_a = q \mathbf{S}_{aj} \mathbf{AIC}_{jj}^{-1} \mathbf{D}_{ja} \mathbf{u}_a + q \mathbf{S}_{aj} \mathbf{AIC}_{jj}^{-1} \mathbf{w}_j^g . \quad (6.4)$$

Based on the splining routines shortly described in section 3.4.3, a coupling matrix \mathbf{H} can be generated that relates structural \mathbf{u}_s and aerodynamic displacements \mathbf{u}_a , equation (6.5), and the matrix in a transposed form is applied in the transformation of structural \mathbf{f}_s^A and aerodynamic forces \mathbf{f}_a , equation (6.6):

$$\mathbf{u}_a = \mathbf{H}_{as} \mathbf{u}_s , \quad (6.5)$$

$$\mathbf{f}_s^A = \mathbf{H}_{sa} \mathbf{f}_a . \quad (6.6)$$

Replacing aerodynamic displacements and forces in equation (6.4) by equation (6.5) and (6.6) finally results in:

$$\mathbf{f}_s^A = q \mathbf{K}^A \mathbf{u}_s + q \mathbf{f}_s^{Ag} , \quad (6.7)$$

where:

$$\mathbf{K}^A = \mathbf{H}_{sa} \mathbf{S}_{aj} \mathbf{AIC}_{jj}^{-1} \mathbf{D}_{ja} \mathbf{H}_{as}, \quad \text{and} \quad \mathbf{f}_s^{Ag} = \mathbf{H}_{sa} \mathbf{S}_{aj} \mathbf{AIC}_{jj}^{-1} \mathbf{w}_j^g.$$

In the equations above \mathbf{K}^A is called the aerodynamic stiffness matrix and directly relates structural displacements to aerodynamic loads acting on the structure.

Inserting equation (6.7) in the static equilibrium equation $\mathbf{K} \mathbf{u}_s = \mathbf{f}_s^A + \mathbf{f}_{ie}$, featuring aeroelastic forces \mathbf{f}_a^A and inertial and external forces \mathbf{f}_{ie} , allows a direct solution for displacement vector \mathbf{u}_s :

$$\mathbf{K} \mathbf{u}_s = q \mathbf{K}^A \mathbf{u}_s + q \mathbf{f}_s^{Ag} + \mathbf{f}_{ie}, \quad (6.8)$$

$$(\mathbf{K} - q \mathbf{K}^A) \mathbf{u}_s = q \mathbf{f}_s^{Ag} + \mathbf{f}_{ie}. \quad (6.9)$$

These set of equations represent a closely coupled structure and aerodynamics system, since no iterative procedure is required to solve for the static equilibrium with displacement dependent aeroelastic forces.

6.2 Correction Methods

Correction methods, with a strong focus on doublet lattice, have received a lot of attention. Giesing et al. [Gie76] suggest methods that require either a correcting of DLM pressures or modifications to the downwash based on the aerodynamic influence coefficients. Palacios et al. [Pal01] provided a survey of the available correction techniques, focusing on unsteady aerodynamic forces. An industrial application of DLM correction is presented in Brink-Spalink et al. [Bri00], who suggest a least square correction method that makes use of unsteady computational fluid dynamics (CFD) results, and a two-dimensional correction method. Both methods are aimed at correcting the **AIC** matrix. In a more recent work, Dimitrov et al. [Dim13] compare gust responses obtained from DLM, CFD, and DLM that are corrected using quasi-steady CFD data.

The sole focus of the research reported here was steady aerodynamic forces, thus deviating from the methods described above, two correction procedures were considered and are discussed in the following sections. In the first method DLM modifications directly available in NASTRAN were employed, sections 6.2.1. The second method is based on modifications made to the forces transferred the from doublet lattice to the structural model, using a higher order aerodynamic method, section 6.2.2.

6.2.1 Doublet Lattice Correction

While the geometric downwash vector \mathbf{w}_j^g , as described in equation (6.2), in an uncorrected DLM consists purely of the input induced by the free stream, NASTRAN provides the possibility to extend the geometric downwash by an additional contribution. In other words, the downwash in each box can be modified by a constant value. The addition can be supplied to NASTRAN in the form of a `W2GJ` matrix. A detailed investigation of this contribution is provided in Kaiser [Kai13]. To this end, a downwash can be defined for each DLM box, corresponding to a local angle of attack change, as illustrated in Figure 6.1. The required box rotations for the emulation of a

camber line are shown in Figure 6.1(a). The chordwise constant rotation of each DLM box as shown in Figure 6.1(b) is used to emulate a twist of the wing section. Both downwash types described in Figure 6.1 can be varied in spanwise direction, allowing for the simulation of cambered airfoil blending and a geometric twist distribution. MODGEN per default provides three W2GJ correction matrices for camber, twist, and the combination of both, which are generated based on the wing planform and the airfoil data provided in the MODGEN input file. Airfoil and planform data suffice to span the underlying aerodynamic surface.

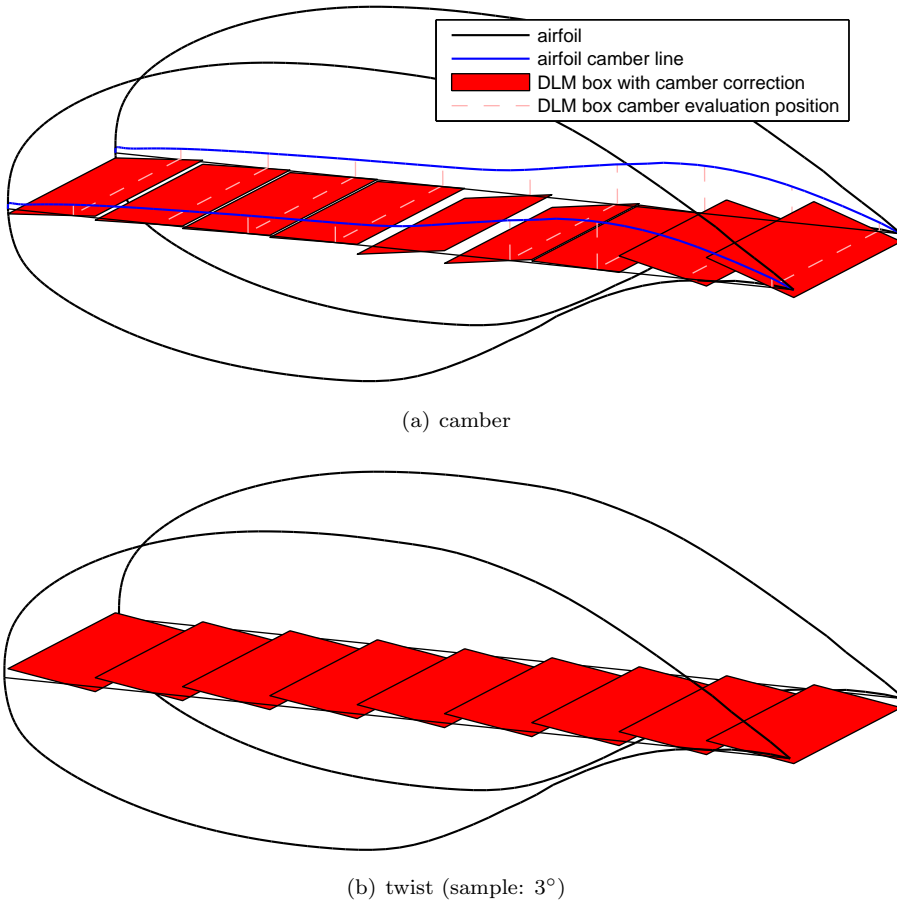


Figure 6.1: *DLM W2GJ correction illustration for a chordwise row of DLM boxes*

The general effects of camber and twist, the latter one corresponding to angle of attack in a two-dimensional case, on the characteristics of an airfoil section, along with an analytic treatment by the theory of thin wing sections can be found in Abbott et al. [Abb59]. The effect of the W2GJ correction will be discussed in chapter 9, however, a first impression of the considerable influence of camber and twist on the chordwise pressure distribution is given below with an investigation of three different airfoils using the two-dimensional panel code *XFOIL*, Drela [Dre89]. The *XFOIL* code is

capable of calculating inviscid and viscous flows and can account for compressibility effects using the *Prandtl-Glauert* transformation, [Kat01].

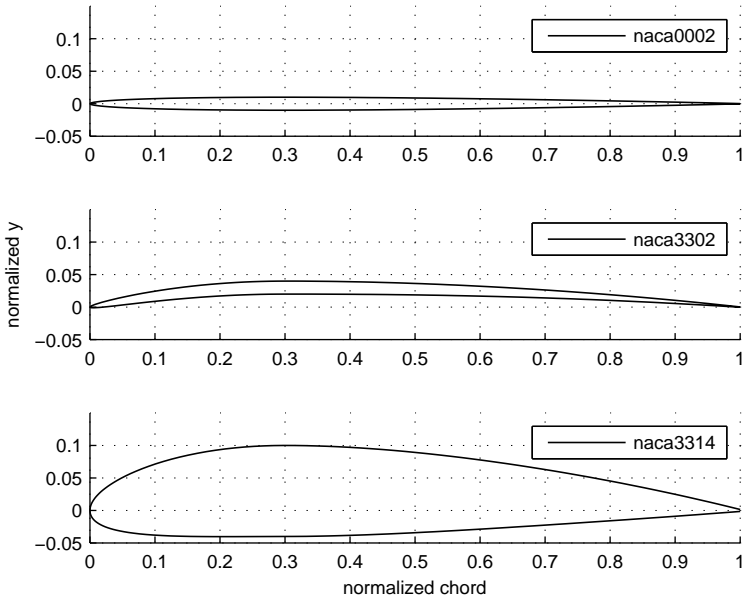
All three airfoils emanate from the *naca* four digit series, as described for example in Anderson [And05]. The first two, *naca0002* and a *naca3302*, were chosen to closely conform with the flat surface as modeled in DLM, apparent from the last two digits in the airfoils declaration which represent a thickness of 2%. While the first airfoil is symmetric, the second one is cambered by 3% with a camber maximum at 30% of the chord, as expressed in the first two digits. In order to demonstrate the influence of airfoil thickness that can not be considered in the W2GJ correction, a third airfoil *naca3314*, equivalent to *naca3302*, only with a thickness of 14% was added to the investigation. The airfoils are shown in Figure 6.2(a).

The calculations were performed for inviscid, but compressible flow conditions at $M = 0.6$. For this *Mach* number the flow is still subsonic except for a very small peak at the nose of *naca0002* at lift generating flow settings. While the *Prandtl-Glauert* transformation is not applicable in this area, it is assumed to not have a substantial influence on the trends that are assumed to be shown with this example. Pressure coefficients C_p were computed for a fixed angle of attack $\alpha = 1^\circ$ and for a fixed lift coefficient $C_l = 0.3$. DLM – due to the mesh methodology – only providing a pressure difference between upper and lower surface, the *XFOIL* results were processed accordingly. The results are summarized in Figure 6.2(b) and 6.2(c).

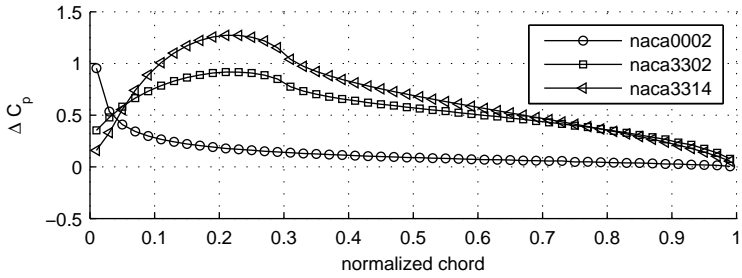
The most prominent difference between uncambered and cambered airfoils *naca0002* and *naca3302* occurs for a fixed angle of attack, Figure 6.2(b). This is quite obvious when bearing in mind that a cambered airfoil also generates lift in the case of $\alpha = 0^\circ$, while a symmetric ones does not. Keeping in mind that the lift is proportional to the area below the ΔC_p curve, the cambered airfoil generates considerably more lift than the uncambered one; $C_l = 0.55$ for *naca3302* compared to $C_l = 0.14$ for *naca0002*. Considering a realistic trimmed flight condition, where independent of a potential correction method a certain lift coefficient is required and not a fixed α , the differences in ΔC_p are still quite prominent, Figure 6.2(c). While the areas below the curves are similar, and so is the lift, the moments about a fixed reference point differ. The moment coefficient about the quarter chord is $C_m = 0$ for the symmetric *naca0002* and $C_m = -0.087$ for the cambered *naca3302*. Aside from a possible geometric twist implementation, it is mainly the improvement of the moment coefficient for cambered airfoils, which makes the W2GJ correction an important element in the advancement of the DLM aero loads. It is emphasized that these results are supposed to show trends rather than absolute values. The *Mach* number for example has a noticeable influence on the lift curve slope and therefore also on the lift for a fixed angle of attack. Nevertheless, the results for the thin symmetric and cambered airfoil are expected to correlate well with uncorrected and W2GJ corrected DLM results.

Airfoil *naca3314*, also shown in the results in Figure 6.2(b) and 6.2(c), demonstrates the influence of airfoil thickness on the chordwise pressure difference. For the same angle of attack it generates $\approx 20\%$ more lift ($C_l = 0.66$) than the thinner version, Figure 6.2(b), while the moment coefficient is, absolutely, only $\approx 2\%$ larger ($C_m = -0.088$).

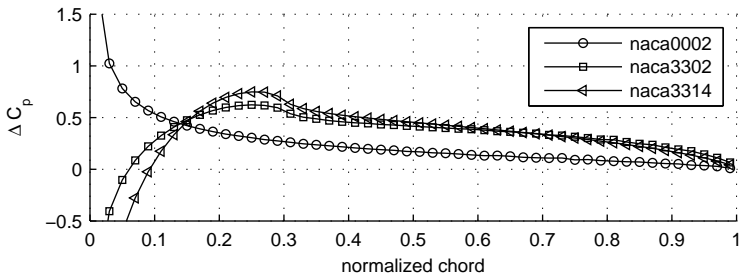
With closely matching moment coefficients the question arises why further corrections beyond W2GJ might still be required. One of the most prominent reasons



(a) airfoils



(b) pressure difference for $\alpha = 1^\circ$, $M = 0.6$



(c) pressure difference for $C_l = 0.3$, $M = 0.6$

Figure 6.2: XFOIL results

is the lack of recompression shocks that can not be covered with DLM. They arise beyond airfoil dependent *Mach* numbers and are usually present in cruise condition, and especially at high *Mach* numbers and high lift load cases. Shocks can have a large influence on the chordwise lift and therefore moment distribution, changing the twist distribution and hence spanwise lift distribution for load cases that drive the structural sizing of the wing structure. Another reason is that in the case of a W2GJ corrected DLM the missing influence of airfoil thickness on the lift coefficient is balanced by an adaption of the angle of attack required to fulfill the trim condition. Not only do the altered lift force vector directions influence the structural design, but also the moment coefficient due to compressible flow is influenced, deviating from the real conditions. These shortcomings lead to the need for an additional correction method, as described in the following section.

6.2.2 CFD Correction

Aerodynamic methods can basically be grouped into lower and higher order methods, with a prominent difference lying in the discretization methodology, which in turn is a result of the governing equations that are to be solved. Lower order methods usually solve the linearized potential flow equation, in which case a surface or even line representation of the component to be investigated in a flow environment is sufficient. The equations result from a linearized version of the *Navier-Stokes* equations, after neglecting the viscosity and vorticity terms, [Kat01]. The doublet lattice method, which forms the basic aerodynamic model throughout this research, belongs to these methods, as does the *XFOIL* code applied in the previous section. An equivalent three-dimensional surface panel code is for example *VSAERO*, Nathman [Nat98]. Three-dimensional panel codes are capable of emulating the real wing surface including the full airfoil geometry and can be coupled to boundary layer codes that act along streamlines on the panel surface to account for viscous effects.

A common downside of linearized potential flow solvers is the inability to capture non-linear effects like recompression shocks. Accordingly, higher order codes have to be applied if a need for an accurate prediction of the steady flow phenomena in the transonic flow regime arises. Full potential solvers, which form the next step towards higher order methods can already cope with non-linear effects. Nevertheless, given increasing computational power and developments in the CFD area increasingly focusing on solvers that deal with the full *Navier-Stokes* or *Euler* equations, a decision was made in favor of the *DLR – German Aerospace Center* unstructured *Navier-Stokes* solver TAU, see Gerhold et al. [Ger97], Schwamborn et al. [Sch06]. The abbreviation CFD stands for *Computational Fluid Dynamics* and denotes methods used to solve the governing equations of a fluid flow. While the term is usually applied in conjunction with higher order volume mesh methods like *Navier-Stokes* solvers, strictly speaking it also applies to lower order methods. In the scientific community, as in this work, its meaning is dedicated to higher order methods exclusively.

Solving the appropriate flow equations necessitates a flow field discretization that differs fundamentally from the ones applicable for lower order methods. Instead of modeling only the surface of the object under investigation, a spatial discretization is required, a sample of which is shown in Figure 6.3. Details on the mesh generation are provided in section 6.4.1.

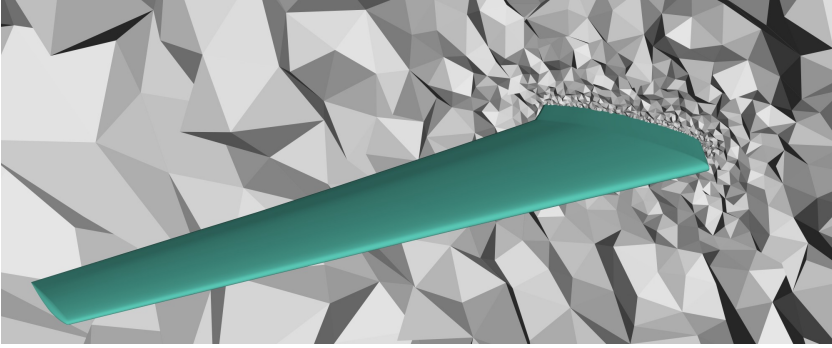


Figure 6.3: *Euler CFD volume mesh*

TAU can be applied either for solving the full *Navier-Stokes* equations with a dedicated boundary layer and turbulence modeling, or in a simplified version, in which the viscous terms in the flow equations are neglected, hence resulting in the *Euler* equations. A main disadvantage of *Euler* compared to *Navier-Stokes* is its inability to resolve flow separation except at sharp corners like trailing edges. This is a direct consequence of disregarding the viscous terms, which in turn also precludes the consideration of friction forces. Moreover, missing viscosity and flow separation can give rise to a biased shock position and shock strength overestimation, see for example Whitfield et al. [Whi81] and Jameson [Jam83]. Nevertheless, due to the considerable time saving when using *Euler* compared to the full *Navier-Stokes* solver, along with much faster mesh generation due to avoiding the necessity for a dedicated boundary layer meshing, the *Euler* solver is applied solely. It constitutes a reasonable compromise between computational effort and the gain in accuracy of the aerodynamic loading, well suited for the application in the structural optimization process.

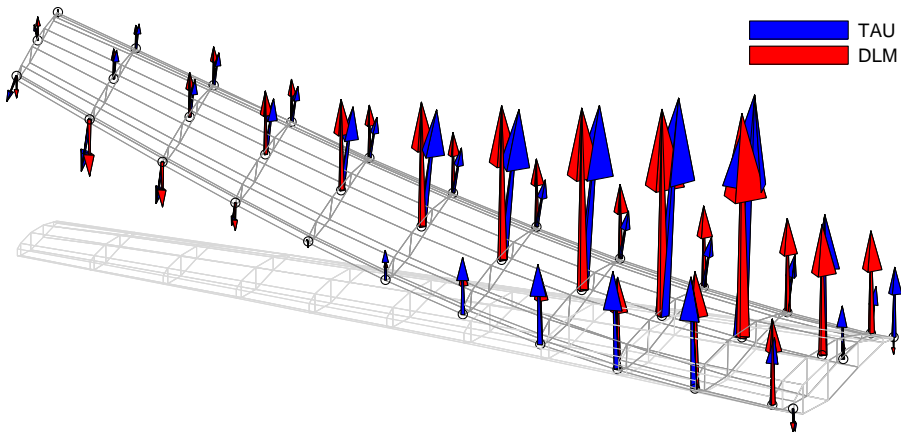


Figure 6.4: *Force vectors at the coupling nodes*

The basic idea behind the entitled CFD correction consists of rectifying aerodynamic loads obtained using the doublet lattice method by means of the supposedly

superior CFD results. To this end, the relevant sizing load cases are analyzed with TAU, considering an appropriate volume mesh deformation that resembles the structural displacements. With the doublet lattice forces concentrated onto the coupling nodes, compare section 3.4.3 and 4.5.2, the same nodes are selected for splining the surface forces obtained from the *Euler* calculation. The difference between the CFD force vector and the DLM force vector at each coupling node is applied as a static amendment to the respective load case. The force vectors on a deformed wing structure are shown in Figure 6.4.

A detailed description of the aero load correction process will be given in the following section 6.3, while the focus of section 6.4 will be the individual CFD related tasks, required to obtain the desired correction forces.

6.3 Process Methodology

The process of correcting the aerodynamic loads obtained with DLM can be seen as an addition to the existing optimization framework as it was introduced in section 2.1. It is defined as a stand-alone module that collaborates with the optimization via well-defined interfaces. Typically, the generation of an appropriate TAU *Euler* mesh is the first indispensable step required to allow a CFD correction, details on which are provided in section 6.4.1.

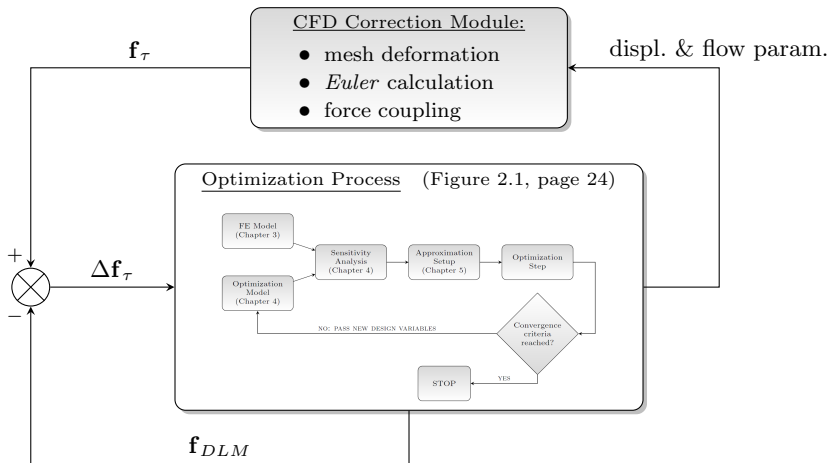


Figure 6.5: CFD correction implementation outside the optimization loop

The new correction process is depicted in Figure 6.5. The CFD module is positioned outside the actual optimization framework. The computation starts with a regular optimization and as yet uncorrected aero forces. Uncorrected in this context only refers to CFD correction, while a correction via W2GJ can always be applied. When the optimization is converged, or when the specified number of iterations is reached, it is stopped. So far, no difference exists compared to a regular optimization.

For each load case that is to be corrected using CFD aero loads, the necessary input is passed to the CFD correction module. The input consist of structural displacements

at the coupling nodes, utilized for the CFD mesh deformation, and the flow parameters that are required to perform an *Euler* calculation. These parameters consist of a *Mach* number, stagnation pressure, density and angle of attack. It is important to note that the *Euler* calculation is performed for the same angle of attack as resulting from the trim calculation in NASTRAN. The necessary data was generated during the sensitivity generation, mainly using the output requests defined in section 4.5. Details on mesh deformation as addressed above are provided in section 6.4.2, and information on the required flow parameters in section 6.4.3. Only symmetric maneuver and cruise load cases are designated for CFD correction, the first due to their potential to drive the structural sizing and the latter due to the evaluation and possible constraining of wing twist. In both cases the corrected aero loading can have a significant influence on the results.

Once the CFD forces are generated and condensed to the coupling nodes, denoted as \mathbf{f}_τ in Figure 6.5, they are subtracted from the appropriate DLM forces \mathbf{f}_{DLM} , yielding the correction forces $\Delta\mathbf{f}_\tau$:

$$\Delta\mathbf{f}_\tau^k = \mathbf{f}_\tau^k - \mathbf{f}_{DLM}^k, \quad (6.10)$$

where superscript k indicates the structural iteration steps for which TAU corrections are generated.

The correction forces are grouped by load case and saved in the appropriate NASTRAN FORCE card format. A new optimization process is initiated, this time including the correction forces during the responses and sensitivity generation. The loop of optimizing and computing new correction forces is continued until an overall convergence is achieved.

Usually, an aeroelastic trim calculation in NASTRAN ensures that the lift forces generated by the doublet lattice model exactly balance the weight vector multiplied with the vector defining the load factor. The application of additional static correction forces at the coupling nodes presupposes the capability to perform a trim solution that incorporates the forces in the static equilibrium equations. NASTRAN does provide this necessity. Consequently, performing a trim calculation along with the additional correction forces implies a force distribution at the coupling nodes in the trimmed solution, which exactly matches the CFD results. Since this only is true if the structural properties and therefore the displacements remain unchanged, this statement strictly speaking does not apply during the optimization. The reason is that during an optimization sequence the correction forces remain constant and will only be updated after n iterations performed in the optimization block. Moreover, the node displacements for the CFD correction module are generated before the last iteration step, as can be seen from Figure 2.1 on page 24.

In the following, an examination of the convergence behavior will be given to demonstrate the acceptance of this approach. Setting up the static equilibrium equation for the $(k+n)^{th}$ iteration leads to:

$$(\mathbf{K} - q\mathbf{K}^A)\mathbf{u}_s^{k+n} = \mathbf{f}_{ie} + \Delta\mathbf{f}_\tau^k, \quad (6.11)$$

where \mathbf{K}^A is the aerodynamic stiffness matrix, which links structural displacements to the aerodynamic forces generated by DLM according to:

$$\mathbf{f}_{DLM} = q\mathbf{K}^A\mathbf{u}_s. \quad (6.12)$$

The derivation of \mathbf{K}^A was presented in section 6.1. Superscript k denotes the last structural iteration step for which TAU correction forces were generated, and accordingly superscript n is the n^{th} subsequent structural iteration step. This notation implies that TAU corrections not necessarily have to be performed for each structural iteration. Vector \mathbf{f}_{ie} represents inertial and external forces. Inserting equation (6.10) and (6.12) in (6.11) yields:

$$\mathbf{K}\mathbf{u}_s^{k+n} - \mathbf{f}_{DLM}^{k+n} = \mathbf{f}_{ie} + \mathbf{f}_\tau^k - \mathbf{f}_{DLM}^k, \quad (6.13)$$

and thus:

$$\mathbf{K}\mathbf{u}_s^{k+n} = \mathbf{f}_{ie} + \mathbf{f}_\tau^k + \Delta\mathbf{f}_{res}, \quad (6.14)$$

where:

$$\Delta\mathbf{f}_{res} = (\mathbf{f}_{DLM}^{k+n} - \mathbf{f}_{DLM}^k). \quad (6.15)$$

Equation (6.14) states that in a converged solution where the residual force $\Delta\mathbf{f}_{res}$ vanishes, the static equilibrium is determined entirely by means of TAU aerodynamic forces \mathbf{f}_τ , keeping in mind that according to equation (6.10) the aerodynamic force vector is a combination of doublet lattice forces and correction forces, $\mathbf{f}_\tau = \mathbf{f}_{DLM} + \Delta\mathbf{f}_\tau$. At this point it should be stressed that the converged aeroelastic deformation \mathbf{u} complies with the TAU aerodynamic forces, and likewise also accounts for the displacement dependent doublet lattice forces according to equation (6.12).

The reason not to perform a CFD correction step along with each optimization step are threefold.

1. Linearly increasing with the number of load cases to be considered for CFD correction, the computational costs can easily be in the time range of an optimizer iteration step, therefore doubling the calculation time.
2. Except for the first iterations, the structural changes from iteration to iteration are usually small, implying only minor changes in the twist distribution and hence correction forces.
3. The optimizer in its current implementation does not allow for a transfer of response damping values from a finished optimization process to a new one. Thus, it is not meaningful to stop the optimization after a single iteration step to generate correction forces. Besides, the first iteration step in a new optimization always requires at least two sensitivity runs, one to find out about the feasibility of the response to decide for the appropriate optimization algorithm, and two, a run to determine the required damping that leads to conservative approximations.

Due primarily to reason (3) the process depicted in Figure 6.5 was later modified to the one shown in Figure 6.6. Instead of terminating the optimization process to compute correction forces, the CFD correction module is placed inside the optimization process. This makes it unnecessary to restart the optimizer when generating a new set of correction forces. Due to the modular layout of the CFD correction no further adjustments are required. As before, the CFD correction module does not have to be called during each structural iteration step. Instead, the correction forces are kept constant until a new set is generated. The number of iterations to be performed

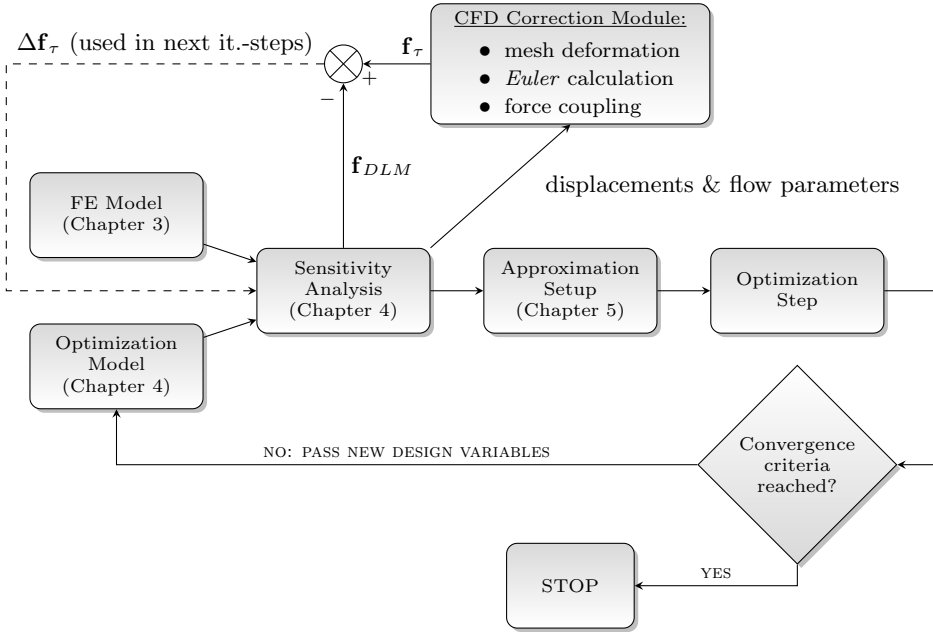


Figure 6.6: CFD correction implementation within the optimization loop

before the next CFD module call, belongs to the steering parameters and is part of the initial input supplied to the optimization process. Investigations have shown that renewing the correction forces every five to ten iterations is sufficient.

This concludes the overview on the process methodology for an aero load correction with CFD forces. In the following, details of the CFD correction module as depicted in Figure 6.5 and 6.6 are presented.

6.4 CFD Correction Module

The CFD correction module takes over the task of computing CFD forces at the coupling nodes, based on the input that is required to perform a TAU calculation on a deformed mesh. The essential steps successively performed in the module are illustrated in Figure 6.7.

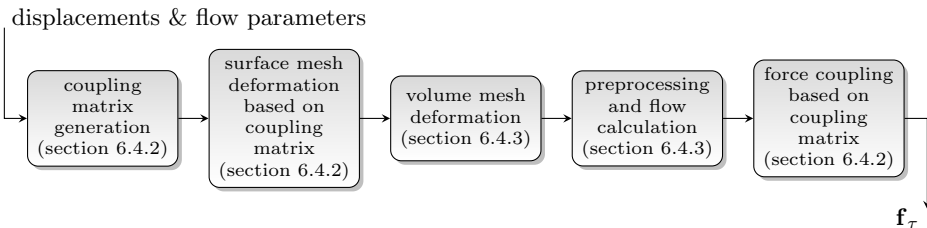


Figure 6.7: CFD correction module flow diagram

Despite not being an immediate component of the correction module, section 6.4.1 starts with a description of CFD mesh generation, followed by an introduction to the routines applied to perform mesh deformation and force coupling based on a coupling matrix, section 6.4.2. The TAU tools required to perform mesh deformation, preprocessing and the flow computation are introduced in section 6.4.3. The emphasis of the research being structural optimization, only a basic overview of the TAU tools will be presented.

6.4.1 Mesh Generation

The generation of volume meshes targeted at CFD computations is an enormously wide field, capturing a large variety of meshing strategies and consequently applicable softwares. For reasons of ease of use and the way of defining the required input, the majority of the CFD meshes employed in this work were generated using the surface modeler and unstructured volume mesher SUMO, Tomac et al. [Tom11].

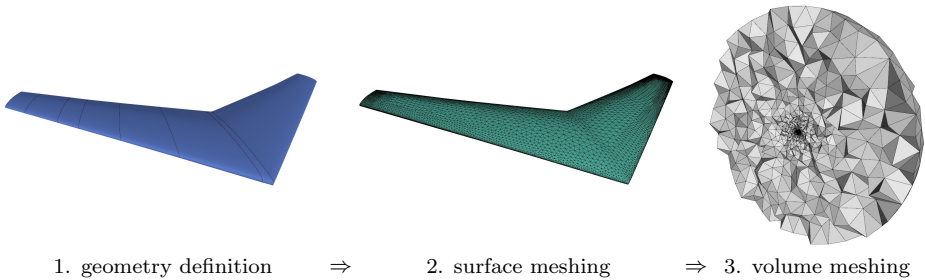


Figure 6.8: SUMO *meshing process*

The mesh generation is based on three subsequent steps, illustrated in Figure 6.8. First, the geometry of the body to be meshed is defined with surface descriptions that can either be imported in text file format, or in the form of *iges* surface entities. The first option necessitates the preparation of planform and airfoil coordinates, very much like those required during the definition of the wing layout for the finite element model generation with MODGEN, chapter 3. Therefore, the MODGEN input is chosen as an adequate means to define the undeformed wing surface in SUMO. The software, which is not yet able to apply a CFD symmetry plane at $y = 0$, requires the consideration of a full volume mesh and consequently geometry model. Due to the exclusive application of symmetric maneuver load cases, a CFD mesh of only one wing half featuring a symmetry plane at $y = 0$ would suffice, saving computation time by reducing the amount of CFD mesh elements.

In the second step the wing surface is discretized with an unstructured mesh consisting only of triangular elements. Several meshing parameter allow for the definition of element sizes and mesh refinements, for example in areas with increased surface curvature, like leading edge or wing tip. The parameters enable for a variation of the mesh density and therefore pressure result resolution, and computational cost.

Finally, in step three the volume mesh is generated based on the surface mesh generated in step two, and the definition of parameters that decide about volume mesh refinement and element restrictions in spatial dimensions. The farfield in SUMO

is defined as a sphere, with the radius being one of the parameters required for the tetrahedra mesh generation. A slice through the spherical volume is shown in Figure 6.8, while Figure 6.3 already gave an impression of the tetrahedra elements in the vicinity of the wing surface. Meshes for this work were generated with a farfield radius R_{far} corresponding to $R_{far} \approx 100 \bar{c}$, with \bar{c} being the wings average chord.

Depending on the intended surface pressure resolution, result accuracy, in connection with for example the computed shock position, and the CFD convergence and computing time, the generated *Euler* meshes usually exhibit $\approx 200,000$ to $300,000$ triangular surface elements and tetrahedra elements ranging from $\approx 0.7 * 10^6$ to $3 * 10^6$. SUMO allows for a mesh export directly in the appropriate TAU mesh format, see [DLR13b].

6.4.2 Mesh Deformation and Force Coupling

In section 3.4.3, coupling between the doublet lattice model and the structure was discussed. This coupling is based on splining routines which are predicated on thin plate theory, [Har72]. While DLM coupling is readily available using built-in NASTRAN functionality, the consideration of external CFD forces consequently necessitates appropriate coupling methods to link CFD and structure. The goal that needs to be accomplished is twofold:

1. **mesh deformation:** mapping of selective finite element displacements on all CFD surface nodes
2. **force coupling:** mapping of the CFD surface forces on selective finite element nodes

It is important to note that these tasks refer to the deformations and forces of the CFD surface elements exclusively. The deformation of the CFD volume mesh, which in turn is based on the deformed surface mesh is part of the TAU preprocessing and will be addressed in section 6.4.3. For the CFD correction process to be applicable, the structural nodes used for coupling have to be the same as the ones applied in the DLM coupling. The concept of a load reference axis for coupling purposes, also depicted in Figure 3.6 on page 50, is introduced in section 3.4.3. These nodes constitute a reasonable choice also in combination with a CFD correction.

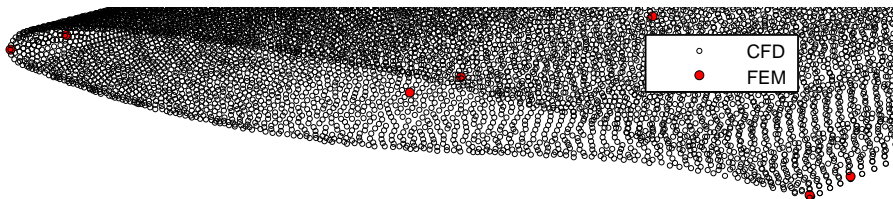


Figure 6.9: *Coupling Nodes*

A possible constellation of coupling nodes in the vicinity of the wing root is illustrated in Figure 6.9. Evidently, the discretization of CFD and FEM differs considerably. In order to couple both, a method to transform linearly structural displacements into CFD displacements in the form:

$$\mathbf{u}_a = \mathbf{H}\mathbf{u}_s, \quad (6.16)$$

needs to be found. Displacement vectors \mathbf{u}_a and \mathbf{u}_s in equation (6.16) correspond to the CFD surface and structural displacements respectively. The coupling matrix \mathbf{H} already appeared in the derivation of coupling forces for the doublet lattice method, equation (6.5) in section 6.1, with the sole difference of incorporating DLM rather than CFD displacements.

Beckert et al. [Bec01] show that the transposed of \mathbf{H} can also be used to achieve the second goal of transforming CFD forces onto the structure:

$$\mathbf{f}_s = \mathbf{H}^T \mathbf{f}_a, \quad (6.17)$$

while preserving force and moment equilibrium and the virtual work of aerodynamic and structural loads. Force vectors \mathbf{f}_s and \mathbf{f}_a in equation (6.17) are CFD nodal forces and FEM nodal forces respectively. A possible result of equation (6.17) is depicted in Figure 6.4 on page 86.

As outlined above, the aim of a coupling method is primarily the construction of a coupling matrix \mathbf{H} . A well-known approach to achieve this are radial basis functions (RBF). Fundamentally, an RBF scales the influence of the scalar value at its center with the radial distance. Adopted to the coupling problem this implies that the displacements of the structural nodes can be transferred to the surrounding CFD nodes by summing up the influence of all RBFs on the CFD nodes. A radial basis function with a problem-tailored influence radius will be assigned to each structural node. The coupling algorithm should allow for the selection of various types of RBFs, suitable for two and three-dimensional applications, when referring to the distribution of the structural coupling nodes. The selection of nodes belonging to the load reference axis along with their plate-like, flat distribution preferably argues for two-dimensional functions in the applications described in this work.

The *DLR-Institute of Aeroelasticity* can look back on a long and continuing tradition in the design and investigation of coupling methods. Construction and applications are described for instance in Neumann et al. [Neu08], Neumann [Neu11] and Neumann et al. [Neu13]. They are readily available and can be referred to, hence saving the development of appropriate codes.

6.4.3 CFD Tools

The TAU CFD environment is set up in single modules, each of which fulfills a specific task. In order to define module specific inputs, the allocation of a TAU parameter file is crucial. Along with a suitable CFD mesh, the TAU parameter file constitutes an indispensable component to perform the required tasks of volume mesh deformation, necessary preprocessing steps, and finally the flow calculation. A detailed list of all parameters that can be specified is given in [DLR13a].

The first tool in the TAU chain is the module performing the volume mesh deformation. It requires a link to the deformed surface mesh as it was generated using the coupling matrix, and allows for the selection of an algorithm either based on radial basis functions or on an advancing front method. The latter is mainly applied in this research.

The subsequent preprocessing module performs mesh type specific actions like the generation of dual grids and the coarse grids in case of specifying the application of a multigrid mode, [DLR13a]. Moreover, the module manages the grid partitioning in

the case of distributing the computation on multiple processors, all with respect to the deformed volume mesh.

Finally, the TAU *Euler* solver is executed. The corresponding module among other things requires the definition of crucial flow parameters, which were passed along with the grid displacements to the CFD correction module, compare Figure 6.7. Therefore, the TAU parameter file needs to be updated each time the CFD correction module is called. The flow parameters required by the solver are *Mach* number, density, temperature, and the angle of attack.

Solving the *Euler* equations on the discretized mesh is an iterative procedure. Hence, during the solver execution, TAU provides a constantly updated monitoring file that lists integral surface values like lift, drag and moment coefficients, and also convergence parameters like density residual and maximum residual in the entire flow field for each iteration step performed. Three events exist for the solver to stop.

1. In case of a successful calculation, convergence is achieved. TAU checks convergence by applying a *Cauchy* convergence control, which monitors the absolute or relative change of lift, drag, and moment coefficient for two iteration steps that are N iterations apart, where N is a user supplied number. If the change drops below a specified margin, the solver stops.
2. If no *Cauchy* convergence is achieved within a specified maximum amount of iterations, the solver stops.
3. If during the execution numerical problems occur, mostly identifiable by *exploding*, hence strongly increasing local flow parameters, the solver stops.

In the above list the latter two stop conditions are treated as non-converged and therefore unsuccessful solutions by the CFD correction module and special measures are taken. A majority of the parameters that are set for the TAU *Euler* solver module specify algorithm, solution strategy and involved variables to be applied in flow solving. The parameters constitute a tradeoff between computing time, required iteration number, convergence behavior, and stability. Among those are a multigrid cycle parameter; a parameter selecting an implicit, *Runge Kutta*, or explicit, *Backward Euler*, time-stepping scheme; and parameters defining coarse and fine grid CFL numbers, where CFL in general defines the ratio of travel distance in the CFD mesh and cell dimension. To cope with CFD convergence problems, different parameter sets are defined beforehand, ranging from presumably fast and instable settings down to slow and stable settings. In the case of an unsuccessful TAU run, the CFD correction module rewrites the parameter file with a new set and starts a new solver run. If no convergence can be achieved even with the most stable set, the CFD correction module quits with forces \mathbf{f}_τ equal to zero. Reasons for nonconverging solutions can either be bad mesh quality or erroneous flow settings.

It should be noted that the above mentioned block of TAU modules can obviously be exchanged with any other CFD environment that provides the required functionality of volume mesh deformation and flow solving.

6.5 Summary

This concludes the description of the aero load correction strategy. Two techniques to enhance the NASTRAN internal DLM were presented. The first method aims at improving the NASTRAN doublet lattice method with correction matrices derived from airfoil coordinates and wing twist. The second method involves flow analysis with higher order CFD methods and a derivation of static correction forces as the difference between CFD and DLM. While the first method can account for airfoil camber and twist only, the second method incorporates fully three-dimensional transonic flow effects, such as recompression shocks and thickness effects. To facilitate the mesh generation process, but also to achieve reasonable calculating times, a decision in favor of an *Euler* solver was made. The drawbacks are the nonconsideration of viscous flow phenomena like separation or a biased shock position especially in off-design regions. Replacing the *Euler* solver by *Navier-Stokes* is only a matter of computational power and mesh generation abilities. The implementation in the CFD correction module will only require an exchange of the corresponding TAU modules.

Part II

Design Studies

CHAPTER 7

Aeroelastic Optimization of a Swept Back Wing

“The excessive increase of anything causes a reaction in the opposite direction.”

Plato

The first application of the stiffness optimization process is focused on the demonstration of general functionality, the introduction of basic terminology, and the methods used to present the optimization results. For this purpose a generic wing model was developed, incorporating the attributes required to exemplify the optimization of structural and aeroelastic responses.

The general outline of the wing model is presented in section 7.1. A definition of critical load cases covering the contemplated objective and constraints is presented in section 7.2. The finite element model, set up with the parametric wing model generation process, is described in section 7.3, details of the optimization model are provided in section 7.4. The implication of the initial stiffness parameters on the structural responses and different result representations are discussed and established in section 7.5. A detailed review of the sensitivities provided by NASTRAN with finite differences is summarized in section 7.6. Two sets of optimizations were performed. One, the minimization of wing skin mass while constraining aileron effectiveness, discussed in section 7.7, and two, the maximization of aileron effectiveness while constraining the wing skin mass, discussed in section 7.8. In both cases, strain and buckling constraints were adopted. The optimizations were performed for balanced and unbalanced laminates, to shed light on the influence of the increased design freedom for the latter laminate type.

This chapter is based on the paper, *Stiffness Optimization of Composite Wings with Aeroelastic Constraints* by J.K.S. Dillinger, T. Klimmek, M.M. Abdalla, & Z. Gürdal, [Dil13c], which appeared in *Journal of Aircraft*, 50.4, pp. 1159-1168, 2013. Note: symbols may have been changed to maintain consistency throughout this thesis.

As this research belongs to the first adoptions of the stiffness optimization process, minor deviations from the methods and models described in the first part of this thesis will be found. The reason for this is the enhancements made to the optimization process after application in the demonstration described in this chapter. When deviations occur, they will be noted in the text.

7.1 Model Description

Considering a possible and also most plausible application of the optimization process in the field of high aspect ratio passenger and transport aircraft, a decision was made to model an *A320* like wing. The original being built from aluminum, a transition to composite skins seems a realistic consideration, keeping in mind that a successor for the very successful *A320* aircraft family produced by *Airbus* might be a logical step in the manufacturers future plans. Nevertheless, only a very simplistic wing model compared to the original was considered, mainly reproducing geometric entities like the wing span of 34.1 m , a wing surface of 122.6 m^2 , and a leading edge back sweep of 26° . The wing was modeled with one transonic airfoil throughout the entire span, featuring a maximum thickness and camber of 11.95% and 1.45% respectively. Moreover, a dihedral of 2° was considered. An overview of the basic planform dimensions is provided in Figure 7.1.

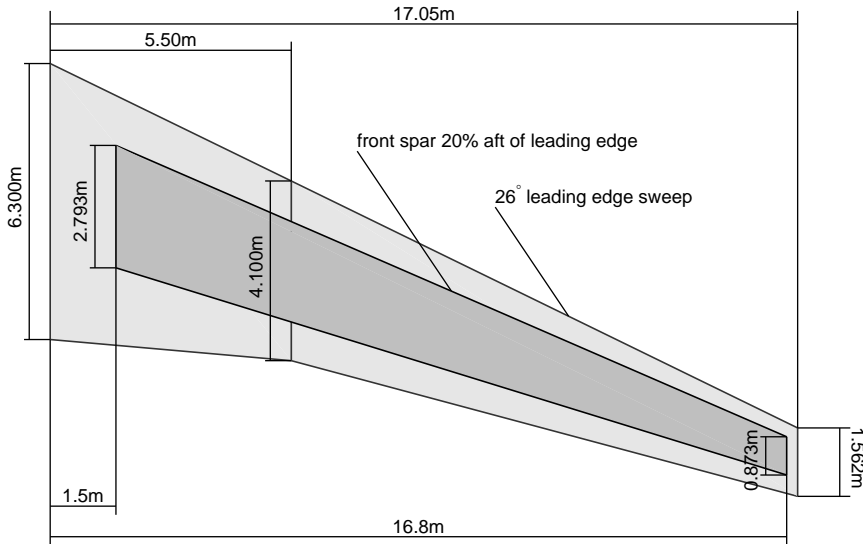


Figure 7.1: *Planform and wing box dimensions*

The load carrying wing box, as well depicted in Figure 7.1, features straight front and rear spar webs. Their locations are defined by the relative chordwise positions at wing root and tip, which is a constant 20% aft of the leading edge for the front spar, and 69% and 74% respectively, for the rear spar. The box does not cover the entire spanwise distention, keeping in mind the existence of a possible center wing

box, which was not incorporated in the investigation. More details on the structural setup will be provided in section 7.3.

7.2 Flight Envelope and Load Cases

In general, the selection of load cases (LC) to be considered in the design of the load carrying structure of an aircraft is well defined in the official design specifications belonging to the type of aircraft class considered. In Europe, those regulations are provided by the *European Aviation Safety Agency, EASA*. The class that applies for large passenger type aircraft is called CS-25 [EAS12]. Each aircraft belonging to a specific class has to comply with the specified regulations for that class.

Typically, CS-25 requires the verification of structural integrity for a large number of load cases, arising from the permutation of flight velocities, flight altitudes, mass cases and center of gravity, and aircraft configurations, the latter denoting for instance states with extended landing gear or various flap settings. Concentrating on the optimization process rather than absolute results, only one mass case was incorporated in the optimization, which will be discussed in more detail in the following section 7.3. Moreover, delimited by the finite element model resolution and detail, and the aerodynamic capabilities of the doublet lattice method, only the cruise configuration was investigated, leaving flight altitude and velocity as the remaining parameters when choosing load cases to be applied in the optimization.

The flight envelope is a visual means of defining the admissible operational range of an aircraft. It depicts the minimum and maximum flight velocities as a function of flight altitude. A simplified version of a flight envelope as it was constructed for selecting sizing and aileron effectiveness load cases for the stiffness optimization process is shown in Figure 7.2. The right boundary of the flight envelope can be generated, based only on the assumption of dive velocity $V_D = 381kts$ (CAS) and Mach number $M_D = 0.89$ above an altitude of 7500 m . The aeroelastic stability margin as claimed in the aircraft regulations (see also section 2.2.1) is obtained when multiplying the velocities of the regular flight envelope with a factor 1.15. In addition to the regular flight envelope, Figure 7.2 constitutes the dive and aeroelastic stability margin as a function of dynamic pressure q and *Mach* number M .

Table 7.1: Load case definition

| LC # | type | Ma [-] | q [Pa] | n_z [g] | H [m] |
|------|---------------------------|--------|---------|-----------|-------|
| 1 | sym., push down, M_D | 0.89 | 21200.0 | -1.0 | 7500 |
| 2 | sym., pull up, M_D | 0.89 | 21200.0 | +2.5 | 7500 |
| 3 | sym., pull up, V_D | 0.58 | 23500.0 | +2.5 | 0 |
| 4 | antisym., roll, $1.15V_D$ | 0.67 | 31500.0 | 0.0 | 0 |
| 5 | antisym., roll, $1.15V_D$ | 0.83 | 29700.0 | 0.0 | 4000 |
| 6 | antisym., roll, V_D | 0.58 | 23500.0 | 0.0 | 0 |
| 7 | antisym., roll, V_D | 0.73 | 22500.0 | 0.0 | 4000 |

Three representative structure sizing load cases were selected from the right boundary of a flight envelope, marked in yellow in Figure 7.2 and listed in table 7.1, LC 1

to 3. They incorporated pull up and push down maneuvers at limit load factors of $+2.5g$ and $-1.0g$, according to certification regulations.

Two load cases to obtain aileron effectiveness responses in terms of roll trims were defined along the aeroelastic stability margin, they are marked in white in Figure 7.2 and listed as LC 4 to 5 in table 7.1. Additional roll trims in altitudes $\geq 7500m$ would require *Mach* numbers equal to 1.0 and therefore beyond the capabilities of the doublet lattice method. Instead, two more roll trims LC 6 and 7 were defined on the dive velocity boundary.

7.3 Finite Element Model

The model generation process, as described in chapter 3, was applied to create an adequate finite element model of the load carrying wing box, the dimensions of the box are depicted in Figure 7.1. Exploiting symmetry, only one wing half had to be considered.

Looking at Figure 7.3 an impression can be gained of the finite element model, consisting of the lower skin, front and rear spar webs, and ribs. The top skin was removed to demonstrate the internal setup. Aside from ribs closing the wing box at root and tip and being positioned parallel to the free stream direction, thirteen equidistant internal ribs with a right angle alignment with respect to the front spar web were modeled.

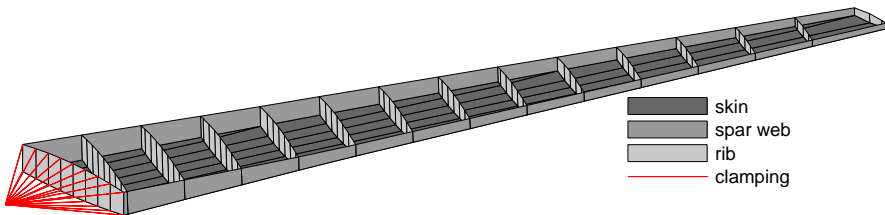


Figure 7.3: *Finite element model*

In order to decrease the wing skin buckling field size and contributing to the overall bending stiffness, seven parallel stringers starting at the wing box root were included in the finite element model. The equidistant distribution in chordwise direction at the wing box root with an interspace of 6%, referring to the local chord, lead to an absolute parallel distance of $\approx 322mm$. The stringers were aligned with the average angle of front and rear spar web, corresponding to 20.3° with respect to the global *y*-axis, as shown in Figure 7.4.

The wing was clamped at the root rib using a rigid element, as depicted in Figure 7.3 and 7.4. The central point of the clamping element is positioned on the symmetry plane at $y = 0$ and is also employed as an attachment point for a central point mass, as described below.

The element resolution in the wing skins was prescribed by the stringer and rib pitch. Each of these zones was discretized by a single shell element, in accordance with the chosen buckling analysis methodology as described in section 5.6.2. For proper connectivity of finite elements in the spar webs and ribs with the wing skin elements,

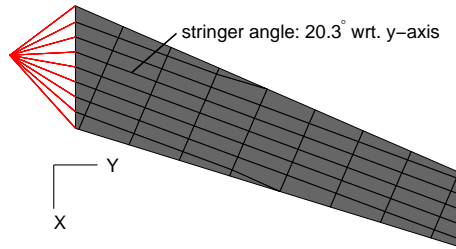


Figure 7.4: *Top skin stringer alignment*

their spanwise and chordwise element spacing had to be selected accordingly. Only the number of elements in wing thickness direction in spar webs and ribs was free to choose and set to one, to limit the amount of elements to a manageable size. The stringer meshing was predetermined by the rib pitch.

Properties

All structural components except for the stringers were modeled using the same fiber material, the ply properties of which are listed in Table 7.2.

Table 7.2: *Single ply material properties*

| E_{11} | E_{22} | G_{12} | ν_{12} | ρ |
|----------------------|---------------------|---------------------|------------|-----------------------|
| $83.0e9 \text{ GPa}$ | $8.5e9 \text{ GPa}$ | $4.2e9 \text{ GPa}$ | 0.35 | 1452 kg/m^3 |

The initial thickness distribution of the wing skins was the same for upper and lower skin, comprising a linear variation from 20.0 mm at the root to 4.0 mm at the tip and a symmetric layup with $[-45_{22.2}/+45_{22.2}/90_{11.19}/0_{44.41}]_s$, where the angle subscripts denote the percentage ply thickness contribution to the overall thickness. The ply angles were defined with respect to an axis that aligned with the average sweep of front and rear spar and hence corresponding to the stringer alignment. The spar shear webs were modeled with a thickness variation from 20.0 mm at the root to 15.0 mm at the tip and a $[-45_{35}/+45_{35}/90_{20}/0_{10}]_s$ layup. The ribs had a constant thickness of 8.0 mm and a quasi-isotropic symmetric layup $[\pm 45/90/0]_s$. According to classical lamination theory the stacking sequences were transformed to membrane and bending stiffness matrices, as requested by the optimizer.

Stringers were modeled as bar elements and properties were kept constant throughout the wing with the cross-sectional and material properties listed in table 7.3 and 7.4 respectively.

Table 7.3: *Stringer cross-sectional properties*

| A | I_1 | I_2 | J |
|-------------------------|-------------------------|-------------------------|-------------------------|
| $1.2000e-3 \text{ m}^2$ | $5.8380e-7 \text{ m}^4$ | $1.7570e-7 \text{ m}^4$ | $2.1710e-8 \text{ m}^4$ |

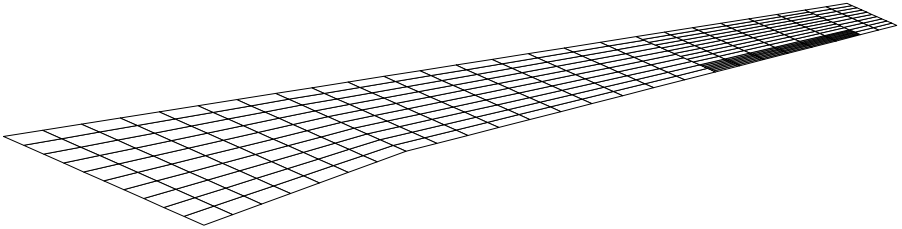
Table 7.4: *Stringer material properties*

| E | G | ν | ρ |
|-------------|-------------|-------|------------------------|
| 143.5e9 GPa | 14.99e9 GPa | 0.392 | 1452 kg/m ³ |

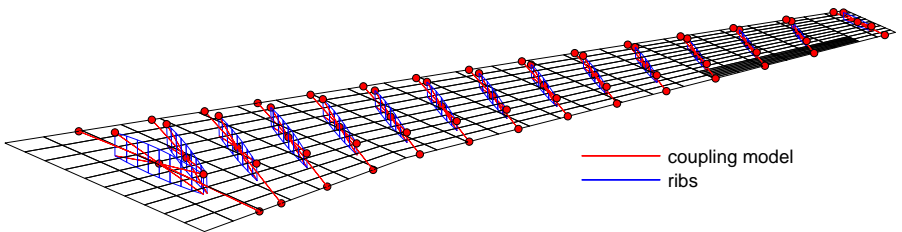
DLM and Coupling

The aerodynamic model, Figure 7.5 is based on the doublet lattice method, as described in section 3.4 and generated by MODGEN. No aero correction in terms of a W2GJ matrix or a CFD correction as described in section 6.2 were applied at this point.

To investigate aileron effectiveness, a trailing edge control surface was provided in the outer wing, ranging from 85% to 95% of the halfspan, corresponding to $y = 14.493\text{ m} - 16.198\text{ m}$, and a depth of 20% of the local chord.

**Figure 7.5:** *Doublet lattice model*

The coupling model was based on the load reference axis definition, compare Figure 3.6 in section 3.4.3, with a slight modification. Two additional rows of coupling points were introduced at the intersection of front and rear spar with the upper wing skin and the ribs. Calculations showed that in this particular case a smoother distribution of the aerodynamic forces could be achieved. The coupling model along with the ribs to which it attaches, and the DLM mesh are shown in Figure 7.6.

**Figure 7.6:** *Coupling model*

Mass

With the intention to demonstrate optimizer functionality rather than predications concerning the optimized absolute numbers such as skin thickness, no additional non-

structural masses like leading and trailing edge, engine, or fuel model were yet considered in the wing. The sole exception was a mass of 35 tons, positioned on the symmetry plane and attached to the clamping element fixing the wing root, to represent an aggregation of half the remaining aircraft mass, consisting of fuselage, tailplanes and payload.

7.4 Optimization Model

The setup of appropriate design fields and responses, along with an overview on response and sensitivity numbers is treated in this section and specialties in the response approximations are discussed.

7.4.1 Design Variables and Responses

Considering the upper and lower wing skin for stiffness optimization, design fields that feature equal stiffness properties were derived according to the methodology described in section 4.1, and are shown in Figure 7.7.

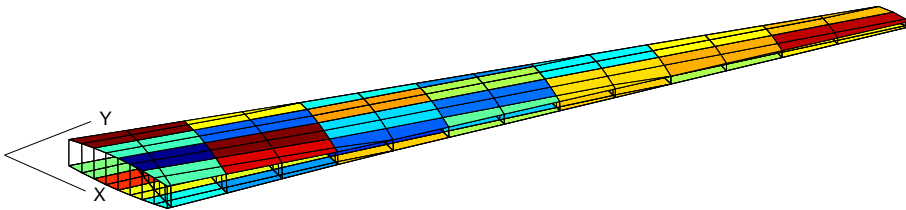


Figure 7.7: *Design fields*

The wing skins were divided into 22 design fields, totaling 44 independent materials. With each field comprising thirteen design variables, the number of design variables amounts to 572 in total. Each wing skin was composed of 84 elements, summing up to 168 elements to be considered for strength and buckling responses.

The responses requested from NASTRAN for three sizing load cases as listed in table 7.1 are shown in table 7.5(a). The amount of stress responses is a result of the six stress responses required in the calculation of the strain and buckling responses, compare table 4.1 on page 57, hence $168 \cdot 3 \cdot 6 = 3024$. Despite not being restrained or set as objective in the optimization, per sizing load case 15 twist responses were requested for monitoring reasons, one for each central load reference axis node in a rib plane, resulting in a multiple of 15 for the total amount of twist responses. To compute aileron effectiveness response and sensitivity, two additional responses according to equation (2.2) on page 29 are necessary. Accordingly, four aileron effectiveness responses require the consideration of twelve NASTRAN responses. Along with 572 design variables this amounts to $\approx 1.8e6$ sensitivities.

A similar list can be set up for the number of responses passed to the optimizer, table 7.5(b). Considering the two most critical buckling modes per element, the number of buckling responses is twice the number of strain failure responses. The total number of sensitivities then sums up to $\approx 0.9e6$.

Table 7.5: *Number of responses*

| (a) NASTRAN | | (b) optimizer | |
|-------------------------|-------|-------------------------------|------|
| # of weight responses | 1 | # of weight responses | 1 |
| # of stress responses | 3024 | # of strain failure responses | 504 |
| # of ail.eff. responses | 4 + 8 | # of buckling responses | 1008 |
| # of twist responses | 45 | # of ail.eff. responses | 4 |
| ⇒ total: | 3082 | # of twist responses | 45 |
| | | ⇒ total: | 1562 |

7.4.2 Approximations

Instead of convexified aeroelastic response approximations, only linear approximations of twist and aileron effectiveness were applied, table 7.6.

Table 7.6: *Response approximations*

| | | | |
|-----------------------|----------------------|---|---|
| strength | \tilde{r}_i | = | $\Phi_i^m : \mathbf{A}_i^{-1} + \Psi_i^m : \mathbf{A}_i + s_i^t \Delta N_i$ |
| buckling | \tilde{r}_i | = | $\Phi_i^b : \mathbf{D}_i^{-1} + s_i^t \Delta N_i$ |
| mass | \tilde{m} | = | $\sum_j \alpha_j h_j$ |
| aileron effectiveness | $\tilde{\eta}_{ail}$ | = | $\sum_j \Psi_j^m : \mathbf{A}_j + \Psi_j^b : \mathbf{D}_j + \alpha_j h_j$ |
| twist | $\tilde{\vartheta}$ | = | $\sum_j \Psi_j^m : \mathbf{A}_j + \Psi_j^b : \mathbf{D}_j + \alpha_j h_j$ |

The strain allowables for constructing the failure envelope and calculation of the strain failure indices are $[\varepsilon_t, \varepsilon_c, \gamma_{xy}] = [0.55\%, -0.70\%, 0.60\%]$. These values already account for a required safety factor of 1.5. Consequently, the load cases listed in table 7.1 are treated as limit loads.

7.5 Starting Design

Starting design in this context denotes the initial thickness and stiffness distributions of the shell entities to be optimized. While structural data were provided in section 7.3 in conjunction with the description of the finite element properties, the focus of this section will be the visual implementation and the consequent initial structural responses.

The starting design for all subsequent optimizations is illustrated in Figure 7.8, with the initial thickness distribution of the wing skins as shown in Figure 7.8(a). As described in section 7.3, the thickness varied linearly in span direction. Shown in Figure 7.8(b), for each field in the upper skin, is a polar plot of the thickness normalized engineering modulus of elasticity. Its derivation was described in section 1.1.3, equation (1.31) on page 12. The x-axis of the material coordinate system, corresponding to the 0° direction, is indicated with a black solid line. As can be seen from the plot in Figure 7.8(b), the main stiffness in the starting design lies in the 0° direction, resulting from the initial layup having the majority of fibers in 0° . The lower side resembles the upper one, so no graphical representation needs to be provided. A detailed explanation on the stiffness distributions to be expected

for prescribed stacking sequences was provided in section 1.1.3, where Figure 1.5(f) on page 13 already introduced the starting design stiffness distribution depicted in Figure 7.8(b). It should be noted that this type of stiffness representation will later on constitute an important contribution to the assessment of optimized designs.

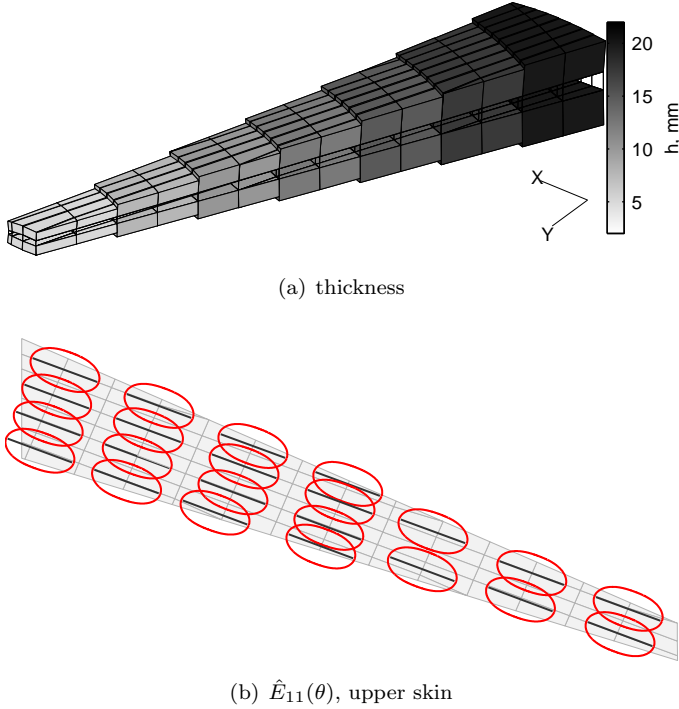


Figure 7.8: Starting design, thickness and stiffness distribution

Based on an agreement on structural properties and along with the load cases summarized in table 7.1, the structural and aeroelastic responses could be computed, the former ones being depicted in different ways in Figure 7.9 and 7.10. Strain and buckling failure indices, as derived in sections 5.6.1 and 5.6.2, are shown in Figure 7.9(a) and 7.9(b) for load cases 1 and 2 in a two-dimensional representation. Element numbers 1 to 84 belong to the upper skin, element numbers 85 to 168 to the lower skin; inner to outer wing respectively. While failure indices for the $n_z = -1.0g$ maneuver LC 1, Figure 7.9(a), remain markedly below the upper limit of $r = 1.0$, the failure indices for the $n_z = +2.5g$ maneuver LC 2, Figure 7.9(b), increase noticeably. Due to the close resemblance with results from LC 2, LC 3 failure indices are not shown. All elements staying within the feasible region and featuring more or less uncritical failure indices indicates a considerable margin of possible weight improvement, the reason being that unstressed elements suggest a material excess. More insight into this will be given in the optimization result descriptions in sections 7.7 and 7.8.

Another method for visualizing failure indices is shown in Figure 7.9(c) and 7.9(d). These plots depict, for each element under consideration, the most active constraint in all three sizing load cases, on a color scale ranging from strain, “Str.,” red color,

to buckling, “Buckl.”, blue color, for upper and lower skin respectively. In the case where both failure indices, strain and buckling, are close, this is indicated by a color change to yellow. Figure 7.9(c), upper skin, for instance features a transition from mainly strain failure indices in the inner wing to buckling failure indices in the outer wing. This is reflected in the two-dimensional failure index plot Figure 7.9(b), which showed that LC 2 gives larger failure indices than LC 1, and that in the upper skin, outer wing, buckling failure indices surmount strain failure indices. Plots of the type

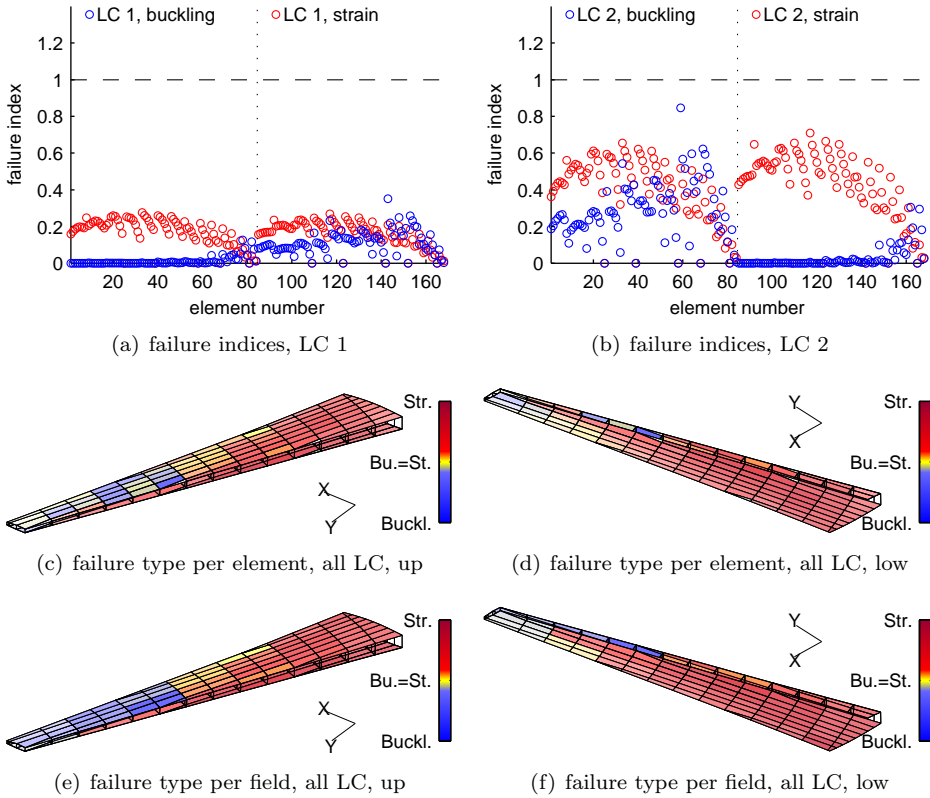


Figure 7.9: Starting design, failure indices

shown in Figure 7.9(c) can also be generated for single load cases, in which case they basically constitute a three-dimensional representation of Figure 7.9(a). The missing information on the magnitude of the failure index is covered by the color intensity. The lighter the color, the lower the maximum failure index. It is important to note that during the optimization eventually within each design field only the element with the highest failure index will primarily drive the thickness and stiffness sizing of the corresponding field unless more than one element outgoes the feasible response region and violates the constraint. In that case the violating elements will share the contribution to the design step. With that said, Figure 7.9(e) and 7.9(f) finally constitute the critical failure types not on element, but on field level, thus allowing for the determination of the dominant and sizing relevant structural failure constraints.

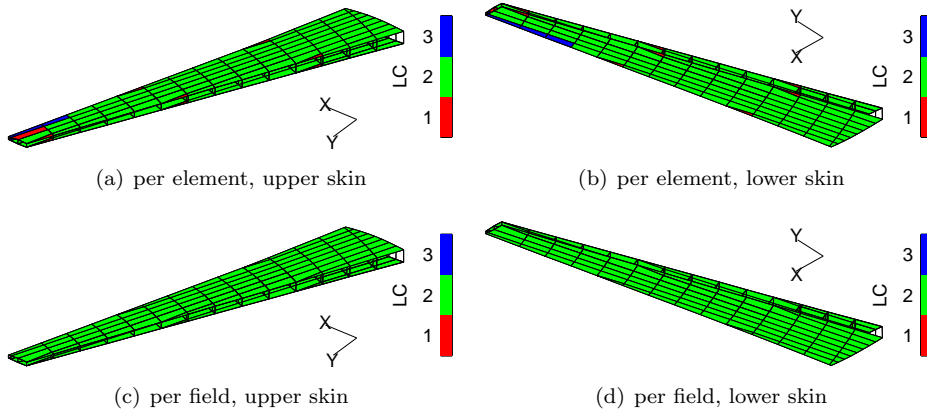


Figure 7.10: *Starting design, sizing load cases*

Instead of concentrating on the failure type, another way of evaluating and visualizing the failure indices is to sort them according to load cases. The sizing load cases that provoke the highest failure index within a design field and therefore drive the optimization are depicted in Figure 7.10(c) and 7.10(d). Clearly, for the starting design load case 2 generates the largest failure indices throughout the entire upper and lower skin. Figure 7.10(a) and 7.10(b) eventually denote the failure load case on element, rather than on field level.

7.6 Sensitivity Check

A brief introduction to the NASTRAN methodology of computing response sensitivities with respect to the design variables was given in section 4.4. In order to review the process of importing, sorting and processing of NASTRAN sensitivities effectively, in this section the comparison of sensitivities emanating from NASTRAN and finite differences is outlined.

Sensitivity generation with finite difference involves the variation of a design variable x by an amount Δx and the corresponding change in the considered response f . A central scheme of second order accuracy, equation (7.1):

$$\left. \frac{\partial f}{\partial x} \right|_{x_0} = \frac{f(x_0 + \Delta x) - f(x_0 - \Delta x)}{2\Delta x} + O(\Delta x^2), \quad (7.1)$$

was used to compute the sensitivities.

To this end, the previously described starting design in combination with load case 2, table 7.1, was considered for a variation of the stiffness parameters belonging to design field 1, Figure 7.11.

Sensitivities were considered for all thirteen design variables emanating from the fields stiffness description. Both stiffness matrices, $\hat{\mathbf{A}}$ and $\hat{\mathbf{D}}$ were varied by an incre-

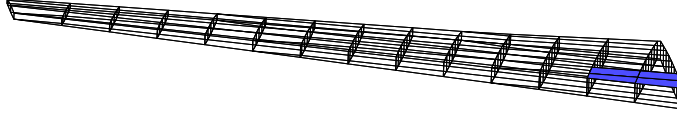


Figure 7.11: Design field 1

ment relating to their trace, equations (7.2) and (7.3):

$$\Delta \hat{\mathbf{A}} = \frac{1}{h} (\text{trace}(\mathbf{A}) * \epsilon) , \quad (7.2)$$

$$\Delta \hat{\mathbf{D}} = \frac{12}{h^3} (\text{trace}(\mathbf{D}) * \epsilon) , \quad (7.3)$$

where ϵ controls the incremental step size, as discussed below. A modified element in the stiffness matrices simply becomes:

$$\hat{A}_{ij}|_{new} = \hat{A}_{ij} + \Delta \hat{A} , \quad (7.4)$$

$$\hat{D}_{ij}|_{new} = \hat{D}_{ij} + \Delta \hat{D} , \quad (7.5)$$

where subindices ij denote the six independent elements within each stiffness matrix. The thickness was varied accordingly, equation (7.6):

$$\Delta \hat{h} = \hat{h} * \epsilon , \quad (7.6)$$

$$\hat{h}|_{new} = \hat{h} + \Delta \hat{h} . \quad (7.7)$$

The dependence of stiffness matrices \mathbf{A} and \mathbf{D} on thickness \hat{h} requires a modification of the normalized stiffness matrices $\hat{\mathbf{A}}$ and $\hat{\mathbf{D}}$, compare equation (1.27) and (1.27) on page 10:

$$\hat{\mathbf{A}}|_{new} = \hat{\mathbf{A}} \frac{\hat{h}}{\hat{h}|_{new}} , \quad (7.8)$$

$$\hat{\mathbf{D}}|_{new} = \hat{\mathbf{D}} \frac{\hat{h}^3}{\hat{h}^3|_{new}} . \quad (7.9)$$

Equations (7.8) and (7.9) ensure invariable stiffness matrices \mathbf{A} and \mathbf{D} when considering the derivation of sensitivities with respect to thickness. Increments were controlled by variable ϵ , which was set to 0.05 for all finite difference calculations. Smaller values for ϵ did not cause considerable changes compared to the one selected.

The force resultant \mathbf{N}_i in each element i belonging to a design field was selected for the sensitivity check. \mathbf{N}_i is computed with shell stresses derived from NASTRAN according to equation (5.43) and repeated here for ease of reading:

$$N_i = \frac{1}{2} \hat{h}_i (\sigma_i^u + \sigma_i^l) . \quad (7.10)$$

Figure 7.12, 7.13 and 7.14 exemplify the sensitivities of stress resultant component N_y with respect to \mathbf{A} , \mathbf{D} and h respectively, as a function of element number. Elements belonging to design field 1, hence the field with varying stiffness, are marked

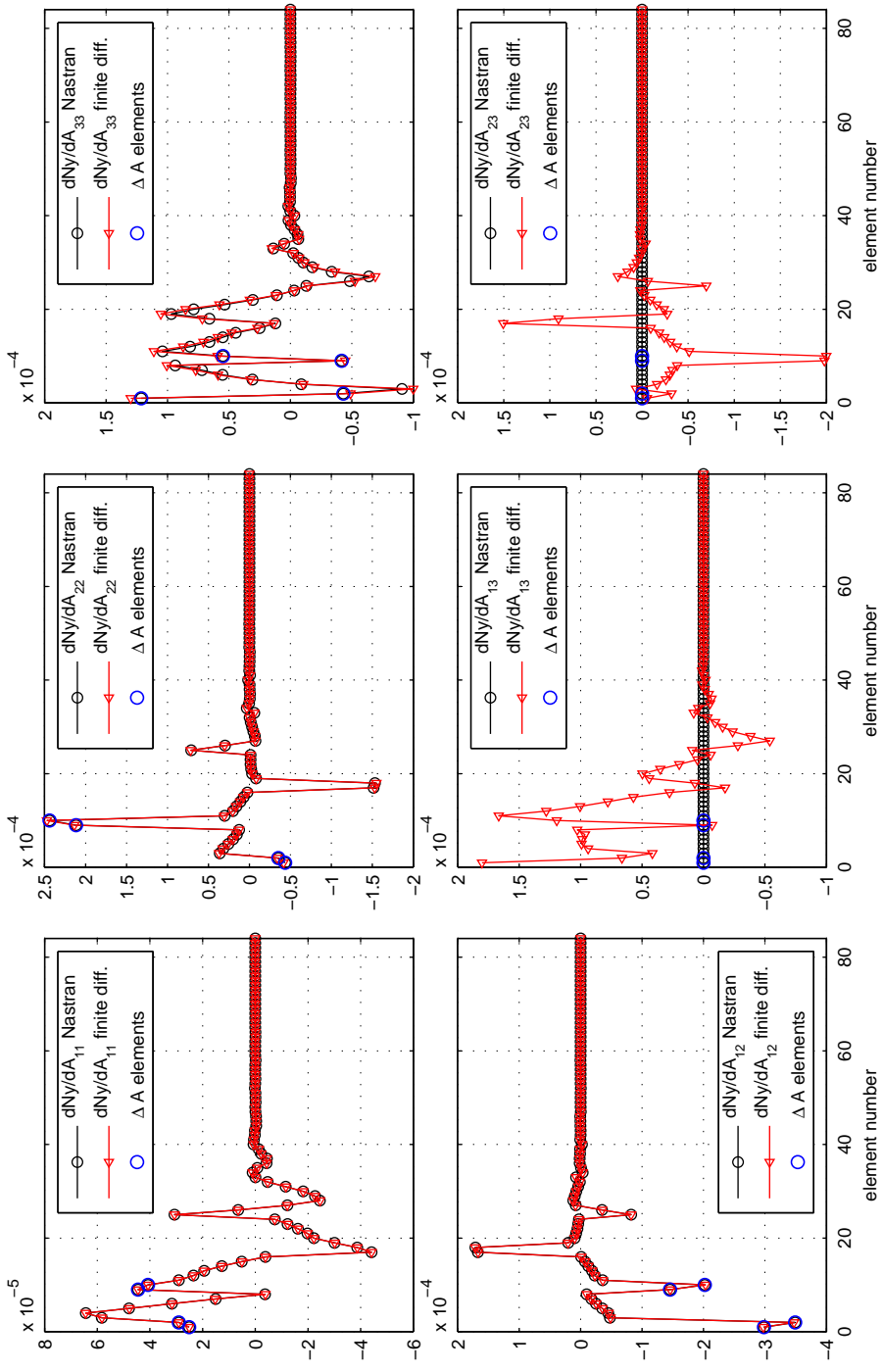


Figure 7.12: $\partial N_y / \partial A$, upper skin

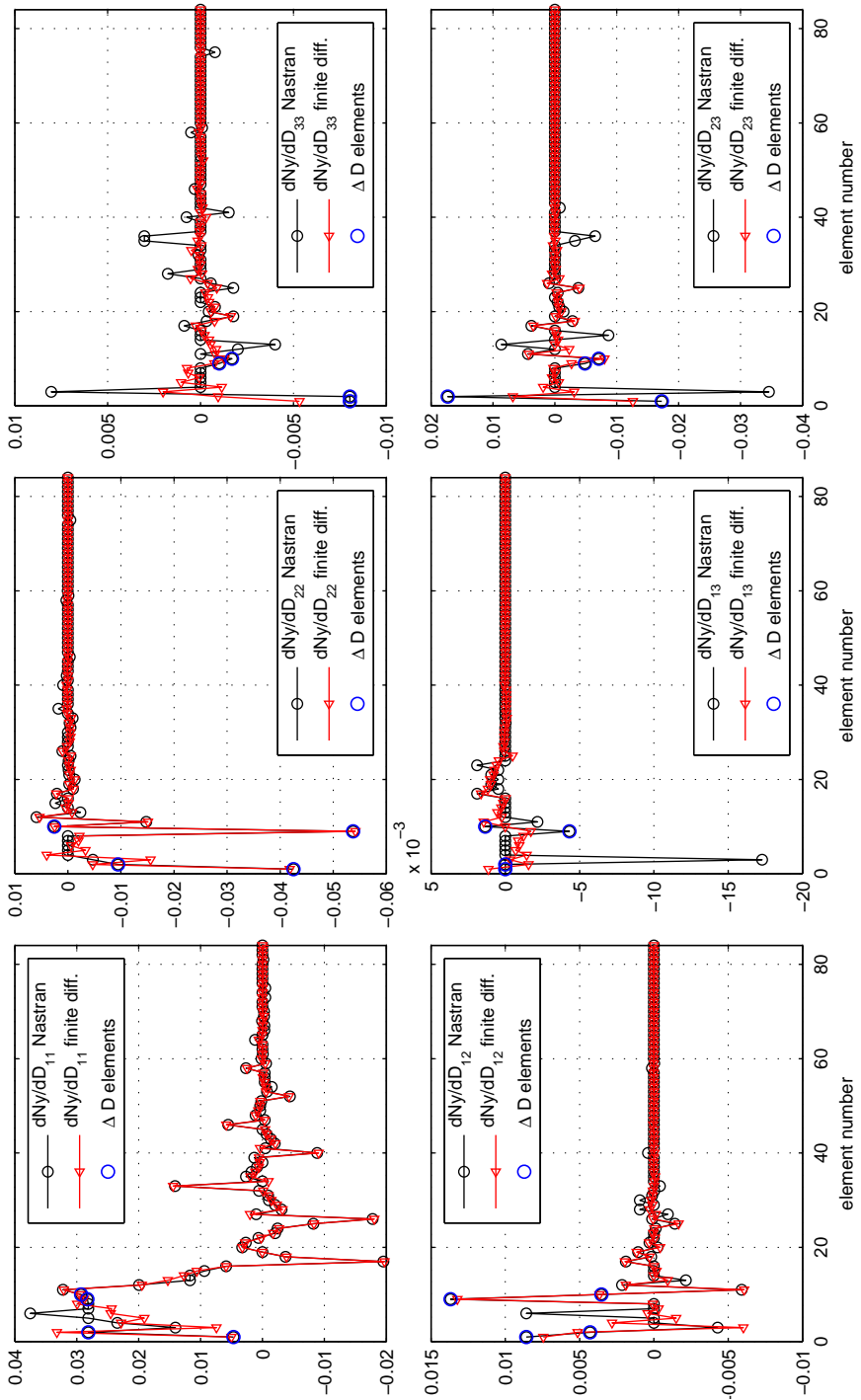


Figure 7.13: $\partial N_y / \partial \mathbf{D}$, upper skin

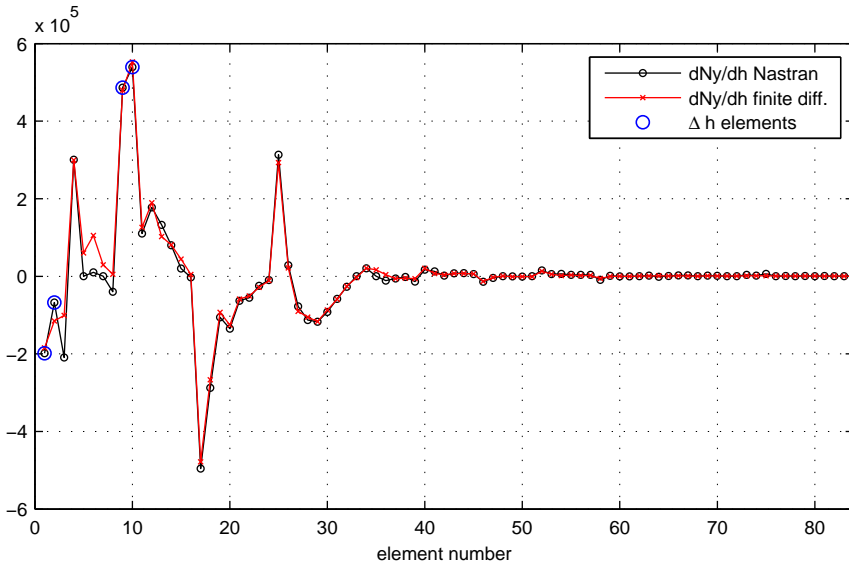


Figure 7.14: $\partial N_y / \partial h$, upper skin

with a blue circle. To preserve clarity, the plots are limited to upper skin elements only.

As indicated in Figure 7.12, the NASTRAN sensitivities with respect to membrane stiffness matrix \mathbf{A} match very well with the results obtained with finite difference, except for the coupling terms A_{13} and A_{23} , for which the NASTRAN sensitivities are zero. Sensitivities with respect to the bending stiffness display some deviations, Figure 7.13. Again, the NASTRAN sensitivities for coupling terms D_{13} and D_{23} , are zero except for a few discrete points. The reason for the deviations can be found in the very small dependence of the stress resultant on the bending stiffness and accompanying numerical issues. However, the wing skins being loaded almost exclusively as membrane rather than bending elements, considerably diminishes the influence of the corresponding bending stiffness sensitivities. NASTRAN and finite difference sensitivities with respect to thickness, Figure 7.14, match again quite closely.

The coupling sensitivities with respect to A_{13} and A_{23} as well as D_{13} and D_{23} being zero is the result of a NASTRAN deficiency, as will be demonstrated in the following. The most prominent feature of a balanced laminate, as it was modeled in the wing skins starting design, section 7.5, is the fact that no coupling of in-plane normal strain $\varepsilon_x, \varepsilon_y$ and shear strain γ_{xy} , and no coupling of out-of-plane bending κ_x, κ_y and twisting κ_{xy} exists (compare section 1.1.1). Accordingly, stiffness matrix elements A_{13} and A_{23} respectively D_{13} and D_{23} are zero. Nevertheless, the sensitivities with respect to those terms are not. For that reason, an additional investigation with the wing skin starting design stacking sequence tilted by 5° , hence $[-40_{22.2} / +50_{22.2} / -85_{11.19} / 5_{44.41}]_s$ was considered, thereby slightly unbalancing the stiffness matrices. The sensitivity results for membrane stiffness sensitivities are shown in Figure 7.15. Clearly, also the NASTRAN off-diagonal sensitivities with respect to A_{13} and A_{23} now closely resemble the finite difference results.

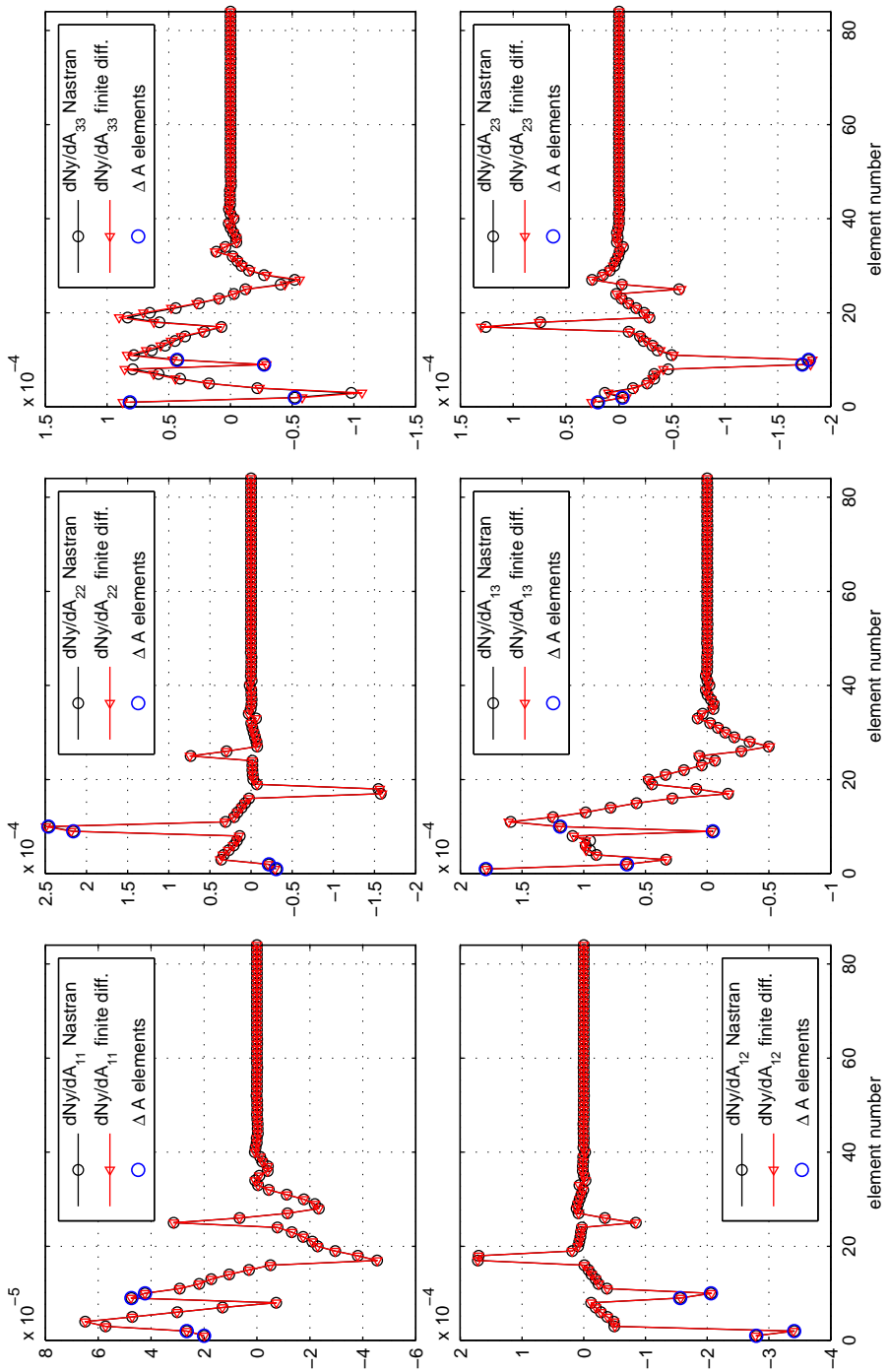


Figure 7.15: $\partial N_y / \partial A$, unbalanced laminate, upper skin

Optimizations featuring balanced laminates will not be influenced by the false NASTRAN sensitivities, since coupling terms will remain zero throughout the optimization. Optimizations featuring unbalanced laminates in contrast require sensitivities with respect to the coupling terms, in which case a rotation of initially balanced starting designs needs to be considered.

7.7 Numerical Results: Mass Minimization

In a first application the wing skin mass was minimized while applying strain and buckling constraints to each element belonging to a design field and for the sizing load cases stated in table 7.1. In addition, aileron effectiveness was constrained to values larger than zero to prevent aileron reversal. In the following sections the results for balanced and unbalanced stiffness matrices are depicted.

The results were confirmed using calculations starting from a different initial design, comprising altered starting stiffnesses and thicknesses. For most of these cases the differences in objective function value were within the accuracy of the stopping criterion defined in Equation (5.3) on page 64; δ_{stop} was set to 0.001, equivalent to an upper limit of 0.1% change in subsequent successful iteration steps. The majority of the design fields showed similar principal stiffness distributions for different optimization runs. Only very few fields exhibited deviations in stiffness distribution or thickness, and if so, in less loaded regions only. Clearly, the fewer constraints active in a field, the more design freedom is given to the optimizer without influencing the objective.

7.7.1 Balanced Laminates

The essence of a stiffness optimization, aside from general characteristics like serviceability, reproducibility and robustness, certainly lies in the achievable quantity of the response defined as the objective. Consequently, the development of the mass objective as function of the iteration steps is depicted in Figure 7.16. As the plot shows, the starting design comprised a wing skin mass of 1122 kg, which was optimized to a minimum of 522 kg after 28 iteration steps. While the largest weight saving steps occurred within the first ≈ 8 iterations, the optimization continued with smaller improvements until the convergence criterion was fulfilled.

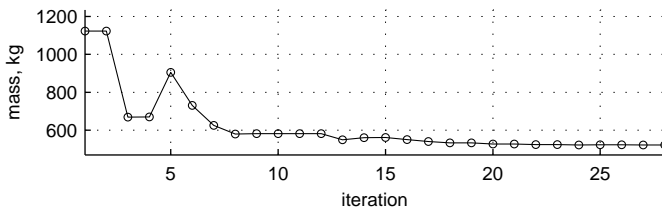


Figure 7.16: Mass development, balanced laminates

The corresponding optimized skin thickness distribution is shown in Figure 7.17. From this plot it can be seen that local increases of stress in an element, especially in the vicinity of ending stringers, led to local thickening of an entire field.

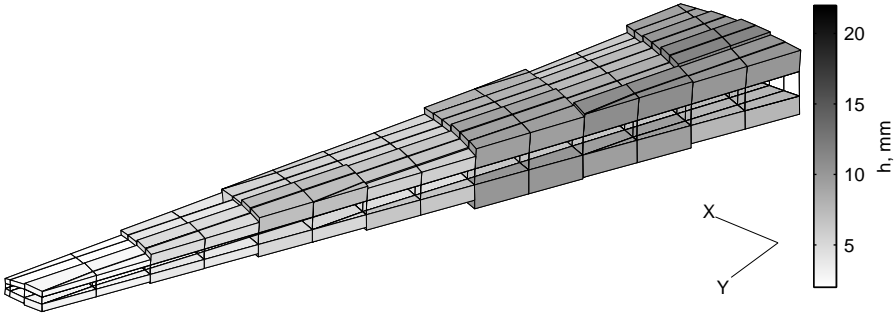


Figure 7.17: *Optimized design, thickness distribution, balanced laminates*

Figure 7.9(a) and 7.9(b) indicated a weight saving potential for the starting design based on the margin of the failure indices with respect to a failure limit of 1.0. The failure indices of load case 1 and 2 for the optimized design are depicted in Figure 7.18. The plots demonstrate a considerable change in the utilization of all elements. For the $-1g$ push down load case 1, Figure 7.18(a), most buckling indices in the lower skin, elements 85-168, reach the limit value of 1.0, also a few elements in the outer wing, upper skin, exhibit increased buckling failure indices. The fieldwise clustering of elements impedes that all elements can reach the limit. The strain failure indices for LC 1 however stay below 0.5 and do not affect the design. The $+2.5g$ pull up load case 2, shown in Figure 7.18(b), apparently causes a considerable influence on the structural layout by providing failure indices close to 1.0 throughout the entire wing. Buckling constraints clearly dominate the upper skin, while strain failures are active only in the inner wing, upper and lower skin.

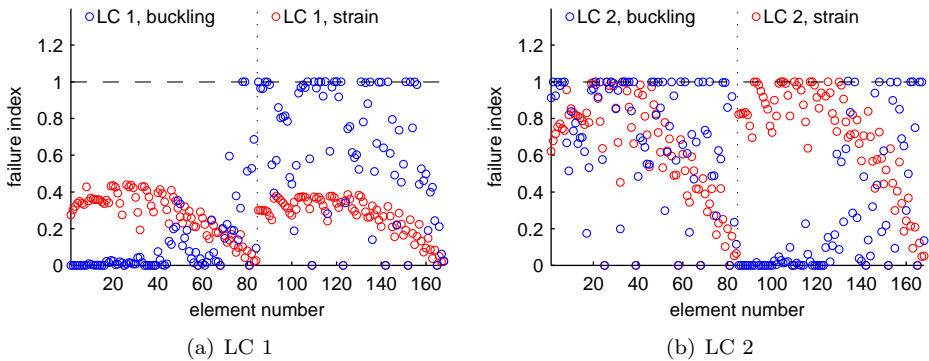


Figure 7.18: *Optimized design, failure indices, balanced laminates*

Looking at Figure 7.19 it becomes clear, which failure type bears the largest influence in the structural layout of the wing skins by summarizing the failure indices of all sizing load cases. Red elements indicate mainly strain and blue mainly buckling failure index dominated elements. It was chosen for an element rather than fieldwise

representation. The plots indicate that both, upper and lower skin are dominated by buckling constraints, while exhibiting nearly equal failure modes in an intermediate region, accented in yellow. Only few regions exist with predominant strain failure, mainly in the lower skin. In principal, Figure 7.19 reflects the results discussed in Figure 7.18.

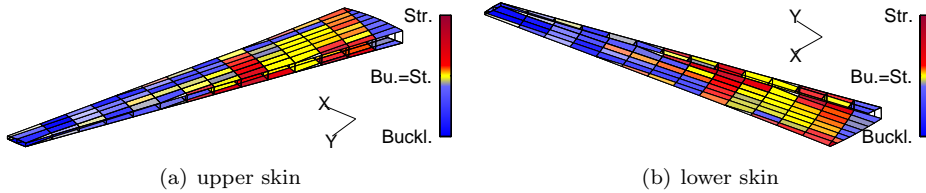


Figure 7.19: *Optimized design, failure type per element, all load cases, balanced laminates*

Finally the load cases featuring the highest failure index within a design field are highlighted in Figure 7.20, therefore driving the structural sizing in this particular region. As already shown in the two-dimensional representation given in Figure 7.18, the $+2.5g$ pull up load case 2 is responsible to a great extent for the highest failure indices in the upper wing skin, while the $-1g$ push down load case 1 dominates, with a few exceptions, most of the lower wing skin. The second $+2.5g$ pull up load case 3, which was not shown in Figure 7.18 due to its slightly lower failure indices when compared to LC 2, apparently does contribute to the maximum failure indices, albeit only in one design field of the lower skin.

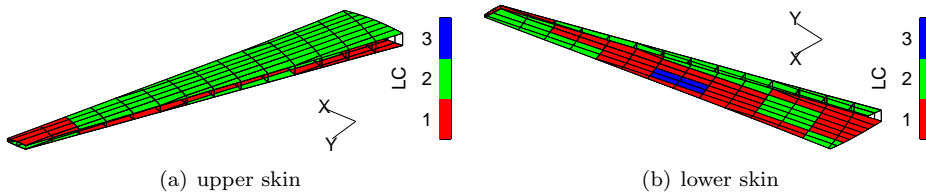


Figure 7.20: *Optimized design, sizing load case per field, balanced laminates*

The most prominent and also dominant design feature when dealing with fiber composites is the directional dependence of stiffness, hence the polar stiffness distribution. In addition to the final thickness distribution shown in Figure 7.17, Figure 7.21 depicts the optimized polar stiffness distribution in each design field by representing the thickness normalized engineering modulus of elasticity, as derived from the membrane stiffness matrix according to equation (1.31) on page 12. The distributions being symmetric with respect to the material coordinate axis, drawn in black, is a direct result of the restriction to balanced laminates.

The stiffness distributions reveal the consequence of a mainly buckling dominated optimization without constraints on twist or deflection. As a result of strain allowables and buckling field size, the main stiffness directions for the mass minimal design were no longer pointing in the span direction but rather at angles of $\approx \pm 45^\circ$ to $\pm 75^\circ$ with

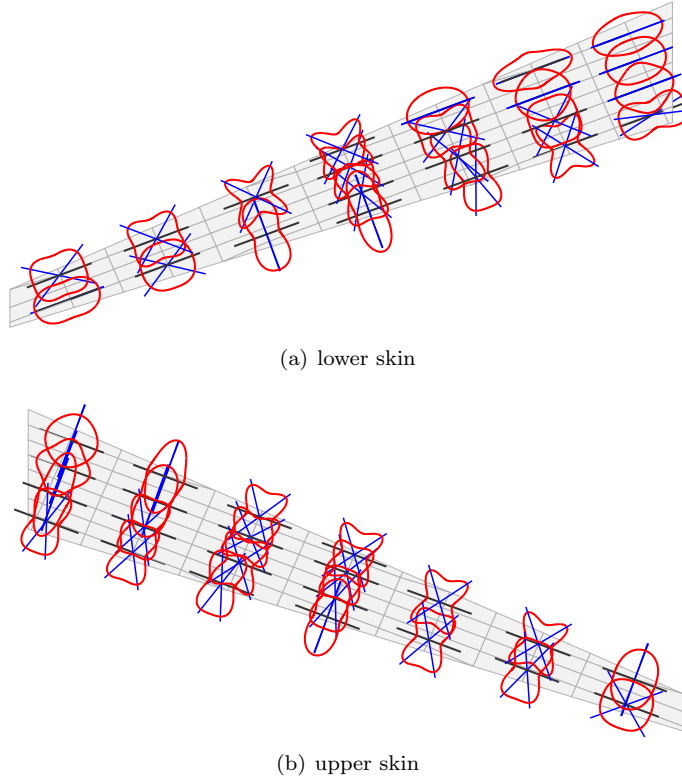


Figure 7.21: *Optimized design, $\hat{E}_{11}(\theta)$, balanced laminates*

respect to the material coordinate system. Only the root region of the wing on the lower side, experiencing the largest tensile strains in $+2.5g$ pull up maneuvers, still had the main stiffness direction aligned with the spanwise direction.

The aileron effectiveness constraint did not become active during the optimization, Figure 7.22. The smallest $\eta_{ail} = 0.0086$ occurred for load case 5. The convergence towards a cross-ply like stiffness distribution with $\approx \pm 45^\circ$ main stiffness direction promoted an increase of the torsional stiffness and helped to maintain aileron effectiveness, compare section 2.2.1.

7.7.2 Unbalanced Laminates

The change from balanced to unbalanced laminates corresponds to a considerable change in the design philosophy, since it both introduces the possibility of additional coupling mechanisms among the in or out-of-plane degrees of freedom, and it allows for a full adjustment of the major stiffness direction. While balanced laminates remain symmetric in their stiffness properties with respect to the material coordinate system they are defined for, unbalanced laminates are not bound to symmetry.

The increased design space is reflected in a lamination parameter quantity doubling. Equation (1.30) on page 11 in section 1.1.2 showed that only the invariants $\mathbf{\Gamma}_2$

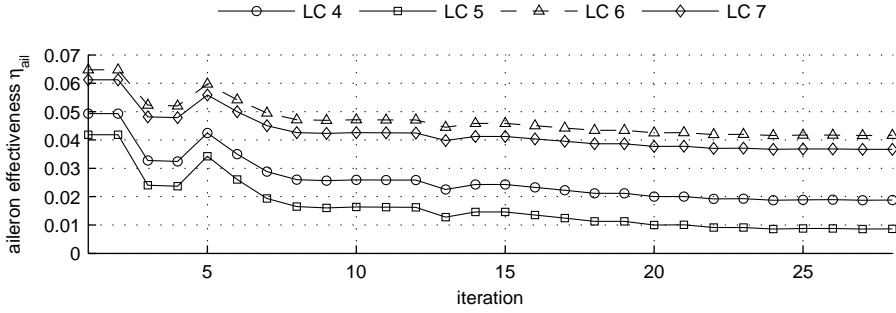


Figure 7.22: Aileron effectiveness η_{ail} development, balanced laminates

and $\mathbf{\Gamma}_4$ add stiffness matrix terms coupling strain and shear or bending and twisting. Other than for balanced laminates, these matrices can now contribute to the stiffness distributions.

Minimizing the wing skin mass with unbalanced laminates thus leads to an optimized weight of 486 kg compared to 522 kg with balanced laminates. This corresponds to $\approx 7\%$ weight saving. The convergence history of skin mass is shown in Figure 7.23. Whenever a constraint is violated, mass is either kept constant or increased until the design resides again in the feasible region, as indicated by the horizontal steps in Figure 7.23. More iterations steps are required to reach convergence compared to the balanced laminate optimization. Nevertheless, this behavior is not generally valid, since depending on the starting point, some optimizations converge faster than others.

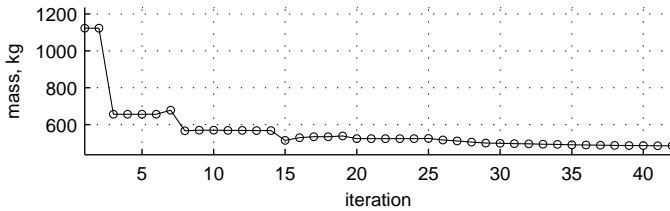


Figure 7.23: Mass development, unbalanced laminates

The optimized thickness distribution in two- and three-dimensional representations are depicted in Figure 7.24. Looking at Figure 7.24(a), the upper skin elements 1 to 84 exhibit considerably larger thicknesses than the lower skin elements. This emphasizes the effect of buckling loads predominantly sizing the structure. While the lower skin is dominated by buckling constraints in the $-1.0g$ push down maneuver LC 1, the upper skin is dominated by buckling constraints in the $+2.5g$ pull up maneuver LC 2, leading to increased thicknesses.

The failure indices shown in Figure 7.25, resemble the balanced results in Figure 7.18, however, even more buckling indices approach the critical value of 1. This is also reflected in the failure type accounting for the highest failure index, Figure 7.26. Other than for Figure 7.19, a fieldwise rather than an elementwise display was chosen,

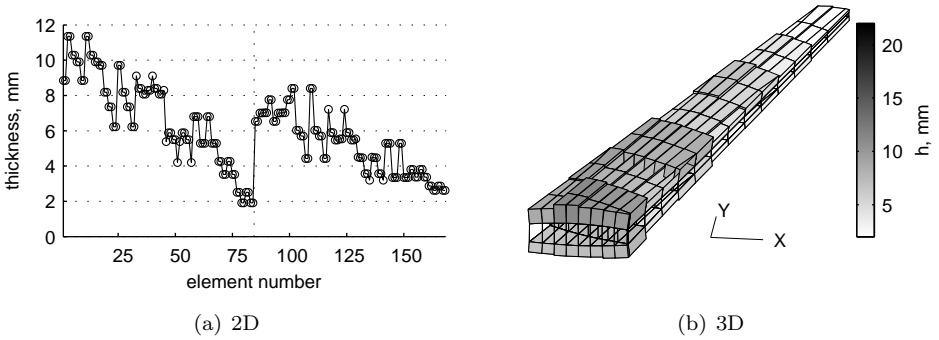


Figure 7.24: Optimized design, thickness distribution, unbalanced laminates

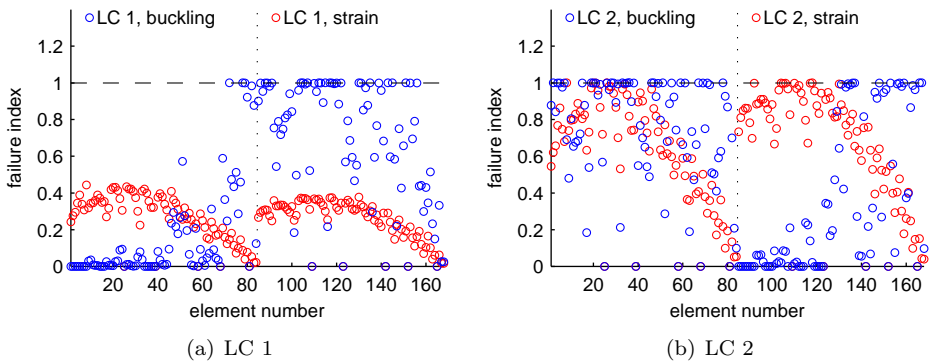


Figure 7.25: Optimized design, failure indices, unbalanced laminates

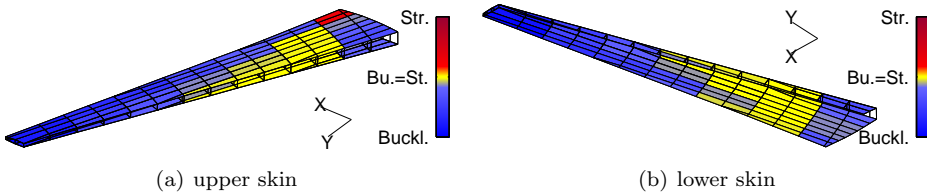


Figure 7.26: Optimized design, failure type per field, all load cases, unbalanced laminates

considering the overall largest failure index per design field and all sizing load cases. Only one field in the upper skin with surpassing strain failure remained. All the other fields were sized predominantly by buckling (blue) or a mix of buckling and strain (yellow).

The aileron effectiveness constraint demands no aileron reversal ($\eta_{ail} \geq 0$) for all the investigated roll load cases and was just reached at the end of the mass optimization, Figure 7.27. Other than for the balanced optimization, η_{ail} thus becomes an active constraint.

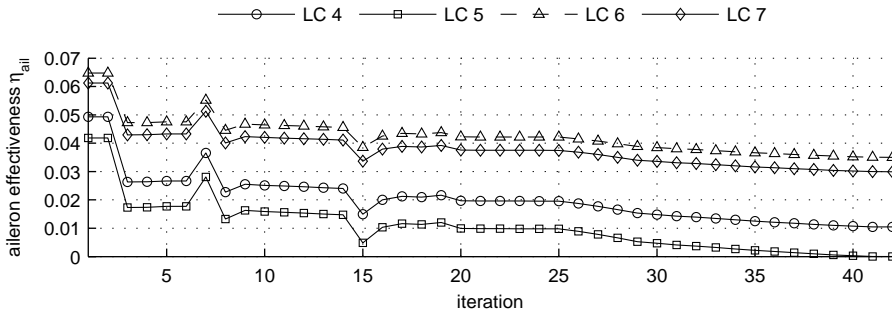
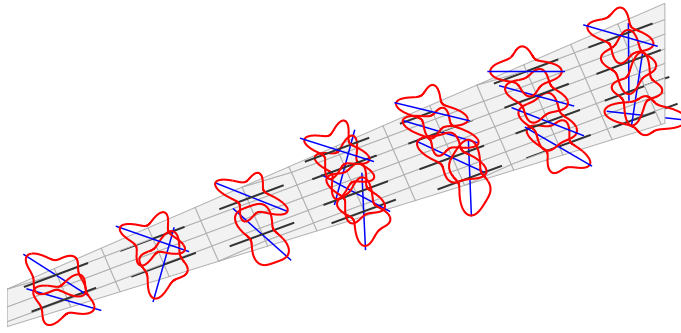


Figure 7.27: Aileron effectiveness η_{ail} development, unbalanced laminates

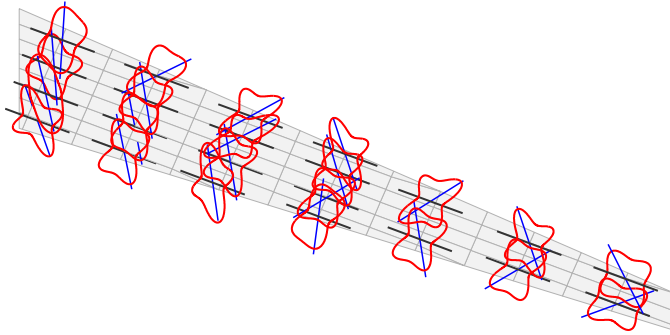
Finally, the most prominent difference between balanced and unbalanced laminates in terms of the optimized stiffness distribution in upper and lower wing skin is depicted in Figure 7.28. While the main stiffness direction in the lower skin mainly points forward and thus promotes a bending-torsion coupling that reduces the angle of attack when bending the wing up, the upper skin does not show any dedicated orientation. Again, this is a result of the upper skin being influenced mainly by buckling constraints in the $+2.5g$ pull up maneuver LC 2, in which case the stiffness distribution is adjusted so to limit the failure index in combination with the objective to achieve.

The reason for weight savings of unbalanced over balanced laminates is shown in Figure 7.29, where the spanwise twist distributions in the $+2.5g$ pull up maneuver LC 2 are compared. A considerably lower twist in the outer wing can be achieved with unbalanced laminates, which in turn leads to an inboard shift of the load distribution and hence lower bending moments towards the wing root. As a consequence, the material required to carry the loads is reduced by the optimizer. It is important to note that the twist distributions in Figure 7.29 do not reflect what is usually to be expected for a backward swept wing. The rationale for this is that the uncorrected doublet lattice method disregards airfoil twist moments. The aerodynamic force acting in the quarter chord, and therefore in front of the elastic wing axis, twists the wing positive, while geometric coupling in an upward bending wing would lead to a negative twist.

An elaboration on the coupling mechanism and aeroelastic effects caused by tilted main stiffness directions will be given in chapter 8, in which the influence of aeroelastic constraints on the achievable minimum weight for a forward swept wing is discussed in detail.



(a) lower skin



(b) upper skin

Figure 7.28: *Optimized design, $\hat{E}_{11}(\theta)$, unbalanced laminates*

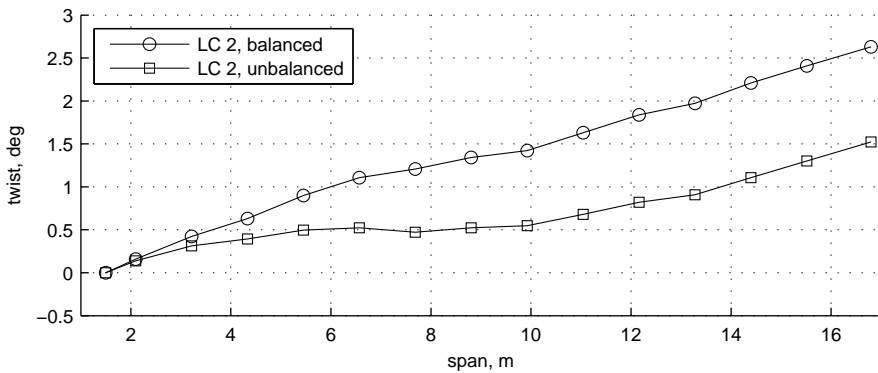


Figure 7.29: *Twist comparison for LC 2*

7.8 Numerical Results: Aileron Effectiveness Maximization

In order to demonstrate the full functionality of the aeroelastic response optimization, instead of mass, aileron effectiveness was set as the objective for maximization, that is minimization of the negative aileron effectiveness, see also section 5.7.1. The mass optimized designs lead to 522 kg and 486 kg skin mass for balanced and unbalanced laminates respectively. To provide a margin for aileron effectiveness improvements, the mass was now constrained to 650 kg for both, balanced and unbalanced laminate wings. The same starting design as for the previous mass minimization, see section 7.5, was applied for the present investigation, keeping in mind that the mass constraint will initially be violated. A typical development of mass in the iteration procedure as resulting from the balanced laminate optimization is shown in Figure 7.30. The optimizer first tried to shift the design into a feasible region, before it started to minimize the objective function.

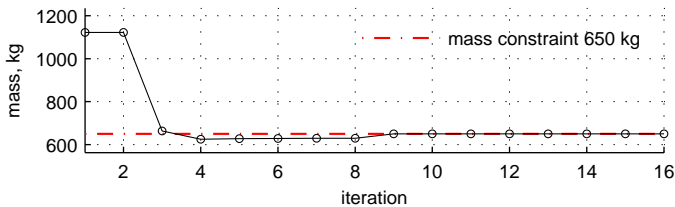


Figure 7.30: Mass development, balanced laminates

7.8.1 Balanced Laminates

The aileron effectiveness development for the load case with the lowest magnitude is shown in Figure 7.31. In the mass minimization study the minimum aileron effectiveness occurred for load case 5, $\eta_{ail} = 0.0086$. In the present study, the optimizer achieves an increase of the most critical aileron effectiveness, again load case 5, to $\eta_{ail} = 0.0357$.

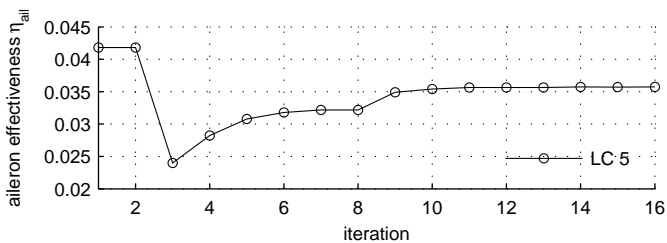


Figure 7.31: Aileron effectiveness η_{ail} development, balanced laminates

Granting a mass reserve with respect to the mass optimal design, the strain and buckling failure indices shown in Figure 7.32 indicate lower overall exploitation of the material. Structural failure is still active throughout the entire wing, yet not as many elements reached the allowable limit as before. This is a direct consequence of the

new objective function, which applies the disposable material such as to maximize aileron effectiveness. Accordingly, the thickness distribution, shown in Figure 7.33,

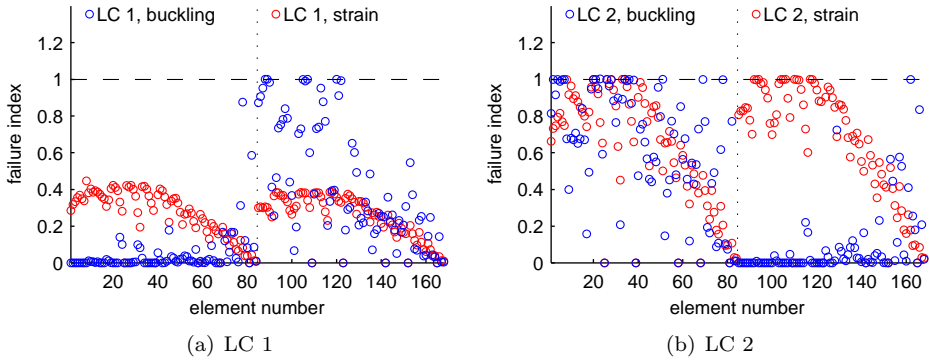


Figure 7.32: *Optimized design, failure indices, balanced laminates*

demonstrates features that do explain the constructive application of the available material. The effective sweep angle of the elastic axis in the inner wing is reduced by increasing the skin thickness in the wing box front in the mid span area, to cause a forward shift of the shear center. Accordingly, the increment in negative twist for an increment in upward bending is reduced, which helps to maintain aileron effectiveness; details on which were provided in section 2.2.1.

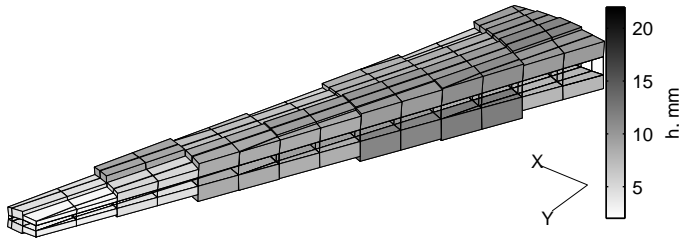


Figure 7.33: *Optimized design, thickness distribution, balanced laminates*

Nevertheless, the most prominent contribution to achieve maximum aileron effectiveness results from the stiffness distribution, see Figure 7.34. In both, the upper and lower wing skin, the optimizer converges to laminates providing extensive torsional stiffness, which in turn leads to the highest possible aileron effectiveness in the case of balanced laminates. This is achieved by lowering the twist deformation resulting from the additional twisting moment induced by the aileron deflection. The torsional stiffness increase is clearly indicated by the symmetrically aligned main stiffness direction at angles of $\approx \pm 40^\circ$ to $\pm 50^\circ$ with respect to the material coordinate system in the mid and outer wing. Accordingly, a comparison with the stiffness distribution in Figure 1.5(d) on page 13 suggests a predominant application of $\pm 45^\circ$ plies.

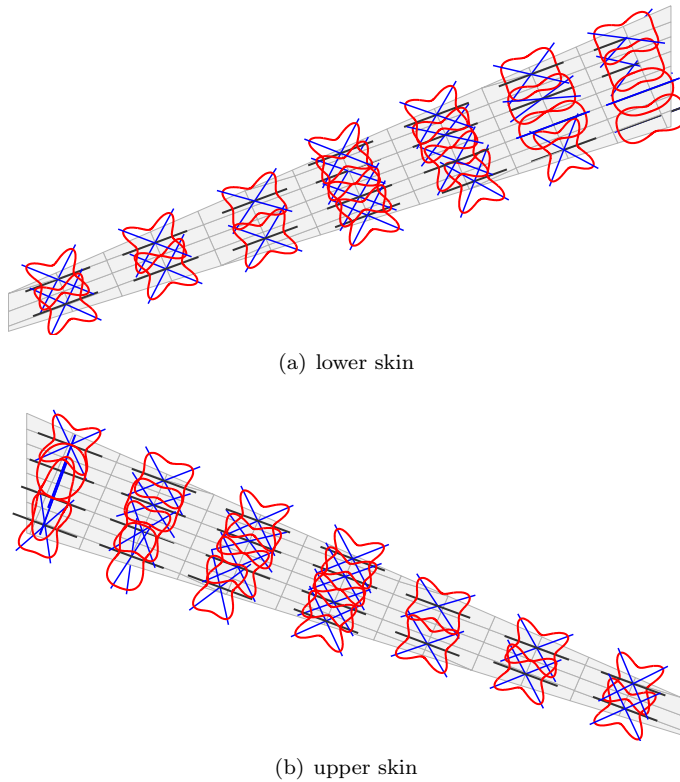


Figure 7.34: *Optimized design, $\hat{E}_{11}(\theta)$, balanced laminates*

7.8.2 Unbalanced Laminates

The full potential of composites in aeroelastic tailoring applications can be tapped when switching from balanced to unbalanced laminates. Unbalancing allows for mechanisms such as bending-torsion coupling and therefore can provide a valuable contribution to improving passive structural deformation behavior, as will be shown in the following.

The aileron effectiveness development of the lowest, most critical roll load case 5 is depicted in Figure 7.35. While in case of balanced laminates the maximization lead to an effectiveness of $\eta_{ail} = 0.0357$, Figure 7.31, the application of unbalanced laminates results in a considerable increase in the objective to $\eta_{ail} = 0.0508$.

As an alternative to the two-dimensional representation of failure indices, the fieldwise strain and buckling failure types are displayed in Figure 7.36. Other than for mass minimization, Figure 7.26, as a consequence of the additional mass available a considerable portion of the fields featured larger failure indices in strain than in buckling. The resulting thickness resembles the one obtained for the balanced case, Figure 7.33, and is skipped accordingly.

The considerable increase in aileron effectiveness to the largest extent can be assigned to the stiffness distribution, depicted in Figure 7.37(a). In order to maximize

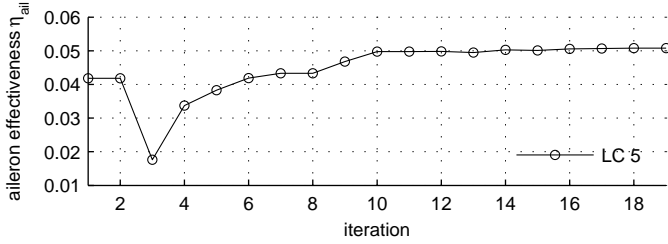


Figure 7.35: Aileron effectiveness η_{ail} development, unbalanced laminates

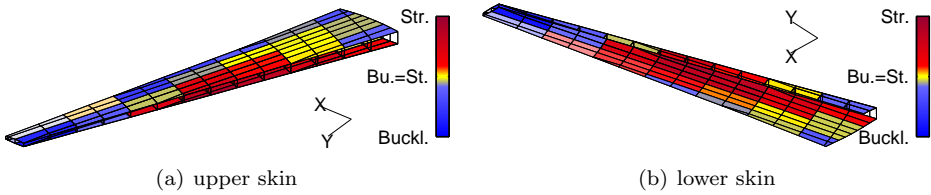


Figure 7.36: Optimized design, failure type per field, all load cases, unbalanced laminates

aileron effectiveness, the maximum stiffness direction is tilted backwards on both the upper and lower skin. Thereby bending-torsion coupling is introduced, causing the wing to twist to larger angles of attack when bending upwards and thus providing a favorable effect for aileron effectiveness. The enormous influence of bending-torsion coupling on the twist distribution is shown in Figure 7.38 for the $+2.5g$ pull up maneuver load case 2, as opposed to the twist distribution resulting from mass minimization for the same load case, Figure 7.29, page 123. While the increase in torsional stiffness with balanced laminates leads to a decrease in tip twist, the tip twist for the unbalanced case increases considerably.

An explanation of how the coupling effects mechanically are obtained is shown in Figure 7.39 for two different coupling cases, one with the main stiffness in both skins directed backward and one with the main stiffness directed forward. Bending the wing up results in compression and tension forces in upper and lower wing skin respectively, which, depending on the direction of the strain shear coupling in the membrane stiffness matrix, will introduce an opposite shear deformation of upper and lower skin. Compatibility of upper and lower skin via the presence of ribs however forces the cross sections to be maintained, so that in conclusion the structure sidesteps by twisting nose up, Figure 7.39(a) or nose down, Figure 7.39(b). Defining a coupling index Ξ as a derivative of twist with respect to z -deflection:

$$\Xi = \frac{\partial \alpha}{\partial z}, \tag{7.11}$$

a positive deflection resulting in increased twist, denoted wash-in, is characterized by a positive coupling index, while a twist decrease, denoted wash-out, reflects in a negative coupling index. Clearly, considering the stiffness distribution shown in Figure 7.37(b), it is the mechanism shown in Figure 7.39(a) that drives the increase in twist and thus aileron effectiveness maximization.

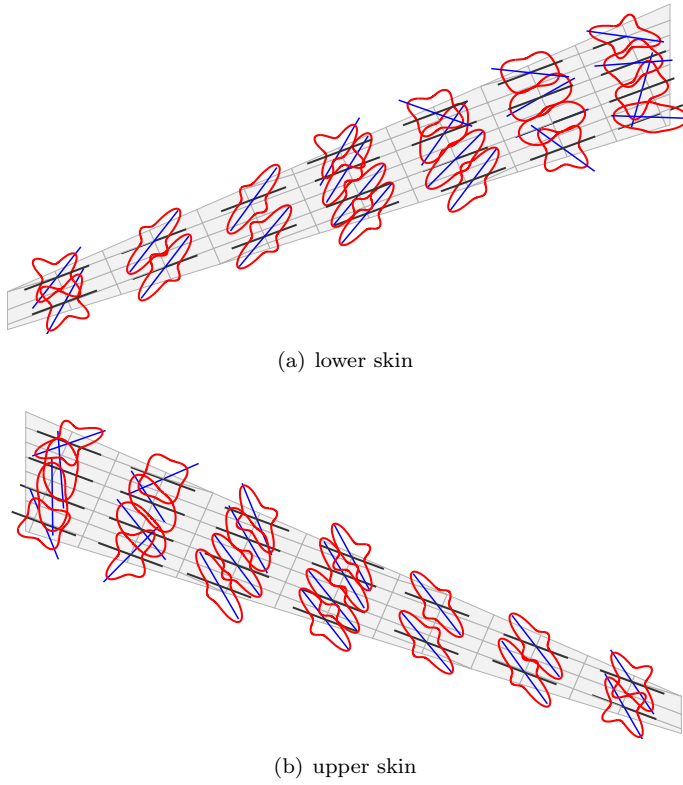


Figure 7.37: *Optimized design, $\hat{E}_{11}(\theta)$, unbalanced laminates*

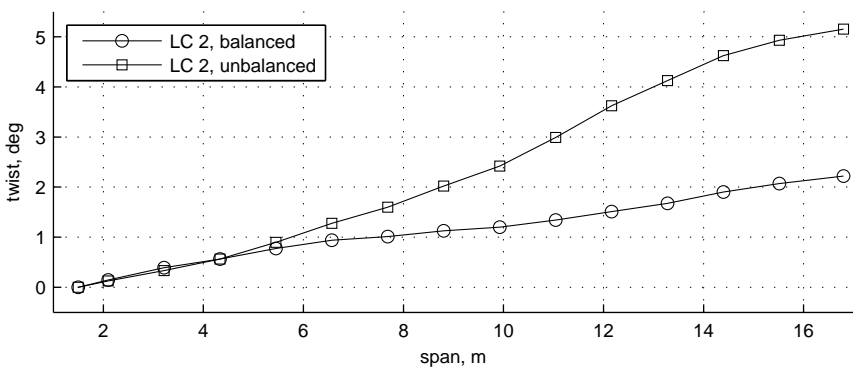
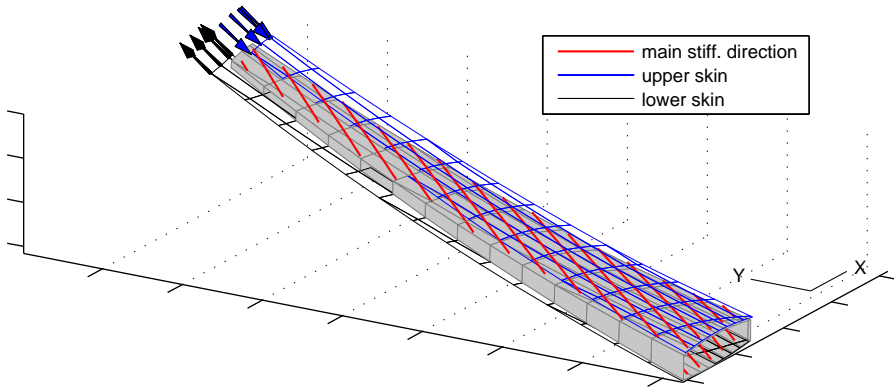
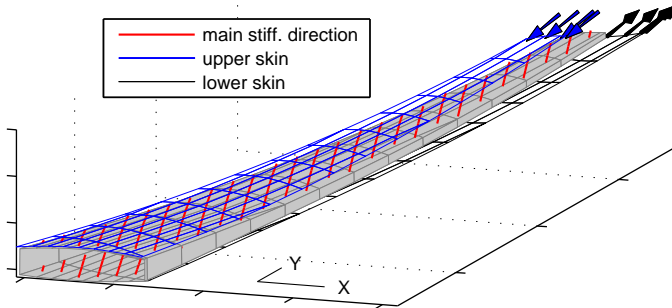


Figure 7.38: *Twist comparison for LC 2*



(a) wash-in: positive coupling index



(b) wash-out: negative coupling index

Figure 7.39: *Bending-torsion coupling*

7.9 Summary

A detailed application of the composite stiffness optimization process including aeroelastic constraints was presented in this chapter. Based on laminate stiffness matrices as design variables, the parameterized setup of a shell finite element model and optimization model was described. A generic wing was designed, serving as a test case to prove the efficacy of the optimization process, including aileron effectiveness as constraint or objective function.

The optimizer was shown to yield efficient convergence behavior for mass and aileron effectiveness optimization. The optimized designs showed a simultaneous utilization of strength and buckling constraints in a majority of the optimized panels, indicating maximum material exploitation. The advantage of unbalanced over balanced laminates was elaborated, demonstrated by considerable savings when minimizing the mass, or aileron effectiveness benefits while constraining mass.

CHAPTER 8

Aeroelastic Optimization of a Forward Swept Wing

“I skate to where the puck is going to be, not where it has been.”

Wayne Gretzky

Forward swept wings with their beneficial influence on laminar flow, and therefore drag reduction and performance increase, have recently seen a resurgence in interest from the research community and industry. The unfavorable structural behavior of such wings resulting from the coupling of bending and torsion, however, aggravates the problem of designing a wing that can aerodynamically outperform classical designs. Yet, in conjunction with matured production technologies in the field of automated fiber placement and steering, new opportunities are arising to deal with these detrimental aeroelastic effects.

The first investigations into the selective application of composite material in forward swept wings for the purpose of divergence elimination were performed in the mid 1970's by Krone [Kro75]. He showed that, by tailoring the properties of the material used in a wing, a considerably lower structural wing weight could be obtained compared to equivalent aluminum wings, even for large sweep angles. This work was extended by Weisshaar [Wei80; Wei81], who has done detailed investigations into the effect of the spanwise stiffness distribution and bending-torsion coupling on divergence velocity, aileron effectiveness and spanwise center of pressure. Librescu et al. [Lib92] investigated aeroelastic tailoring effects for large aspect ratio forward swept wings by means of a thin-walled composite beam, while Ringertz [Rin94] studied the influence of divergence and flutter constraints on the minimum achievable weight of swept back

This chapter is based on the paper, *Static Aeroelastic Stiffness Optimization and Investigation of Forward Swept Composite Wings* by J.K.S. Dillinger, M.M. Abdalla, T. Klimmek, & Z. Gürdal, [Dil13a], which was presented at the 10th World Congress on Structural and Multidisciplinary Optimization, Orlando, Florida, 2013. Note: symbols may have been changed to maintain consistency throughout this thesis.

and swept forward composite wings featuring laminate thickness as design variables. A detailed investigation of the influence induced by bending stiffness optimization on critical flutter and divergence speed, especially the contribution of bending-torsion coupling for a composite plate wing, is provided by Kameyama et al. [Kam07]. Using lamination parameter it is shown that the impact of sweep on optimized wing weight is considerably reduced when taking out-of-plane coupling into account.

Having established the functionality of the optimization process in the previous chapter, the research presented in this chapter is aimed at a detailed investigation of the influence exerted by aeroelastic constraints on the optimized wing skin mass of swept forward composite wings.

The wings were allowed to have variable stiffness, i.e., a varying thickness and stiffness matrices in the wing skins, and the use of balanced and unbalanced laminates was considered. Aside from common mass and stress responses, the aeroelastic responses aileron effectiveness, divergence and wing twist are incorporated. Taking mass as an objective function, different sets of constraints on the structural and aeroelastic responses are investigated. The influence of minimum aileron effectiveness, divergence pressure and twist on the wing skin mass are analyzed. Load alleviation is a direct consequence of the mass objective and inherent to optimization with aeroelastic loads. Therefore, it is not necessary to consider it explicitly as a response. The essential difference of balanced and unbalanced laminates with their effects on mass and stiffness distribution is presented, and the influence of leading edge sweep angle on the optimized skin masses is investigated, subject again to variable sets of constraints.

To that end, according to the geometry outline described in section 8.1, finite element models with variable sweep angles were generated, comprising distributed fuel masses, non-structural masses and thus multiple mass cases, details of which are presented in section 8.3. Details and special features related to the optimization model are discussed in section 8.4. The influence of the three aeroelastic constraints aileron effectiveness, divergence and twist on wing skin mass is investigated and summarized in sections 8.6 to 8.8, followed by some general remarks on stringers in section 8.9.

8.1 Model Description

The wing dimensions were inspired by the research conducted in the DLR project *LamAiR* [Sei11; Kru12] in which the aim was to develop an *A320* like configuration, featuring a forward swept wing with increased laminar flow regimes for reduced skin friction drag, and rear mounted engines. The absolute leading edge sweep required to obtain similar transonic pressure drag behavior for a backward as for a forward swept wing is considerably lower for the latter one. The decrease in cross flow as a result of decreased sweep angle helps to postpone the transition from laminar to turbulent flow, therefore promoting a forward swept wing when aiming at increased aerodynamic performance. The wing geometry and the position of the load carrying wing box within the planform are depicted in Figure 8.1. The initial leading edge sweep angle was $\xi = -16.8^\circ$. In order to investigate the influence of sweep angle on the optimized wing skin masses, two additional wings were modeled with sweep angles of -10.0° and -3.2° , respectively. All other parameters like span, root and tip chord, and therefore the wing area of $131.1 m^2$, box-position and aileron location remained

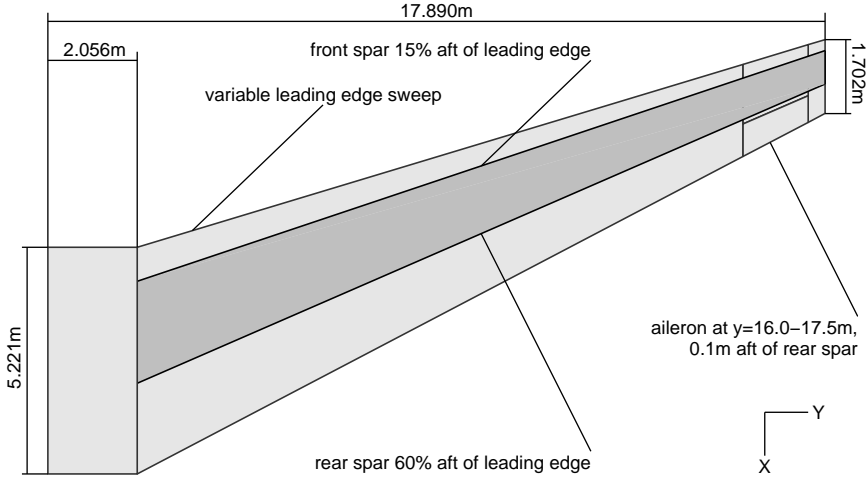


Figure 8.1: *Planform and wing box dimensions*

unchanged, ensuring the comparableness between the designs. The dihedral was fixed to 4.0° . The applied airfoils exhibited a thickness variation from $\approx 14\%$ at the wing root to $\approx 11.5\%$ at the tip, along with a spanwise decreasing camber of $\approx 2.0 - 1.2\%$.

8.2 Flight Envelope and Load Cases

An introduction to the regulatory background that stipulates the load case matrix consisting of a combination of flight velocity, flight altitude, mass cases and center of gravity, and aircraft configuration, was provided in section 7.2. While the same argumentation also applies to the present aircraft, in contrast to the previous example more cases and a more detailed mass model was considered, details of which will be provided in section 8.3.

The flight envelope as it was derived only based on the assumption of dive velocity $V_D = 395 \text{ kts}$ (CAS) and Mach number $M_D = 0.87$ above an altitude of 6700 m , along with the aeroelastic stability margin is depicted in Figure 8.2. In addition to the regular flight envelope, Figure 8.2 constitutes the dive and aeroelastic stability margin as a function of dynamic pressure q and *Mach* number M . The flight envelope was employed for the derivation of meaningful load cases. To that end, symmetric maneuver load cases are marked in yellow, cruise load case in green, and rolling load cases in white. An overview on the selected cases is provided in table 8.1.

The four sizing load cases (1–4) corresponded to flight conditions on the admissible flight range boundary with variable altitude and load factor. The cruise load case (7) corresponded to the design *Mach* number and altitude. Aileron effectiveness, load cases (12 – 13), was calculated for velocities 15% above the admissible flight range velocities, and for the dive *Mach* number in case of velocities that would clearly violate the admissible range of the doublet lattice method, load case (14 – 15). Finally, divergence pressure q_{div} was tested for the dive *Mach* number, load case (16).

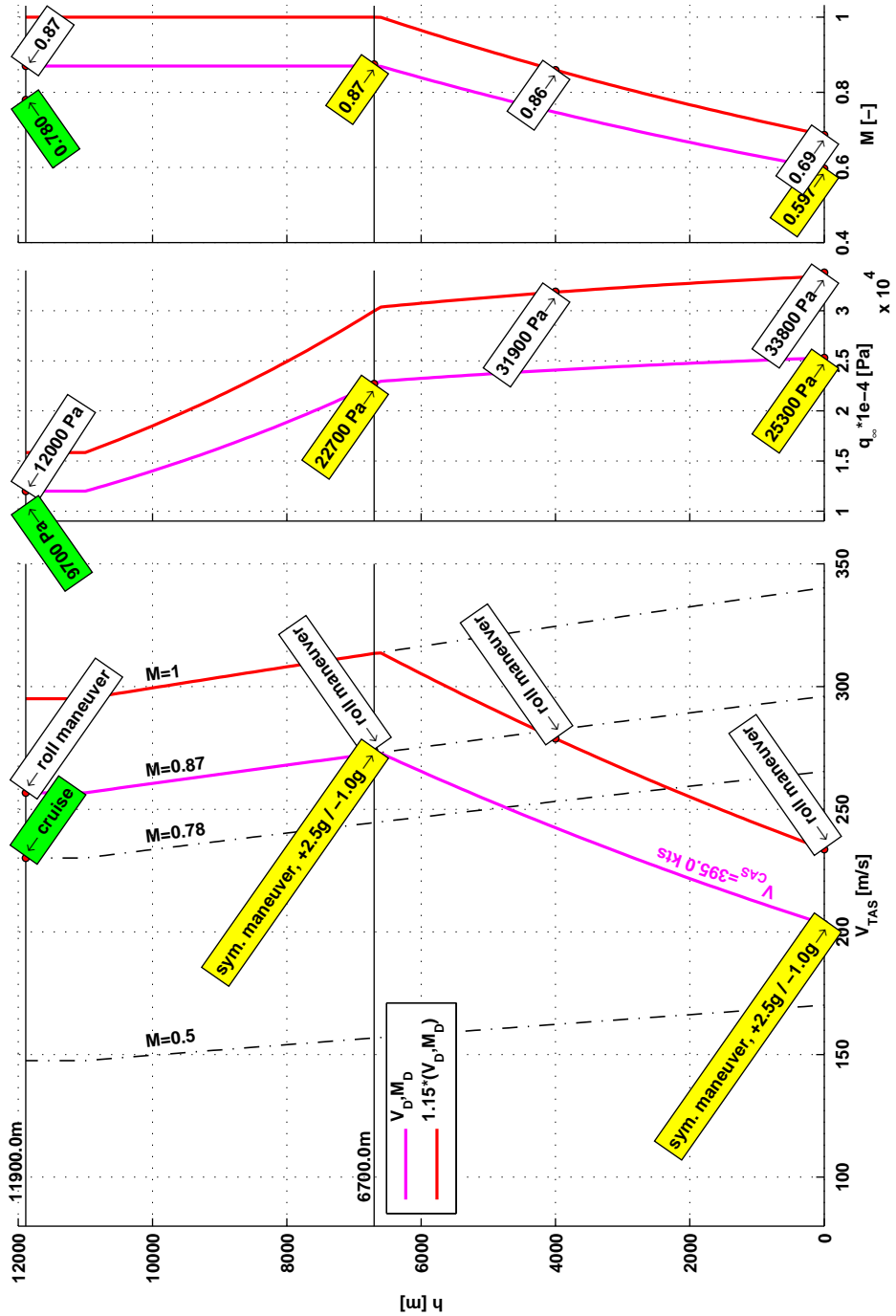


Figure 8.2: Flight envelope

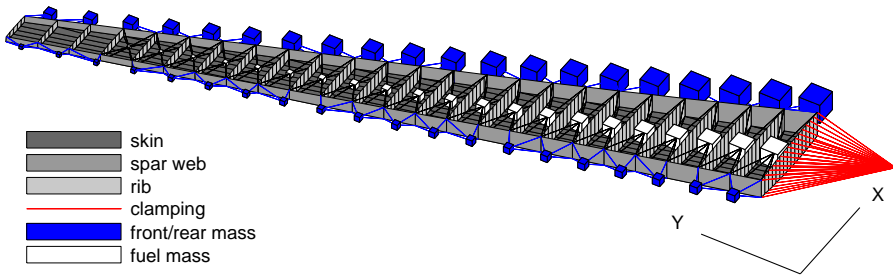
Table 8.1: *Load case definition*

| LC # | type | Ma [-] | q [Pa] | n_z [g] | H [m] |
|------|---------------------------|--------|--------|-----------|-------|
| 1 | sym., push down, V_D | 0.597 | 25300 | -1.0 | 0 |
| 2 | sym., pull up, V_D | 0.597 | 25300 | +2.5 | 0 |
| 3 | sym., push down, M_D | 0.870 | 22700 | -1.0 | 6700 |
| 4 | sym., pull up, M_D | 0.870 | 22700 | +2.5 | 6700 |
| 7 | sym., cruise, M_D | 0.780 | 9700 | +1.0 | 11900 |
| 12 | antisym., roll, $1.15V_D$ | 0.690 | 33800 | | 0 |
| 13 | antisym., roll, $1.15V_D$ | 0.860 | 31900 | | 4000 |
| 14 | antisym., roll, V_D | 0.870 | 22700 | | 6700 |
| 15 | antisym., roll, V_D | 0.870 | 12000 | | 11900 |
| 16 | divergence, V_D | 0.870 | | | |

8.3 Finite Element Model

The parametric model generator MODGEN as described in chapter 3, was used to generate the NASTRAN finite element models of the load carrying wing box. MODGEN's parametric structure allowed for a simple variation of the sweep angle by only a few changes in the standardized text input file.

An overview on the finite element model for a sweep angle of $\xi = -16.8^\circ$ is provided in Figure 8.3. The model was clamped at the wing root using a rigid element. As indicated by the plot, several non-structural masses were attached to the wing box, as will be discussed in more detail hereafter. In total 25 ribs, including the ones at root and tip, were modeled and distributed equidistant in spanwise direction. They were aligned parallel to the free stream and thus to the global x -axis.

**Figure 8.3:** *Finite element model*

Stringers extended parallel to the front spar in spanwise direction, a 3% stringer pitch with respect to the root chord, measured in chordwise direction is shown in Figure 8.4. With the front spar swept forward by $\approx -18.5^\circ$, the result was an absolute parallel stringer distance of $\approx 149\text{ mm}$ in case of $\xi = -16.8^\circ$ leading edge sweep.

The element distribution in the wing skins was again predetermined by the stringer and rib distance. Each of these fields was discretized by a single shell element, as required by the buckling analysis methodology. One element was considered in wing thickness direction, affecting only ribs and spar webs.

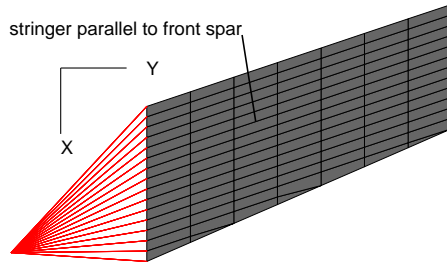


Figure 8.4: *Top skin stringer alignment*

Properties

With a few exceptions, the structural properties resembled those applied in the previous application, chapter 7. All the structural components except for the stringers were modeled using the same fiber material, the ply properties of which are listed in Table 8.2.

Table 8.2: *Single ply material properties*

| E_{11} | E_{22} | G_{12} | ν_{12} | ρ |
|----------------------|---------------------|---------------------|------------|-----------------------|
| $83.0e9 \text{ GPa}$ | $8.5e9 \text{ GPa}$ | $4.2e9 \text{ GPa}$ | 0.35 | 1452 kg/m^3 |

The initial thickness distribution of the wing skins was the same for upper and lower skin, comprising a linear variation from 25.0 mm at the root to 5.0 mm at the tip and a symmetric layup with $[-45_{22.2}/+45_{22.2}/90_{11.19}/0_{44.41}]_s$, where the angle subscripts denote the percentage ply thickness contribution to the overall thickness. The ply angles were defined with respect to an axis that aligned with the average sweep of front and rear spar. The spar shear webs were modeled with a thickness variation from 20.0 mm at the root to 15.0 mm at the tip and a $[-45_{35}/+45_{35}/90_{20}/0_{10}]_s$ layup. The ribs had a constant thickness of 8.0 mm and a quasi-isotropic symmetric layup $[\pm 45/90/0]_s$. According to classical lamination theory the stacking sequences were transformed to membrane and bending stiffness matrices, as requested by the optimizer.

Stringers made of titanium were modeled as bar elements and properties were kept constant throughout the wing using the cross-sectional and material properties listed in table 8.3 and 8.4 respectively.

Table 8.3: *Stringer cross-sectional properties*

| A | I_1 | I_2 | J |
|------------------------|------------------------|------------------------|------------------------|
| $6.079e-4 \text{ m}^2$ | $1.715e-7 \text{ m}^4$ | $1.808e-7 \text{ m}^4$ | $6.291e-9 \text{ m}^4$ |

DLM and Coupling

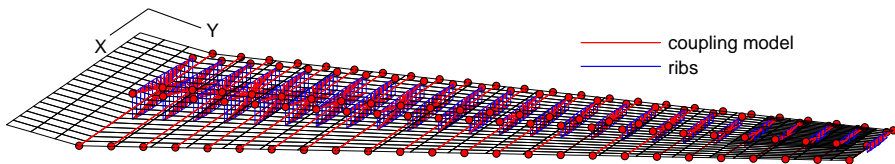
The doublet lattice model along with the coupling model required to link it to the finite element model is depicted in Figure 8.5.

Table 8.4: *Stringer material properties*

| E | G | ν | ρ |
|-------------|-------------|-------|--------------------------|
| 88.32e9 GPa | 32.61e9 GPa | 0.354 | 4058.3 kg/m ³ |

As shown in Figure 8.1, an aileron with a hinge line 0.1 m aft of the rear spar was placed in the outer wing, ranging from $y = 16\text{ m} - 17.5\text{ m}$ and activated for the aileron effectiveness responses.

In addition to the three coupling nodes belonging to the load reference axis, compare section 3.4.3, two additional points per rib on front and rear spar were selected. Accordingly, five structural nodes per rib plane exist, which were coupled to the aerodynamic model via NASTRAN SPLINE1 cards.

**Figure 8.5:** *Coupling model and DLM*

The doublet lattice model was enhanced by the consideration of a W2GJ correction matrix generated by MODGEN, based on the two-dimensional airfoil shapes applied in the definition of the aerodynamic wing contour. The process was discussed in detail in section 6.2.1.

Mass

The mass model that was developed for a flexible mass case generation along with the MODGEN model basically consisted of four parts:

1. **wing structural mass:** inherent in the finite element model of the load carrying wing box
2. **non-structural mass:** weight that is not captured with the MODGEN finite element model, like leading edge structure, high lift devices, flaps, ailerons, local reinforcements, actuators and so forth
3. **fuel mass:** wing tank fuel model
4. **remaining mass:** summation of other aircraft components such as fuselage and tails to achieve a mass model for the right half of the aircraft

The first point was covered by the finite element model, the second one required an estimation based on the type of aircraft and wing dimensions. The spanwise masses that were assumed to summarize the non-structural masses in front and aft of the wing box are plotted in Figure 8.6, a visual representation of which is also provided in Figure 8.3. They summed up to 374.8 kg and 421.5 kg respectively.

The third contribution to the overall mass came from the fuel model, which was generated using the MODGEN functionality described in section 3.3.2. The wing fuel

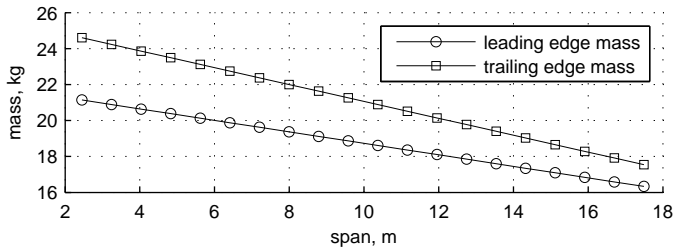


Figure 8.6: *Non-structural masses*

tank was divided into three separate parts, as depicted in Figure 8.7. The total fuel mass in the right wing amounted to 8425 kg , which included an artificial center wing tank (CWT) with a capacity of 1850 kg . Table 8.5 states hypothetical fuel cases (FC), where “filling level” denotes a multiplication factor for all rib-bay fuel masses of the corresponding tank.

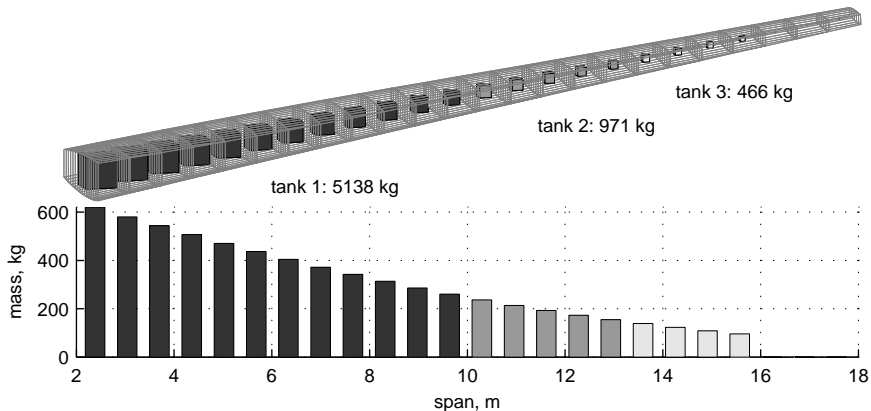


Figure 8.7: *Fuel masses*

All remaining aircraft components, like fuselage, tailplanes and engines summed up to 31550 kg . Assuming a total passenger mass of 14250 kg for the fully loaded aircraft, the aircraft mass cases listed in table 8.6 are obtained, and they formed the fourth contribution in the above list. It is important to note that only half the mass listed in table 8.6 had to be attached to the clamping element node on the symmetry plane, since only half the aircraft was incorporated in the optimization.

The combination of fuel case FC and aircraft mass ACM made up a mass case MC. Other than in the first optimizer application that featured only one mass case, the combination of load case and mass case is denoted sub case (SC), reflecting the NASTRAN terminology of separate analysis within a single solver run. The sub case number is a combination of mass case and load case number. All combinations considered in the optimization are listed in table 8.7. However, in the context of this work, the NASTRAN-inspired designation as sub case will be replaced again by load case, which represents a generally accepted denomination throughout the aircraft industry.

Table 8.5: *Fuel cases*

| FC # | CWT | filling level tank # | | | description |
|------|---------|----------------------|-----|-----|--|
| | | 1 | 2 | 3 | |
| 1 | 1850 kg | 1.0 | 1.0 | 1.0 | all full (not used) |
| 2 | 925 kg | 0.5 | 1.0 | 1.0 | inner half empty |
| 3 | 925 kg | 0.0 | 0.5 | 1.0 | inner empty, mid half empty (not used) |
| 4 | 925 kg | 0.0 | 0.0 | 1.0 | inner and mid empty |
| 5 | 1850 kg | 0.0 | 0.0 | 0.0 | wing empty, full CWT |
| 6 | 0 kg | 0.0 | 0.0 | 0.0 | all empty (not used) |

Table 8.6: *Aircraft mass*

| ACM # | mass | description |
|-------|----------|-------------|
| 1 | 45800 kg | full pax |
| 2 | 38675 kg | half pax |
| 3 | 31550 kg | no pax |

Table 8.7: *Load case definition*

| SC # | LC # | MC # | FC # | ACM # | description |
|------|------|------|------|-------|-------------------------------|
| 1001 | 1 | 1 | 5 | 1 | sizing -1.0g |
| 1002 | 2 | | | | sizing +2.5g |
| 1003 | 3 | | | | sizing -1.0g |
| 1004 | 4 | | | | sizing +2.5g |
| 1012 | 12 | | | | aileron effectiveness |
| 1013 | 13 | | | | aileron effectiveness |
| 1014 | 14 | | | | aileron effectiveness |
| 1015 | 15 | | | | aileron effectiveness |
| 2007 | 7 | 2 | 2 | 1 | twist, begin cruise |
| 2016 | 16 | | | | divergence |
| 3007 | 7 | 3 | 4 | 1 | twist, end cruise |
| 4007 | 7 | 4 | 2 | 2 | twist, begin cruise, half pax |
| 5007 | 7 | 5 | 4 | 2 | twist, end cruise, half pax |

LC 4007 will for instance refer to SC 4007 depicted in table 8.7.

In total, five different mass cases were modeled, assuming the most unfavorable combination of empty wing tanks and maximum passenger load was considered for sizing load cases 1 – 4. The cruise load case 7 was investigated for a wing fuel loading approximately corresponding to begin, and end of cruise flight, and for maximum and half passenger loading, totaling four more mass cases. The constant flight altitude for all cruise load cases implies an iso-altitude consideration. The aileron effectiveness load cases 12 – 15 and divergence load case 16 were independent of mass distribution and could therefore be computed along with one of the depicted mass cases.

8.4 Optimization Model

Creation of the optimization model implies the clustering of elements into design fields, each of which comprises its own set of membrane and bending stiffness matrices, and a thickness, see Figure 8.8. Upper and lower skin having the same design field resolution, the optimization model was made up of a total of 70 design fields. The spars and ribs were not included in the optimization. Each design field required six design variables per stiffness matrix and one design variable for the thickness, amounting to thirteen design variables per field and therefore 910 design variables to be defined in NASTRAN.

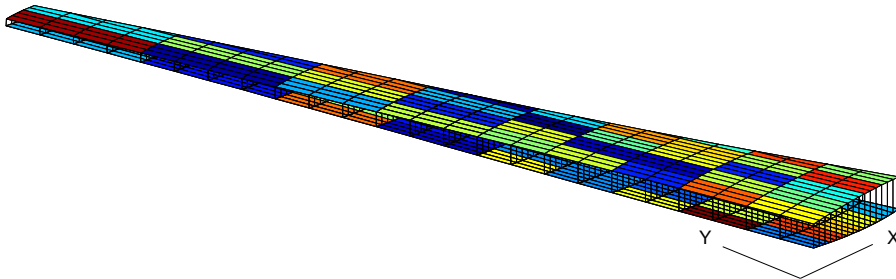


Figure 8.8: *Design fields*

The computation of the strain and buckling factors and sensitivities for each element that is part of the optimization model, necessitated the generation of stress responses in the two in-plane and shear direction in their local element material coordinate systems. NASTRAN provides the responses at the lower and upper laminate end, eventually requiring six responses per element and load case. The FE model comprising 247 elements in each, upper and lower skin, led to 2964 NASTRAN stress responses per sizing load case. Other NASTRAN responses included in the optimization were mass, aileron effectiveness as a combination of two aeroelastic stability derivatives, divergence and twist. The latter response was asked for at every node of the load reference axis; according to the amount of ribs at 25 spanwise locations. The NASTRAN responses following from the optimization load cases specified in table 8.7 are listed in table 8.8(a), noting that twist responses were generated for cruise and sizing load cases. Along with 910 design variables this amounted to $\approx 11e6$ sensitivities.

Table 8.8: *Number of responses*

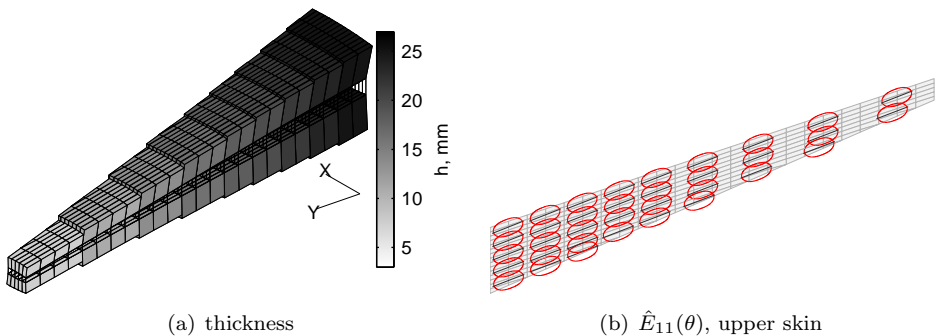
| (a) NASTRAN | | (b) optimizer | |
|-------------------------|-------|-------------------------------|------|
| # of weight responses | 1 | # of weight responses | 1 |
| # of stress responses | 11856 | # of strain failure responses | 1976 |
| # of ail.eff. responses | 4 + 8 | # of buckling responses | 3952 |
| # of twist responses | 200 | # of ail.eff. responses | 4 |
| # of diverg. responses | 1 | # of twist responses | 4 |
| ⇒ total: | 12070 | # of diverg. responses | 1 |
| | | ⇒ total: | 5938 |

The response numbers when converting the NASTRAN sensitivities to approximations that were passed to the optimizer are listed in table 8.8(b). The design fields comprising in total 494 shell elements lead to 1976 strain failure responses for the four sizing load cases. Considering two buckling modes per element, the amount of buckling failure responses was twice the amount of strain failures. Instead of considering all twist responses in the optimization, only tip twist in case of the four cruise load cases were included as possible constraints in the optimizer. Along with 910 design variables the total amount of sensitivities summed up to $\approx 5.4e6$ elements.

Other than for the first optimizer application described in chapter 7, no exception from the approximations as derived in sections 5.6, 5.7, and summarized in table 5.1 on page 78 were made. This also implies the application of response convexification in case of the aeroelastic responses. The strain allowables required for the failure envelope construction were set to $[\varepsilon_t, \varepsilon_c, \gamma_{xy}] = [0.5\%, -0.4\%, 0.4\%]$ and thus below the values chosen for the optimizations presented in chapter 7. The main reason was the intention to trigger strain, rather than buckling failure.

8.5 Starting Design

The wing with a nose sweep angle of $\xi = -16.8^\circ$ will in the following be denoted the basic configuration, the wings comprising $\xi = -10.0^\circ$ and $\xi = -3.2^\circ$ nose sweep angle as configuration 1 and 2, respectively. The starting design features presented in this section refer to the basic configuration.

**Figure 8.9:** *Starting design, thickness and stiffness distribution*

The initial structural properties resembled closely the ones applied for the backward swept wing optimization, thickness and stiffness distribution are depicted in Figure 8.9.

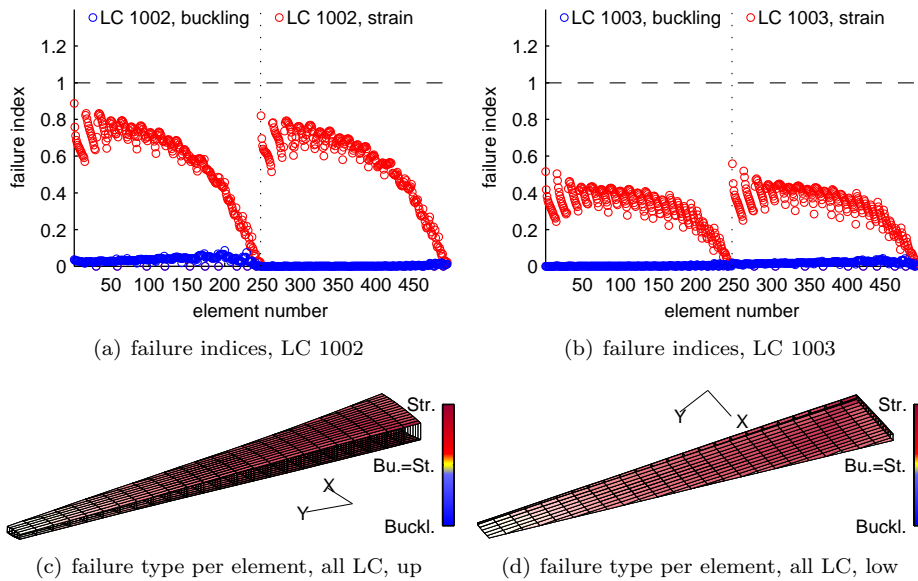


Figure 8.10: Starting design, failure indices

Along with the sizing load case definitions given in table 8.7 the strength and buckling failure indices were computed. The failure indices for the $+2.5g$ maneuver LC 1002 are plotted in Figure 8.10(a), and the failure indices for the $-1.0g$ maneuver LC 1003 in Figure 8.10(b), which initially generated the largest failure indices. Interestingly enough, it was not one particular flight level that yielded the largest failure indices for both, $+2.5g$ and $-1.0g$ maneuver, but a mix of the two investigated altitudes 0 m and 6700 m . However, the resulting failure indices featured values sufficiently smaller than 1.0, affirming the starting design was feasible and offering potential for mass minimization.

Figure 8.10(c) and 8.10(d) indicate what could already be derived from the failure index plots shown in Figure 8.10(a) and 8.10(b). The starting design was clearly dominated by strain failure rather than buckling failure, the reason being the reduced failure strains compared to the backward swept wing, and more importantly the decrease in buckling field size due to the application of more ribs and a reduced stringer pitch.

In trying to converge to a global, rather than a local optimum, two additional optimizations aside from the regular starting point were considered for each case, one comprising an altered starting thickness distribution and the other one a tilt of the initial laminate angles. The results discussed in the following sections always take into consideration the run with the lowest mass of the three starting designs. In most cases, the lowest mass was confirmed by at least one of the other starting points, which also showed similar principal stiffness distributions in the majority of the design fields.

Mass optimizations for all three wing configurations, always comprising the regular strength and buckling failure index constraints, along with one additional aeroelastic constraint are presented in the following sections. This approach allowed for an explicit distinction to be made between the influence of aeroelastic constraints on wing mass, and the effect of balanced and unbalanced laminates.

8.6 Numerical Results: Aileron Effectiveness Constraint

In the first set of optimizations a mass minimization objective along with the application of a lower limit aileron effectiveness constraint for all designated aileron effectiveness load cases was considered:

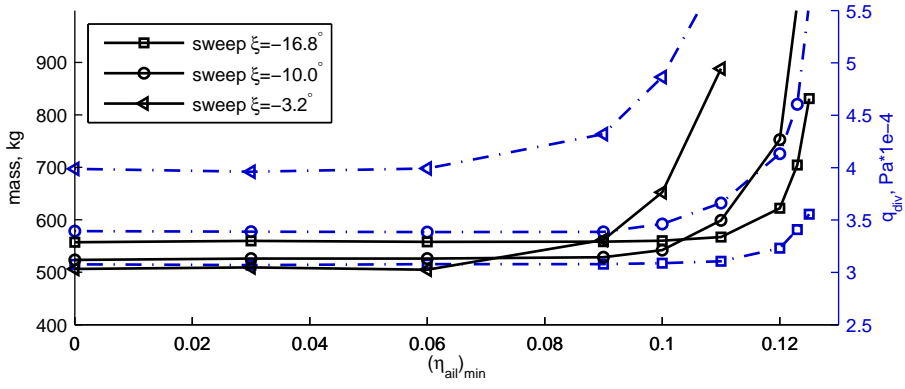
$$\eta_{ail} \geq (\eta_{ail})_{min} . \quad (8.1)$$

Additionally, regular structural constraints on strain and buckling were implemented. No other aeroelastic constraints were involved. $(\eta_{ail})_{min}$ was varied in finite steps from 0, no reversal, to 0.125 and the corresponding optimizations were performed for balanced and unbalanced laminates. The optimization results are summarized in Figure 8.11, separated into balanced and unbalanced laminate optimizations in Figure 8.11(a) and 8.11(b). The graphs indicate the development of minimized wing skin mass as a function of the applied lower limit on aileron effectiveness. That is, each marker corresponds to an optimized wing. Results are presented for all three of the investigated sweep configurations. In addition, the associated, yet unconstrained divergence pressure response is shown as blue lines. In order to facilitate comparability, balanced and unbalanced optimization results for the basic configuration exhibiting $\xi = -16.8^\circ$ leading edge sweep are depicted in Figure 8.11(c).

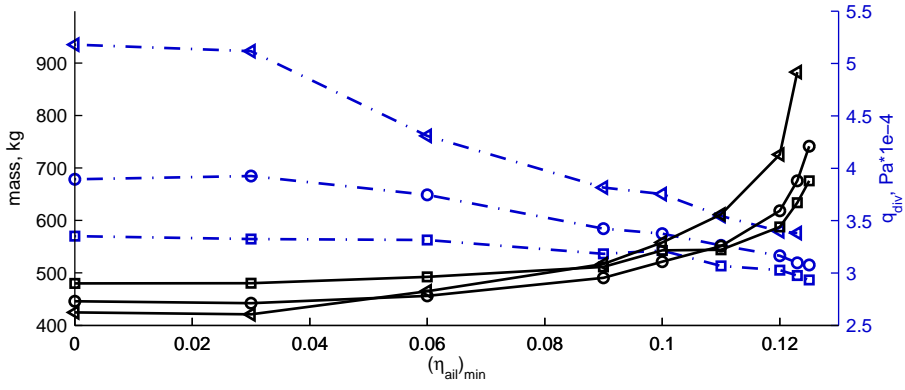
A detailed definition of aileron effectiveness was presented in section 2.2.1. Due to the geometric coupling effects on a forward swept wing, the angle of attack in the outer wing increases when bending the wing up. This in general supports aileron effectiveness, making a forward swept wing, usually, not vulnerable to aileron reversal. At the same time, the aileron effectiveness load cases, as considered in the present investigation, would only require preservation of positive values $\eta_{ail} \geq 0$, so no aileron reversal. However, the achievement of minimum roll rates for specific flight conditions might require an increased effectiveness, therefore justifying the present investigation.

Starting with the comparison of balanced versus unbalanced laminate optimizations shown in Figure 8.11(c), a clear advantage of the additional freedom in design space inherent in unbalanced designs can be seen. For an aileron effectiveness constraint demanding no reversal, $(\eta_{ail})_{min} = 0$, the weight benefit amounted to $\approx 14 - 16\%$ for the basic and also for the two other investigated forward sweep configurations.

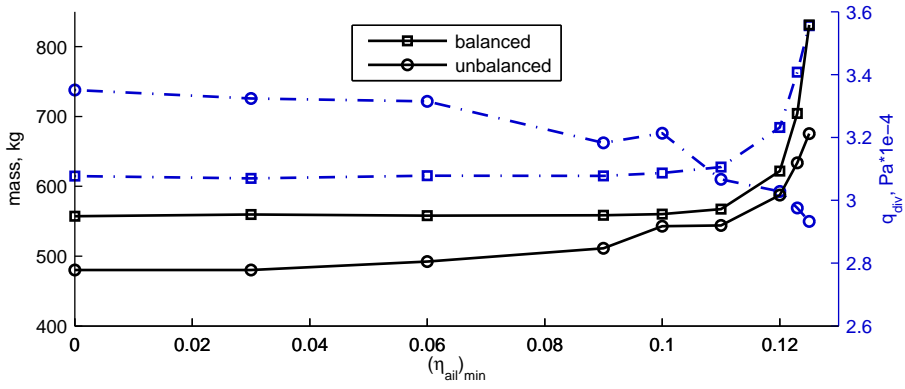
A similar influence of sweep angle on the optimized skin weight could be observed for balanced and unbalanced laminates. In Figure 8.11(a) a weight decrease of $\approx 9\%$ when decreasing forward sweep from $\xi = -16.8^\circ$ to $\xi = -3.2^\circ$ is shown. The mass showed horizontal development for an increasing aileron effectiveness constraint and thus implied a not yet active aeroelastic constraint; in this case the optimizations were only bound by strain and buckling limitations. The basic configuration particularly was influenced by $(\eta_{ail})_{min}$ only for higher constraint values. As a result, beyond



(a) balanced



(b) unbalanced



(c) comparison of balanced and unbalanced laminates for the basic configuration ($\xi = -16.8^\circ$)

Figure 8.11: Wing skin mass as function of minimum aileron effectiveness $(\eta_{ail})_{min}$

a certain $(\eta_{ail})_{min}$ the conditions changed and the basic configuration featured the lowest mass compared to the less swept wings.

The unconstrained divergence pressure showed distinct differences between unbalanced and balanced laminates. For unbalanced laminates the divergence pressure was considerably larger in the case of configuration 2 and decreased quickly for an increasing $(\eta_{ail})_{min}$ constraint. In the case of balanced laminates the trend was the opposite, hence an increasing divergence pressure for increasing $(\eta_{ail})_{min}$ constraint.

To identify the implication of increasing aileron effectiveness requirements on the design variables, the polar stiffness distribution in the design fields of the upper skin for four different $(\eta_{ail})_{min}$ constraints, increasing row-wise, are depicted in Figure 8.12. The balanced laminates are shown in the left column, and the unbalanced laminate optimizations in the right column. A black solid line is used to depict the material coordinate system, while the blue line is used to indicate the direction of maximum stiffness. The first row corresponds to an optimization requiring no aileron reversal. Both laminate types showed a distinct stiffness alignment in the spanwise direction in the root and mid spanwise region. While the balanced laminates developed towards more homogeneous distributions in the outer wing, the main stiffness direction with unbalanced laminates was tilted forward, establishing a bending-torsion coupling that let the wing twist towards more negative local angles of attack when bending up. This corresponds to the effect depicted in Figure 7.39(b) on page 129. Effecting a twist towards smaller angles of attack in the outer wing causes a shift of the total lift force inward, the result of which are decreased bending moments in the wing root area. As a consequence, the material supporting the loads could be reduced. In the next row, Figure 8.12(c) and 8.12(d), stiffness distributions for aileron effectiveness constraint $\eta_{ail} \geq 0.09$ are depicted, which is just at the border towards noticeable increases in wing skin weight, compare Figure 8.11(c). While the constraint for the balanced laminate was ineffective and hence yielded identical stiffness distributions compared to the previous $\eta_{ail} \geq 0$ optimization, stiffness distributions in the outer wing of the unbalanced laminate optimization now pointed in the opposite, backward direction. This implies a positive coupling index as depicted in the coupling explanation in Figure 7.39(a) on page 129. Further rising the aileron effectiveness constraint to $\eta_{ail} \geq 0.11$ caused the polar stiffness in the outer wing to stretch further, pronouncing bending-torsion coupling. The most outward design fields developed towards maximization of torsional stiffness, Figure 8.12(f). In the case of balanced laminates, Figure 8.12(e), the stiffness distributions in the outer wing changed considerably. The alignment of maximum stiffness in the $\pm 45^\circ$ direction clearly promoted torsional stiffness. This development extended inboard for the final aileron effectiveness constraint $\eta_{ail} \geq 0.125$, Figure 8.12(g). The same holds for unbalanced laminates, Figure 8.12(h) where an increasing number of design fields showed maximum stiffness directions tilted backwards.

The stiffness development discussed here constitutes the unconstrained divergence pressure development depicted in Figure 8.11. While an increase in torsional stiffness with rising aileron effectiveness for balanced laminates helped to increase divergence pressure, an increase in coupling index for the unbalanced laminates caused a diminishment.

In the following, some specific results for a rather severe aileron effectiveness constraint $\eta_{ail} \geq 0.11$ will be presented. The results depicted in Figure 8.13 exemplify the

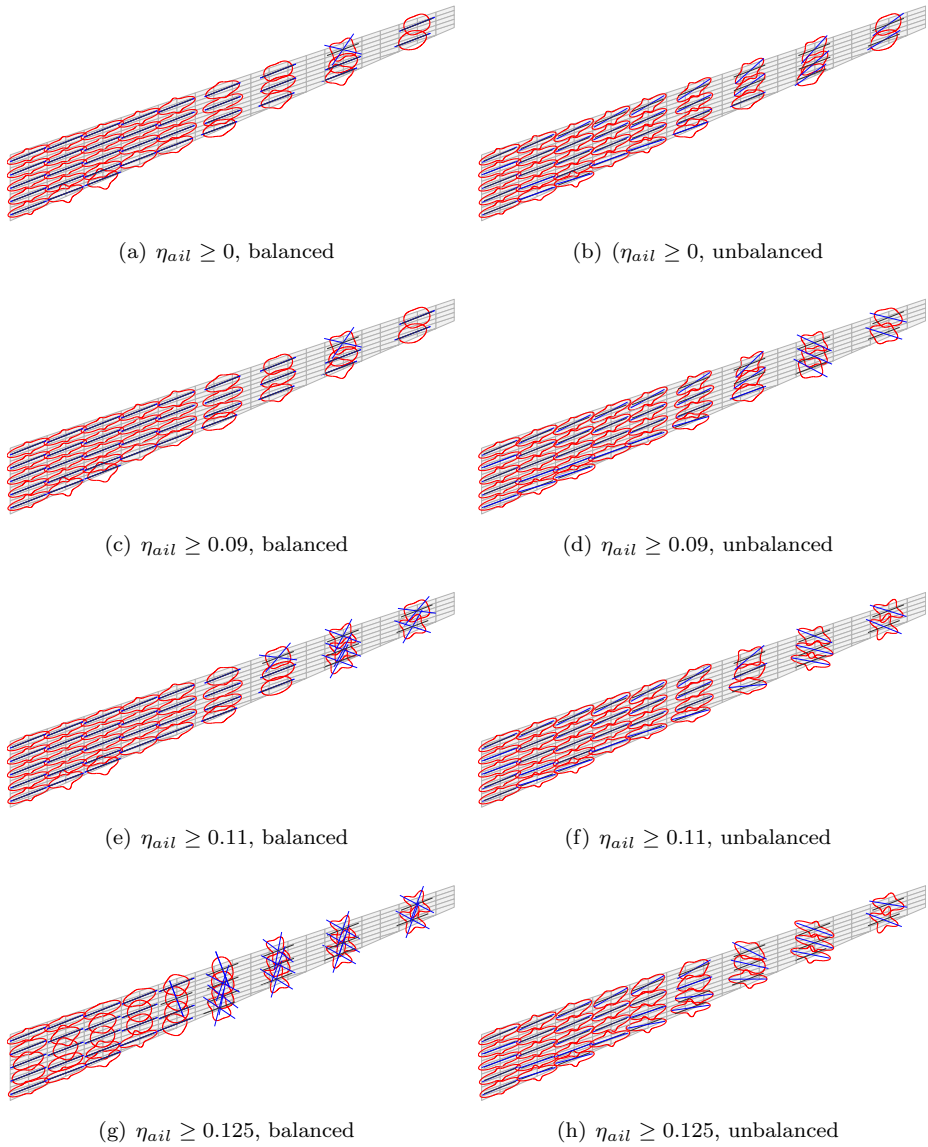


Figure 8.12: Optimized design, basic configuration, $\hat{E}_{11}(\theta)$ upper skin for different $(\eta_{ail})_{min}$ constraints

optimized thickness distributions. To meet the constraint with balanced laminates, the thickness was increased in the frontal part, Figure 8.13(a), while in the case of unbalanced laminates the distribution was more consistent, Figure 8.13(b).

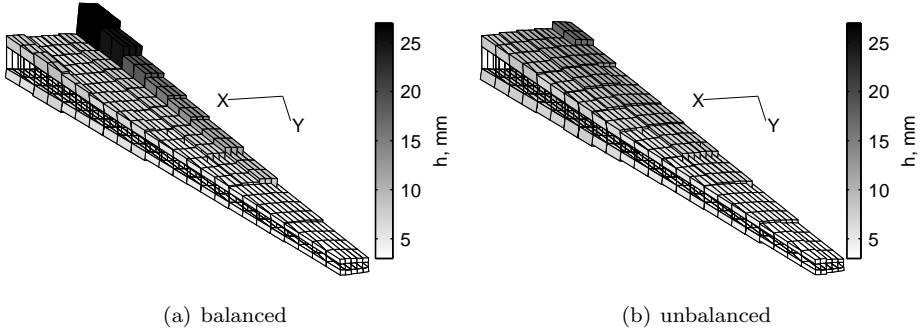


Figure 8.13: *Optimized design, basic configuration, thickness distribution for $\eta_{ail} \geq 0.11$*

A typical aileron effectiveness development is shown in Figure 8.14. LC 1009 generated the lowest response and therefore provided an active constraint during the optimization, which is indicated by the response settling right on the aileron effectiveness boundary $\eta_{ail} = 0.11$.

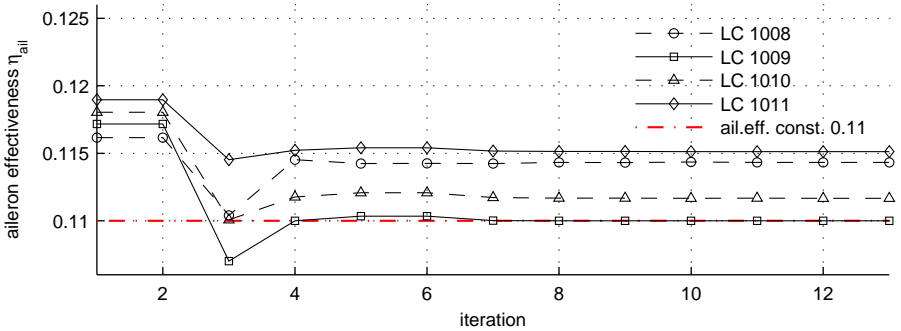


Figure 8.14: *Basic configuration, aileron effectiveness η_{ail} development, unbalanced laminates, $\eta_{ail} \geq 0.11$*

Finally from Figure 8.15(a) and 8.15(b) it can be seen that sizing was mainly driven by the $+2.5g$ maneuver load case 1002 in both the upper and lower skin. Of the two $-1.0g$ load cases 1001 and 1003 it was only LC 1003 that contributed to the sizing of some design fields. Accordingly, Figure 8.15(c) and 8.15(d) depict the failure indices in upper, element numbers 1 to 247, and lower skin, element numbers 248 to 494, for load cases 1002 and 1003. Both graphs demonstrate a clear dominance of strain over buckling failure indices. An explicit visualization of strain prevalence is provided in Figure 8.15(e) and 8.15(f), plotting the failure type in upper and lower wing skin. Only the outer wing was sized by buckling constraints, the reason being that with decreasing aerodynamic loads towards the wing tip the shell thicknesses

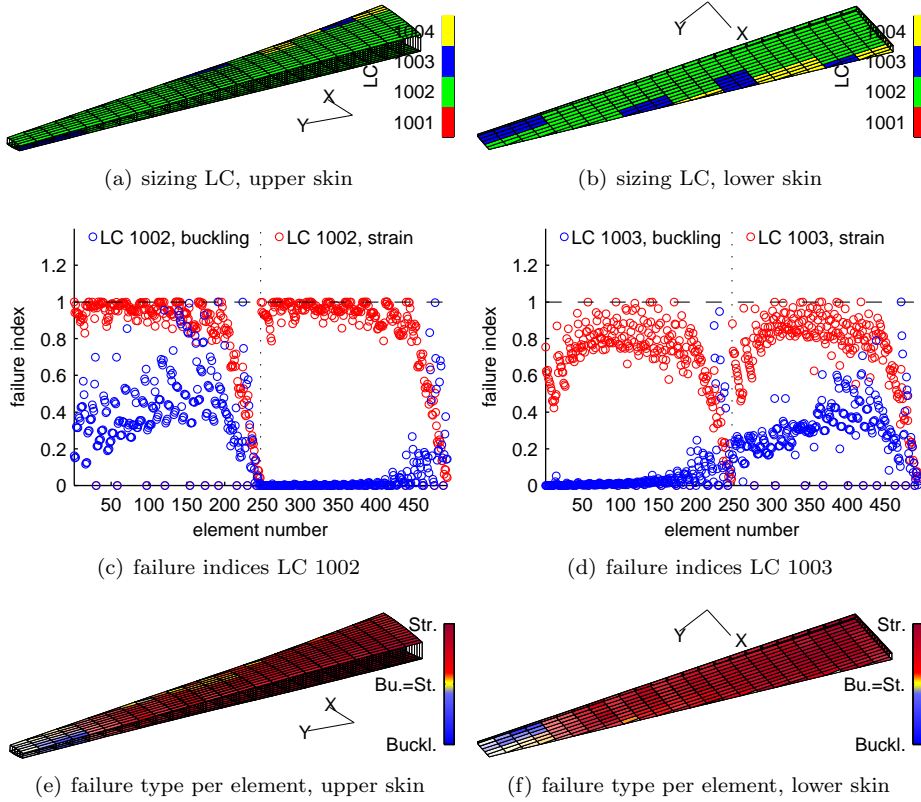


Figure 8.15: *Optimized design, basic configuration, failure index representations, unbalanced laminates $\eta_{ail} \geq 0.11$*

were decreased. While the shell membrane stiffness decreases linearly with thickness h , bending stiffness decreases with h^3 , thus promoting buckling failure.

8.7 Numerical Results: Divergence Pressure Constraint

The next set of optimizations also comprised a mass minimization objective while replacing the aileron effectiveness constraint with a constraint on divergence pressure, a detailed description of which is provided in section 2.2.2. Aside from the aeroelastic constraint:

$$q_{div} \geq (q_{div})_{min} , \tag{8.2}$$

only regular structural constraints on strain and buckling were applied. The divergence pressure was varied in finite steps from 30000 Pa to 50000 Pa and the corresponding optimizations were performed for balanced and unbalanced laminates.

Other than for aileron effectiveness, the geometric coupling effect for a forward swept wing has a considerable detrimental impact on divergence. It constitutes one

of the main reasons why the consideration of forward swept wings usually ends up with distinct weight penalties and finally a refusal of the concept. Accordingly, the present investigation provided an interesting insight into the possibilities offered by variable stiffness composite wing optimization.

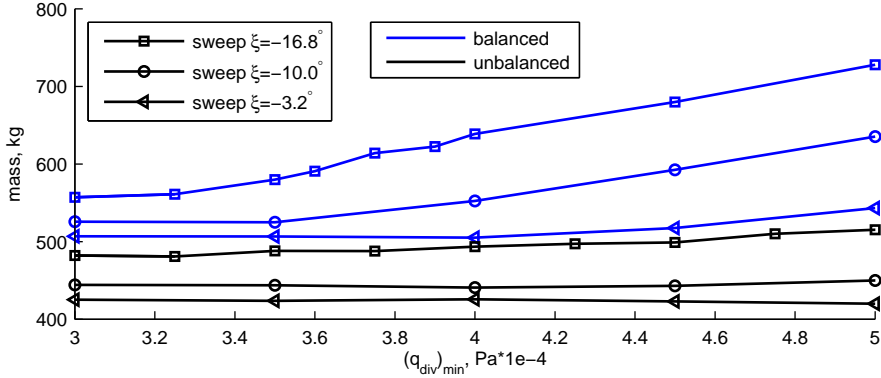


Figure 8.16: Wing skin mass as function of minimum divergence pressure $(q_{div})_{min}$

The influence of a divergence pressure constraint on the optimized wing skin mass is summarized in Figure 8.16. Each marker corresponds to an optimized design. Balanced laminate designs are drawn in blue, unbalanced designs in black. The plot contains all the investigated sweep configurations.

A first prominent feature, and also the reason for being able to plot balanced and unbalanced designs in a single diagram unambiguously, is that unbalanced laminates clearly outperformed the balanced designs. Even the wing with the least forward sweep of $\xi = -3.2^\circ$ and balanced laminates had a higher mass for all the investigated divergence pressures than the basic configuration with an $\xi = -16.8^\circ$ sweep, but optimized with unbalanced laminates.

In the case of balanced laminates, the influence of $(q_{div})_{min}$ was reflected in a weight increase with increasing divergence pressure. While for configuration 2, comprising a forward sweep of $\xi = -3.2^\circ$, the weight increment was moderate, the weight penalty increased with larger forward sweeps.

A very different behavior could be observed for the unbalanced designs. Nearly no influence of the constraint on wing skin mass was identifiable for the smaller forward sweep angles, configurations 1 and 2, suggesting that the constraint was nowhere active. While this is true for the smallest forward sweep angle $\xi = -3.2^\circ$, it did become active for $\xi = -10.0^\circ$ and $q_{div} \geq 40000 Pa$. However, the optimization with unbalanced laminates was able to meet the constraint with nearly no weight increase. Even for the largest forward sweep the weight increase with increasing divergence pressure constraint was very moderate. The unbalanced optimization thus featured for instance $\approx 23\%$ weight saving for $q_{div} \geq 40000 Pa$ compared to balanced laminates and even more for larger divergence pressure constraints.

In order to identify the characteristics that were responsible for the described effects, the design variables were explored. The stiffness distributions for two divergence pressure constraints in vertical order, and balanced and unbalanced optimizations in

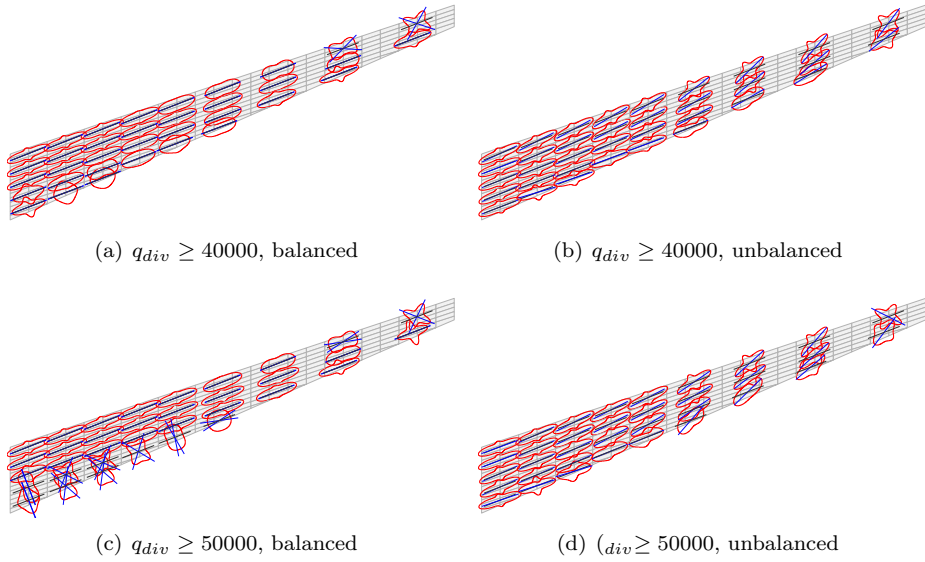


Figure 8.17: Optimized design, basic configuration, $\hat{E}_{11}(\theta)$ upper skin for different $(q_{div})_{min}$ constraints

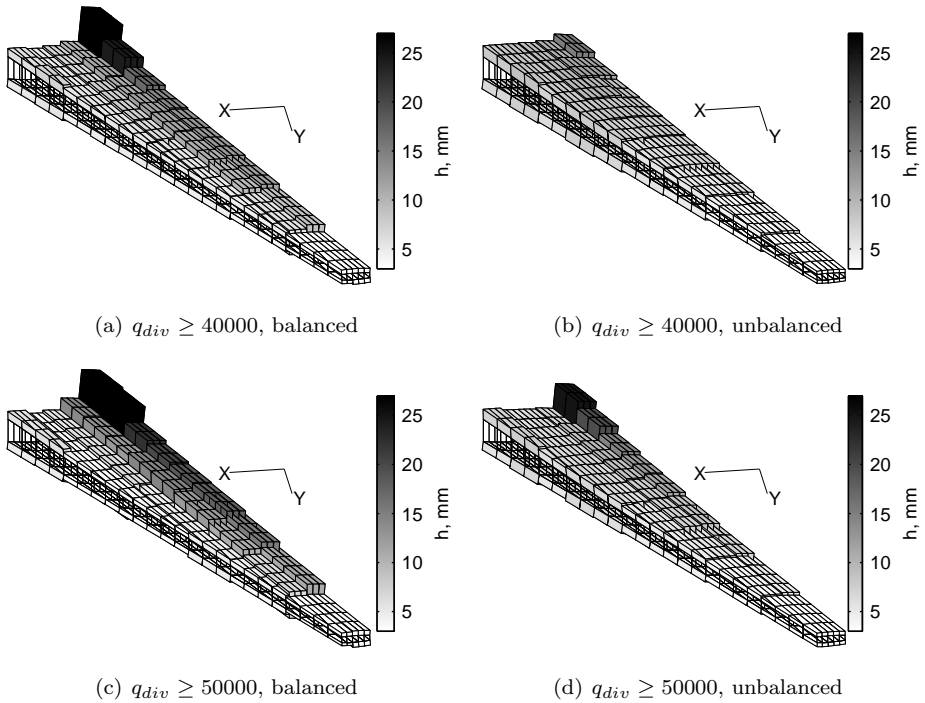


Figure 8.18: Optimized design, basic configuration, thickness distribution for different $(q_{div})_{min}$ constraints

horizontal order are plotted in Figure 8.17. The corresponding thicknesses are summarized in Figure 8.18. Looking at Figure 8.17(a) and 8.17(c), compliance with the divergence constraint for an optimization with balanced laminates did not provide significant resources in terms of unexceptional stiffness distributions. Other than for aileron effectiveness, an increase in torsional stiffness, as suggested by equation (2.7) on page 31, does not necessarily result in a weight optimal solution. The two-dimensional treatment disregards the geometric coupling involved in the final twist distribution of the forward swept wing. An increase in torsional stiffness would go along with a decrease in bending stiffness, therefore increased bending deflection and eventually an increase in twist induced by geometric coupling. The more prominent measure in fulfilling the divergence constraints was realized by the thickness distribution, Figure 8.18(a) and 8.18(c). In both figures a distinctive thickness increase along the front spar, amplifying with increasing $(q_{div})_{min}$ can be seen. Two effects were provoked by this, one, the sweep angle of the elastic axis was decreased, leading to a reduced geometric coupling, and two, the cross-sectional shear center moved forward, which according to equation (2.7), page 31, results in an increase in divergence pressure by reducing the distance to the aerodynamic center. Apparently, to support the elastic axis adjustment, in case of the largest divergence pressure constraint, Figure 8.17(c), the spanwise stiffness close to the rear spar in the root region was decreased considerably by adjusting the main stiffness direction to angles of $\approx \pm 45^\circ$ to $\pm 90^\circ$ with respect to the material coordinate system, depicted as black solid line.

Comparing the balanced laminate thickness with the unbalanced counterparts, see Figure 8.18(b) and 8.18(d), discloses the reason for the weight penalty of balanced over unbalanced laminates. Only for the largest divergence pressure constraints, Figure 8.18(d), did the optimization with unbalanced laminates start to adopt the thickness methodology described for balanced laminates. Figure 8.18(b) again depicts a gradually changing thickness distribution. Rather than thickness, the dominant contribution in fulfilling the divergence pressure constraint was introduced by the stiffness distribution, see Figure 8.17(b) and 8.17(d). With the inner wing dominated by stiffness distributions clearly expanding in the spanwise direction, the main stiffness direction tilted forward, gradually increasing, from mid to the outer wing design fields. The bending-torsion coupling introduced by tilting the stiffness featured a negative coupling index, as depicted in Figure 7.39(b) on page 129. Accordingly, the wing twists towards smaller angles of attack when bending up, thus counteracting the geometric coupling. Coupling in this respect acts as a form of artificial increase in torsional stiffness, since the wing with coupling shows less twist increase when bending upward than a wing without coupling.

To substantiate the described behavior, exemplary plots of the spanwise twist distributions for the $-1.0g$ load case 1001 and the $+2.5g$ load case 1002, balanced and unbalanced laminates are given in Figure 8.19. For both laminate type three different optimized wings are compared, varying only in divergence pressure constraint. With increasing $(q_{div})_{min}$, both laminate types showed a decrease in positive twist for LC 1002, caused by the thickness effects described for balanced laminates, and stiffness coupling effects described for unbalanced laminates. To that effect, the twist in case of the negative acceleration $-1.0g$ load case 1001 increased to less negative values with increasing $(q_{div})_{min}$ constraint. The rationale behind the $-1.0g$ load case to result in absolutely larger twist angles than the $+2.5g$ load case is the contribution of the

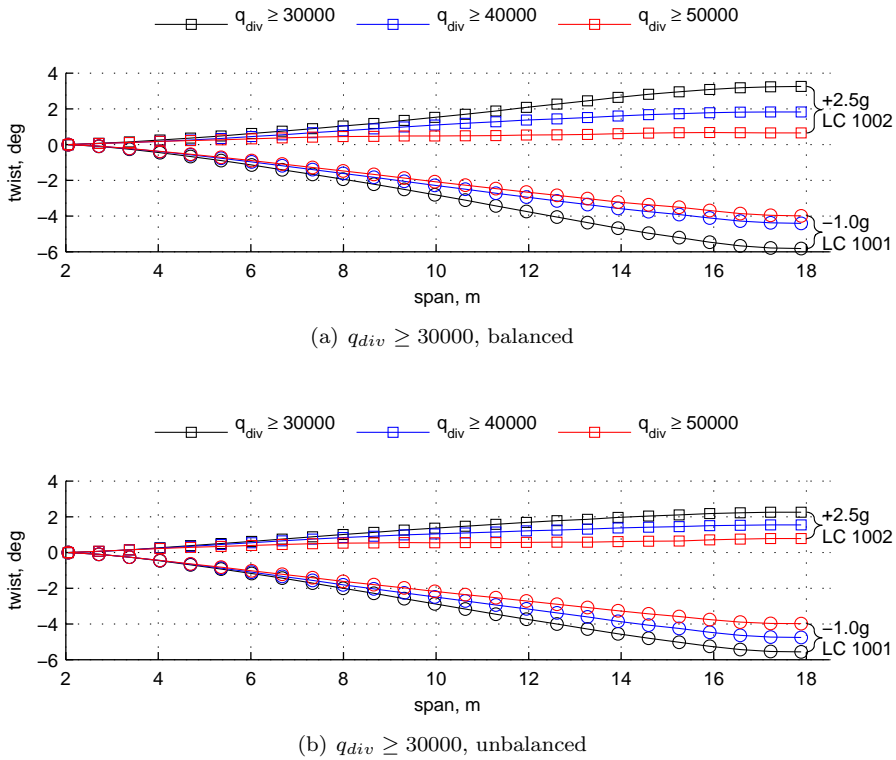


Figure 8.19: Optimized design, basic configuration, twist distribution for different $(q_{div})_{min}$ constraints

negative airfoil moment, realized by the consideration of a W2GJ camber correction.

In order to demonstrate an equivalent behavior for the other configurations in terms of optimized thickness and stiffness distributions, the optimized designs for wing configurations 1 and 2, comprising $\xi = -10.0^\circ$ and $\xi = -3.2^\circ$ leading edge sweep and a divergence pressure constraint of $q_{div} \geq 40000$ are depicted in Figure 8.20. The same coupling mechanism as for the basic configuration in the outer wing were activated. It was shown in Figure 8.16 that for reduced sweep the divergence constraint starts to influence the design only for larger divergence pressure constraints. To this end, the negative coupling index established in the stiffness distributions shown in Figure 8.20(b) and 8.20(d) to a certain amount is accounted for by mass reduction as consequence of inboard shifting aerodynamic loads. An equivalent behavior could already be observed in the optimizations presented in the previous section 8.6, in the case of ineffective aileron constraints.

Due to the resemblance of the failure index distributions with previously presented failure index plots, these will be skipped in this section. Nonetheless, on a final note, a typical active divergence pressure response development, demonstrating the functionality of the aeroelastic constraint is depicted in Figure 8.21.

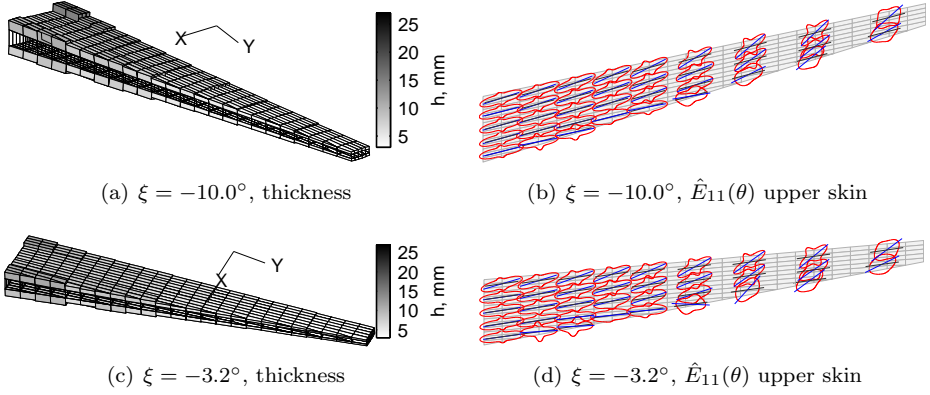


Figure 8.20: *Optimized design, unbalanced laminates, $q_{div} \geq 40000$*

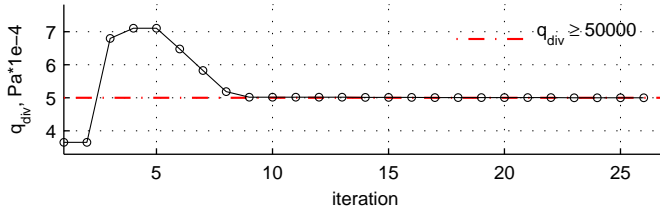


Figure 8.21: *Divergence pressure development, basic configuration, unbalanced laminates, $q_{div} \geq 50000$*

8.8 Numerical Results: Twist Constraint

In contrast to divergence and aileron effectiveness, elastic wing twist is not constrained explicitly by aircraft regulations. Nevertheless, the wing twist distribution as function of span is an important aeroelastic parameter when it comes to designing an optimal aerodynamic shape for minimum induced drag. Therefore, twist was considered as a third aeroelastic constraint in the present investigation. With the tendency of a forward swept wing to increase aerodynamic twist when bending up, the twist constraint was set as an upper bound. The constraint can be written as:

$$\alpha_{tip} \leq (\alpha_{tip})_{max} . \quad (8.3)$$

Assuming the twist distribution to be of highest importance in cruise flight, the tip twist was constrained for load cases 2007, 3007, 4007 and 5007 as listed in table 8.7. Here, the first two LC simulate a mass case with full passenger capacity and the last two LC a mass case with half passenger capacity, at the beginning and end of cruise flight respectively.

The results for balanced and unbalanced laminates are summarized in Figure 8.22. Again, a clear advantage in optimized mass existed for all three configurations with unbalanced laminates. While for $\alpha_{tip} \leq 1.0^\circ$ a mass saving of 13 – 18%, depending on sweep angle, could be achieved, the mass difference not only increased for smaller tip

twist constraints, but with unbalanced laminates twist constraints could be reached that were unattainable with balanced laminates. The optimized masses of the less swept configurations 1 and 2 in case of unbalanced laminates showed only marginal weight increases with a decreasing tip twist constraint, therefore designating inactive twist constraints for the larger $(\alpha_{tip})_{max}$.

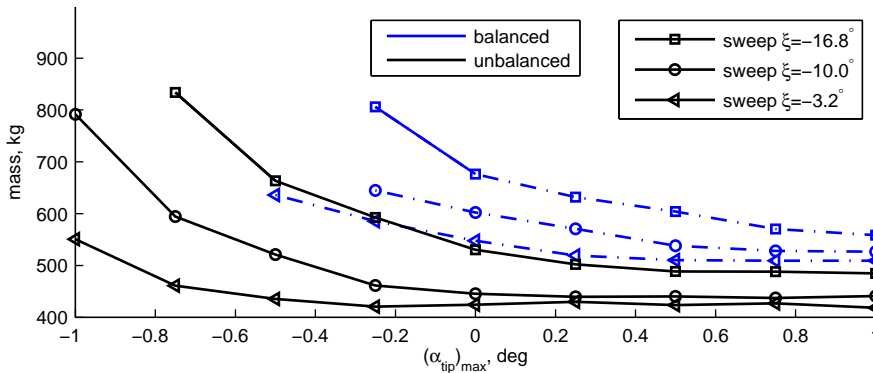


Figure 8.22: Wing skin mass as function of maximum tip twist $(\alpha_{tip})_{max}$

For the basic configuration, the stiffness and thickness distributions for tip twist constraints $\alpha_{tip} \leq 0.25^\circ$ and $\alpha_{tip} \leq -0.25^\circ$, vertical order, and balanced and unbalanced laminates, horizontal order, are depicted in Figure 8.23 and 8.24. The lower twist angle corresponds to the minimum achievable $(\alpha_{tip})_{max}$ in a balanced laminate design. The application of bending-torsion coupling when optimizing with unbalanced laminates represents an effective means to fulfill the twist constraints, see Figure 8.23(b) and 8.23(d). The stiffness distributions in the mid and outer wing were tilted forward, resulting in a negative coupling index and going along with a twist reduction at the tip. In the case of balanced laminate designs, see Figure 8.23(a) and 8.23(c), no coupling existed and thus the stiffness distribution at least for $\alpha_{tip} \leq 0.25^\circ$ showed a spanwise alignment for a majority of the design fields. Tightening the constraint to $\alpha_{tip} \leq -0.25^\circ$ led to the same effect observed for the divergence pressure constraint. The optimizer weakened the rear part of the wing box by aligning the maximum stiffness direction exactly at 90° with respect to the material axis, see Figure 8.23(c). Looking at the corresponding thickness distribution, see Figure 8.24(c), reveals the extraordinary charges that had to be considered to comply with the twist constraint. The skin thickness in the most forward row of the design fields increased considerably to shift the elastic axis forward and thus a reduction in the nose up twisting moment induced by aerodynamic lift. The equivalent thickness distributions with unbalanced laminates, see Figure 8.24(b) and 8.24(d) showed smooth thickness variations and only a much attenuated form of frontal thickness increase of the corresponding balanced laminate design for $\alpha_{tip} \leq -0.25^\circ$.

Optimization results for an upper limit $\alpha_{tip} \leq -0.75^\circ$ that could only be achieved with an unbalanced design are shown in Figure 8.25. The thickness distribution with a few exceptions closely resembled the balanced optimization for $\alpha_{tip} \leq -0.25^\circ$, see Figure 8.24(c), pointing out that once the stiffness coupling possibilities were maxed

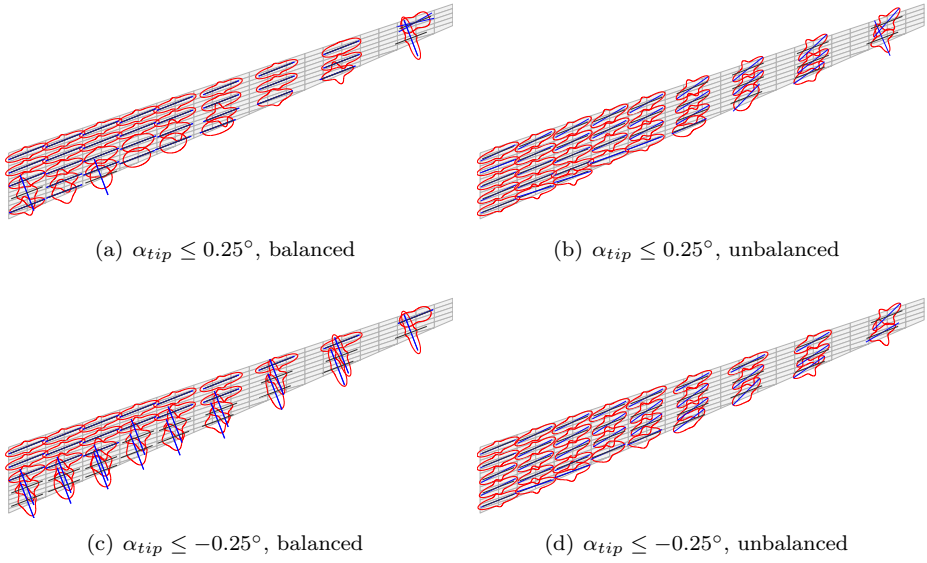


Figure 8.23: *Optimized design, basic configuration, $\hat{E}_{11}(\theta)$ upper skin for different $(\alpha_{tip})_{max}$ constraints*

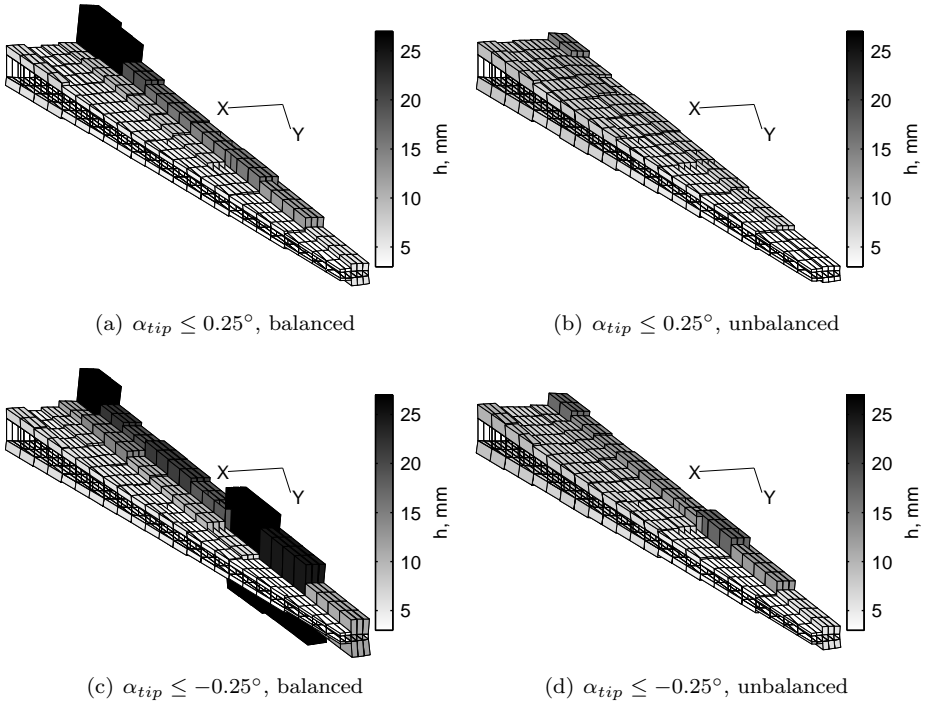


Figure 8.24: *Optimized design, basic configuration, thickness distribution for different $(\alpha_{tip})_{max}$ constraints*

out, an unbalanced laminate design also had to adopt the thickness distribution to comply with the aeroelastic constraint.

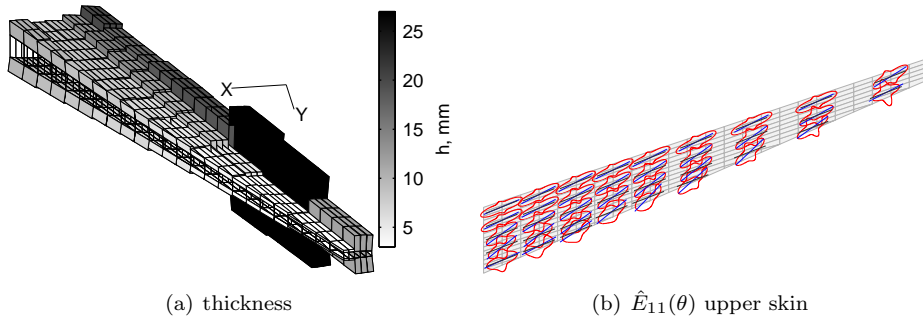
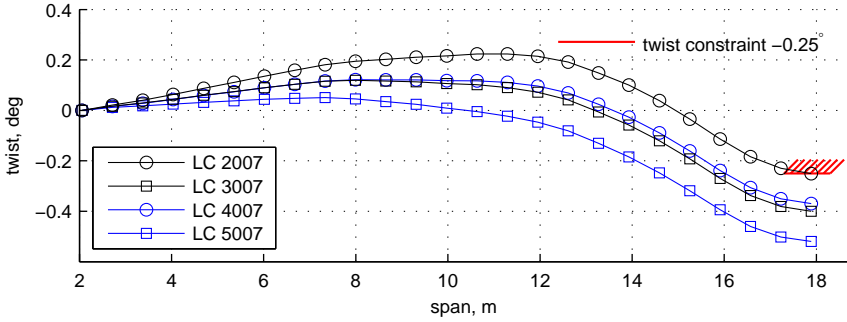


Figure 8.25: *Optimized design, basic configuration, unbalanced laminates, $\alpha_{tip} \leq -0.75^\circ$*

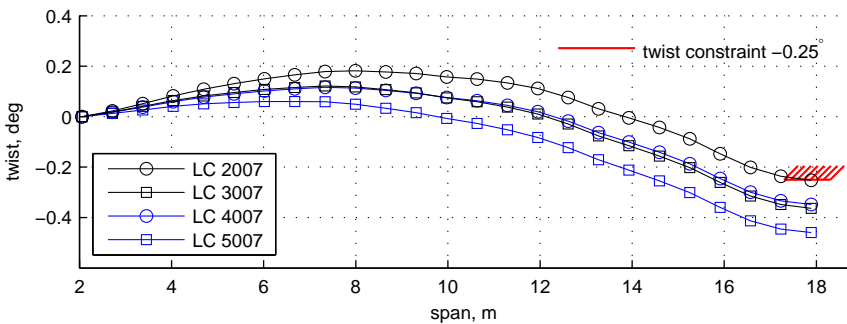
The twist distributions for optimized designs with a tip twist constraint $\alpha_{tip} \leq -0.25^\circ$ are shown in Figure 8.26 for balanced and unbalanced laminates. As demanded by the constraint, the largest tip twist of all four cruise load cases exactly matched the prescribed limit. An important point to notice is that neither fuel cases corresponding to begin and end cruise, marked in the same color in Figure 8.26, nor passenger capacity had an appreciable influence on the twist distribution. The tip twist variation as a result of fuel burning during cruise stayed below 0.2° for all the cases investigated, independent of balanced or unbalanced laminates. Certainly, the results were highly dependent on the applied flight conditions in terms of *Mach* number and flight level, while keeping in mind that the iso-altitude and constant *Mach* number considerations in the present investigation led to varying lift coefficients for the load cases depicted in Figure 8.26. Moreover, the employed fuel sequence was generic and not based on real aircraft data. However, the results give an indication of the twist effects to be expected in a wing from mass distribution variations.

8.9 Some Remarks on Stringers

The stiffness distribution optimizations presented in this and all other application chapters of part II of the work assume constant stringer properties, hence stringer stiffnesses are not part of the optimization model. The most prominent reason to do so is the focus of the optimization process on shell-like structural entities. This focus is evident in the formulation of the response approximations, which are expressed as linear and reciprocal functions of the laminate stiffness matrices and thicknesses. Nevertheless, depending primarily on the stringer stiffness, part of the wing bending and coupling stiffness are captured by the stringers and their orientation. The larger the share contributed by stringers, the more the wing skins are assigned to the task of providing torsional stiffness, support of bending-torsion coupling effects, and preservation of the aerodynamic shape. This is demonstrated for instance in the stiffness distributions shown in Figure 8.12 on page 146 in case of aileron effectiveness, or in Figure 8.17 on page 150 in case of a divergence pressure constraint. While the root and mid wing region feature a strong alignment of stiffnesses in the spanwise direction,



(a) balanced



(b) unbalanced

Figure 8.26: *Optimized design, basic configuration, twist distribution for $\alpha_{tip} \leq -0.25^\circ$*

stiffnesses develop into distributions supporting torsional stiffness in the tip region of the wing. The reason for this is the increased contribution of stringers to the bending stiffness in the tip region.

In the development of the process towards a possible application in an industrial environment, the inclusion of stringers in the optimization will constitute an important next step, thus allowing the optimizer to determine the optimal ratio of stringer and wing skin contributions to the overall wing stiffness. Consideration of stringer optimization in the current formulation could for instance be achieved by assigning a *virtual* design field to each group of constant property stringers. Treating the stringers as simple bars with a prescribed elastic modulus then allows for a description of stiffness and mass properties solely depending on the bar area, which in turn can be linked to the regular thickness design variable in the approximation formulation. Stringer strain constraints can be formulated as functions of thickness only. In a more detailed stringer consideration, the stringer cross section could also be modeled by means of shell elements, and thus the full set of design variables available in each design field would apply. This however requires the specification of stringer topology and outer dimensions. Keeping in mind that the buckling analysis employed in this work implies simply supported boundary conditions for all four buckling field edges, in the case of stringer inclusion in the optimization model a revision of the buckling assessment would be required.

8.10 Summary

A detailed investigation into the influence of aeroelastic constraints and sweep angle on the optimized mass of three forward swept wings was presented. The wings featured equal wing area and span, and therefore also equal wing loading and aspect ratio. They were analyzed and optimized for a fixed set of mass and load cases. The optimizer was shown to yield consistent results for balanced and unbalanced laminates. Unbalanced laminates showed clear advantages over balanced laminates for all aeroelastic constraints considered. The divergence constraint particularly, usually requiring a stiffened and therefore heavier wing structure in the case of forward swept wings, was shown to incur no weight penalty when the structure was optimized using unbalanced laminates.

It should be noted that results will differ to some extent when spar webs are included in the optimization. They are expected to have a noticeable influence on the optimized skin thickness in case of severe aeroelastic demands. Some of the depicted thickness distributions showed local thickness increases close to the front and/or rear spar, which will be alleviated when spar webs are included in the optimization. Moreover, keeping in mind the intended production strategy, thickness variations among adjacent design fields are limited to a certain amount, beyond which the practicability of the optimized design is debatable.

Eventually, the mass savings presented are assumed to show trends rather than absolute values of what is possible using unbalanced laminates. The source of the largest possible errors remains the neglect of transonic effects in the application of a doublet lattice method. Inclusion of more accurate aerodynamic loads via incorporating an *Euler* solver in the design process will be discussed in the following chapter.

CHAPTER 9

Aeroelastic Optimization With Aero Correction

“Flying is learning how to throw yourself at the ground and miss.”

Douglas Adams

In the two preceding chapters the general functionality of the optimization process involving structural and aeroelastic responses was established. While the swept back wing optimizations discussed in chapter 7 were performed without correction of the static aerodynamic forces, optimizations of the forwards swept wing, presented in chapter 8, already incorporated a correction of the doublet lattice method in terms of a DLM camber adjustment using a W2GJ matrix; details on the latter were presented in section 6.2.1.

Given that the meaningful scope of application of the doublet lattice method is limited to recompression shock free and attached flows, and the fact that the investigated transport aircraft-like wings operate very well in transonic flight regimes, it is necessary to provide an appropriate method for the correction of aerodynamic loads acting on the wing, the reason being that consideration of non-linear aerodynamic effects is expected to result in a credible improvement of the optimized stiffnesses. The correction method, comprising the computation of aerodynamic forces using the CFD solver TAU was developed and presented in chapter 6. Its application, along with the generation of the required analysis models and accompanying convergence studies will be demonstrated in this chapter.

The reference model selected for aeroelastic optimization with aero corrections in terms of geometry corresponded exactly to the forward swept wing example used in chapter 8, see section 8.1 on page 132. The flight envelope was also the same as that used in chapter 8, see Figure 8.2 on page 134, along with the depicted load cases, which are described in detail in section 8.2. For ease of reading, the load cases are listed again in table 9.1.

Adjustments to the finite element and DLM modeling resulting from the further development of modeling techniques in MODGEN will be outlined in section 9.1, along with a brief description of the optimization model. The generation of an appropriate CFD mesh for TAU *Euler* computations is discussed in section 9.2, while a primal

Table 9.1: *Load case definition*

| LC # | type | Ma [-] | q [Pa] | n_z [g] | H [m] |
|------|---------------------------|--------|--------|-----------|-------|
| 1 | sym., push down, V_D | 0.597 | 25300 | -1.0 | 0 |
| 2 | sym., pull up, V_D | 0.597 | 25300 | +2.5 | 0 |
| 3 | sym., push down, M_D | 0.870 | 22700 | -1.0 | 6700 |
| 4 | sym., pull up, M_D | 0.870 | 22700 | +2.5 | 6700 |
| 7 | sym., cruise, M_D | 0.780 | 9700 | +1.0 | 11900 |
| 12 | antisym., roll, $1.15V_D$ | 0.690 | 33800 | | 0 |
| 13 | antisym., roll, $1.15V_D$ | 0.860 | 31900 | | 4000 |
| 14 | antisym., roll, V_D | 0.870 | 22700 | | 6700 |
| 15 | antisym., roll, V_D | 0.870 | 12000 | | 11900 |
| 16 | divergence, V_D | 0.870 | | | |

application of the CFD correction module in a static trim calculation is shown in section 9.3. Optimization results for a mass minimization with aeroelastic constraints are presented in section 9.4, focusing especially on the structural implications due to modified aerodynamic forces. The general capability of the optimization process to allow for multiple structural entities in the optimization model using an investigation of the impact of appending shear webs to the design fields is discussed and evaluated in section 9.5.

With the focus of this thesis being the stiffness optimization process as the first of three optimization steps towards a manufacturable structure by featuring membrane and bending stiffness matrices as design parameter, in section 9.6 an application of the second optimization step eventually will be demonstrated, which generates stacking sequences based on the optimized stiffnesses. A brief introduction to the underlying theory is provided in section 2.3.

9.1 Finite Element and Optimization Model

Given the ever improving modeling capabilities in the parametric finite element model generation with MODGEN on the one hand, but mainly due to a direct implication of the CFD correction, a modified parametric modeling strategy was applied to generate the required structural and aerodynamic models. The original finite element model generation is described in section 8.3.

To understand the necessity for remodeling, the DLM correction procedure and the CFD mesh generation procedure will be briefly addressed below. As outlined in section 6.2.1, the DLM camber and twist correction matrix W2GJ is generated based on the aerodynamic surface spanned by the underlying airfoil stations. MODGEN determines the DLM box correction angle by analyzing the corresponding camber surface, which in turn is derived from the wing aerodynamic surface. In the parametric construction of the finite element model as described in chapter 8, the MODGEN technique of splined aerodynamic surface generation, spanning several airfoil stations, was selected. The CFD mesh generation, section 6.4.1, however, is based on a purely linear interpolation of adjacent airfoil stations. This causes an unintended difference in the aerodynamic surfaces used for DLM correction and for the CFD mesh generation.

Consequently, instead of spanning a splined surface over several airfoils as done in the first wing model, the new wing model linearly varies the aerodynamic surfaces from airfoil to airfoil. The implications for the underlying FEM structure are depicted in Figure 9.1, in which the two resulting wing boxes are shown in different colors. The

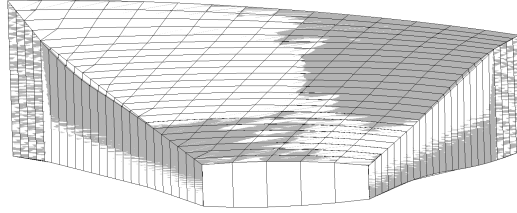


Figure 9.1: *FEM wing box, chapter 8 model in gray, chapter 9 model in white*

expected impact on the structural behavior of the wing compared to the first model is negligible, since the structural extent in thickness direction of the wing was preserved throughout. Other than the explicated modeling modification mentioned above, the finite element model comprised an identical rib, spar and stringer setup along with the same structural and material properties in combination with the same element resolution.

Another distinction of the present model compared to the previous model was that only points belonging to the load reference axis and the attached rigid bar connections extending to leading and trailing edge, were considered for aerodynamic force coupling. Thus, coupling corresponded to the technique envisaged in section 3.4.2 on page 49. The corresponding coupling nodes are depicted in Figure 9.2. As a result

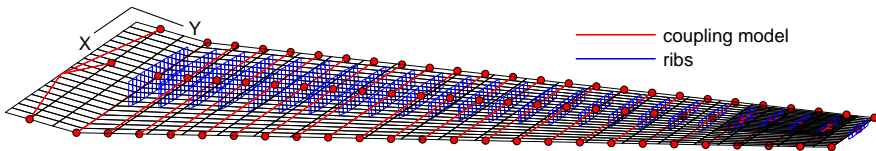


Figure 9.2: *Coupling model and DLM*

of modeling the load carrying structure without the center wing box, while simultaneously extending the aerodynamic model until the x-z symmetry plane, as required to obtain a meaningful spanwise load distribution, all the aerodynamic loading generated in the root area would be transferred to the first coupling node row, however due to the fact that the first rib is clamped, the large aerodynamic loading on this coupling row would not have an influence on the structural loading. Nevertheless, in order to obtain a more regular distribution of coupled aero forces, an additional row of coupling nodes was introduced in the wing root area, Figure 9.2, the consequence of which will be discussed later in section 9.3.

Using the adapted finite element modeling technique described above, slightly modified fuel masses resulted, Figure 9.3, compared with those shown in Figure 8.7 on page 138. All the other masses like non-structural, aircraft and payload masses concurred with those applied in the previous model.

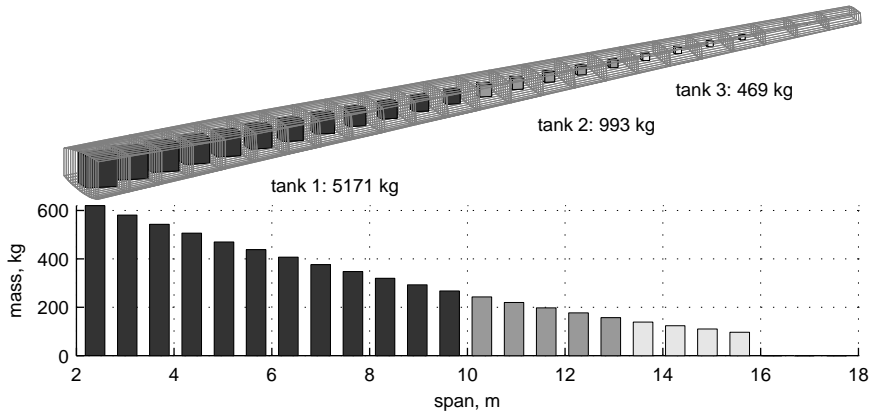


Figure 9.3: *Fuel masses*

As before, the optimization model comprised in total 68 design fields, Figure 9.4, accordingly the number of design variables was identical to those for the previous model. Since the same load cases were employed, the response numbers to be considered in NASTRAN and the optimizer did not change, see table 8.8 on page 141. Approximations for strain and buckling failure, aileron effectiveness, divergence and

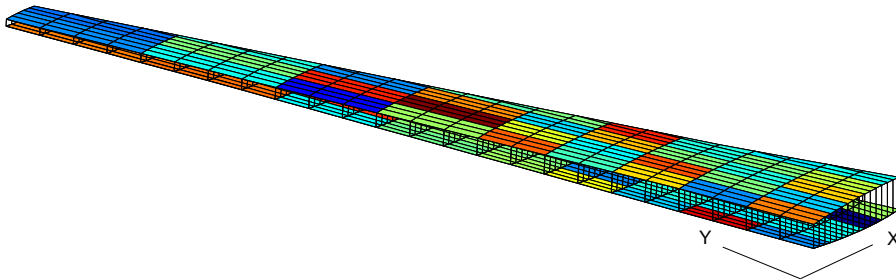


Figure 9.4: *Design fields*

twist were implemented according to the derivations to be found in sections 5.6, 5.7, and summarized in table 5.1 on page 78. This included the convexification of aeroelastic responses. The strain allowables required for the failure envelope construction were set to $[\varepsilon_t, \varepsilon_c, \gamma_{xy}] = [0.5\%, -0.4\%, 0.4\%]$, and thus were identical to the optimization without CFD correction, see section 8.4.

9.2 CFD Model

The CFD mesh was generated according to the process described in section 6.4.1 and based on the same planform and airfoil coordinate input defined for the generation of the finite element model.

In order to determine the appropriate mesh resolution that would be required to achieve convergence of the important aerodynamic quantities like lift and moment, a

convergence study was performed. Several meshes, comprising different surface and volume resolutions were generated with SUMO. To construct realistic test conditions, all the meshes were investigated for the same mesh deformation state found for a previously conducted optimization run. With the aero correction method expected to alter in particular the force distribution for load cases with recompression shocks, load case 4 from table 9.1 was selected as test case for mesh convergence.

The results for the six different meshes are presented in Figure 9.5, in which the aerodynamic coefficients C_L , C_m and C_D as a function of the number of tetrahedra making up the mesh are shown. As stated by the figure, the coefficients converged

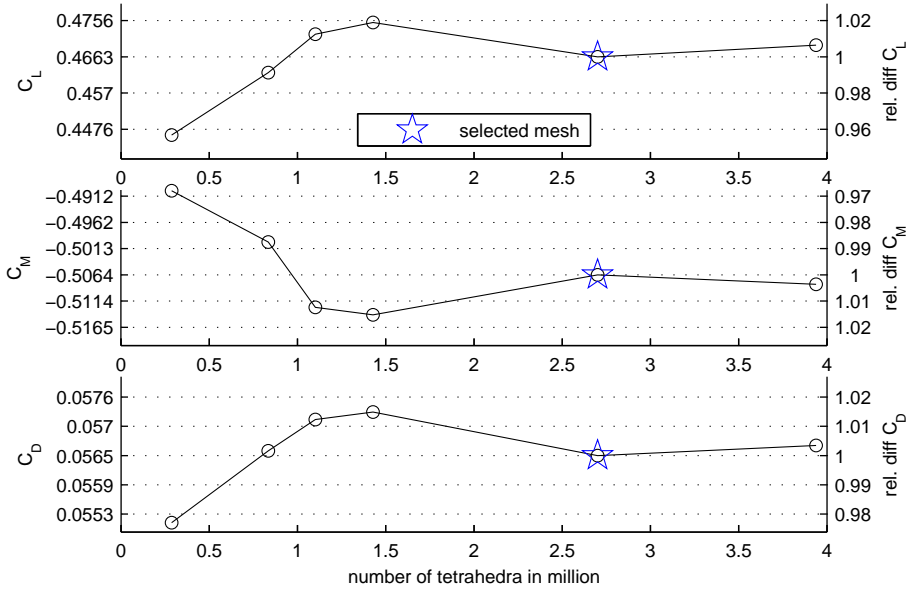


Figure 9.5: TAU *Euler* convergence study

to nearly steady values for meshes with element numbers above $\approx 1.5 \cdot 10^6$. The mesh that was finally selected for the aero correction process consisted of $\approx 2.7 \cdot 10^6$ tetrahedra and is marked by a blue star in Figure 9.5. The y-axis on the right side of each graph quantifies the relative difference of the corresponding coefficients with respect to the coefficient generated with the selected mesh. For all three coefficients the relative difference with respect to the mesh that featured the highest resolution was smaller than 1%. Moreover, distributing the TAU *Euler* computation on six processors, and by this being able to perform the optimization process on a single desktop computer, the $2.7 \cdot 10^6$ tetrahedra mesh resulted in very moderate computational costs of $\approx 3 - 5$ minutes for a single CFD run, depending on the residual convergence behavior. Considering eight load cases to be corrected led to an ≈ 40 minutes calculation time for a full set of correction forces. This will be linked to the computational costs of sensitivity generation and optimization in section 9.4.

The selected mesh comprised $\approx 315,000$ surface triangles, a spanwise section of which is shown in Figure 9.6, to give an impression on the element density and distribution as it was achieved using diverse SUMO meshing parameters, among which

the most influential were the minimum and maximum edge length. They were set to 11 mm and 110 mm respectively.

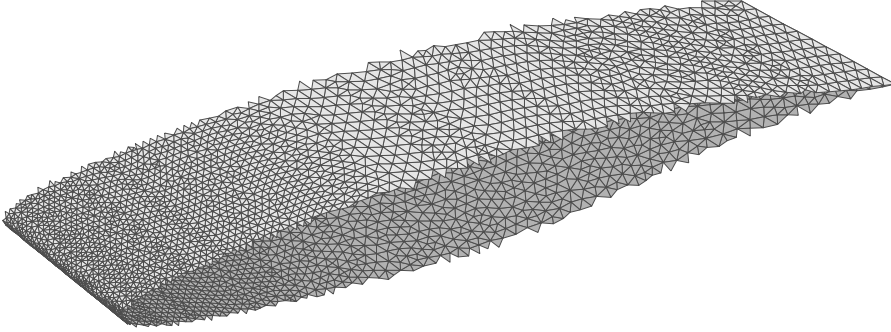


Figure 9.6: Mesh section generated with SUMO

9.3 Aeroelastic Trim Application

In order to separate the effects of a newly applied CFD aero correction from the effects induced by a stiffness optimization, the general functionality of the CFD correction module was demonstrated using a classical static aeroelastic trim application. In doing so, the most prominent differences between the results of the applied aerodynamic methods could be highlighted, thereby also constituting graphical means for the assessment of the result.

The iterative procedure to determine the aeroelastic deformation considering TAU correction forces can be expressed as:

$$\mathbf{u}_s^{k+1} = \mathbf{K}^{-1} (\mathbf{f}_{DLM}^{k+1} + \Delta \mathbf{f}_\tau^k + \mathbf{f}_{ie}) , \quad (9.1)$$

with:

$$\Delta \mathbf{f}_\tau^k = \mathbf{f}_\tau^k - \mathbf{f}_{DLM}^k , \quad (9.2)$$

where superscript k denotes the iteration step and \mathbf{f}_{ie} corresponding to the summation of constant inertial and external forces. An iterative procedure which performs deformation and aerodynamic analysis in a sequential order is referred to as a weakly coupled system, whereas in a closely coupled system the aerodynamic forces can be expressed directly as a function of displacement, thus allowing for a direct solution of the static equilibrium equation. In section 6.1 it was shown that for the doublet lattice method alone, a close coupling is realized in NASTRAN.

A mass minimized version of the present forward swept wing, resulting from a stiffness optimization with unbalanced laminates and considering aero correction, provided the structural basis for the trim investigation. Details on the design will be provided in section 9.4. The symmetric load cases 1 – 4 and 7, compare table 9.1, later also to be corrected in the optimization run, were considered for static trimming, with the latter one for various mass cases.

According to equation (9.1) convergence can be tested by monitoring a characteristic deflection. This is shown in Figure 9.7, exemplarily for two sizing and two cruise load cases, using the z -deflection of the outermost spanwise load reference axis grid point, representing the tip of the wing, Figure 9.8. The load case numbering again

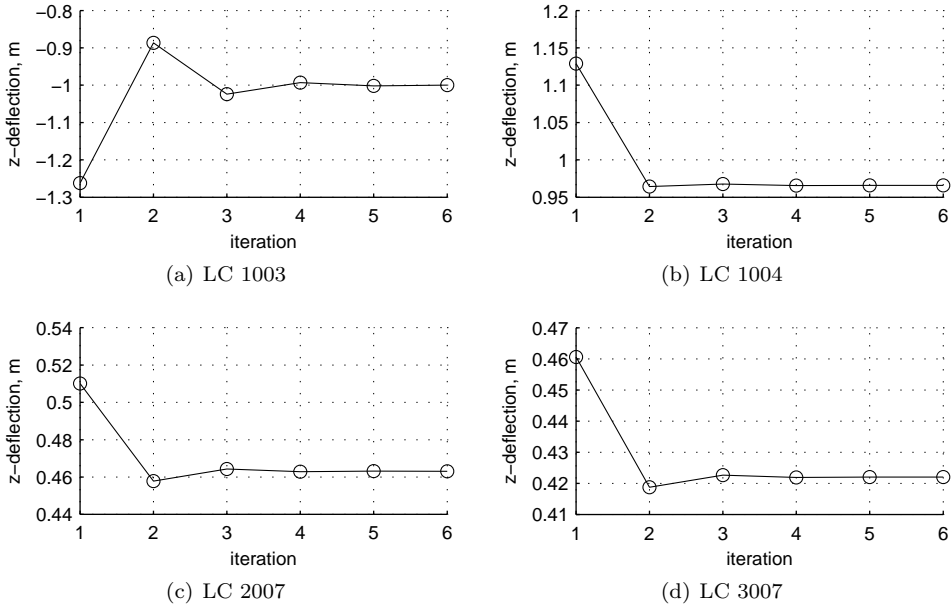


Figure 9.7: *Tip deflection development for static trim*

corresponded to the definition given in table 8.7 on page 139, where the last two digits identify the load case and the first digit the mass case. In the finite element solution of iteration $k = 1$ TAU forces \mathbf{f}_τ^0 were not yet included since they will be generated only afterwards, for a CFD mesh deformation which is based on the displacement results of the FE analysis. Accordingly, only DLM forces affected the deflection for iteration $k = 1$. From the second iteration on, TAU forces based on the previous FE analysis were included. The figure shows that once the correction forces are considered from iteration two on, convergence was achieved after three to four iteration steps.

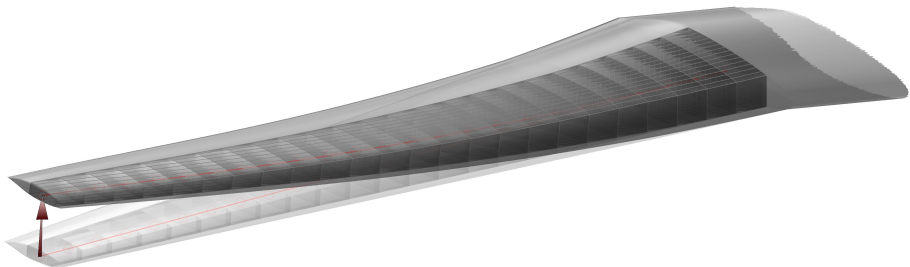


Figure 9.8: *Deformed FEM and CFD with z -deflection control point*

A second and equivalent means for testing the trim convergence behavior, as suggested by equation (9.1), consists of monitoring the iterative behavior of the aerodynamic forces, Figure 9.9. Depicted in the upper axis is the aero force development for DLM and TAU respectively. $|\mathbf{f}_{aero}|$ denotes the magnitude of the sum over all aerodynamic forces in the xz -plane, thus, in the absence of viscous drag, corresponding to the magnitude of the resulting force vector of lift and induced drag. Instead of summing forces on the different surface discretizations of DLM and TAU, forces in the coupling nodes were consulted. Examples of the aero forces for two sizing load cases featuring $n_z = -1.0g$ and $n_z = +2.5g$ respectively, are depicted in Figure 9.9(a) and 9.9(b). A first thing to notice is the quick convergence of the summarized nodal forces after three to four iteration steps. A second very important finding is the convergence of the resulting TAU force towards exactly the same value as the DLM force in the first iteration step $k = 1$, which did not, as yet, comprise the correction forces. This implies that the combination of \mathbf{f}_{DLM} and correction $\Delta\mathbf{f}_\tau$ in the converged solution exactly reflects \mathbf{f}_τ , as it was stated in equation (9.2):

$$\mathbf{f}_\tau = \mathbf{f}_{DLM} + \Delta\mathbf{f}_\tau. \quad (9.3)$$

The corresponding force magnitude reflects the constant lift force required to balance aircraft weight multiplied by the load factor.

The lower axes in Figure 9.9 depict the relative differences of the DLM and TAU force magnitudes, which apparently can be quite considerable, Figure 9.9(a). In sec-

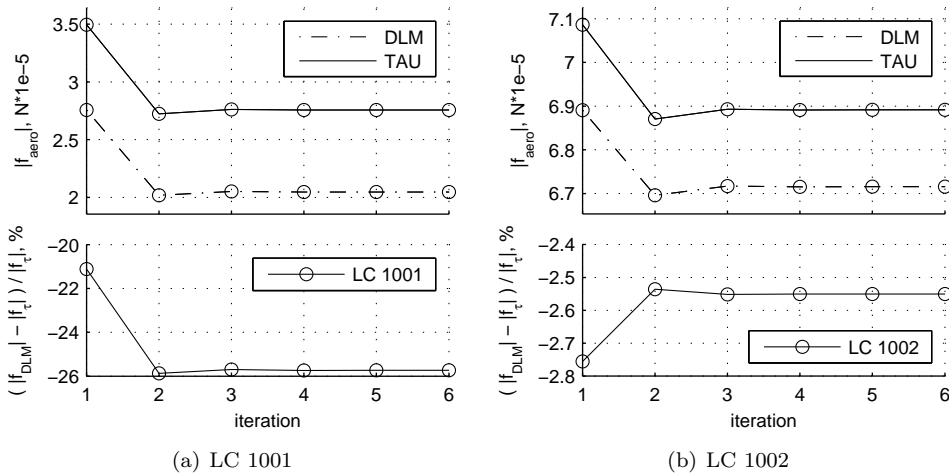
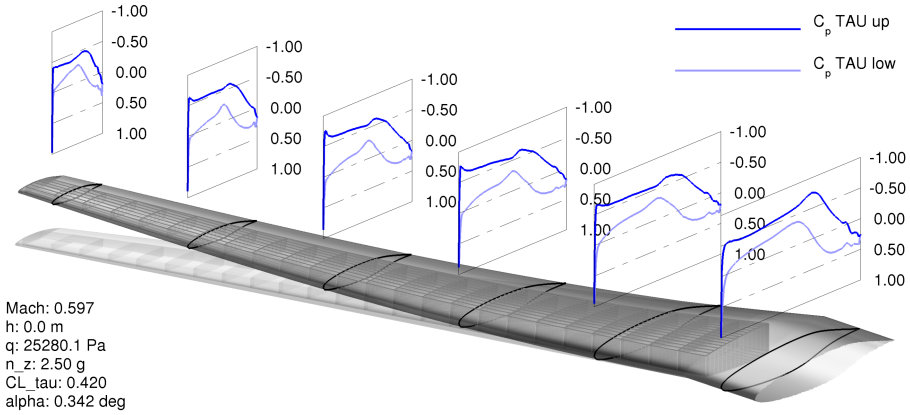


Figure 9.9: Aero force development for static trim

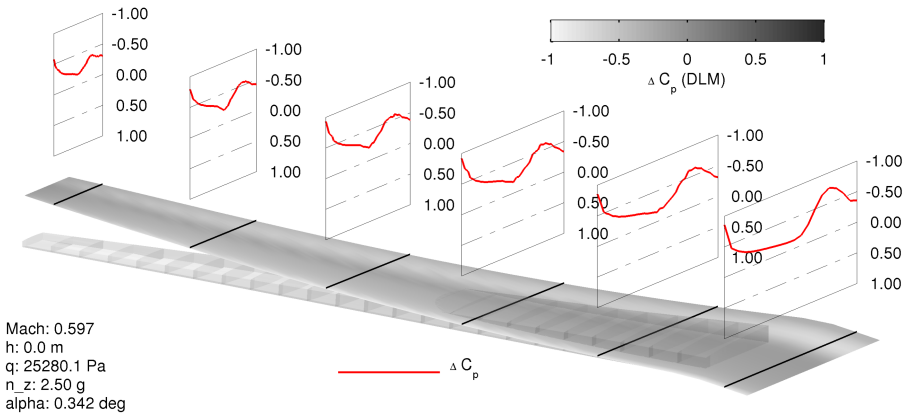
tion 6.3 it was explained that the TAU *Euler* calculation, apart from an equivalent mesh deformation, is performed for the same angle of attack as that resulting from the NASTRAN trim analysis. Thus, the converged difference between $|\mathbf{f}_{DLM}|$ and $|\mathbf{f}_\tau|$ is based only on aerodynamic discrepancies among the two discretization and analysis methods. To facilitate the interpretation of results emanating from a combined aerodynamic loading with doublet lattice and correction forces, different means for analyzing and illustrating the aerodynamic data are available.

The most general, and also unbiased, comparison comprises the surface pressure before splining to the coupling nodes. Due to the different discretization in DLM and CFD, the *least common denominator* is a comparison of pressure difference ΔC_p between the upper and lower wing surface. Routines were implemented in the result post processing that allowed for intersecting FEM, DLM, and CFD meshes, and in the latter case to reduce the upper and lower surface pressure data to ΔC_p . A comparison for LC 1002, hence a sizing load case with $n_z = +2.5g$ and a rather low *Mach* number of $M = 0.597$ is shown in Figure 9.10. TAU pressure distributions at equidistant spanwise stations, based on surface cuts on the deformed CFD mesh, represented as shaded surface, are shown in Figure 9.10(a), in addition, the undeflected FEM and CFD mesh are depicted to facilitate the assessment of unscaled wing deformation. The C_p distribution indicated no recompression shocks throughout the wing and an equivalent representation plotting the surface *Mach* number instead of C_p confirmed $M < 1$. The deformed finite element model is plotted as well, to demonstrate the meaningful CFD mesh deformation. Later on, a two-dimensional illustration will more explicitly show the coincidence of the two meshes. Performing similar cuts on the doublet lattice model led to the results depicted in Figure 9.10(b). Due to the two-dimensional discretization in DLM, only a pressure difference exists, which in the figure is also represented in the shading of the deformed doublet lattice model. As a direct consequence of camber correction using the W2GJ matrix, the ΔC_p distribution deviates considerably from a regular flat plate pressure distribution as it would be expected when omitting the correction. Finally, in Figure 9.10(c) a direct comparison of the TAU and DLM pressure differences is presented. Evidently, the corrected DLM was in good agreement with the higher order aerodynamic CFD method TAU. In all the depicted sections, DLM reproduced the main trends, although slightly downstream of the TAU results. With the DLM mesh featuring a considerably coarser discretization, no data were available at the trailing edge; the largest deviations therefore occurred at these positions.

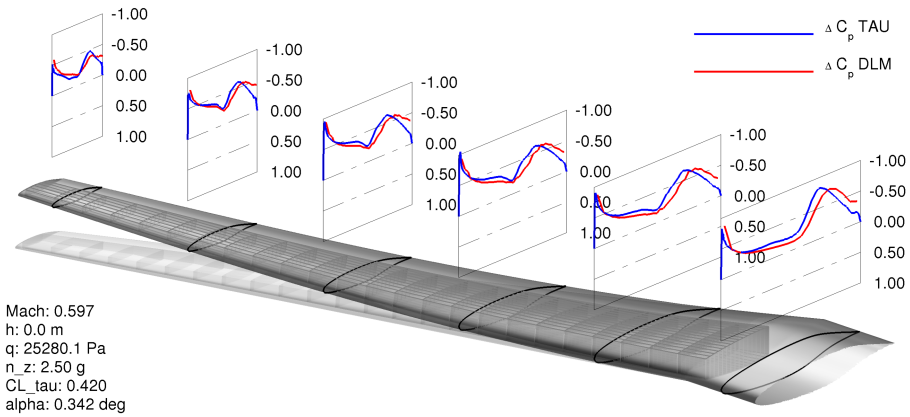
An entirely different behavior is revealed when looking at the second $n_z = +2.5g$ sizing load case 1004, see Figure 9.11. The free stream *Mach* number was considerably higher, resulting in a strong shock on the upper and on the lower wing surface, Figure 9.11(a). The shock on the lower surface can be explained by the laminar pressure distribution characteristics of the disposed airfoils. The, as yet shock free, pressure distributions shown in Figure 9.10(a) indicated a favorable pressure gradient on the lower skin, followed by a rather steep pressure recovery, giving the airfoil a rear loading characteristic. Later it will be shown that for the cruise *Mach* number the local *Mach* stays just below $M = 1$, however, under severe loading conditions as in LC 1004 a recompression shock arouse. The pressure difference ΔC_p from DLM, Figure 9.11(b), in turn showed no considerable differences when compared to the previous distribution, Figure 9.10(b), except for alterations in the pressure peak on the nose and the interaction with the pressure level on the first half of the airfoil; the reason for which can be found in the altered angle of attack and local twist distribution, however, the general pressure distribution characteristic does not change. A direct comparison of TAU and DLM pressure difference ΔC_p , Figure 9.11(c), revealed substantial deviations. The recompression shocks exerted a considerable influence on the pressure difference ΔC_p . As a result of the large negative pressure difference in the back, and a decrease in the frontal part with respect to the doublet lattice results, the



(a) C_p TAU

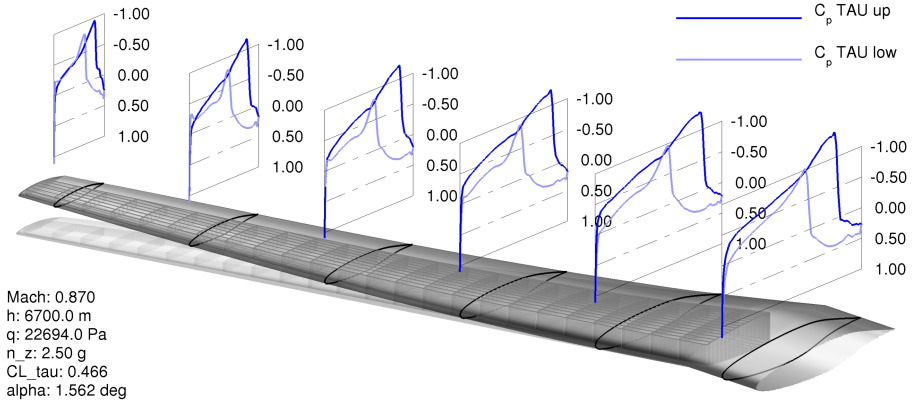


(b) ΔC_p DLM

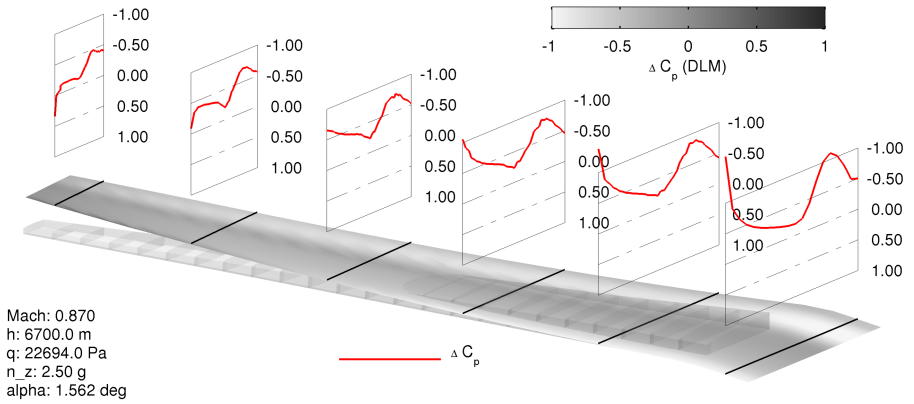


(c) ΔC_p comparison

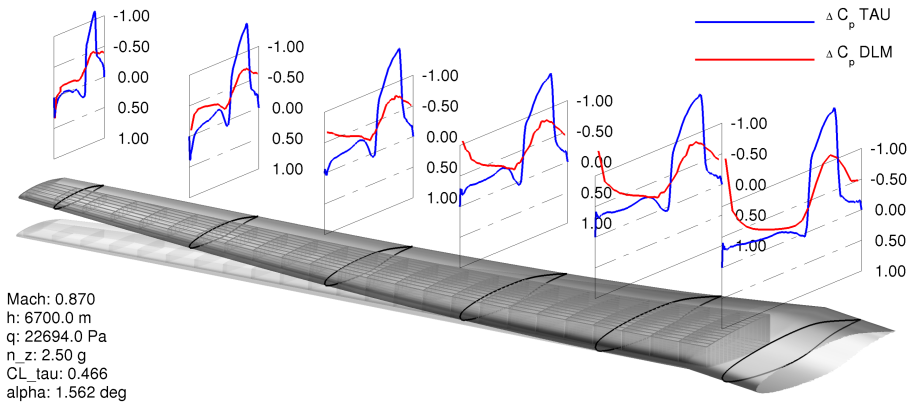
Figure 9.10: LC 1002, surface pressures for the converged trim solution



(a) C_p TAU



(b) ΔC_p DLM



(c) ΔC_p comparison

Figure 9.11: LC 1004, surface pressures for the converged trim solution

TAU distribution was expected to cause a larger nose-down, thus negative twisting moment.

With the wing structure being loaded not by surface forces but by aerodynamic loads splined to the structure coupling nodes, another reasonable assessment of the aerodynamic methods and of the force splining routines could be made using a node-wise force comparison as depicted in Figure 9.12 for load cases 1002 and 1004. The

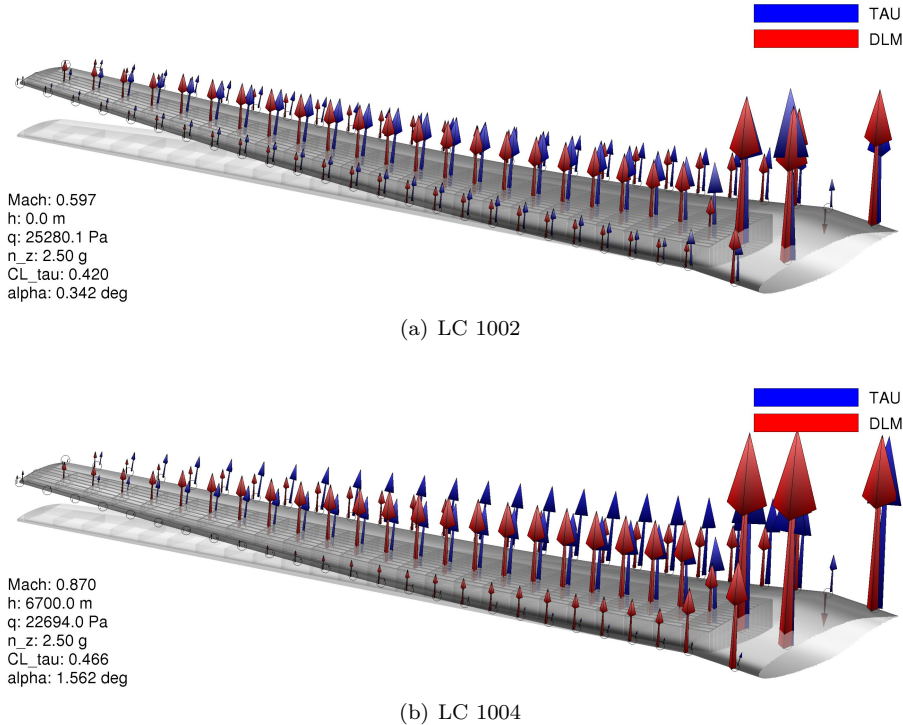
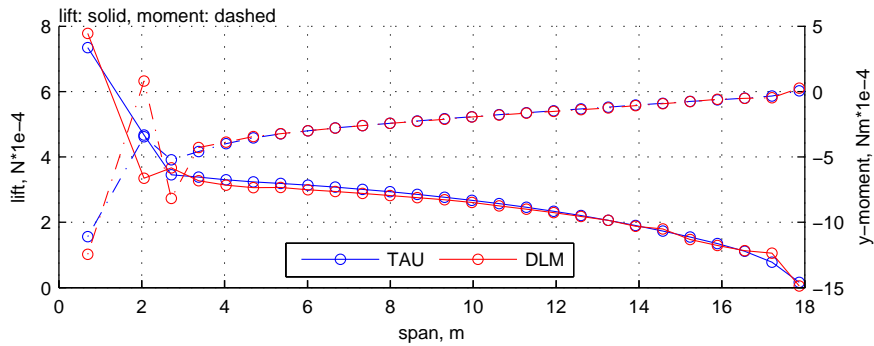


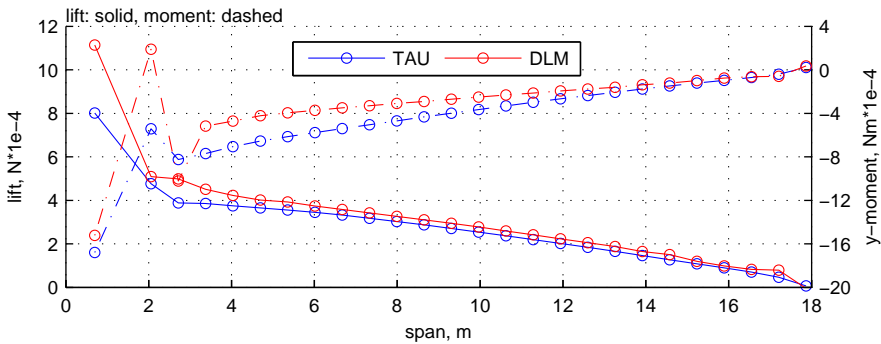
Figure 9.12: Coupling node force vectors for the converged trim solution

forces reflected very well the behavior which could already be deduced from the pressure difference plots. The data shown in Figure 9.10(c) demonstrated consistent results for TAU and DLM and moreover that a considerable part of the lift is generated in the rearward part due to airfoils promoting rear loading. Both features could be recovered in the corresponding force distribution, Figure 9.12(a). Forces on the load reference axis and the spanwise rows along leading and trailing edge confirmed the good agreement of TAU and DLM force vectors, which were deliberately separated slightly in chordwise direction to improve visibility. As could already be concluded from the pressure difference distribution for LC 1004, Figure 9.11(c), the recompression shocks altered the force distribution considerably. This is reflected in the corresponding coupling forces, Figure 9.12(b). In the case of TAU, coupling forces in the leading edge coupling nodes reduced considerably, while at the same time increasing at the trailing edge; DLM forces, however, retained the characteristics from the lower *Mach* number solution. In conclusion, aerodynamic loads from TAU in-

duced considerably larger negative, thus nose down, twisting moments compared to DLM. The latter result will be demonstrated using spanwise force distributions, but before, some remarks on coupling forces in the wing root region will be given. It was mentioned in section 9.1 that an additional coupling row was introduced in the root region to better distribute the aerodynamic forces. As a result of the increased spanwise spacing in the root region compared to the rest of the wing, the forces in the first two chordwise coupling rows exceeded the remaining ones, Figure 9.12. In addition, independent of the applied plate spline coupling methodology in the case of doublet lattice, or the radial basis function technique in the case of TAU, the coupling forces in the root area showed irregular spanwise distributions. For both load cases, the irregular force distribution can be seen in Figure 9.12 as a considerable drop in the force z-component at the trailing edge node in the second spanwise row. The DLM force even pointed in the opposite, negative direction. The reason for this lies in the articulate wing planform kink towards the center wing box, depicted in Figure 8.1 on page 133. Despite the fact that both coupling methods are based on different theories to establish the coupling matrix, both methods indicated problems with irregular coupling point distributions. Introducing an additional row of coupling points, or disregarding the planform kink by extrapolating the main wings coupling points inward, did not improve the force distribution.



(a) LC 1002



(b) LC 1004

Figure 9.13: Spanwise force and moment distribution for the converged trim solution

The implications of the fluctuations are shown in Figure 9.13. The plots depict spanwise lift and moment distributions resulting from summing up the three coupling forces belonging to each rib, hence the corresponding load reference axis point and the two rigidly connected grid points on the leading and trailing edge. The moment was computed about each sections local quarter chord. Especially the moment distribution, marked as dashed line, exemplifies the influence of the discussed force fluctuations. It should be stressed that in both methods, TAU and DLM, the same angle of attack α was applied. As a result of the increased wing area to be covered per coupling row in the root section, the lift force increases noticeably in that region. For the lower *Mach* number load case 1002, Figure 9.13(a), the moment distribution of TAU and DLM matched almost perfectly except for the root region. The lift predicted by TAU slightly exceeded the one generated in DLM. This behavior was already observed in the two-dimensional analysis presented in section 6.2.1 and is the consequence of neglecting airfoil thickness in case of DLM. Other than that, the inclusion of a W2GJ proves to yield an excellent means for correcting doublet lattice in a shock free flow regime. An uncorrected DLM, thus corresponding to an uncambered flat plate would instead have led to zero quarter chord moment, see for example [Abb59].

A very different outcome was observed for LC 1004, Figure 9.13(b), which was shown to comprise recompression shocks on both, upper and lower skin, Figure 9.11(a). The most prominent differences occurred for the moment distribution. Other than for the low *Mach* number load case, LC 1004 revealed considerable differences between TAU and DLM moment distributions. TAU predicted a $\approx 50\%$ larger negative moment about the y -axis than DLM throughout the entire span. The consequence of this will be depicted in section 9.4 when comparing optimizations with and without aero correction.

The spanwise TAU lift force on the other hand was now smaller than the corresponding DLM forces. With the thickness effect usually resulting in larger lift coefficients in TAU as compared to DLM, the increased *Mach* number compared to the previously studied LC 1002 was found to be responsible for the reversed order. An

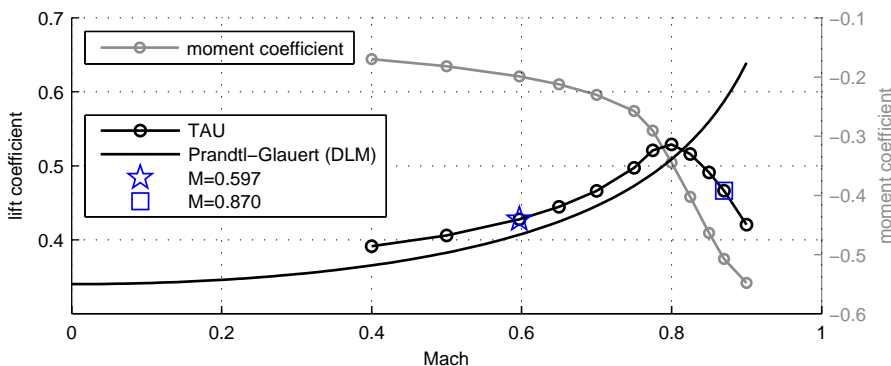


Figure 9.14: *Mach dependency study*

explanation is provided in Figure 9.14, displaying the development of lift coefficient as function of *Mach* number. The corresponding TAU *Euler* calculations were based on the converged results of LC 1004 by fixing all essential parameters like dynamic pres-

sure, density, mesh deformation, angle of attack, and only varying the *Mach* number. The resulting lift coefficients are plotted in Figure 9.14.

Figure 9.14 moreover depicts the *Mach* number dependent lift coefficient resulting from a *Prandtl-Glauert* correction. The *Prandtl-Glauert* correction factor being defined as (Bertin et al. [Ber98]):

$$\beta = \sqrt{1 - M^2}, \quad (9.4)$$

is used in the governing equations of the doublet lattice method to account for compressible, yet shock free flows. The factor can be used to correct the incompressible sectional lift curve slope:

$$C_{l_\alpha}|_{\text{comp.}} = \frac{C_{l_\alpha}}{\beta}. \quad (9.5)$$

According to Anderson [And05], the lift curve slope C_{L_α} of a finite wing can be computed from the sectional slope C_{l_α} using lifting line theory :

$$C_{L_\alpha} = \frac{C_{l_\alpha}}{1 + \frac{C_{l_\alpha}}{\pi\Lambda}}. \quad (9.6)$$

Rewriting equation (9.6) for compressible flow by inserting equation (9.5) yields the compressible lift curve slope for a finite wing with aspect ratio Λ :

$$C_{L_\alpha}|_{\text{comp.}} = \frac{C_{l_\alpha}}{\beta + \frac{C_{l_\alpha}}{\pi\Lambda}}. \quad (9.7)$$

Noting that $C_l = C_{l_\alpha}(\alpha - \alpha_0)$ and assuming the sectional lift curve slope to be $C_{l_\alpha} = 2\pi$, the compressible lift coefficient for a finite wing becomes:

$$C_L|_{\text{comp.}} = \frac{2\pi(\alpha - \alpha_0)}{\beta + \frac{2}{\Lambda}}. \quad (9.8)$$

Equation (9.8) was used to calculate the *Prandtl-Glauert* curve shown in Figure 9.14. $\Lambda = b^2/S_{ref}$ was computed from the planform data provided in section 8.1, page 132. The constant term $2\pi(\alpha - \alpha_0)$ was derived from the compressible DLM lift coefficient resulting from LC 1002, featuring $M = 0.597$.

Figure 9.14 confirms a reasonable analogy in lift coefficient development for doublet lattice and TAU *Euler* up to a *Mach* number of $M \approx 0.8$. Up to this value, differences between the aerodynamic methods can be assigned to the missing thickness representation in DLM, however, beyond $M \approx 0.8$ the lift coefficients in DLM continue to increase, while the TAU results show a characteristic peak, followed by a decrease in C_L . Ultimately, this behavior clarifies the higher lift forces of DLM compared to TAU shown in Figure 9.13(b). Moreover, this underlines the fact that the applied *Prandtl-Glauert* correction can only yield reasonable aerodynamic forces up to *Mach* numbers where a wing is still free of recompression shocks. Both lift and moment coefficient show a strong interaction with increasing *Mach* number, as stated the gray line belonging to the right y-axis in Figure 9.14.

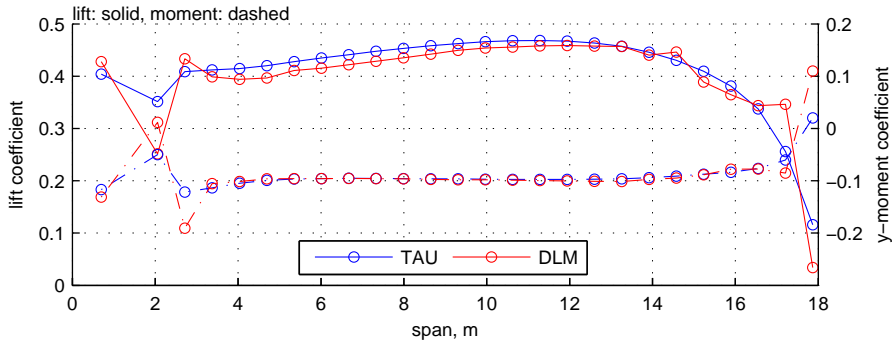
Based on the force and moment data given in Figure 9.13 it was possible to appraise their normalized counterpart. To do so, planform strips according to the

spanwise distribution of load reference axis points were defined, to provide the required reference strip area s_{ref} and the reference chord c_{ref} required for the normalization:

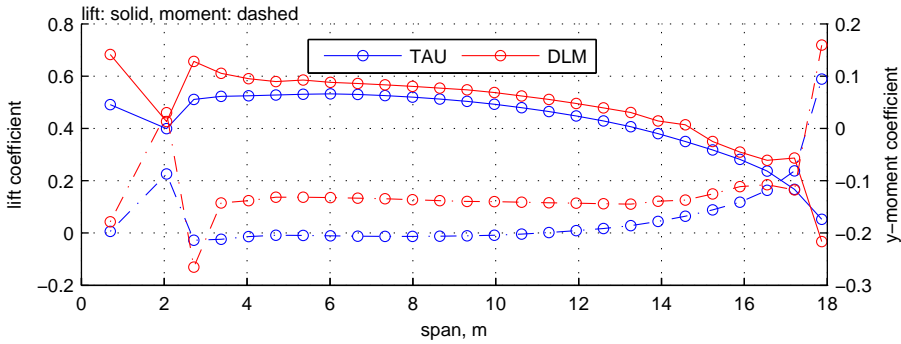
$$C_l = \frac{\text{lift}}{q s_{ref}}, \tag{9.9}$$

$$C_{m_y} = \frac{\text{y-moment}}{q s_{ref} c_{ref}}. \tag{9.10}$$

The corresponding lift and moment coefficients are plotted in Figure 9.15. While the same conclusions as those drawn from the distributions in Figure 9.13 still hold, the coefficients gave some more insight into the differences in load and moment distributions found between TAU and DLM. Normalization of force and moment with the



(a) LC 1002



(b) LC 1004

Figure 9.15: *Spanwise force and moment coefficient distribution for the converged trim solution*

strip area caused a considerable reduction in the root region fluctuations, however, it aggravated fluctuations in the DLM distribution tip region. They are located in the aileron region which in turn was modeled with a refined DLM mesh discretization to better capture the local effects. The moment coefficient shown in Figure 9.15(a) showed a perfectly constant value over large parts of the span and served as a meaningful test of the TAU and DLM splining method, in a sense that, from incompressible

airfoil theory, e.g. [Abb59] it follows that the moment coefficient about the quarter chord is not a function of lift coefficient.

Finally, it should be noted that grid points belonging to the first two spanwise coupling rows were rigidly connected to the clamping node. The first row was connected directly to the clamping node, compare Figure 9.2, while the second row attached to the root rib, which in turn was rigidly connected to the clamping node. Thus, forces acting on these nodes did not contribute to the elastic deformation of the structure and hence did not affect the deformation and optimization results.

This concludes the detailed investigation of the functional efficiency of the TAU correction module developed in section 6.4. The iterative correction process was shown to converge quickly when considering constant stiffness properties of the supporting structure.

9.4 Numerical Results: Mass Minimization

Having demonstrated the functionality of the aero correction process in a pure trim application, the application and interaction within the stiffness optimization process was tested. While the wing skin mass was defined as the objective for minimization, the structural constraints again comprised strain and buckling failure for all shell elements belonging to the specified design fields. In terms of aeroelastic responses, only aileron effectiveness and divergence were constrained, while no constraint was defined for twist. Aileron effectiveness for the four load cases depicted in Figure 8.2, page 134, and listed in table 8.1, repeated in table 9.1, was limited by a lower bound to $\eta_{ail} \geq 0$, to be free of aileron reversal. Divergence was constrained to a lower limit of $q_{div} \geq 35000 Pa$ at a Mach number of $M = 0.87$. Verifying this limitation using Figure 8.2 on page 134 demonstrates a reasonable clearance with respect to the aeroelastic stability margin.

The starting design exactly resembled the one used in the forward swept wing study, presented in section 8.5. In order to confirm the mass minimization results, various variations of the starting design, comprising modifications on thickness and stacking sequence, were optimized in parallel. Except for sporadic exceptions, all the starting designs led to the same optimum in terms of minimum mass and optimized thickness and stiffness.

The minimized masses of the investigated combinations with and without aero correction as well as balanced and unbalanced laminates are listed in table 9.2. As

Table 9.2: *Optimized wing skin masses*

| | balanced | unbalanced |
|----------------------|----------|------------|
| with aero correction | 576.2 kg | 403.9 kg |
| no aero correction | 563.1 kg | 423.7 kg |

illustrated by the table, consideration of the aero correction did not imply a fixed impact on optimized mass, given by the fact that the mass increased for balanced, and decreased for unbalanced laminates. Anyway, the intention of the aero correction lies in the improvement of sizing loads and the enhanced determination of the aeroelastic responses. Owing to the considerable mass savings of unbalanced over balanced

laminates, the sections focus will be placed on the results attained with unbalanced laminates. In response to the vast amount of significant results generated by the stiffness optimization using aero correction forces, in what follows, depending on the particular structural or aerodynamic focus, the most interesting load cases only are selected for presentation, while the results for load cases with either similar or *regular* results were skipped.

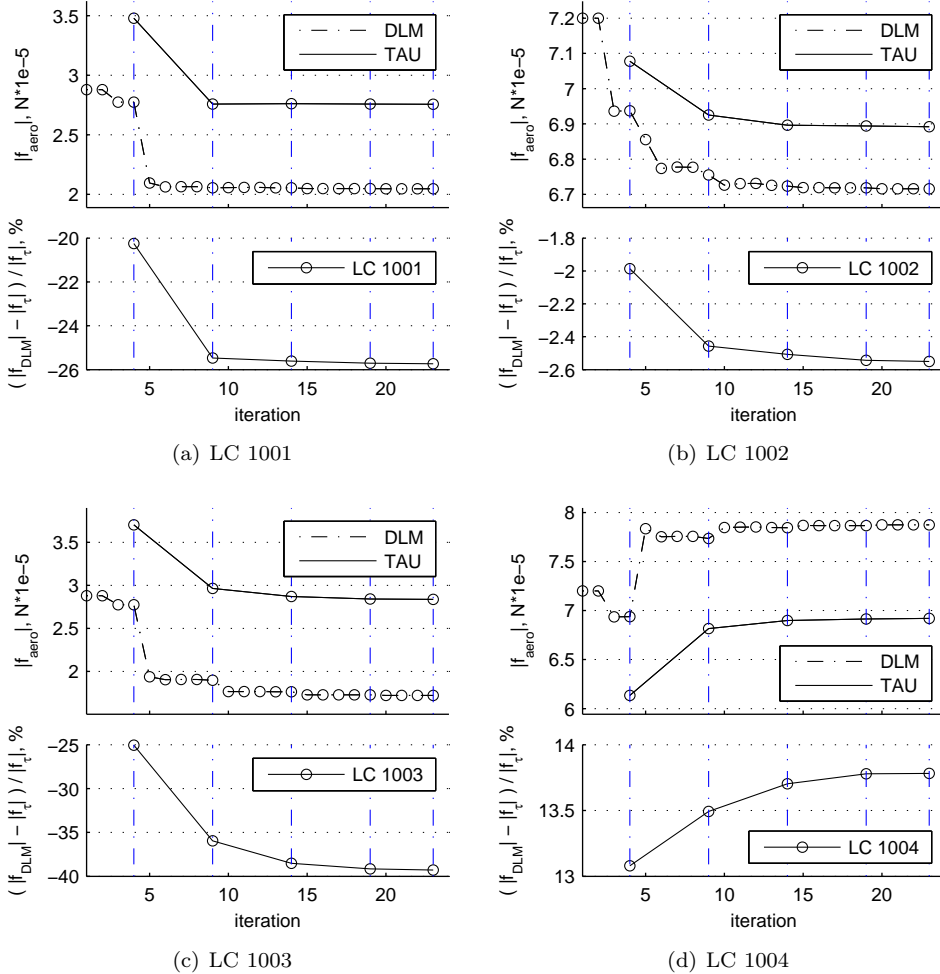


Figure 9.16: Aero force development, unbalanced laminates

In a first step, the aero force development during the stiffness optimization was reviewed to ensure convergence of the structural properties, and of the correction forces. The results for the four sizing load cases are depicted in Figure 9.16. While a similar investigation was also performed for the trim application, see Figure 9.9, the application of the aero correction in the optimization process implied some general differences. Selecting the optimization process with the CFD correction module be-

ing called within the optimization loop, Figure 6.6 on page 90, a TAU correction run was requested every five structure iterations. The dashed blue lines in Figure 9.16 indicate a TAU correction run at the 4th, 9th, 14th . . . iteration step. Accordingly, the new correction forces were only available for these iterations, while DLM forces were generated during each iteration step. The graphs state that the TAU and DLM forces for all sizing load cases converged to steady values, while in parallel the optimization process minimized the mass objective by modifying the stiffness properties and thus the aeroelastic behavior. The trim application already proved a fast convergence with constant structural properties, and the stiffness changes during the optimization did not considerably deteriorate the convergence behavior. Nevertheless, comparing the results shown in Figure 9.16 to those shown in Figure 9.9 reveals a more gradual correction force change during the optimization, compared to the already good agreement seen with respect to the final state for the second TAU correction step in the trim application.

9.4.1 Optimization Results

The above discussion of the aeroelastic force convergence was a prerequisite for proving the validity of the mass optimized design that will be discussed in the following.

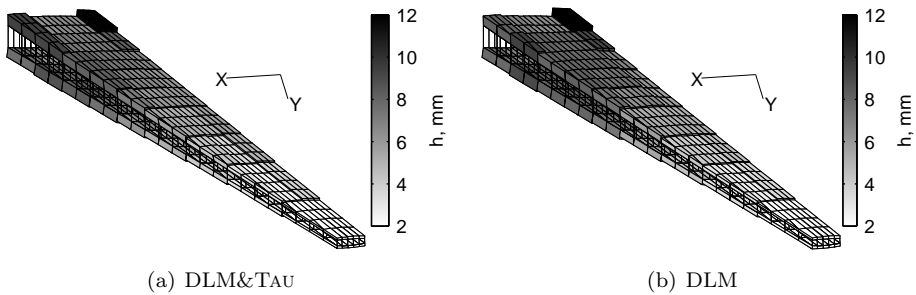


Figure 9.17: *Optimized design, thickness distribution, unbalanced laminates*

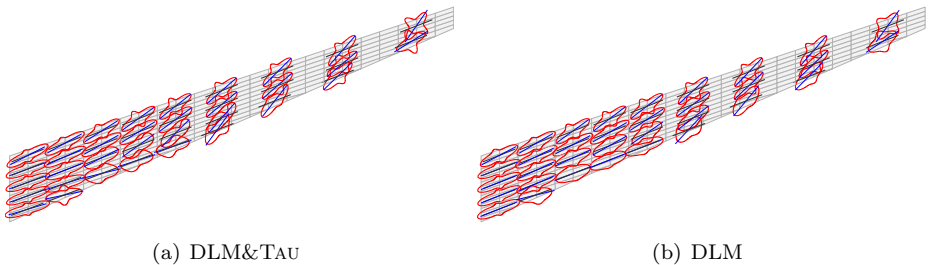


Figure 9.18: *Optimized design, $\hat{E}_{11}(\theta)$ upper skin, unbalanced laminates*

Looking at table 9.2 it can be seen that the weight differences between optimizations with and without aero correction were only $\approx 5\%$, indicating rather small differences

in terms of optimized thicknesses, see Figure 9.17. Nearly no differences could be detected, except for slight modifications along the front spar. “DLM+TAU” denotes an optimization with aero correction, while only “DLM” denotes an optimization without aero correction. Similar results were found for the stiffness distributions, see Figure 9.18, where only marginal deviations between the two $\hat{E}_{11}(\theta)$ could be identified. In search of a weight optimal solution, bending-torsion coupling was introduced by tilting the major stiffness direction from inner to outer wing gradually forward. The negative coupling index thus led to a negative twisting tendency when bending the wing up. Thereby the center of lift could be shifted inward, eventually reducing the root bending moment. Interestingly, the optimization with aero correction led

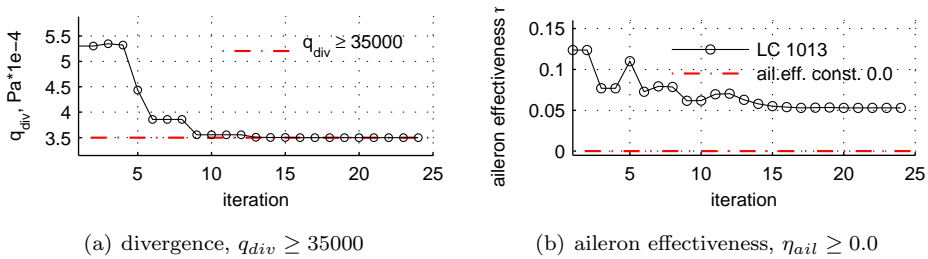


Figure 9.19: Aeroelastic constraints development, DLM+TAU, unbalanced laminates

to an active divergence pressure constraint, Figure 9.19(a), while it was not active when optimizing with DLM only, however, in both optimization scenarios, with or without aero correction, mass minimization dominated the stiffness distribution, so that the aero correction only led to slight modifications of the thickness mainly. The aileron effectiveness remained clearly in the feasible domain, the lowest, still inactive response is shown in Figure 9.19(b).

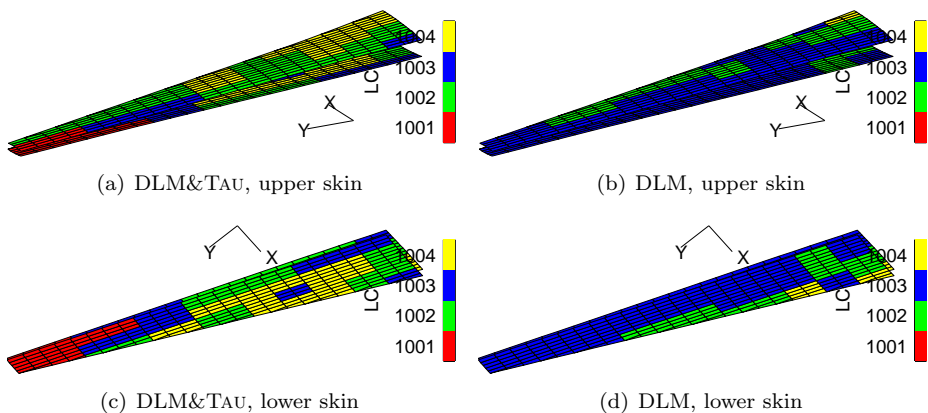


Figure 9.20: Optimized design, sizing load case per field, unbalanced laminates

More prominent differences when applying aero correction revealed when looking at the load cases that accounted for the highest strength or buckling failure index in

each design field, Figure 9.20. Plots in the left column depict upper and lower skin of the optimized model including aero correction, the equivalent, but without aero correction, is shown in the right column. While wing skin sizing for the optimization without aero correction was clearly dominated by $n_z = +2.5g$ LC 1002 and $n_z = -1.0g$ LC 1003 and only a few design fields being sized by LC 1004 and none by LC 1001, the allowance for aero correction led to a perceptibly different distribution. Distinct spanwise and chordwise regions developed, comprising all sizing load cases considered in the optimization. Making only a minor contribution when optimizing without aero correction, the high $Mach$ number pull up maneuver LC 1004 now contributed considerably to the sizing, allocating approximately the same area as the low $Mach$ number pull up maneuver LC 1002. In the outer wing $n_z = -1.0g$ LC 1001 developed more influence on sizing as compared to the optimization without correction. The high $Mach$ number push down LC 1003, which dominated large parts of the wing skins when optimizing without correction, only showed minor sizing contributions when the aero correction was applied. It should be noted that the failure indices for different load cases simultaneously rested on the constraint in the optimized design, and accordingly only slight differences in the index can cause a swap from one sizing load case to the other. The failure indices are discussed in more detail later on in Figure 9.24.

9.4.2 Aeroelastic Results

The differences in twist for an optimization with aero correction compared to an optimization without, is depicted in Figure 9.21, in which the spanwise twist distribution for two high $Mach$ number sizing load cases 1003 and 1004, and for two representative cruise load cases 2007 and 5007, featuring the largest mass variation among the investigated cruise conditions, compare table 8.7 on page 139, are shown. Unexpectedly,

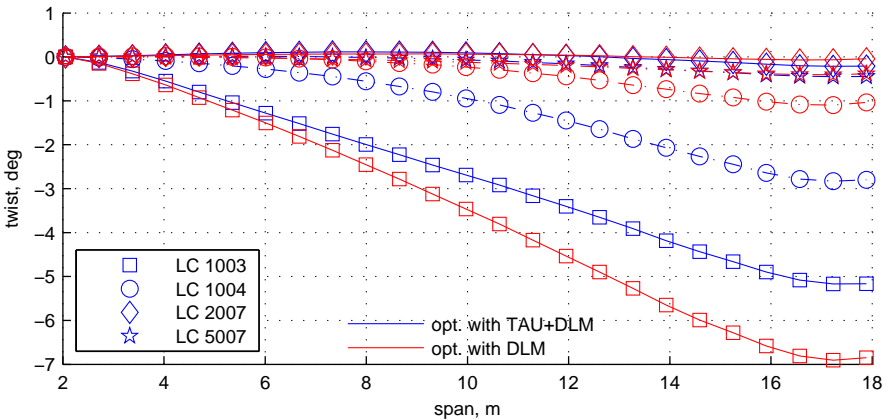


Figure 9.21: *Optimized design, twist distribution with and without aero correction, unbalanced laminates*

the $n_z = +2.5g$ pull up maneuver LC 1004 in both optimizations showed a negative tip twist, differing by $\approx 2^\circ$. The reason for this could be found in the bending-torsion

coupling evoked by the variable stiffness orientation, see Figure 9.18. The twist distribution promoted compliance with the divergence pressure constraint and helped to alleviate loads in the outer wing, thus supporting mass minimization. The twist being more negative when considering aero correction could be attributed to the different structural designs and to the more negative aerodynamic airfoil moment, as explained in section 9.3 for the trim application. As a result of the superposition of geometric coupling of the forward swept wing, and the negative aerodynamic twisting moment, and despite the lower inertial and therefore aerodynamic loading in case of the $n_z = -1.0g$ push down maneuver LC 1003, the wing twisted considerably more negatively for LC 1003 compared to LC 1004. Again, the difference between the aero corrected design and non-corrected design could mainly be attributed to the different aerodynamic moment distribution.

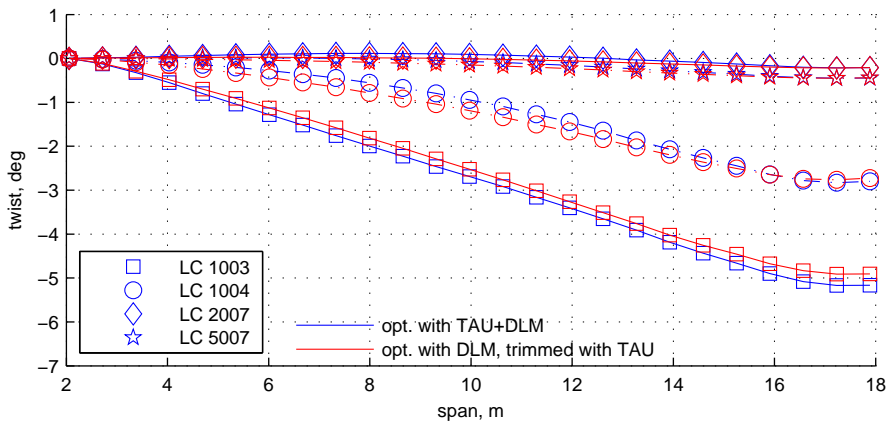


Figure 9.22: *Optimized design, twist distribution with and without aero correction, DLM trimmed with TAU, unbalanced laminates*

To determine how the wing structure, optimized with pure DLM, would behave under more realistic loading conditions, a trim analysis as described in section 9.3 was executed, thus allowing for an assessment of the potential error induced by the simplified aerodynamics. Twist results of the optimization with and without aero correction are depicted in Figure 9.22. The plot acknowledges the trend that was already evident in the design variable plots, Figure 9.17 and 9.18. As a result of the apparently connatural designs, the twist distributions for the four selected load cases are very similar. As expected, the influence of the minor differences in twist on the spanwise lift and moment distribution proved to be minimal; the results for the high *Mach* number load cases 1003 and 1004 are depicted in Figure 9.23. The first two chordwise coupling rows in the root section of the wing were not plotted as they did not contribute to the elastic deformation, see section 9.3. Evidently, hardly any differences were visible for the lift and moment distributions.

Given that the strain and buckling failure indices are very sensitive with respect to small changes in stiffness, another comparison between the optimization with aero correction, and the optimization with pure DLM, but trimmed with TAU afterwards,

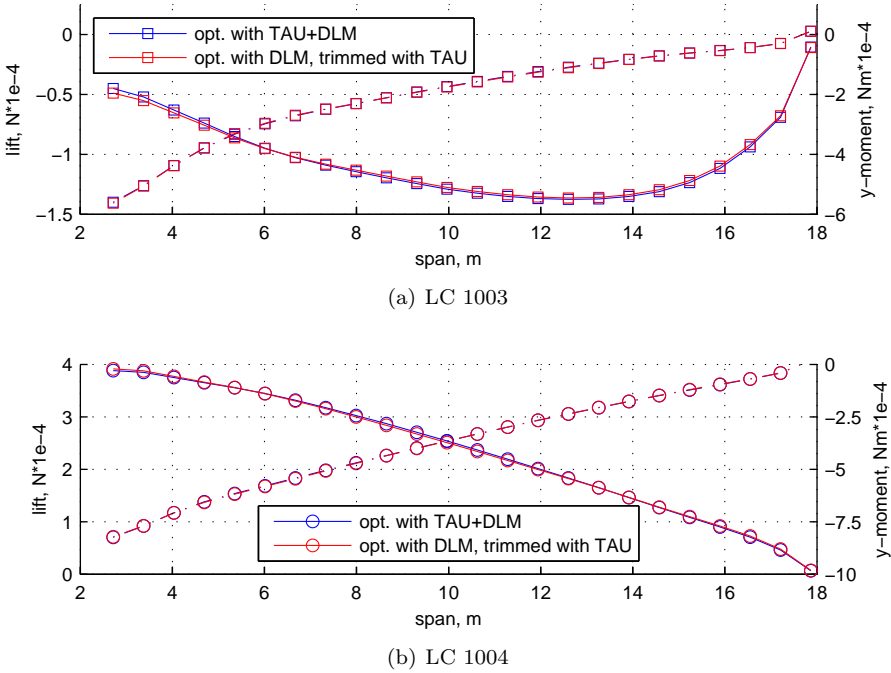
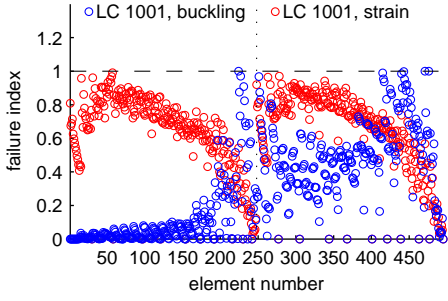
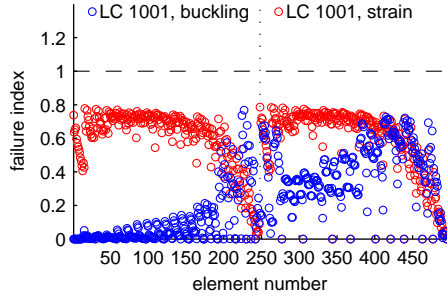


Figure 9.23: *Optimized design, spanwise force and moment distribution, unbalanced laminates*

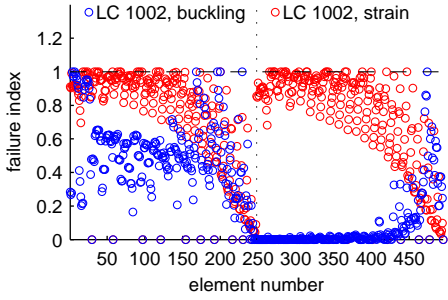
is depicted in Figure 9.24. Shown are the failure indices for all four sizing load cases, with element numbers 1 to 247 belonging to the upper skin, and element numbers 248 to 494 to the lower skin. The left column depicts the responses for the regular analysis including correction forces. All the strain and buckling failure responses for all sizing load cases were smaller or equal than 1.0, hence within the feasible range. However, with many responses settling right on the feasible design border there is an indication of a maximized material exploitation. The inner and mid wing were clearly dominated by strain failure constraints in both, the upper and lower skin. Mostly the outer wing region, elements ≈ 150 to 247 in the upper skin, and elements ≈ 400 to 494 in the lower skin, showed increased buckling failure indices that also contributed to the sizing. As expected, the elements in compression featured larger buckling failure indices than elements in the tension regions. The right column of Figure 9.24 depicts results of the structure optimized with DLM, but trimmed with TAU. The distributions clearly point to the fact that, despite the seemingly similar optimized design variables, Figure 9.17 and 9.18, the inclusion of correction forces had a very noticeable influence on failure indices. The larger wing skin weight of the DLM-optimized structure is reflected in smaller failure indices for load cases 1001 to 1003, however, load case 1004, Figure 9.24(h), showed considerable violations of the failure index constraint. When assuming the TAU calculations to predict better the real aerodynamic loading, the results indicated that an optimization using DLM only is not necessarily conservative.



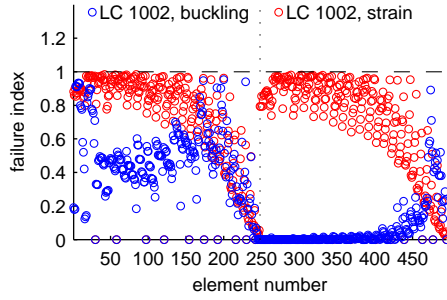
(a) LC 1001, opt. with DLM&TAU



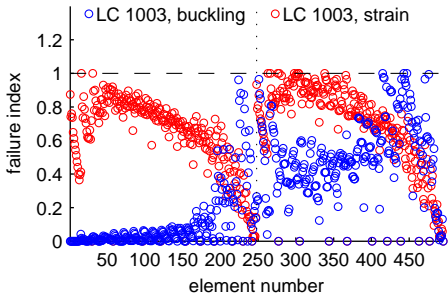
(b) LC 1001, opt. with DLM, TAU trim



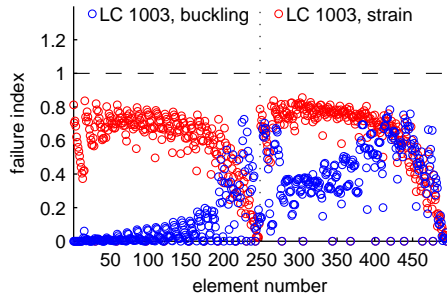
(c) LC 1002, opt. with DLM&TAU



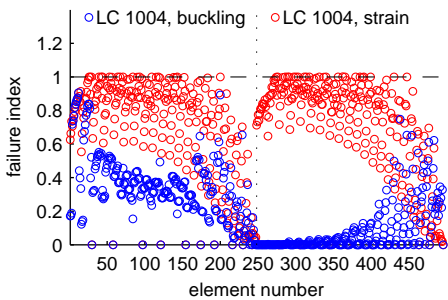
(d) LC 1002, opt. with DLM, TAU trim



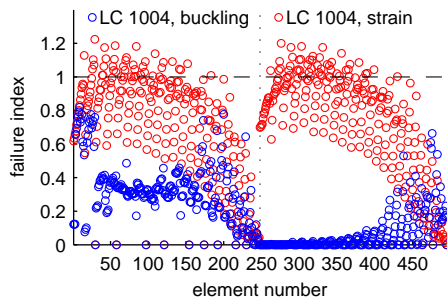
(e) LC 1003, opt. with DLM&TAU



(f) LC 1003, opt. with DLM, TAU trim



(g) LC 1004, opt. with DLM&TAU



(h) LC 1004, opt. with DLM, TAU trim

Figure 9.24: *Optimized design, failure indices, unbalanced laminates*

In order to emphasize the influence of the aero correction on the optimization results in terms of modified structural properties, the wing that was optimized with an aero correction was analyzed without correction forces. To this end, the converged correction force vectors $\Delta \mathbf{f}_\tau$ for each load case were set to zero. Both analyses, with and without correction force for the same wing structure, had to fulfill the static trim conditions defined by the particular load cases. Since the aircraft weight in the analyses was identical, this implied that an identical overall lift force had to be generated. This is demonstrated by means of the spanwise lift force and moment distributions, Figure 9.25, in which the results for the push down and pull up maneuver load cases at $M = 0.87$, LC 1003 and 1004 are shown. Due to the only small differences between the analyses with and without the converged correction force $\Delta \mathbf{f}_\tau$, LC 1001 and 1002 were skipped. While the sum of lift forces for the calculations with and without $\Delta \mathbf{f}_\tau$ were the same, the distributions without correction indicated absolutely larger lift forces in the outer wing. In both cases this could be attributed to the difference in y-moment, which twisted the wing more negatively in case of LC 1003 and more positively in case of LC 1004, keeping in mind that a negative moment twists the wing nose down.

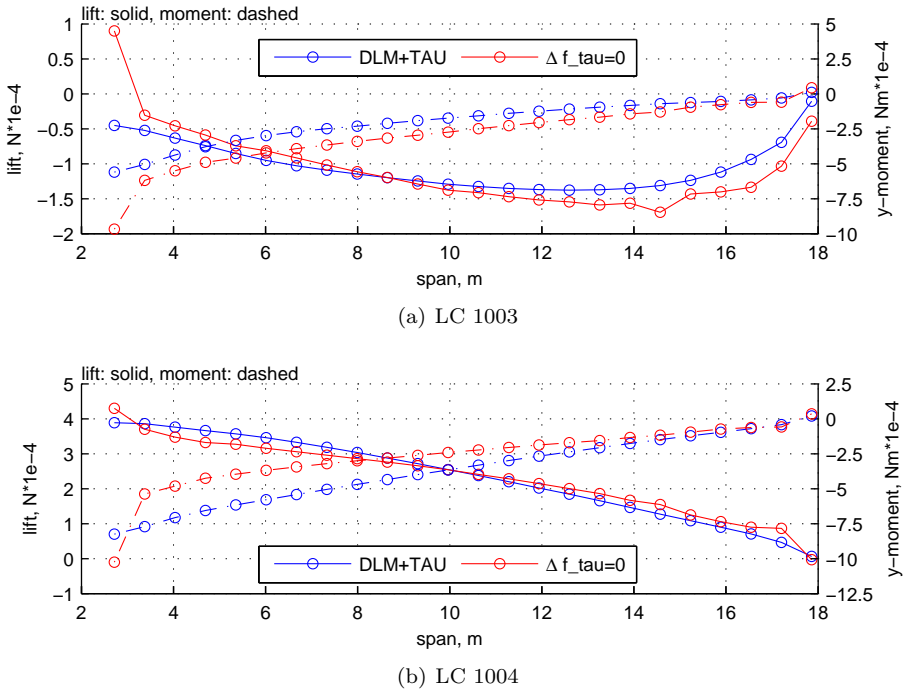


Figure 9.25: Optimized design, spanwise force and moment distribution, with (blue) and without (red) applied correction force $\Delta \mathbf{f}_\tau$

While the absolutely larger y-moment for $\Delta \mathbf{f}_\tau$ twisted the wing to smaller angles of attack and therefore increased negative lift in the outer wing for the negative load factor load case 1003, the opposite happened in case of the positive load factor load case 1004. Inferring from the associated failure indices shown in Figure 9.24(e) and

9.24(g) it could be argued that the corrected lift and moment distribution for LC 1003 produced considerable failure index rise, while the opposite occurred for LC 1004, where the decreased y-moment mainly led to an alleviation of failure indices.

9.4.3 Aerodynamic Results

Having focused on the positive load factor load cases 1002 and 1004 when discussing aerodynamic details in section 9.3, the two remaining sizing load cases 1001 and 1003 will be highlighted in this section. Referring to table 9.1 on page 160, LC 1001 and 1003 correspond to the negative load factor counterparts of LC 1002 and 1004, hence to a low and a high *Mach* number load case respectively.

The pressure difference distributions of TAU and DLM at equidistant spanwise stations are presented in Figure 9.26. Each plot in addition depicts the undeformed and deformed FE and CFD mesh. As a result of the negative load factor $n_z = -1.0g$, the wing needed to generate a down force equivalent to the aircraft weight. The corresponding pressure distributions featured a considerable negative pressure peak on the lower wing surface nose, which in turn led to the dominant positive peak in the pressure difference distribution shown in Figure 9.26. The airfoils rear loading characteristic as a result of the associated camber line was reflected in a negative pressure difference in the rear portion of the airfoil, still contributing a positive lift force. The net surface below the ΔC_p curve, however, was positive, thus resulting in negative, downward overall lift force. Again, the doublet lattice W2GJ camber correction accounted for an important contribution to the good agreement of TAU and DLM ΔC_p . In the leading edge region, the finite discretization of DLM did not allow for covering the full pressure peak as was possible with the distinctly finer TAU mesh. Deviations also existed in the trailing edge region, which due to their distance to the airfoil quarter chord led to deviations in the twisting moment, as will be shown later. The mesh cuts depicted in Figure 9.26 along with the pressure difference distribution were designated for supervising the CFD mesh deformation, see section 6.4.2 for a description of this process. The coincidence of the finite element and CFD mesh, evident throughout all the depicted cut stations, demonstrated the operability of the deformation routines on the basis of the selected coupling points.

The distinct influence of a *Mach* number increase from $M = 0.597$ for LC 1001 to $M = 0.87$ for LC 1003 is shown in Figure 9.27 to 9.30, in which the pressure and force results for LC 1003 are plotted. In Figure 9.27 strong recompression shocks in the TAU pressure distribution can be seen, with the outermost pressure cut indicating two shocks on the lower surface. Details on the *Mach* number distribution are provided in Figure 9.28, where the line plots are used to indicate the *Mach* number on upper and lower surface, along with a *Mach*-equivalent surface shading on the deformed wing. The strong recompression shock on the lower surface is clearly accented by the sharp change in the shades of gray in Figure 9.28, two of which are visible in the wing tip region of the lower surface.

As a consequence of the shocks, the pressure difference distributions depicted in Figure 9.29 no longer show many similarities. While the DLM distribution maintained the characteristics depicted in Figure 9.26 for LC 1001, the TAU distribution changed entirely, reflecting the two recompression shocks by sharp pressure changes. The consequences of this for the coupling forces are illustrated in Figure 9.30. Compared

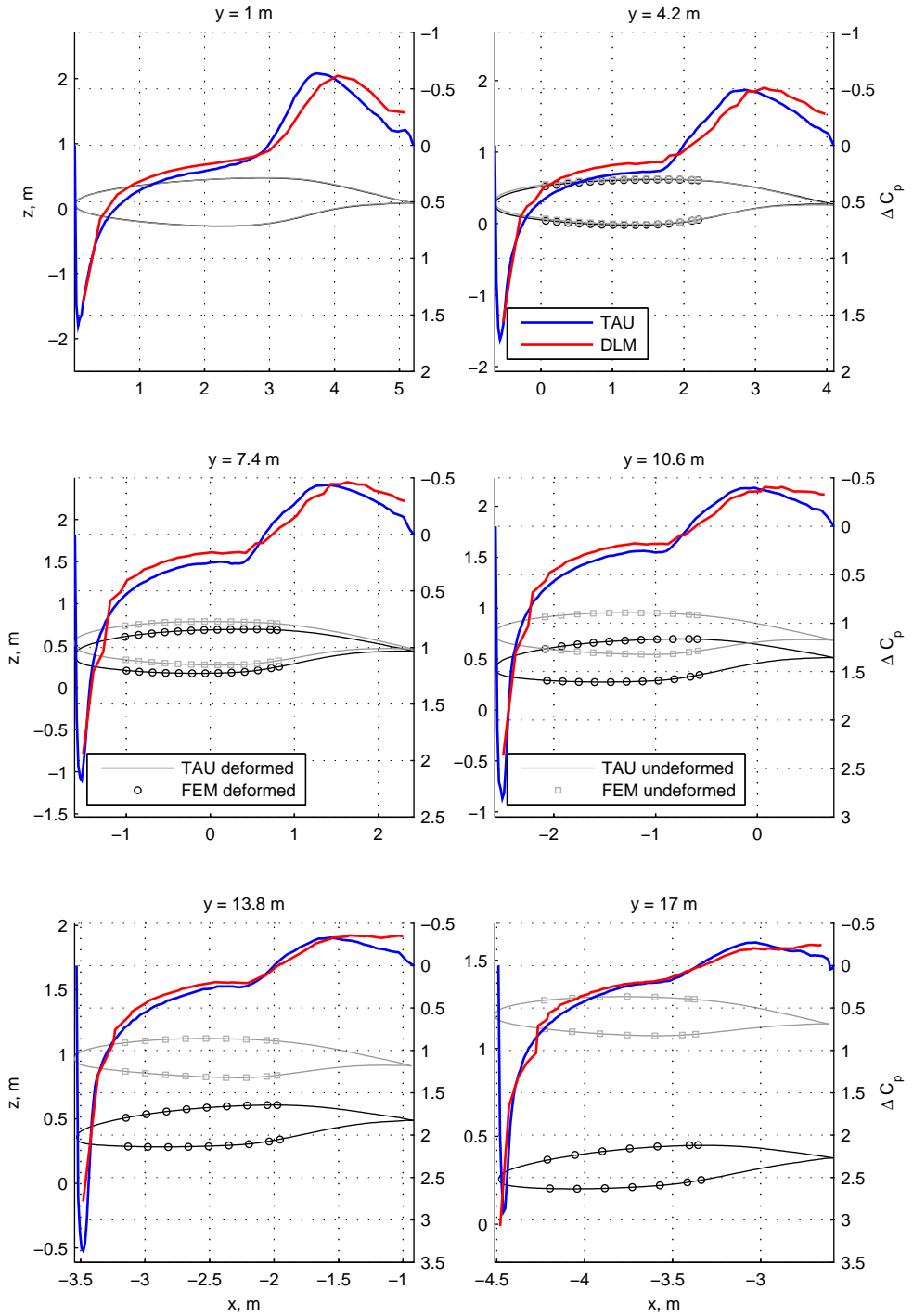


Figure 9.26: Optimized design, LC 1001, ΔC_p comparison, unbalanced laminates

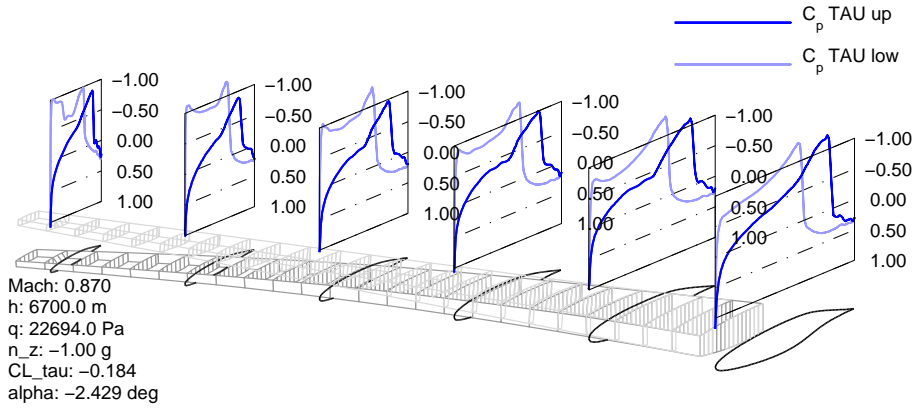


Figure 9.27: Optimized design, LC 1003, C_p TAU, unbalanced laminates

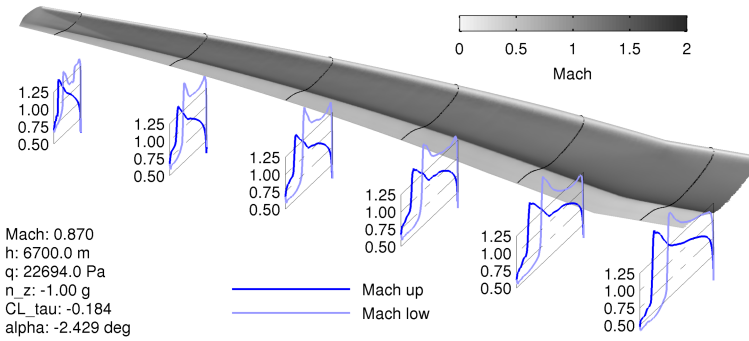


Figure 9.28: Optimized design, LC 1003, Mach number, lower surface, unbalanced laminates

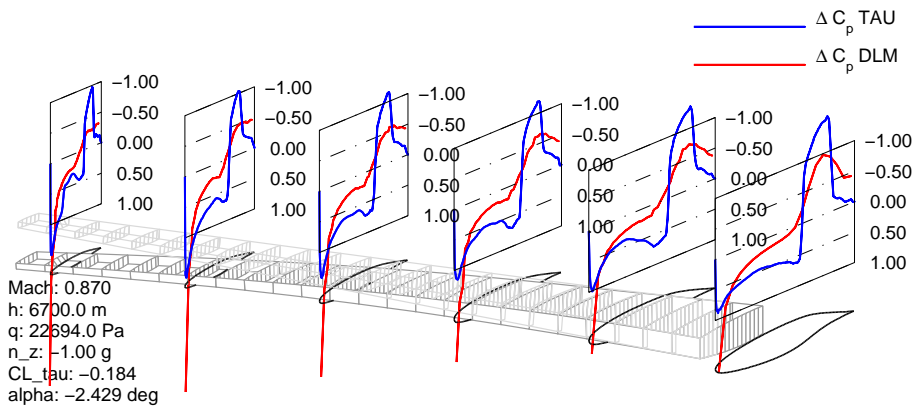


Figure 9.29: Optimized design, LC 1003, ΔC_p comparison, unbalanced laminates

to DLM, TAU generated less downforce in the leading edge region and higher lift at the trailing edge. Moreover, it was striking that the DLM pressure difference distributions provided for nearly zero force at the center nodes in each rib. Due to the similarity of TAU and DLM coupling forces for LC 1001, they will not be presented here.

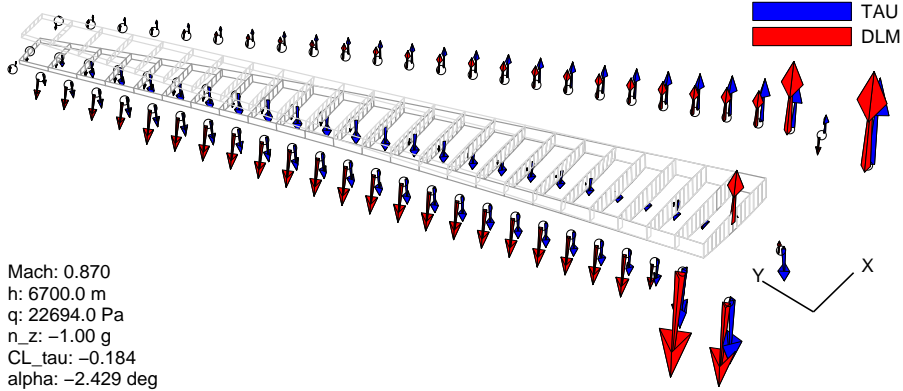
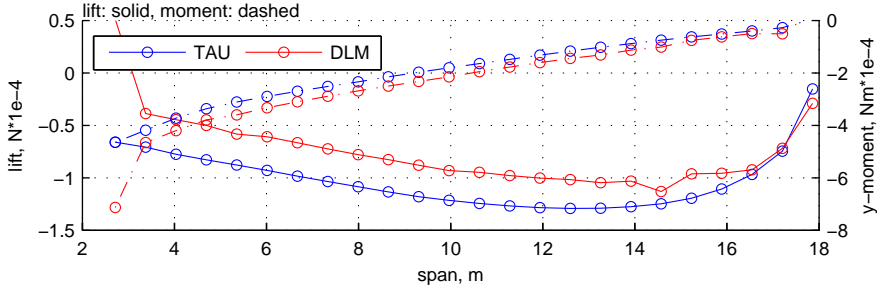


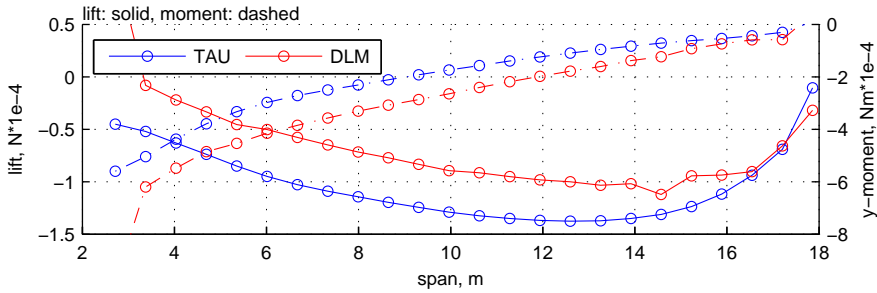
Figure 9.30: *Optimized design, LC 1003, coupling node force vectors, unbalanced laminates*

Optimized spanwise force and moment distributions for LC 1001 and 1003 are shown in Figure 9.31. As it was already concluded from the pressure difference distributions shown in Figure 9.26, the DLM moment distribution for LC 1001, Figure 9.31(a), featured slightly larger values than that obtained with TAU. The difference in lift force seemed to be more prominent. While lift and moment distributions for the corresponding $n_z = +2.5g$ low *Mach* number load case 1002, Figure 9.13 on page 171, showed perfect agreement in moment and a good agreement in lift, the absolute differences in lift according to Figure 9.31(a) approximately doubled. The largest disagreement is seen in Figure 9.16(a), in which the convergence behavior of the correction forces was shown. As expected, the deviations between TAU and DLM increased for the high *Mach* number load case 1003, Figure 9.31(b). Referring to Figure 9.16(c), the relative error rose from $\approx 26\%$ for LC 1001 to $\approx 40\%$ for LC 1003.

Demonstrating possible drawbacks of DLM compared to TAU in cruise flight conditions, the aerodynamic results for one of the investigated cruise load cases, LC 3007, eventually are summarized in Figure 9.32. As defined by the load case number, mass case three (compare table 8.6 and 8.7 on page 139) comprised a full passenger loading and a fuel loading corresponding to the end of cruise flight. The *Mach* number distribution depicted in Figure 9.32(a) indicated a strong shock on the upper surface only in the root region. In the mid and outer wing the recompression shock appeared only in a considerably attenuated form, but then with a clear inverse notch just upstream of the actual pressure recovery. Throughout the span the lower surface did not demonstrate recompression shocks as it remained slightly below $M = 1$. The implications of the described *Mach* distribution on ΔC_p are depicted in Figure 9.32(b). The agreement of TAU and DLM was not very good, especially in the mid and inner wing region. The spanwise net force and moment distributions resulting from ΔC_p , Figure 9.32(c), showed a considerably good agreement at least in the outer wing. In the mid and inner wing however, deviations increased for both, lift and moment distribution,



(a) LC 1001



(b) LC 1003

Figure 9.31: *Optimized design, LC 1003, spanwise force and moment distribution, unbalanced laminates*

thus demonstrating the potential of an aero correction with TAU.

Although the cruise load cases did not contribute to the structural sizing, the corresponding wing twist distribution is very important when it comes to aerodynamic performance. It has already been shown, Figure 9.21 and 9.22, that the influence of aero correction on the optimized structural design twist distribution in cruise was rather marginal. Nevertheless, this can only be ensured for the investigated laminar airfoil wing, featuring merely weak shocks in cruise flight. Consideration of the aero correction on a wing exhibiting different shock characteristics in cruise, is believed to yield a different influence on the twist distribution.

Finally, to complete the spectrum of investigated load case types, in Figure 9.33 an impression on the doublet lattice and coupling force results for one of the four aileron effectiveness roll load cases considered in the optimization is provided. Other than sizing and cruise, the aileron effectiveness load cases were not incorporated in the CFD correction loop. As a consequence of the roll motion analysis for $\alpha = 0^\circ$ in NASTRAN, the wing experienced a span dependent angle of attack α_y that can be expressed as function of roll velocity ω :

$$\alpha_y = \tan^{-1} \left(\frac{\omega y}{V_\infty} \right). \quad (9.11)$$

This was reflected in the pressure difference distribution along the span, featuring an increasing pressure peak on the nose towards the wing tip. The implication of the

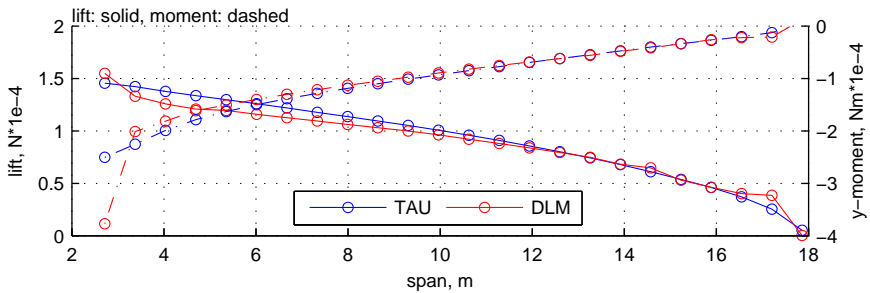
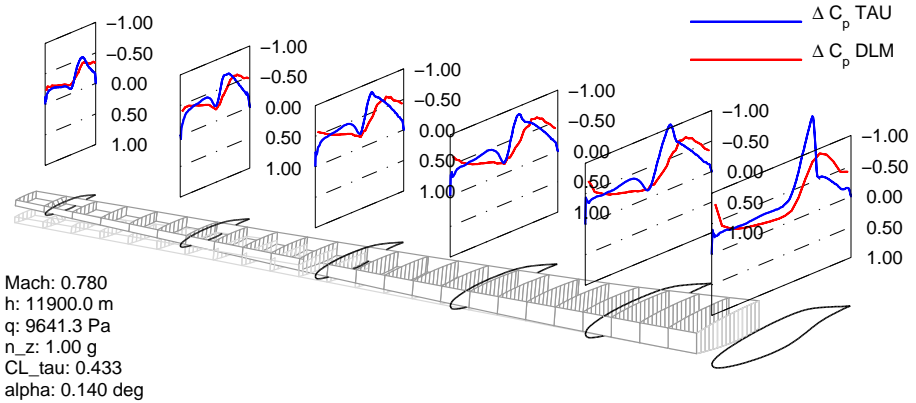
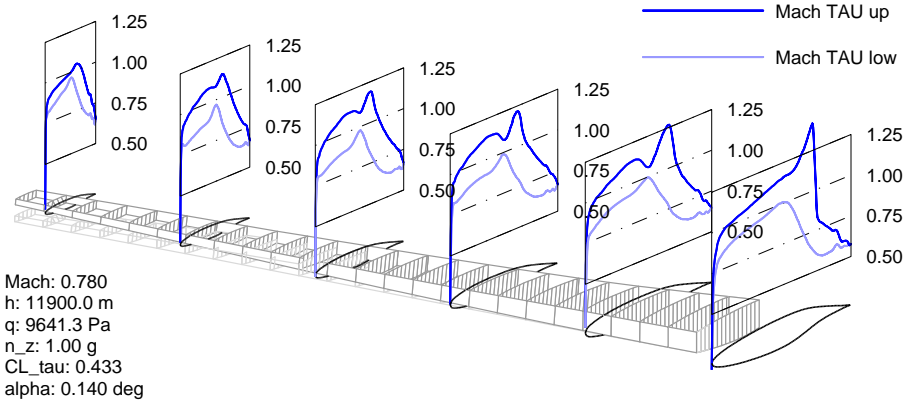


Figure 9.32: Optimized design, cruise load case 3007, unbalanced laminates

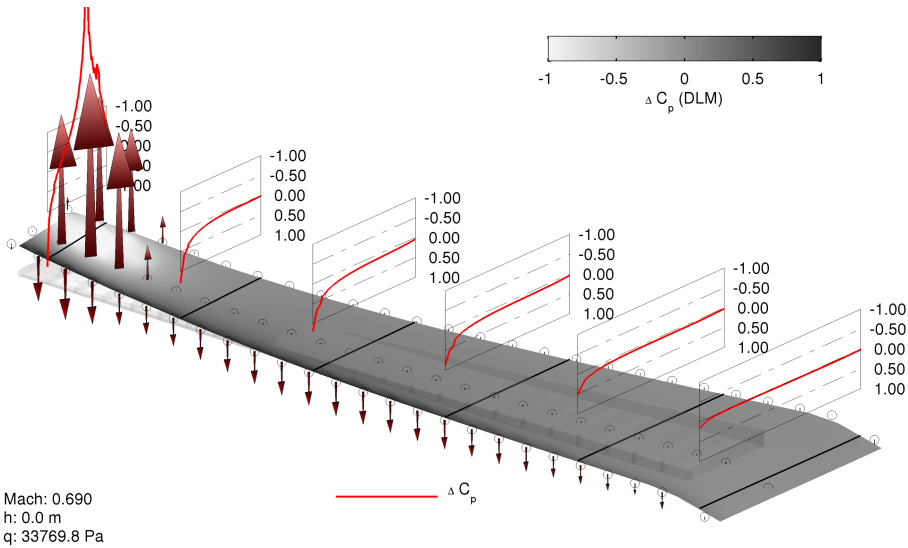


Figure 9.33: *Optimized design, aileron effectiveness LC 1012, ΔC_p and coupling node force vectors, unbalanced laminates*

aileron deflection was clearly noticeable in the strong pressure difference decrease in the aileron region, motivated by the local change in camber on the one hand, and by the discontinuity at the DLM hinge line on the other hand. In section 2.2.1 on page 27 it was mentioned that a unit aileron deflection $\delta = 1.0$ was applied in the derivation, keeping in mind that, due to system linearity, the deflection magnitude does not influence the normalized coefficients. The unit deflection corresponding to $\delta = 57.3^\circ$ was now reflected in the large pressure peak. Accordingly, the coupling force nodes showed large upward lift in the aileron region and, as a result of the induced angle of attack, counteracted the lift forces in the rest of the wing. It is interesting to note that the W2GJ influence is not reflected in the NASTRAN roll motion analysis. Considering the derivation of aileron effectiveness in section 2.2.1, it can be seen that only gradients with respect to aileron deflection and roll are involved in the calculation of the static equilibrium for a constant roll velocity. Since airfoil camber only shifts the lift curve up or down, but does not influence its gradient, it effectively does not influence aileron effectiveness.

9.5 Numerical Results: Mass Minimization Including Shear Webs

In order to give a short impression of the capability to include more structural entities than just the wing skins in the optimization process, the results of a forward swept wing mass minimization including the shear webs will be presented in this section.

To this end, the model developed for the preceding mass minimization was adopted completely, comprising finite element model, load case definitions, mass cases, and also the CFD model, applied in the affiliated aero correction process. The optimization model was adapted to the modified application region, the new design field setup

is depicted in Figure 9.34. While the wing skin distribution, Figure 9.34(a), was adopted from the previously presented mass optimization, 18 additional design fields were introduced in the shear webs, Figure 9.34(b), totaling to 86 fields.

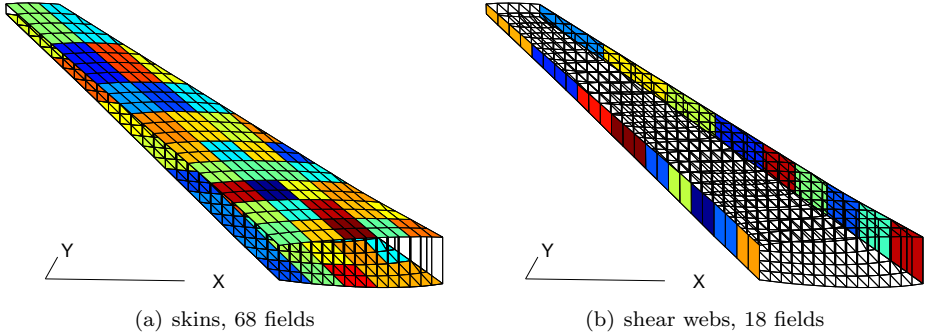


Figure 9.34: Design fields

The sum of wing skin and shear web mass formed the objective to be minimized, while applying regular strain and buckling constraints on each element involved in the design fields. As before, aileron effectiveness and divergence were constrained to $\eta_{ail} \geq 0.0$ and $q_{div} \geq 35000$, respectively. Several starting designs were investigated to consolidate the optimal solution by reproducing it with independent optimizations.

The optimization yielded a minimum mass for wing skins and shear webs of 511.5 kg, 413.7 kg of which was allocated to the wing skins, and 97.8 kg to the shear webs. In comparison to the mass minimization that did not feature shear webs in the

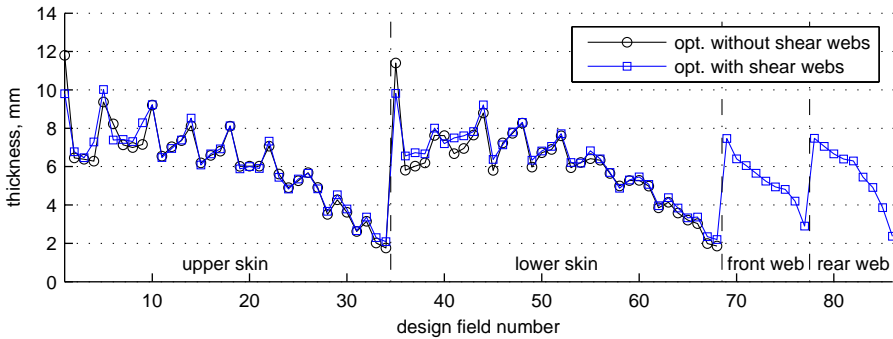


Figure 9.35: Optimized design, thickness comparison, unbalanced laminates

optimization model and which yielded a minimized mass of 403.9 kg, see table 9.2, the change in wing skin mass was rather marginal. A direct comparison of the optimized design field thicknesses, Figure 9.35, indicated only small deviations in the root region and closely matching values in the mid and tip region of the wing. The optimized thickness distribution in the shear webs is plotted in Figure 9.36, and as indicated already in the two-dimensional representation of Figure 9.35 shows a monotonously decreasing shell thickness towards the wing tip. It should be noted that the shear web

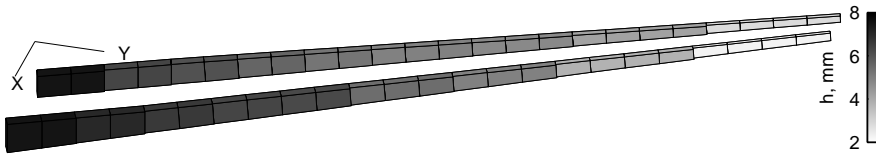


Figure 9.36: *Optimized design, shear web thickness, unbalanced laminates*

thickness when not being part of the optimization model was fixed to 20.0 mm at the root and 15.0 mm at the tip, linearly varying, see page 136 in the previous chapter, thus resulting in a non-optimized shear web weight of $\approx 313\text{ kg}$.

The optimized stiffness distributions are plotted in Figure 9.37. The distributions in the wing skins, Figure 9.37(a) and 9.37(b), resembled closely the previous results of the skin-only optimization. The newly designed stiffness distributions in the shear webs are shown in Figure 9.37(c).

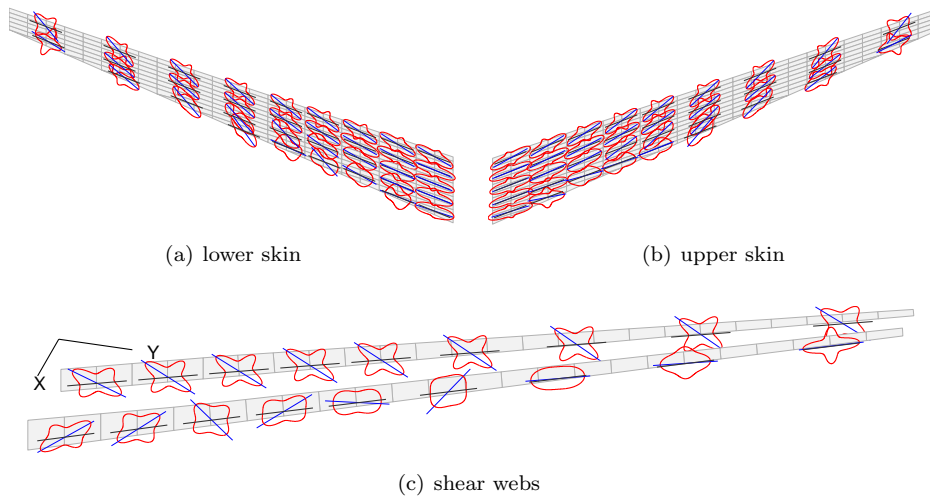


Figure 9.37: *Optimized design, $\hat{E}_{11}(\theta)$, unbalanced laminates*

As can be seen from the plot, optimization for minimal mass resulted in a clear tendency towards major stiffness directions of $\approx \pm 45^\circ$ in the front spar, thus, it resembled a classical shear web layup, where $\pm 45^\circ$ cross-ply fiber angles constitute the optimum distribution in terms of load path and hence maximum material exploitation. The rear spar did not show a clear tendency in major stiffness alignment, but rather a span dependent, locally optimal solution. With the chordwise aerodynamic center laying in the vicinity of the quarter chord, it is the front spar which usually carries a considerable part of the shear force. Consequently, the optimization adopted the stiffness distribution accordingly. As for the wing skin stiffness distributions, the same forward tilting of the main stiffness direction as in the skin-only optimization was observed, resulting in a negative coupling index and thus a decrease in wing twist when bending up.

The sizing load cases in each design field are illustrated in Figure 9.38. Compared to the results without shear web optimization, Figure 9.20(a) and 9.20(c), LC 1001 gained some more influence in the lower skin of the outer wing. Other than that,

no major changes occurred. It is interesting to note that despite the not particularly different thickness distribution in the front and rear spars, see Figure 9.35, completely different sizing load cases were responsible for their sizing, Figure 9.38(c).

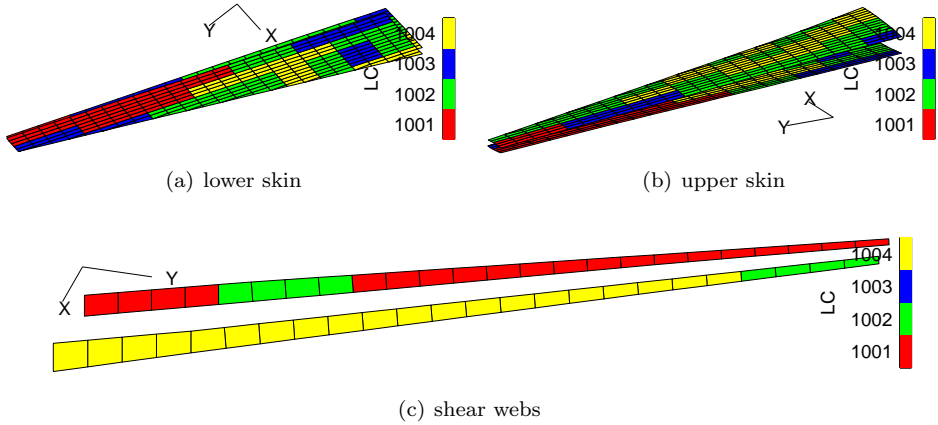


Figure 9.38: *Optimized design, sizing load case per field, unbalanced laminates*

A deeper insight could be obtained by investigating failure indices directly, see Figure 9.39. Elements 496 to 519 belonged to the front spar, elements 520 to 543 to the rear spar. While the rear spar was sized exclusively by LC 1004, with a single exception in in

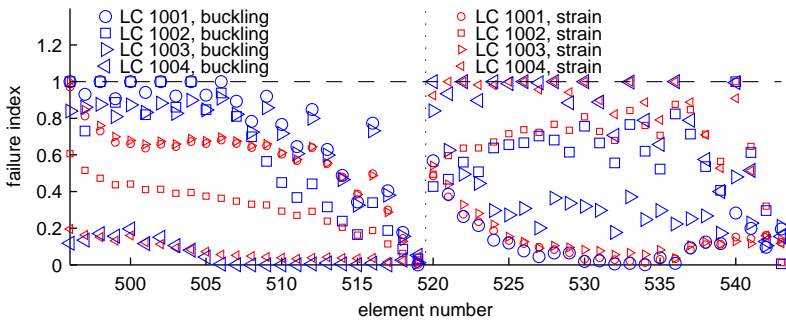


Figure 9.39: *Optimized design, failure indices in the shear webs, unbalanced laminates*

the outer wing, the front spar was clearly dominated by LC 1001 and 1002, reaching simultaneously the limit failure value 1.0. This confirms what already had been depicted in the previous section 9.4; Figure 9.38(c) on its own does not necessarily allow for a clear understanding concerning the most important load cases, since for example other than deduced from it, LC 1002 according to the results depicted in Figure 9.39 was equally important. Moreover, the buckling failure dominance in the front spar, and simultaneous buckling and strain failure in the rear spar is clearly shown in Figure 9.39.

This concludes the example of including multiple structural entities in a stiffness optimization. Since the aeroelastic and aerodynamic results closely resembled those depicted in the skin-only optimization, they will not be discussed further.

9.6 Numerical Results: Stacking Sequence Optimization

Succeeding the continuous optimization process, eventually the preliminary results of a stacking sequence optimization will be presented in this section. Denoting the results “preliminary” should suggest that the depicted data constitute the first stacking sequences obtained for a large scale application. An introduction to the theory of a stacking sequence table (SST) based genetic algorithm optimization and the generation of global multi-point approximations using a modified *Shepard* interpolation is provided in section 2.3.

The same forward swept wing as described earlier in this chapter served as the testbed for the SST optimization. The continuous stiffness optimization, with unbalanced laminates and without consideration of the aero correction module, led to a minimum weight of 423.7 kg, see also table 9.2 on page 175. Accordingly, the thick-

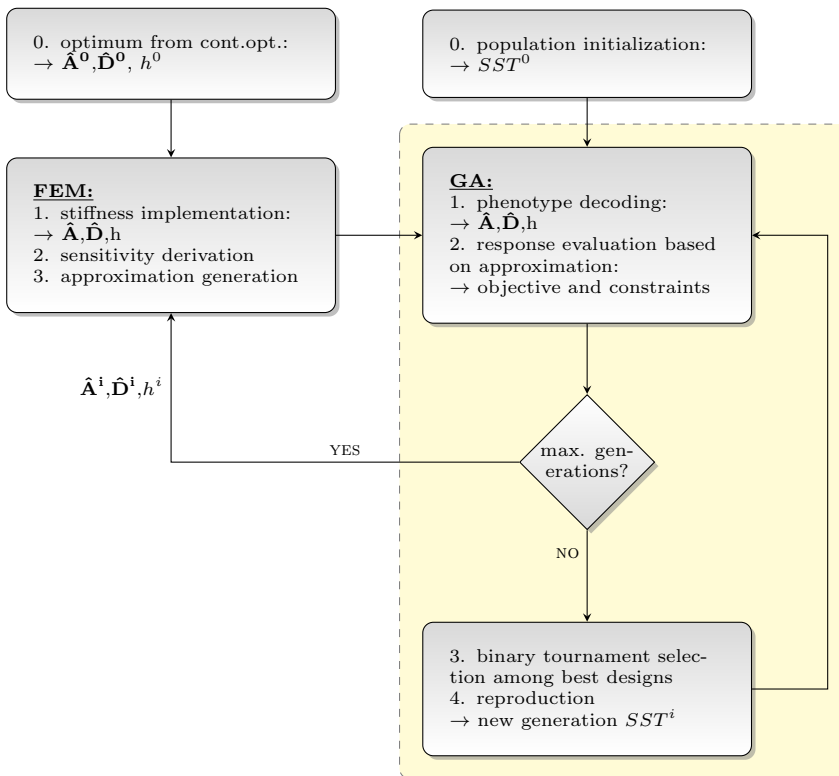


Figure 9.40: Schematic overview of the GA stacking sequence optimization in combination with successive approximations

ness and stiffness distributions as shown in Figure 9.17(b) and 9.18(b) constituted the starting design for the genetic algorithm (GA) SST optimization; slight modifications to this design will be discussed below. They are denoted $\hat{\mathbf{A}}^0, \hat{\mathbf{D}}^0, h^0$ in the process overview depicted in Figure 2.9 on page 39, which is repeated here for ease of reading, Figure 9.40.

The optimization model as shown in Figure 9.4 on page 162 consisted of 68 fields, amounting to 34 fields per wing skin. For the SST optimization, the upper and lower wing skin were addressed by two independent SST's, so as not to impose additional design space constraints by combining structurally separated entities. The design field numbers are depicted in Figure 9.41. A variety of possible objective functions

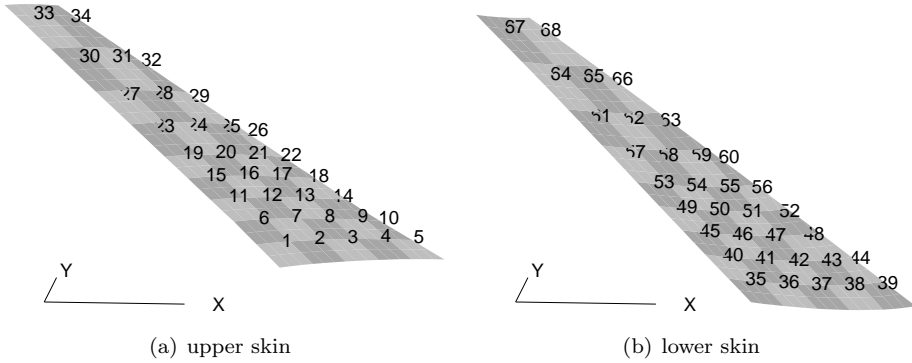


Figure 9.41: *Design field numbering*

for the SST optimization are listed in table 2.5, page 41. Meddaikar [Med13] has demonstrated good results when applying an objective *direct optimization* in a stacking sequence derivation for a wind-tunnel model comprising only few design fields. The same objective was also selected for the present application: that is, mass was defined as the objective to be minimized in the GA. Applying exactly the same load cases as those used for the stiffness optimization resulted in identical constraints on strain and buckling. The same aileron effectiveness constraint $\eta_{ail} \geq 0$ and divergence constraint $q_{div} \geq 35000 Pa$ were also applied. The parameters required for the GA optimization are listed in table 9.3.

Table 9.3: *GA parameters and guidelines*

| | |
|--|--------------------------|
| population size | 150 |
| mutation probability | 0.8 |
| crossover probability | 0.5 |
| number of generations | 600 |
| min/max number of plies | 18/68 |
| ply thickness | 0.25 mm |
| max. dropped plies between fields | 40 |
| fiber angles | 15°-steps |
| max. contiguous plies | 4 |
| damage tolerance | outer ply $\pm 45^\circ$ |
| max. disorientation between adjacent plies | 45° |

The GA mutation rate being unnaturally high was a consequence of a problem specific need for an adequate exploration of the design space in combination with the mutation definition, see section 2.3.2. The effect of a single ply angle mutation within a stack of

e.g. 50 plies is probably rather small, accordingly, a high mutation rate can effectively increase the search radius. Setting the amount of ply drops between adjacent fields to 40 was done to deactivate the corresponding guideline and thus allow a fair comparison of the stiffness and SST optimizations. The maximum ply number $N_{max} = 68$ was defined by the thickest design field in the continuous optimization, the prescribed single ply thickness and an additional margin to address possible drawbacks of a finite stacking sequence compared to a continuous stiffness representation. A manufacturing guideline, stating that at least each fourth ply should not be dropped, plus an additional layer for symmetry reasons, led to $N_{min} = N_{max}/4 + 1 = 18$. It was for the sake of N_{min} resulting in a minimum thickness of $h_{min} = 4.5\text{ mm}$ that the stiffness optimization was repeated with an updated lower thickness limit, previously amounting to $h_{min} = 1.0\text{ mm}$, which then served a basis for the GA optimization.

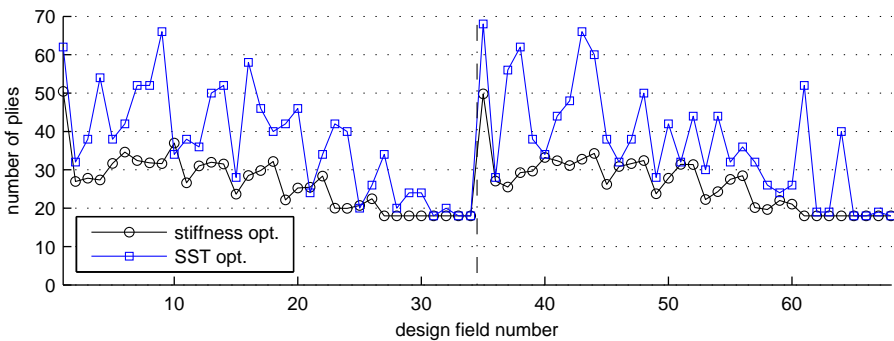


Figure 9.42: Stiffness and SST optimization, ply numbers, ply thickness 0.25 mm, unbalanced laminates

The results for the unbalanced laminate GA stacking sequence optimization after five global multi-point approximation loops, depicted in Figure 9.40, will be presented in the following. Figure 9.42 depicts a comparison of design field ply numbers, noting that the stiffness optimization values are only virtual, obtained by dividing the optimized thicknesses with the thickness of a single ply. Design field numbers were assigned as shown in Figure 9.41. Apparently, the SST optimization was not

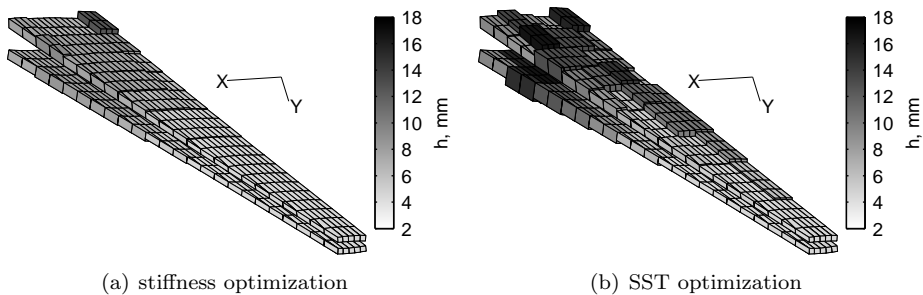


Figure 9.43: Stiffness and SST optimization, thickness distribution, unbalanced laminates

able in achieving a thickness distribution equivalent to the one obtained for the stiffness optimization. While the optimized mass for the stiffness optimization amounted to 448.1 kg, the stacking sequence mass summed up to 634.7 kg, corresponding to $\approx 42\%$ weight penalty. The three-dimensional thickness comparison shown in Figure 9.43 moreover indicates that the irregular distribution in case of the SST optimization might not yet constitute the best possible solution, since in the discrete case a rather steady decrease in thickness towards the tip should also be expected.

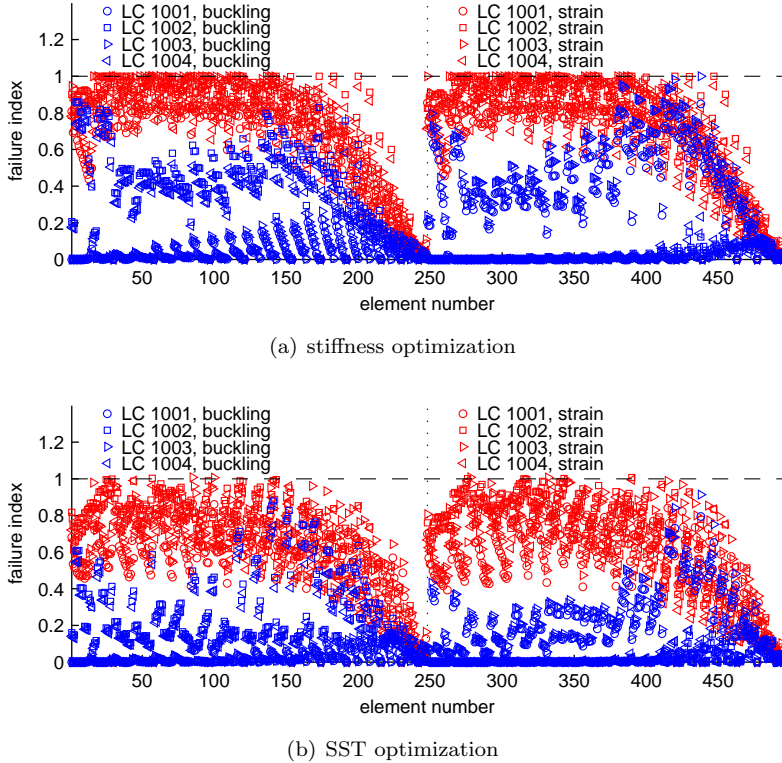


Figure 9.44: *Stiffness and SST optimization, failure indices, unbalanced laminates*

A comparison of strain and buckling failure indices for all four sizing load cases, element numbers 1 to 247 belonging to the upper skin, and element numbers 248 to 494 to the lower skin, is presented in Figure 9.44. As expected from the increased skin thickness, considerably fewer elements reach the failure boundary in the case of the SST optimization. Moreover, very few elements exceed the limit failure index at 1.0 by $\approx 1\%$. This can be attributed to the deviations of the approximated responses with respect to the real response, the latter of which is computed only after finishing the inner GA loop.

A comparison of stiffness distributions for continuous and SST optimization, Figure 9.45, reveals equivalent trends. As for the continuous optimization, also in the SST optimization the main stiffness direction was tilted forward. However, the polar plots indicate a rather smeared distribution with a less articulate directional alignment.

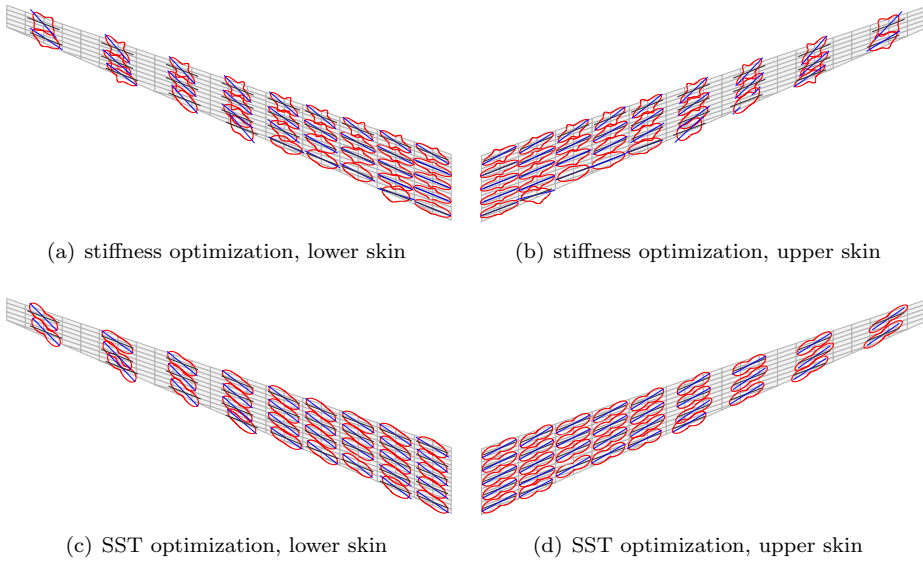


Figure 9.45: *Stiffness and SST optimization, $\hat{E}_{11}(\theta)$, unbalanced laminates*

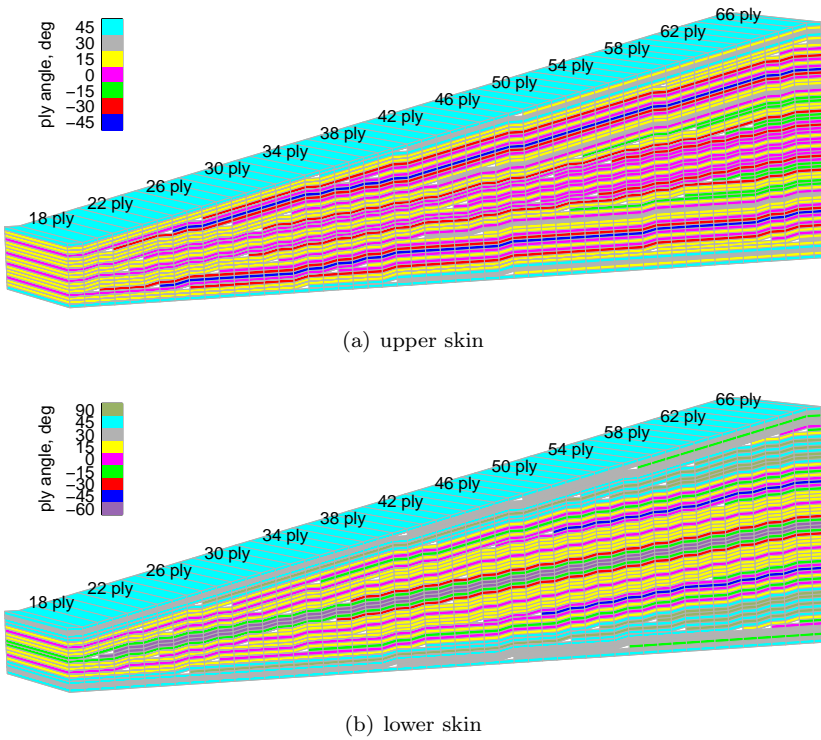


Figure 9.46: *SST, unbalanced laminates*

Visualizations of the optimized SST for the upper and lower wing skin are provided in Figure 9.46(a) and 9.46(b), respectively. The positive fiber angles correspond to a forward tilt of the fibers, seen in span direction. While these plots can be used to determine the stacking sequence in each of the design fields by correlating the ply numbers with Figure 9.41 and 9.42, the plots true purpose is to depict the dominant fiber angles on the one hand, and an inspection of guidelines on the other hand. Starting with the guidelines and referring to table 9.3 on page 195, it could be verified that the damage tolerance guideline is fulfilled by the outer, imposed, 45° ply, as well as the compliance with the ply contiguity guideline, requiring no more than four consecutive plies with the same angle. The disorientation guideline, asking for a change in ply angle of adjacent plies being smaller than 45° , could also be verified, although it needs to be noted that it can be a tedious task when it is based only on the graphical representation. Concerning fiber angles it could be observed that the upper skin was dominated by 0° and 15° plies. The lower skin showed a clear dominance of 15° , followed by 45° plies. Accordingly, the stiffness distributions for the lower skin, Figure 9.45(c), indicated a greater forward tilt of the main stiffness direction, compared to the upper skin, Figure 9.45(d). As a result of omitting a guideline defining the minimum amount of plies per fiber angle, in this case ranging from -90° to 90° in steps of 15° , the plies in the upper skin remained within a range of $\pm 45^\circ$. Hence, there were no fibers in chord direction. The guideline was omitted to avoid additional constraints in the initialization and reproduction of the stacking sequence tables. Instead, a guideline limiting the ratio between maximum and minimum membrane stiffness was implemented, the theory for which was derived by Abdalla et al. [Abd09]. The lower skin featured a few plies outside the $\pm 45^\circ$ range, which could also be observed in the more ellipse-like stiffness distributions shown in Figure 9.45(c).

For the sake of completeness, but also because it constitutes a key result in SST optimization, the full stacking sequence tables of upper and lower skin are provided in table 9.4 and 9.5.

Despite the, as yet, rather large differences in the optimized minimum weight for the SST optimization compared to the continuous optimization, it is believed that further investigation into the determining guidelines and a survey of previously proposed objective functions will further improve the SST results. Moreover, the application of a single SST for the entire upper and lower skin is in all probability not meaningful for an industrial implementation. Subdivision of each skin into more than one part would greatly relieve the constraints imposed by the addressed guidelines. This becomes clear when imagining the limiting case where a separate SST for each design field is applied, in which case the SST optimization should be able to closely resemble the continuous stiffness optimization result.

9.7 Summary

A detailed insight into the application and implications of a doublet lattice force correction using a higher order CFD method and a first application of the stacking sequence optimization was discussed in this chapter.

The trim application described in section 9.3 demonstrated the general functionality and convergence of the correction procedure, and highlighted the differences to

be expected when using the two aerodynamic methods TAU and DLM. The improvements made in the doublet lattice method due to using a W2GJ camber correction and the limitations of this correction with the emergence of recompression shocks were discussed. It was shown that consideration of the camber correction did greatly improve DLM quality when applied in shock free conditions. The effects of aero correction consideration on mass minimization, emphasizing the differences with respect to optimizations that did not feature an aero correction were discussed in detail in section 9.4. Finally, optimizer functionality in conjunction with multiple structural entities, a mass minimization covering wing skins and shear webs in the optimization model, was demonstrated in section 9.5.

The applied *Euler* method proved to converge reliably with the mesh generated in SUMO and described in section 9.2. Nevertheless, it should be mentioned that the *Euler* method has a limited application region. With increasing angle of attack and thus lift coefficient, *Euler* predicts the shock to move more and more downstream, increasing in strength. Flow separation, other than at the sharp trailing edge, cannot be modeled. Accordingly, in the case of severe aerodynamic load conditions the *Euler* results will start to deviate from what can be expected in reality. A possible solution to this problem is to increase CFD fidelity further, and thus consideration of the full *Navier-Stokes* equations along with viscous boundary layers and turbulence modeling. Apart from the need for a new CFD mesh topology including a prismatic sub-layer, the required changes to the developed CFD correction module are minimal. However, this is beyond the scope of the research reported here, but should be investigated.

Eventually, the application of a stacking sequence optimization based on the results from a continuous stiffness optimization was demonstrated, proving the functionality of the process.

Part III

Summary

CHAPTER 10

Conclusions and Recommendations

*“Good night, good night! Parting is such sweet sorrow, that I shall say
good night till it be morrow.”*

William Shakespeare

10.1 Conclusions

Composites have a great potential for performance improvement when used in the load carrying structural components of an aircraft. The benefits can be manifold, from weight decrease, to controlling elastic deformation behavior to fatigue resistance. In order to tap the potential advantages of composites over conventional, standardized and computationally well-explored homogeneous materials, new design methodologies are required and have been under development ever since the benefits of composites were recognized. Primarily through the use of variable stiffness laminates and the concomitant extension of the design space, new design possibilities are arising. The ability to exploit deliberately the orthotropic nature of composites in a variable stiffness design is commonly known as stiffness tailoring, or, in conjunction with an aeroelastically deforming structure, as aeroelastic tailoring. It is at this point the work presented in this thesis started, aiming at, as stated in the objective, the

development of a variable stiffness optimization process that incorporated the possibility of considering static aeroelastic responses in the structural design of aircraft wings.

The research done to achieve this aim is divided in this thesis into a part describing the optimization methodology, and a part dedicated to the application in several design studies. Conclusions drawn from both parts are summarized in section 10.1.1 and section 10.1.2.

10.1.1 Stiffness Optimization Process

In the first part of the thesis the development of a design framework suited for variable stiffness laminate optimization of composite structures with static aeroelastic responses was presented. The global structure of the successive subproblem iteration scheme was introduced in chapter 2 and linked to subsequent chapters in which the contributing components were discussed in more detail. This comprised the particularities associated with the derivation of responses and sensitivities using the selected finite element solver NASTRAN and the development of response approximations.

In a first step, the parametric model generator MODGEN was prepared for the derivation of suitable finite element, doublet lattice and mass models. This included the provision for stiffness matrix modeling as a basis for orthotropic composite material properties. In order to regulate the spatial stiffness resolution and thereby the complexity of the optimization problem, the concept of design fields was introduced. A design field corresponds to a group of finite elements that all feature the same material properties, expressed as membrane and bending stiffness matrix and thickness. Accordingly, in this case each design field comprised thirteen design variables, from which six were attributed to each of the stiffness matrices and one for thickness. Changing a design variable of a design field eventually modifies the stiffness properties in each of the associated finite elements. The design field implementation allowed for arbitrary spanwise and chordwise field distributions. While the mere implementation of design variables and responses in NASTRAN complied with a standardized formalism, customized output features were considered. This took the form of determining relevant matrices, such as sensitivities, responses, aeroelastic pressures and forces, and displacements.

The convex, separable and conservative approximation formulation developed by IJsselmuiden [IJs11] was adopted in the optimization process. It features linear and reciprocal contributions in membrane and bending stiffness matrices and a linear contribution in thickness. Convexity of the reciprocal terms in the approximation formulation had to be ensured a priori. Physical insight into the element based structural responses strength and buckling allowed for a dedicated selection of linear and reciprocal sensitivities, also ensuring convexity of the approximation. Since mass only depends on thickness, no particular action in respect of convexity was required. The global aeroelastic responses aileron effectiveness, divergence and twist did not allow for the derivation of an explicit dependency of the responses on stiffness matrices, however, to maximize the reciprocal share in the response approximation, a convexification procedure was implemented. The procedure comprised an evaluation of the eigenvalues belonging to the reciprocal sensitivity matrix. Negative eigenvalues, indicating non-convexity, were separated and expressed in terms of a linear sensitivity instead. Thus, convexity of the approximation could be ensured, while maximizing the reciprocal contribution.

A correction procedure for the enhancement of aeroelastic loads using a higher order aerodynamic method was developed, which played a key role in the variable stiffness optimization process. The correction comprised two parts, one aimed at modifying the NASTRAN internal DLM using a camber correction, and one that modified the DLM aeroelastic loads at the coupling nodes using CFD. The modular setup allowed the aero correction process to be inserted easily into the existing stiffness optimization framework.

10.1.2 Wing Design with Aeroelastic Constraints

The design studies performed in the second part of the thesis primarily served as testbeds and benchmarks for the developed optimization framework. Comprising different levels of complexity, the case studies demonstrated the functionality of the stiffness optimization process including aeroelastic responses.

In a first application, the general functionality was tested using a generic, *A320* like wing structure, chapter 7. Three maneuver and four aileron effectiveness load cases in combination with one mass case without fuel consideration served as the basis for a mass minimization and aileron effectiveness maximization. The optimization model comprised 44 design fields in the upper and lower wing skin. To verify the sensitivities supplied by the finite element solver, a comparison with respect to sensitivities generated with a finite difference approach was made. The test revealed a shortcoming in the sensitivities related to the coupling terms (1, 3) and (2, 3) in the stiffness matrices. It was discovered that only unbalanced laminates with non-zero entries in the coupling terms would also yield appropriate sensitivities. As the intention is to also apply the optimization with unbalanced laminates, it is recommended to initiate the optimization with a starting design that is comprised of unbalanced laminates.

The results of a mass minimization study with an aileron reversal constraint indicated a mix of element failure types, with a dominance of buckling failure in the outer wing and simultaneous failure in strength and buckling in the mid and inner wing, and a mix in load cases contributing to the sizing. Failure indices in the upper and lower wing skin, in particular for the $n_z = +2.5g$ pull up maneuver, stated maximum material exploitation by simultaneously reaching limit failure indices throughout the entire wing skin. While the above was true for both optimizations, balanced and unbalanced, the difference in mass between the two was considerable, amounting to 486 kg wing skin mass with unbalanced, compared to 522 kg with balanced laminates. As a result of buckling dominance in both, balanced and unbalanced optimizations, the stiffness distributions did not feature dedicated alignment with a, presumable, spanwise load path. A comparison of twist distributions for a $n_z = +2.5g$ pull up maneuver indicated a lower tip twist in the case of unbalanced laminates, accounting for the weight savings by shifting the center of lift towards the root.

Replacing the mass minimization objective with an aileron effectiveness maximization while constraining mass to an upper limit of 650 kg again revealed clear advantages of unbalanced over balanced laminates. The aileron effectiveness increased from $\eta_{ail} = 0.0357$ to $\eta_{ail} = 0.0508$. Moreover, an explicit impact of the new η_{ail} objective on the stiffness distribution could be observed. Distributions for the balanced optimization indicated a distinct increase in torsional stiffness with an adjustment of the main stiffness direction at angles of $\approx \pm 45^\circ$. Thus, the tendency of the wing to sidestep the additional twisting moment induced by an aileron deflection was decreased, in return leading to increase in aileron effectiveness. Pronounced adoption of bending-torsion coupling could be observed in the case of the unbalanced optimization. With the main stiffness direction tilted backwards in the upper and lower skin, the tendency towards twist increase when bending the wing up was induced, counteracting the regular tendency of twisting towards more negative angles for a downward deflected aileron. In this context, a coupling index Ξ was defined, indicating the tendency of the wing to twist positively or negatively when bending up.

Owing to a forward swept wings aeroelasticity driven disadvantages in terms of wing weight, a detailed investigation into the effect of aeroelastic constraints on the skin mass for a forward swept wing was conducted, chapter 8. The wing geometry, along with basic flight envelope parameters was adopted from the DLR project *LamAiR*. Apart from the regular geometry featuring a leading edge sweep of $\xi = -16.8^\circ$, two additional wings with less sweep were also investigated. Provision for a fuel model along with variable passenger loading required the consideration of multiple mass cases and thus sensitivity analyses in the preparation of the response approximations. The optimization model consisted of 70 design fields in the upper and lower wing skin.

In a first set of optimizations, the influence of an aileron effectiveness constraint $(\eta_{ail})_{min}$ was investigated. With wing skin mass as the objective to be minimized, the only other constraints considered were strain and buckling. It could be shown that unbalanced laminates for all aileron effectiveness constraint limits outperformed the balanced designs by savings of $\approx 15\%$ in wing skin mass. As expected, smaller sweep angles resulted in lower wing skin masses. With increasing $(\eta_{ail})_{min}$ the same tendencies in stiffness distribution as in the previous optimization of the swept back wing could be observed. While in the case of balanced laminates the torsional stiffness was maximized, the main stiffness direction in the case of unbalanced laminates tilted backwards, supporting a positive coupling index.

The influence of a divergence pressure constraint $(q_{div})_{min}$ was investigated in a second set of optimizations. The most prominent outcome was the minimal influence of $(q_{div})_{min}$ on wing skin mass for unbalanced laminates. While only the wing featuring the largest leading edge sweep still showed a slight weight increase with increasing $(q_{div})_{min}$, no weight increase at all could be observed for the other, less swept geometries. Compared to the balanced laminate designs, the savings in wing skin mass amounted to $\approx 15\%$ for the lowest investigated constraint, further increasing with increasing divergence pressure. A survey of the design variable development revealed a bending-torsion coupling tendency with a negative coupling index for the unbalanced laminates. Accordingly, bending the wing up will result in a twist decrease and thus counteract the divergence affinity. Balanced laminates, missing the degree of freedom of tilting the main stiffness direction, could comply with an increasing $(q_{div})_{min}$ constraint only by the use of local thickness increases and thus suffered mass penalties compared to unbalanced laminates.

The third set of optimizations highlighted the influence of an upper limit on tip twist $(\alpha_{tip})_{max}$ for a cruise load case. Again, unbalanced laminate designs clearly outperformed balanced laminates for all investigated $(\alpha_{tip})_{max}$ constraints and sweep angles. Unbalanced laminates allowed for twist constraints that could not be accomplished with balanced designs. In complying with the upper limit on $(\alpha_{tip})_{max}$, the stiffness distributions indicated a negative coupling index by tilting the main stiffness direction in the outer wing forward. The balanced laminate designs could only achieve the lower constraint values by locally modifying the thickness distribution.

The final demonstration of the optimization framework was focused on possible implications of the aero correction procedure. The geometry used for this demonstration was a forward swept wing, and it resembled the previously introduced *LamAiR* configuration. Using a pure trim application without structural optimization application, fast convergence behavior of the CFD correction forces was confirmed.

Only three to four finite element steps in combination with CFD calculations were required to achieve a static equilibrium. A comparison of the converged DLM and TAU pressure difference distributions for the $n_z = +2.5g$ load cases revealed a good agreement of surface pressures and thus coupling forces in the absence of recompression shocks. The camber correction using a W2GJ matrix yielded a sensible enhancement when compared to an uncorrected flat plate distribution. In the presence of recompression shocks, arising at higher *Mach* numbers, however, large deviations between DLM and TAU were observed. The consequences for the coupling forces and hence the spanwise lift and moment distribution were clearly noticeable. The DLM limitations could be depicted using a CFD based *Mach* number variation study, which showed that beyond $M = 0.8$ the *Prandtl-Glauert* correction factor implemented in DLM was not capable of reproducing the adverse influence of shocks on the lift coefficient.

The provision for aero correction in a subsequent mass minimization, including strength, buckling, aileron reversal and divergence constraints revealed noticeable differences when compared to equivalent optimizations without aero correction. While wing skin mass increased in the case of balanced laminates, it decreased for unbalanced laminates when considering aero correction, indicating that the correction did not imply a prescribed, but a case dependent impact on the optimized design. In the case of changing stiffnesses during the optimization procedure, the correction forces also showed convergence to steady values in the optimized design. It was found that an aero correction step every five structural iteration steps was sufficient to obtain both aero force and structural convergence. While only two load cases dominated the design field sizing when omitting aero correction, all four maneuver load cases contributed to the sizing when optimizing with aero correction. Moreover, large deviations in spanwise twist for the optimized structures with and without aero correction could be observed. Trimming the purely DLM optimized structure with CFD results revealed nearly identical twist distributions. The latter was a direct implication of the apparently similar skin thickness and stiffness distributions resulting from optimizations with and without correction. However, closer consideration of failure indices revealed that the DLM optimized structure would fail under more realistic CFD loading conditions, thus attesting the potential benefit, and also necessity for a correction method.

Demonstrating the ability to include additional structural entities aside from the wing skins, a similar mass minimization as before, but with the consideration of shear webs in the optimization model, was performed. The optimization process proved to yield meaningful thickness and stiffness distributions in the shear webs, with a dominance of buckling failure in the front spar and mixed failure types in the rear spar.

Finally, the functionality of the stacking sequence optimization process was demonstrated. Despite the, as yet, rather large differences in optimized mass compared to that obtained using a continuous stiffness optimization, reasonable stiffness distributions were obtained while still complying with the major guidelines involved in a discrete layup design.

10.2 Recommendations

The variable stiffness optimization framework described in this thesis has been shown to generate valuable results when applied in the structural design of typical passenger or transport aircraft configurations. Despite, or actually because of this, several points still need to be addressed, that will support further development of the process towards an optimal exploitation of composite materials in load carrying components and the actual implementation in real world structures.

Provision for unsteady aeroelastic responses in the optimization, like gust loads and flutter, would considerably extend the scope of operation of the framework. In the current state, gust and flutter analyses must be performed as post-processing steps with no direct feedback for the optimization. While gust loads could be approximated using quasi-steady DLM load cases modified by constant correction forces, NASTRAN does provide for responses and sensitivities with respect to critical flutter speed. The consideration of unsteady aeroelastic responses simultaneously would require a structural and aerodynamic representation of the entire aircraft in the FE analysis. This will also improve the quality of the static aeroelastic trim analysis by incorporating force and moment equilibrium through the use of tailplanes.

The current formulation of the optimization problem in terms of membrane and bending stiffness matrices is tailored for the optimization of shell-like structural entities. An extension to include one-dimensional stringer properties in the optimization would have a significant influence on the overall optimum design. In an initial approach, allowing for application of the framework in its current setup, stringer properties could be described using additional, *virtual* design fields. A more detailed discussion was provided in section 8.9.

The current formulation of the buckling failure response and sensitivity tool implies each simply supported buckling field is represented by a single shell element. Consequently, the element resolution in design fields comprising buckling responses is prescribed to one element covering for instance the skin between two ribs and two stringers. To be able to increase the resolution, a modified buckling formulation would be required, capable of incorporating variable loading within a single buckling field. Moreover, a refinement of the failure envelope applied in the derivation of strain failure responses and sensitivities would contribute to an enhancement in the quantitative estimates of absolute optimal weight.

Concerning aero correction, a next step towards realistic aeroelastic loads would be to switch from *Euler* to a higher order CFD method like *Reynolds-averaged Navier-Stokes*, RANS, that is capable of dissolving the boundary layer and non-linear flow separation effects.

As for the approximation based optimization algorithm, a screening of active and inactive constraints would help to reduce the amount of constraints requiring simultaneous monitoring, thus enabling the consideration of far more sizing load cases. This will be required if the framework is to be used in an industrial environment.

It should be noted that a first utilization of the optimization framework in the aeroelastic design of a wind-tunnel model is scheduled for testing in 2015. The stacking sequence optimization will involve constraints to ensure the producibility in a hand-layup technique. Static deformation tests prior to the wind-tunnel campaign will be performed to check compliance with the deformations targeted during design.

APPENDIX A

Finite Element Analysis Alter

A.1 Sensitivities and Responses

A.1.1 File Management Statements

```
ASSIGN OUTPUT4='FSP_02_opt_resp1.op4', unit=92,unformatted
ASSIGN OUTPUT4='FSP_02_opt_resp2.op4', unit=93,unformatted
ASSIGN OUTPUT4='FSP_02_opt_sens.op4', unit=94,unformatted
ASSIGN OUTPUT2='FSP_02_opt_dscmcol.op2', unit=95,unformatted
```

A.1.2 Executive Control Statements

```
COMPILE SUBDMAP=EXITOPT, LIST
ALTER 'IF ( DSPRINT ) DSAPRT '$
  OUTPUT4 R1VALRG, , , // -1/92 // 16 $
  OUTPUT4 , , , // -2/92 $
  $
  OUTPUT4 R2VALRG, , , // -1/93 // 16 $
  OUTPUT4 , , , // -2/93 $
  $
  OUTPUT4 DSCM2, , , // -1/94 // 16 $
  OUTPUT4 , , , // -2/94 $
  $
  OUTPUT2 DSCMCOL, , , // -1/95 / 'DSCMCOL' $
  OUTPUT2 , , , // -9/95 / $
```

A.2 Aerodynamics

A.2.1 File Management Statements

```
ASSIGN OUTPUT4='aeroforce_trim_sol.op4', unit=91,formatted
$
```

```

ASSIGN OUTPUT4='aeroforce_DLM_FFAJ2.op4', unit=101,formatted
ASSIGN OUTPUT4='aeroforce_DLM_FFAJ.op4', unit=102,formatted
ASSIGN OUTPUT4='aeroforce_DLM_UKTOTAL.op4', unit=103,formatted
$
ASSIGN OUTPUT4='aeroforce_PRG.op4', unit=96,formatted
ASSIGN OUTPUT4='aeroforce_PRGPERG.op4', unit=97,formatted
ASSIGN OUTPUT4='aeroforce_AIPG.op4', unit=98,formatted

```

A.2.2 Executive Control Statements

```

compile aestatrs list
$ ----- Trim Variables
ALTER 1221 $
OUTPUT4 UX,,,,//0/91///16
TABPT UX,UXDAT,,,,// 'LONG' / $
$
$ ----- DLM Forces at Box Centers
ALTER 1247
MATPRN UKTOTAL,,,,// $
OUTPUT4 UKTOTAL,,,,//0/103///16 $
OUTPUT4 ,,,,// -2/103 $
$
ALTER 1257
MATPRN FFAJ2,,,,// $
OUTPUT4 FFAJ2,,,,//0/101///16 $
OUTPUT4 ,,,,// -2/101 $
$
ALTER 1266
MATPRN FFAJ,,,,// $
OUTPUT4 FFAJ,,,,//0/102///16 $
OUTPUT4 ,,,,// -2/102 $
$
$ ----- DLM Forces at Grid Points
alter 'append.*aipg.*aipgf' $
  type db sils ,gpls $
  message //'rigid (aero) forces' $
  matgpr gpls ,uset ,sils ,prg //'g' $
  OUTPUT4 prg,,,,//0/96///16 $
  OUTPUT4 ,,,,// -2/96 $
  $
  message //'elastic (aero) forces' $
  add5   prg ,perg ,,,,/prgperg/// $
  matgpr gpls ,uset ,sils ,prgperg //'g' $
  OUTPUT4 prgperg,,,,//0/97///16 $
  OUTPUT4 ,,,,// -2/97 $
  $
  message //'elastic (aero + applied - inertial) forces' $
  matgpr gpls ,uset ,sils ,aipg //'g' $

```

```

OUTPUT4 aipg , , , //0/98//16 $
OUTPUT4 , , , // -2/98 $

```

A.3 Displacements

A.3.1 File Management Statements

```

ASSIGN OUTPUT4='disp.op4', unit=99,formatted

```

A.3.2 Executive Control Statements

```

COMPILE SEDRCVR LIST
ALTER 34
  message //'write displacements to file' $
  OUTPUT4 UG, , , // -1/99//16 $
  OUTPUT4 , , , // -2/99 $

```

A.4 Correcting Alters

A.4.1 Executive Control Statements, Alter 1

```

$ ALTER to correct sensitivity order, 2012-05-14, MSC support
compile pslgdv
alter 'bcdr'(7),''
      BCDR      CASEau//0/' '/0//s,n,mbcflg////////-1 $

```

A.4.2 Executive Control Statements, Alter 2

```

$ ALTER to correct mixed SPC, multiple lc, MSC support
compile respn list
alter 'spaw2'(1,-1),'' $
  PARAML  UGx//'TRAILER'/1/S,N,nrow $ no. of rows reqd.

```


- [Abb59] I. H. Abbott and A. E. Von Doenhoff. *Theory of Wing Sections, Including a Summary of Airfoil Data*. Dover Books on Aeronautical Engineering Series. Dover Publications, 1959.
- [Abd07a] M. M. Abdalla, R. De Breuker, and Z. Gürdal. “Aeroelastic Tailoring of Variable-Stiffness Slender Wings for Minimum Compliance.” In: *International Forum on Aeroelasticity and Structural Dynamics (IFASD)*. IF-117. Stockholm, 2007.
- [Abd07b] M. M. Abdalla, S. Setoodeh, and Z. Gürdal. “Design of variable stiffness composite panels for maximum fundamental frequency using lamination parameters.” In: *Composite Structures* 81.2 (2007), pp. 283–291.
- [Abd09] M. M. Abdalla, Z. Gürdal, and C. Kassapoglu. “Formulation of Composite Laminate Robustness Constraint in Lamination Parameters Space.” In: *50th AIAA/ASME/ASCE/AHS/ASC Structures, Structural Dynamics, and Materials Conference*. Palm Springs, CA, May 2009.
- [Ada04] D. B. Adams, L. T. Watson, Z. Gürdal, and C. M. Anderson-Cook. “Genetic Algorithm Optimization and Blending of Composite Laminates by Locally Reducing Laminate Thickness.” In: *Adv. Eng. Softw.* 35.1 (2004), pp. 35–43.
- [Alb69] E. Albano and W. P. Rodden. “A doublet-lattice method for calculating lift distributions on oscillating surfaces in subsonic flows.” In: *AIAA Journal* 7.2 (1969), pp. 279–285.
- [And05] J. Anderson. *Fundamentals of Aerodynamics*. McGraw-Hill, Oct. 2005.
- [Bab89] I. Babuška, M. Griebel, and J. Pitkäranta. “The problem of selecting the shape functions for a p-type finite element.” In: *International Journal for Numerical Methods in Engineering* 28.8 (1989), pp. 1891–1908.
- [Bal96] R. J. Balling and J. Sobieszczyński-Sobieski. “Optimization of coupled systems: A critical overview of approaches.” In: *AIAA journal* 34.1 (1996), pp. 6–17.

- [Bec01] A. Beckert and H. Wendland. “Multivariate interpolation for fluid-structure-interaction problems using radial basis functions.” In: *Aerospace Science and Technology* 5.2 (2001), pp. 125–134.
- [Ber98] J. J. Bertin and M. L. Smith. *Aerodynamics for Engineers*. Prentice Hall, 1998.
- [Blo08] A. W. Blom, S. Setoodeh, J. M. A. M. Hol, and Z. Gürdal. “Design of variable-stiffness conical shells for maximum fundamental eigenfrequency.” In: *Computers & Structures* 86.9 (2008), pp. 870–878.
- [Blo09] M. W. Bloomfield, J. E. Herencia, and P. M. Weaver. “Enhanced two-level optimization of anisotropic laminated composite plates with strength and buckling constraints.” In: *Thin-Walled Structures* 47.11 (2009), pp. 1161–1167.
- [Blo10] A. W. Blom, M. M. Abdalla, and Z. Gürdal. “Optimization of course locations in fiber-placed panels for general fiber angle distributions.” In: *Composites Science and Technology* 70.4 (2010), pp. 564–570.
- [Bri00] J. Brink-Spalink and J. Bruns. “Correction of unsteady aerodynamic influence coefficients using experimental or CFD data.” In: *41st AIAA/ASME/ASCE/AHS/ASC Structures, Structural Dynamics and Materials Conference*. Atlanta, GA, Apr. 2000.
- [Dan94] I. M. Daniel and O. Ishai. *Engineering Mechanics of Composite Materials*. Oxford University Press, 1994.
- [Dil13a] J. K. S. Dillinger, M. M. Abdalla, T. Klimmek, and Z. Gürdal. “Static Aeroelastic Stiffness Optimization and Investigation of Forward Swept Composite Wings.” In: *10th World Congress on Structural and Multidisciplinary Optimization*. Orlando, FL, May 2013.
- [Dil13b] J. K. S. Dillinger, R. Butler, G. Waibel, and L. M. M. Boermans. “Aerodynamic and Structural Design of the Open Class Sailplane Concordia.” In: *Technical Soaring, accepted for publication* (2013).
- [Dil13c] J. K. S. Dillinger, T. Klimmek, M. M. Abdalla, and Z. Gürdal. “Stiffness Optimization of Composite Wings with Aeroelastic Constraints.” In: *Journal of Aircraft* 50.4 (2013), pp. 1159–1168.
- [Dim13] D. Dimitrov and R. Thormann. “DLM-Correction Method for Aerodynamic Gust Response Prediction.” In: *International Forum on Aeroelasticity and Structural Dynamics (IFASD)*. June 2013.
- [DLR13a] DLR. *TAU-Code User Guide, Release 2013.1.0*. 2013.
- [DLR13b] DLR. *Technical Documentation of the DLR TAU-Code Release 2013.1.0*. Tech. rep. Braunschweig: Institute of Aerodynamics and Flow Technology, 2013.
- [Dre89] M. Drela. “XFOIL: An Analysis and Design System for Low Reynolds Number Airfoils.” In: *Low Reynolds Number Aerodynamics SE - 1*. Ed. by T. Mueller. Vol. 54. 1989,
- [EAS12] EASA. *Certification Specifications and Acceptable Means of Compliance for Large Aeroplanes, CS25*. Tech. rep. EASA, 2012.

- [Eas99] F. E. Eastep, V. A. Tischler, V. V.B., and N. S. Khot. “Aeroelastic tailoring of composite structures.” In: *Journal of Aircraft* 36.6 (1999), pp. 1041–1047.
- [Fuk94] H. Fukunaga, H. Sekine, and M. Sato. “Optimal Design of Symmetric Laminated Plates for Fundamental Frequency.” In: *Journal of Sound and Vibration* 171.2 (1994), pp. 219–229.
- [Fuk95] H. Fukunaga, H. Sekine, M. Sato, and A. Iino. “Buckling design of symmetrically laminated plates using lamination parameters.” In: *Computers and Structures* 57.4 (1995), pp. 643–649.
- [Gan03] V. B. Gantovnik, C. M. Anderson-Cook, Z. Gürdal, and L. T. Watson. “A genetic algorithm with memory for mixed discrete-continuous design optimization.” In: *Computers & Structures* 81.20 (2003).
- [Ger97] T. Gerhold, M. Galle, O. Friedrich, and J. Evans. “Calculation of complex three-dimensional configurations employing the DLR-tau-code.” In: *35th Aerospace Sciences Meeting and Exhibit*. Reno, NV, Jan. 1997.
- [Ghi09] H. Ghiasi, D. Pasini, and L. Lessard. “Optimum stacking sequence design of composite materials Part I: Constant stiffness design.” In: *Composite Structures* 90.1 (2009).
- [Ghi10] H. Ghiasi, K. Fayazbakhsh, D. Pasini, and L. Lessard. “Optimum stacking sequence design of composite materials Part II: Variable stiffness design.” In: *Composite Structures* 93.1 (2010).
- [Gie71] J. P. Giesing, T. P. Kalman, and W. P. Rodden. *Subsonic Unsteady Aerodynamics for General Configurations. Part I. Volume I. Direct Application of the Nonplanar Doublet-Lattice Method*. Defense Technical Information Center, 1971.
- [Gie76] J. P. Giesing, T. P. Kalman, and W. P. Rodden. *Correction Factor Techniques for Improving Aerodynamic Prediction Methods*. Tech. rep. McDonnell-Douglas Corp., Long Beach, Calif.: National Aeronautics and Space Administration, 1976.
- [Gre87] J. A. Green. “Aeroelastic tailoring of aft-swept high-aspect-ratio composite wings.” In: *Journal of Aircraft* 24.11 (1987), pp. 812–819.
- [Gro86] B. Grossman, Z. Gürdal, and R. T. Haftka. “Integrated aerodynamic/structural design of a sailplane wing.” In: *Aircraft Systems, Design and Technology Meeting*. Dayton, OH, Oct. 1986.
- [Guo12] S. Guo, D. Li, and Y. Liu. “Multi-objective optimization of a composite wing subject to strength and aeroelastic constraints.” In: *Proceedings of the Institution of Mechanical Engineers, Part G Journal of Aerospace Engineering* 226.9 (2012), pp. 1095–1106.
- [Gur99] Z. Gürdal, R. T. Haftka, and P. Hajela. *Design and optimization of laminated composite materials*. A Wiley-Interscience publication. Wiley, 1999.
- [Haf77] R. T. Haftka. “Optimization of flexible wing structures subject to strength and induced drag constraints.” In: *AIAA Journal* 15.8 (1977), pp. 1101–1106.

- [Haf92] R. T. Haftka and Z. Gürdal. *Elements of structural optimization*. Solid mechanics and its applications. Kluwer Academic Publishers, 1992.
- [Ham97] V. B. Hammer, M. P. Bendsoe, R. Lipton, and P. Pedersen. “Parametrization in laminate design for optimal compliance.” In: *International Journal of Solids and Structures* 34.4 (1997), pp. 415–434.
- [Har72] R. L. Harder and R. N. Desmarais. “Interpolation using surface splines.” In: *Journal of Aircraft* 9.2 (1972), pp. 189–191.
- [Her07] J. E. Herencia, P. M. Weaver, and M. I. Friswell. “Morphing Wing Design via Aeroelastic Tailoring.” In: *48th AIAA/ASME/ASCE/AHS/ASC Structures, Structural Dynamics, and Materials Conference*. AIAA-2007-2217. Waikiki, HI, 2007.
- [Hol84] S. J. Hollowell and J. Dungundji. “Aeroelastic Flutter and Divergence of Stiffness Coupled, Graphite Epoxy Cantilevered Plates.” In: *Journal of Aircraft* 21.1 (1984), pp. 69–76.
- [IJs08] S. T. IJsselmuiden, M. M. Abdalla, and Z. Gürdal. “Implementation of Strength-Based Failure Criteria in the Lamination Parameter Design Space.” In: *AIAA Journal* 46.7 (2008), pp. 1826–1834.
- [IJs09] S. T. IJsselmuiden, M. M. Abdalla, O. Seresta, and Z. Gürdal. “Multi-step blended stacking sequence design of panel assemblies with buckling constraints.” In: *Composites Part B: Engineering* 40.4 (2009), pp. 329–336.
- [IJs10] S. T. IJsselmuiden, M. M. Abdalla, and Z. Gürdal. “Optimization of Variable-Stiffness Panels for Maximum Buckling Load Using Lamination Parameters.” In: *AIAA Journal* 48.1 (2010), pp. 134–143.
- [IJs11] S. T. IJsselmuiden. “Optimal Design of Variable Stiffness Composite Structures Using Lamination Parameters.” PhD Thesis. TU Delft, 2011.
- [Iri11] F.-X. Irisarri, M. M. Abdalla, and Z. Gürdal. “Improved Shepard’s Method for the Optimization of Composite Structures.” In: *AIAA Journal* 49.12 (2011), pp. 2726–2736.
- [Iri13] F.-X. Irisarri, A. Lasseigne, F.-H. Leroy, and R. Le Riche. “Optimal design of laminated composite structures with ply drops using stacking sequence tables.” In: *Composite Structures* 107 (2013), pp. 559–569.
- [Jam83] A. Jameson. “The Evolution of Computational Methods in Aerodynamics.” In: *Journal of Applied Mechanics* 50.4b (1983), pp. 1052–1070.
- [Jr 81] L. A. Jr, Schmit. “Structural synthesis - Its genesis and development.” In: *AIAA Journal* 19.10 (1981), pp. 1249–1263.
- [Kai13] C. Kaiser. *Alternative Querruderarchitekturen für Verkehrsflugzeuge und aeroelastische Untersuchungen zur Rollmomentenerzeugung, IB-232-2013J08*. Tech. rep. Göttingen: Institute of Aeroelasticity, 2013.
- [Kam07] M. Kameyama and H. Fukunaga. “Optimum design of composite plate wings for aeroelastic characteristics using lamination parameters.” In: *Computers and Structures* 85.3-4 (2007), pp. 213–224.

- [Kat01] J. Katz and A. Plotkin. *Low-Speed Aerodynamics*. Cambridge Aerospace Series. Cambridge University Press, 2001.
- [Ken13] G. J. Kennedy and J. Martins. “A laminate parametrization technique for discrete ply-angle problems with manufacturing constraints.” In: *Structural and Multidisciplinary Optimization* 48.2 (2013), pp. 379–393.
- [Kha11] A. Khani, S. T. IJsselmuiden, M. M. Abdalla, and Z. Gürdal. “Design of variable stiffness panels for maximum strength using lamination parameters.” In: *Composites Part B: Engineering* 42.3 (2011), pp. 546–552.
- [Kli09] T. Klimmek. “Parameterization of topology and geometry for the multidisciplinary optimization of wing structures.” In: *CEAS 2009 - European Air and Space Conference*. Manchester, UK, 2009.
- [Kli12] T. Klimmek. *ModGen Benutzerhandbuch*. Göttingen - DLR Institute of Aeroelasticity, 2012.
- [Kom06] Z. Komargodski and D. Levin. “Hermite Type Moving-least-squares Approximations.” In: *Comput. Math. Appl.* 51.8 (2006), pp. 1223–1232.
- [Kro75] N. J. J. Krone. “Divergence Elimination with Advanced Composites.” In: *AIAA paper* 75-1009 (1975).
- [Kru12] M. Kruse, T. Wunderlich, and L. Heinrich. “A Conceptual Study of a Transonic NLF Transport Aircraft with Forward Swept Wings.” In: *30th AIAA Applied Aerodynamics Conference*. New Orleans, FL, June 2012.
- [Leg12] J. A. Leggett, B. Elias, and D. T. Shedd. *Aviation and the European Union’s Emission Trading Scheme, R42392*. Tech. rep. Congressional Research Service, 2012.
- [Leo12] D. M. Leon, C. E. Souza, J. S. O. Fonseca, and R. G. A. Silva. “Aeroelastic tailoring using fiber orientation and topology optimization.” In: *Structural and Multidisciplinary Optimization* 46.5 (2012), pp. 663–677.
- [Lib92] L. Librescu and O. Song. “On the static aeroelastic tailoring of composite aircraft swept wings modelled as thin-walled beam structures.” In: *Composites Engineering* 2.5-7 (1992), pp. 497–512.
- [Liu00] B. Liu, R. T. Haftka, and M. A. Akgün. “Two-level composite wing structural optimization using response surfaces.” In: *Structural and Multidisciplinary Optimization* 20.2 (2000),
- [Liu04] B. Liu, R. T. Haftka, and P. Trompette. “Maximization of buckling loads of composite panels using flexural lamination parameters.” In: *Structural and Multidisciplinary Optimization* 26.1 (2004), pp. 28–36.
- [Liu13] D. Liu and V. V. Toropov. “A lamination parameter-based strategy for solving an integer-continuous problem arising in composite optimization.” In: *Computers & Structures* 128 (2013), pp. 170–174.
- [Mar13] J. R. R. A. Martins and A. B. Lambe. “Multidisciplinary Design Optimization: A Survey of Architectures.” In: *AIAA Journal* 51 (2013), pp. 2049–2075.

- [Med13] Y. Meddaikar. “Composite Optimization using a Modified Shepard’s Method and Stacking Sequence Tables.” Master Thesis. Delft University of Technology, 2013.
- [Meg99] T. H. G. Megson. *Aircraft Structures for Engineering Students*. Refereed Engineering. Edward Arnold, 1999.
- [Mik93] M. Miki and Y. Sugiyama. “Optimum design of laminated composite plates using lamination parameters.” In: *AIAA Journal* 31.5 (1993), pp. 921–922.
- [Mit99] M. Mitchell. *An introduction to genetic algorithms*. 5th ed. Cambridge, MA: The MIT Press, 1999.
- [Moo04] G. J. Moore and MacNeal-Schwendler Corporation. *MSC.Nastran 2004, Design Sensitivity and Optimization User’s Guide*. Santa Ana, CA: MacNeal-Schwendler Corp., 2004.
- [Nag11] A. P. Nagy. “Isogeometric design optimisation.” PhD Thesis. TU Delft, 2011.
- [Nat98] J. K. Nathman. “Subsonic Panel Methods—Second (Order) Thoughts.” In: *AIAA Paper* (1998), pp. 98–5563.
- [Neu08] J. Neumann, J. Nitzsche, and R. Voss. “Aeroelastic Analysis by Coupled Non-Linear Time Domain Simulation.” In: *AVT-154 Specialists Meeting on Advanced Methods in Aeroelasticity*. Loen, May 2008.
- [Neu11] J. Neumann. *Zur Berücksichtigung der Gewichtskräfte im Modalansatz, DLR-IB 232-2011 J 04*. Tech. rep. 2011, p. 35.
- [Neu13] J. Neumann and W. Krüger. “Coupling Strategies for Large Industrial Models.” In: *Computational Flight Testing SE - 14*. Vol. 123. 2013, pp. 207–222.
- [Niu88] M. C.-Y. Niu. *Airframe Structural Design: Practical Design Information and Data on Aircraft Structures*. Hong Kong: Conmilit Press Ltd, 1988.
- [Olm93] R. Olmedo and Z. Gürdal. “Buckling Response of Laminates with Spatially Varying Fiber Orientations.” In: *34th Structures, Structural Dynamics and Materials Conference*. La Jolla, CA, Apr. 1993, pp. 2261–2269.
- [Pal01] R. Palacios, H. Climent, A. Karlsson, and B. Winzell. “Assessment of strategies for correcting linear unsteady aerodynamics using CFD or experimental results.” In: *International Forum on Aeroelasticity and Structural Dynamics (IFASD)*. June 2001.
- [Ray04] M. Raymond. *MSC.Nastran 2005, DMAP Programmer’s Guide, Volume 1*. MacNeal-Schwendler Corp., 2004.
- [Rin94] U. T. Ringertz. “On structural optimization with aeroelasticity constraints.” In: *Structural and Multidisciplinary Optimization* 8.1 (1994), pp. 16–23.
- [Rod04] W. P. Rodden, E. H. Johnson, and MacNeal-Schwendler Corporation. *MSC.Nastran Version 68, Aeroelastic Analysis User’s Guide*. Santa Ana, CA: MacNeal-Schwendler Corp., 2004.

- [Rod72] W. P. Rodden, J. P. Giesing, and T. P. Kalman. “Refinement of the nonplanar aspects of the subsonic doublet-lattice lifting surface method.” In: *Journal of Aircraft* 9.1 (1972), pp. 69–73.
- [Sch02] G. Schuhmacher, I. Murra, L. Wang, A. Laxander, O. O’Leary, and M. Herold. “Multidisciplinary Design Optimization of a Regional Aircraft Wing Box.” In: *9th AIAA/ISSMO Symposium on Multidisciplinary Analysis and Optimization*. Sept. 2002.
- [Sch06] D. Schwamborn, T. Gerhold, and R. Heinrich. “The DLR TAU-Code: Recent Applications in Research and Industry.” In: *ECCOMAS CFD Conference*. Egmond aan Zee, Sept. 2006.
- [Sch07] H. Schürmann. *Konstruieren mit Faser-Kunststoff-Verbunden*. VDI-Buch. Springer London, Limited, 2007.
- [Sch73] L. A. Schmit Jr and B. Farshi. “Optimum laminate design for strength and stiffness.” In: *International Journal for Numerical Methods in Engineering* 7.4 (1973), pp. 519–536.
- [Sch77] L. A. Schmit Jr and B. Farshi. “Optimum Design of Laminated Fibre Composite Plates.” In: *International Journal for Numerical Methods in Engineering* 11.4 (1977), pp. 623–640.
- [Sei11] A. Seitz, M. Kruse, T. Wunderlich, J. Bold, and L. Heinrich. “The DLR Project LamAiR: Design of a NLF Forward Swept Wing for Short and Medium Range Transport Application.” In: *29th AIAA Applied Aerodynamics Conference*. Reston, VA, June 2011.
- [Sen04] M. Sensmeier and J. Samareh. “A Study of Vehicle Structural Layouts in Post-WWII Aircraft.” In: *45th AIAA/ASME/ASCE/AHS/ASC Structures, Structural Dynamics, and Materials Conference*. Palm Springs, CA, Apr. 2004.
- [Set06a] S. Setoodeh, M. M. Abdalla, and Z. Gürdal. “Approximate feasible regions for lamination parameters.” In: *Collection of Technical Papers - 11th AIAA/ISSMO Multidisciplinary Analysis and Optimization Conference*. Vol. 2. Portsmouth, VA, 2006, pp. 814–822.
- [Set06b] S. Setoodeh, M. M. Abdalla, and Z. Gürdal. “Design of variable-stiffness laminates using lamination parameters.” In: *Composites Part B: Engineering* 37.4-5 (2006), pp. 301–309.
- [She68] D. Shepard. “A Two-dimensional Interpolation Function for Irregularly-spaced Data.” In: *Proceedings of the 1968 23rd ACM National Conference*. ACM ’68. New York, NY: ACM, 1968, pp. 517–524.
- [Shi86] M. H. Shirk, T. J. Hertz, and T. A. Weisshaar. “Aeroelastic tailoring - Theory, practice, and promise.” In: *Journal of Aircraft* 23.1 (1986), pp. 6–18.
- [Sim02] M. Simons. *Segelflugzeuge 1945 - 1965*. Equip, 2002.
- [Sob90] J. Sobieszcanski-Sobieski. “Sensitivity Analysis and Multidisciplinary Optimization for Aircraft Design: Recent Advances and Results.” In: *Journal of Aircraft* 27.12 (1990), pp. 993–1001.

- [Sob97] J. Sobieszczanski-Sobieski and R. T. Haftka. "Multidisciplinary aerospace design optimization: survey of recent developments." In: *Structural optimization* 14.1 (1997), pp. 1–23.
- [Sta79] J. H. Starnes Jr and R. T. Haftka. "Preliminary Design of Composite Wings for Buckling, Strength, and Displacement Constraints." In: *Journal of Aircraft* 16.8 (1979), pp. 564–570.
- [Sto13] O. Stodieck, J. E. Cooper, P. M. Weaver, and P. Kealy. "Improved aeroelastic tailoring using tow-steered composites." In: *Composite Structures* 106 (2013), pp. 703–715.
- [Tho99] F. Thomas and J. Milgram. *Fundamentals of Sailplane Design*. College Park Press, 1999.
- [Thu10] G. Thuwis, R. De Breuker, M. M. Abdalla, and Z. Gürdal. "Aeroelastic tailoring using lamination parameters." In: *Structural and Multidisciplinary Optimization* 41.4 (2010), pp. 637–646.
- [Tom11] M. Tomac and D. Eller. "From geometry to CFD grids - An automated approach for conceptual design." In: *Progress in Aerospace Sciences* 47.8 (2011), pp. 589–596.
- [Tsa68] S. W. Tsai and N. J. Pagano. *Invariant properties of composite materials*. Defense Technical Information Center, 1968.
- [Tsa80] S. W. Tsai and H. Hahn. *Introduction to Composite Materials*. Technomic Publishing Co, 1980.
- [US 96] U.S. Product Data Association. *Initial Graphics Exchange Specification, IGES 5.3*. Tech. rep. Charleston: U.S. Product Data Association, 1996.
- [Van11] J. M. J. F. Van Campen. "Optimum lay-up design of variable stiffness composite structures." PhD Thesis. TU Delft, 2011.
- [Van12] J. M. J. F. Van Campen, C. Kassapoglou, and Z. Gürdal. "Generating realistic laminate fiber angle distributions for optimal variable stiffness laminates." In: *Composites Part B: Engineering* 43.2 (2012), pp. 354–360.
- [Van89] G. N. Vanderplaats and T. A. Weisshaar. "Optimum design of composite structures." In: *International Journal for Numerical Methods in Engineering* 27.2 (1989), pp. 437–448.
- [Ven99] S. Venkataraman and R. T. Haftka. "Optimization of composite panels- A review." In: *American Society for Composites, 14th Technical Conference*. Fairborn, OH, 1999, pp. 479–488.
- [Wei80] T. A. Weisshaar. "Divergence of Forward Swept Composite Wings." In: *Journal of Aircraft* 17.6 (1980), pp. 442–448.
- [Wei81] T. A. Weisshaar. "Aeroelastic Tailoring of Forward Swept Composite Wings." In: *Journal of Aircraft* 18.8 (1981), pp. 669–676.
- [Wei98] T. A. Weisshaar. "Aeroelastic Tailoring for Improved UAV Performance." In: *Aviation* 37.10 (1998), pp. 1461–1471.

- [Whi81] D. Whitfield, A. Jameson, and W. Schmidt. *Viscid-Inviscid Interaction on Airfoils Using Euler and Inverse Boundary-Layer Equations*. Tech. rep. Göttingen: DFVLR-AAVA, US-German Data Exchange Meeting, 1981.
- [Wit10] A. de Wit and F. van Keulen. “Overview of Methods for Multi-Level and/or Multi-Disciplinary Optimization.” In: *51st AIAA/ASME/ASCE/AHS/ASC Structures, Structural Dynamics, and Materials Conference*. Orlando, FL, Apr. 2010.
- [Wri08] J. R. Wright and J. E. Cooper. *Introduction to Aircraft Aeroelasticity and Loads*. Aerospace Series (PEP) Series. John Wiley & Sons, 2008.
- [Zie00] O. C. Zienkiewicz and R. L. Taylor. *The Finite Element Method - Volume 1: The Basis*. 5th ed. The Finite Element Method. Oxford: Butterworth-Heinemann, 2000.

Johannes Karl Stefan Dillinger was born on the 6th of November 1976 in Bernkastel-Kues. His parents Christiane and Stefan considered using Maria as his middle name, but then decided to go for his fathers and grandfathers names instead. Luckily and also a little sadly. He grew up about three kilometers from Bernkastel, in the little village of Wehlen, home of the famous Riesling vineyard *Wehlener Sonnenuhr* and of the only suspension bridge along the Mosel river. After finishing primary school in Wehlen, he went to the big city, attending the Nikolaus-von-Kues Gymnasium in Bernkastel, where he received his Abitur in 1995. A ten month interlude in the german military caused him to realize that time spent rather pointlessly can also teach you a lesson, namely, that starting his agreed job as an aircraft technician for the military was nothing he wanted to do in the years to come.



A game-changing encounter with a model plane catalog from *Graupner* in 1985, which is still in his possession, secretly hidden in a huge pile of catalogs he has collected since then, let him fall in love with everything to do with flying. Although some of the model planes he began to build for some reasons decided not to fly, his determination to know why was larger than the disappointment of seeing them crash and sometimes even vaporize into balsa wood clouds. So, he started his academic career in the field of Aerospace Engineering at the Fachhochschule Aachen in 1996, from where he graduated with distinction in 2000. During this time he had the opportunity to study for one semester in 1999 at the University of Missouri/Rolla, USA, followed by another stay abroad at the Technische Universiteit Delft, Netherlands, where he wrote his Diploma Thesis about the aerodynamic design of a span extension for a sailplane, the type of aircraft he loves the most. Since then, the aerodynamic design of everything that is assumed to be really aerodynamic has played a role in his life, giving him the chance to work on some very interesting flying and also ground vehicles. He still is very happy to get a call every now and then from his mentor Loek Boermans, informing him about nice new projects.

Having decided to continue his studies at Delft at the chair of Aerospace Structures

with a Master focusing on fiber reinforced materials, he bridged the remaining time till the winter semester 2001, and also a bit further, with his first, real world job at the CFD company *Flowmotion*, performing aerodynamic analyses on the *Cargolifter* airship, sadly the project went on to, financially, vaporize. The Master Thesis that he started in 2003 was a crucial experience and a once in a lifetime opportunity in one, allowing him to participate in the aerodynamic and structural design of a new open class sailplane. This finally was a plane that did not vaporize, it went on successfully to participate in the World Gliding Championships of 2012.

After graduating with honors from Delft at the end of 2006, a 9-month interlude in Luxembourg, working as a project engineer for a lightweight material company *Euro-Composites*, ended with an offer from the *DLR - Institute of Aeroelasticity* in Göttingen, where he started in late summer 2007 as a research scientist and has stayed ever since. In close collaboration with the Aerospace Structures chair at TU Delft the opportunity arose to combine work and academia in a PhD dissertation. Which you now hold in your hands or are reading from your screen.

In his spare time Johannes enjoys bicycle riding, running, paragliding, the lovely Mosel river, Riesling wine, carbon fiber eyewear, and vaporizing, still, some model airplanes. He pretends to play the piano, french horn and tuba, unfortunately all three only to a level that allows him to perform at carnival parties rather than concerts.

Most likely none of the above will compare to the challenges he and his girlfriend Melanie (wife? when did I hand this in?) will be facing next. Children are the future

☺

Journal Papers:

J.K.S. Dillinger, T. Klimmek, M.M. Abdalla, & Z. Gürdal. *Stiffness Optimization of Composite Wings with Aeroelastic Constraints*. Journal of Aircraft, 50.4, pp. 1159-1168, 2013.

B. Stickan, J.K.S. Dillinger, G. Schewe. *Computational Aeroelastic Investigation of a Transonic Limit-Cycle-Oscillation Experiment at a Transport Aircraft Wing Model*. Journal of Fluids and Structures, accepted for publication, 2013.

J.K.S. Dillinger, R. Butler, G. Waibel, L.M.M. Boermans. *Aerodynamic and Structural Design of the Open Class Sailplane Concordia*. Technical Soaring, accepted for publication, 2013.

Conference Papers:

R. De Breuker, M.M. Abdalla, N. Werter, L. Vandewaeter, E. Ferede, J.K.S. Dillinger, W. Krüger. *An Aeroelastic Multi-Fidelity Approach for Aeroelastic Tailoring*. International Forum on Aeroelasticity & Structural Dynamics (IFASD), Bristol, 2013.

J.K.S. Dillinger, M.M. Abdalla, T. Klimmek, & Z. Gürdal. *Static Aeroelastic Stiffness Optimization and Investigation of Forward Swept Composite Wings*. 10th World Congress on Structural and Multidisciplinary Optimization, Orlando, Florida, 2013.

J.K.S. Dillinger, M.M. Abdalla, T. Klimmek, M.M. Abdalla, & Z. Gürdal. *Stiffness Optimization of Composite Wings with Aeroelastic Constraints*. 14th AIAA/ISSMO Multidisciplinary Analysis and Optimization Conference, Indianapolis, Indiana, 2012.

M. Ritter and J. Dillinger. *Nonlinear numerical flight dynamics for the prediction of maneuver loads*. IFASD 2011 - 15th International Forum on Aeroelasticity and Structural Dynamics, Paris, 2011.

B. Stickan, J.K.S. Dillinger. *Influence of a Detailed Structural Modeling on Steady and Unsteady Aerodynamics Using the Example of the Aerostabil Windtunnel Model*. 11th ONERA-DLR Aerospace Symposium, ODAS, Toulouse, 2011.

B. Stickan, J.K.S. Dillinger, G. Schewe. *Coupled CFD-CSM Simulations of Aerostabil Windtunnel Experiments, Considering Structural Shell Modelling*. 17th DGLR / STAB Fach-Symposium zur Strömungsmechanik, Berlin, 2010.

Stellingen

behorende bij het proefschrift

Static Aeroelastic Optimization of Composite Wings with Variable Stiffness Laminates

Johannes Karl Stefan Dillinger

4 juni 2014

1. De optimalisatie van de stijfheidsverdeling van composieten vleugels met aeroelastische randvoorwaarden draagt significant bij aan de reductie van massa, tijd en geld. De droom van elke vliegtuigbouwer, zou men denken.
2. De optimalisatie van composieten vleugels is meer dan de koppeling tussen buiging en torsie. Deze koppeling is eerder een middel dan een doel.
3. In het algemeen geven ongebalanceerde variabele stijfheidslaminaten betere resultaten dan gebalanceerde. Dit geldt vaak ook voor ongebalanceerde en gebalanceerde mensen.
4. Het is niet nodig om expliciet te kijken naar vermindering van de belastingen of het buigmoment in de vleugelwortel wanneer men massa minimaliseert.
5. Proberen om elke dag de vrije tijd te maximaliseren leidt in het algemeen tot minder vrije tijd.
6. De regel van drie: Inschatten dat iets in n dagen gedaan kan worden, terwijl het in werkelijkheid $\approx 3n$ dagen duurt.
7. Ingenieurs kunnen zelfs de vreemdste numerieke resultaten verklaren. Dit is een gave, maar zeker ook een gevaar.
8. Wezens die in staat zijn om in n dimensies te kijken, waarbij n significant groter is dan 3, zullen de optimalisatiekoningen zijn, wanneer ze op aarde zullen aankomen.
9. Aeroelasticiteit bevindt zich op de grens tussen de twee leerstoelen van constructies en aerodynamica. Echter, zonder aeroelasticiteit zouden deze twee stoelen ofwel een houtblok ofwel een vliegend tapijt zijn. Maar wanneer je beiden in de lucht probeert te gooien, wordt het duidelijk: geen van beide stoelen zal oprijzen zoals de aeroelastische stoel...
10. Het weze duidelijk dat *Mosel Riesling* geen oplossing is voor stresserende situaties, zeker niet wanneer men een doctoraat afwerkt, en doch, hij smaakt fantastisch.

*Deze stellingen worden opponeerbaar en verdedigbaar geacht
en zijn als zodanig goedgekeurd door de promotor Prof. dr. Z. Gürdal.*

Propositions

accompanying the thesis

Static Aeroelastic Optimization of Composite Wings with Variable Stiffness Laminates

Johannes Karl Stefan Dillinger

4 June 2014

1. The consideration of aeroelastic constraints in a composite wing stiffness optimization contributes significantly to saving mass, time and money. A manufacturer's dream, one should think.
2. There is more to composite wing optimization than just bending-torsion coupling. It is foremost a means, rather than a goal.
3. In general, variable stiffness unbalanced laminates outperform balanced ones. Interestingly enough, the same often applies to unbalanced and balanced individuals.
4. There is no need to explicitly worry about load reduction or root bending moment when mass is the optimization objective.
5. Generally, attempts to optimize daily routines towards an increase of spare time results in a decrease of the latter.
6. Rule of three: Estimations may suggest that something will require n days to be completed, yet reality proves that it will be completed only after $\approx 3n$ days.
7. Engineers are capable of providing explanations for each ever so weird computational result. This is as much a gift as it is a danger.
8. Species that can see n dimensions, where n is considerably larger than 3, will be the kings of optimization, once they arrive on earth.
9. Aeroelasticity usually seems a bit *caught between the chairs* of structures and aerodynamics. However, without aeroelasticity the chair will either be a wooden block or a flying carpet. Try to throw both of them in the air, then you'll get the picture: none will soar like the aeroelastic chair...
10. It goes without saying that *Mosel Riesling* is not the solution to stressful situations, especially when finishing a PhD, and yet, it tastes awesome.

*These propositions are regarded as opposable and defensible,
and have been approved as such by the supervisor Prof. dr. Z. Gürdal.*

Static Aeroelastic Optimization of Composite Wings with Variable Stiffness Laminates

Static Aeroelastic Optimization of Composite Wings J.K.S. Dillinger

 TU Delft

ISBN 978-94-6203-589-8



9 789462 035898

Johannes Karl Stefan Dillinger